



**HAL**  
open science

# Silicon photonics based on monolithic integration of III-V nanostructures on silicon

Thanh Tra Nguyen

► **To cite this version:**

Thanh Tra Nguyen. Silicon photonics based on monolithic integration of III-V nanostructures on silicon. Other [cond-mat.other]. INSA de Rennes, 2013. English. NNT: 2013ISAR0021 . tel-01065999

**HAL Id: tel-01065999**

**<https://theses.hal.science/tel-01065999>**

Submitted on 19 Sep 2014

**HAL** is a multi-disciplinary open access archive for the deposit and dissemination of scientific research documents, whether they are published or not. The documents may come from teaching and research institutions in France or abroad, or from public or private research centers.

L'archive ouverte pluridisciplinaire **HAL**, est destinée au dépôt et à la diffusion de documents scientifiques de niveau recherche, publiés ou non, émanant des établissements d'enseignement et de recherche français ou étrangers, des laboratoires publics ou privés.

Thèse



**THESE INSA Rennes**  
sous le sceau de l'Université européenne de Bretagne  
pour obtenir le titre de  
**DOCTEUR DE L'INSA DE RENNES**  
Spécialité : Physique-Optoélectronique

présentée par  
**Thanh Tra NGUYEN**

**ECOLE DOCTORALE : SDLM**  
**LABORATOIRE : FOTON-OHM INSA de Rennes**

# Silicon photonics based on monolithic integration of III-V nanostructures on silicon

**Thèse soutenue le 17.09.2013**  
devant le jury composé de :

**Nicolas BERTRU**

Prof. des Universités, FOTON-OHM, INSA de Rennes / Président  
**Daniel BOUCHIER**

Dir. de recherche CNRS, Institut d'Electronique Fondamentale,  
Orsay / Rapporteur

**Chantal FONTAINE**

Dir. de recherche CNRS, Laboratoire d'Analyse et d'Architecture  
des Systèmes, Toulouse / Rapporteur

**Guillaume SAINT-GIRONS**

Chargé de Recherche CNRS HDR, Institut des Nanosciences de  
Lyon / Examineur

**Alexandre BOULLE**

Chargé de Recherche CNRS, Science des Procédés Céramiques  
et de Traitements de Surface, Université de Limoges / Examineur

**Charles CORNET**

MCF, FOTON-OHM, INSA de Rennes / Co-encadrant de thèse

**Olivier DURAND**

Prof. des Universités, FOTON-OHM, INSA de Rennes / Directeur  
de thèse

# Silicon photonics based on monolithic integration of III-V nanostructures on silicon

Thanh Tra NGUYEN



---

---

# REMERCIEMENTS

---

---

Ce travail de thèse a été réalisé au laboratoire FOTON (Fonction Optiques pour les TélécommunicatiONs) – équipe OHM (Optoélectronique – Hétéroépitaxie et Matériaux) à l'INSA de Rennes, sous le support financier des projets ANR SINPHONIC et OPTOSI. Je tiens tout d'abord à remercier Monsieur Alain LE CORRE, directeur de l'unité, de m'avoir accueilli au sein du laboratoire.

Je remercie vivement Monsieur Daniel BOUCHIER, directeur de recherche CNRS, directeur adjoint de l'Institut d'Électronique Fondamental à Orsay, et Madame Chantal FONTAINE, directrice de recherche CNRS, LAAS à Toulouse, d'avoir accepté de rapporter ce manuscrit. Je voudrais remercier également aux autres membres du jury : Monsieur Guillaume SAINT-GIRONS, chargé de recherche CNRS (INL, Lyon), Monsieur Alexandre BOULLE, chargé de recherche CNRS (SPCTS, université de Limoges), Monsieur Nicolas BERTRU, Professeur à l'INSA de Rennes. Merci Nicolas d'avoir présidé ma soutenance, et un grand merci aux Messieurs Dame du jury d'avoir passé un long trajet pour assister à ma soutenance.

Je remercie mes chers encadrants : Monsieur Olivier DURAND, Monsieur Charles CORNET et Monsieur Antoine LETOUBLON. Je les remercie de m'avoir confié ce sujet intéressant et de m'avoir encadré tout au long de ces 3 années, qui sont toujours là pour m'aider et me donner des conseils pour que je puisse mener à bien ce travail de thèse. J'apprécie leur patience, leur enthousiasme et leur temps investi sur moi. Je les suis très reconnaissant de m'avoir transmis leur savoir au cours de ces années. Leur grande rigueur a été la clé du bon déroulement de ce travail et a permis d'aboutir dans les meilleures conditions.

Pendant ces 3 années de thèse, j'ai effectué 2 campagnes d'expérience au Synchrotron à Grenoble (ESRF) pour analyser des défauts plans dans des nano-couches de GaP/Si(001). Je souhaite remercier Madame Nathalie BOUDET et Monsieur Jean-François BERAR, les scientifiques sur la ligne de lumière BM02 (D2AM) à l'ESRF pour leur support technique et leur aide pour des réglages pendant les expériences. Mes

remerciements s'adressent également à Madame Anne PONCHET et Monsieur Julien STODOLNA au CEMES, Toulouse pour les jolies images de TEM des échantillons de GaP/Si. Je remercie aussi Monsieur Pascal TURBAN à l'Institut de Physique de Rennes pour des mesures STM des boîtes quantiques InGaAs/GaP, Madame Valérie DEMANGE au laboratoire LCSIM à l'Université de Rennes 1 de m'avoir permis à utiliser le diffractomètre Bruker D8 pour analyser mes échantillons durant ces 3 années.

Il est venu le moment de remercier mes collègues les plus proches, mes « co-bureaux » et « co-labo », qui m'ont partagé des moments aussi bien agréables au laboratoire : Cédric ROBERT, Thomas QUINCI, Sami ALMOSNI, Kamil KLAIME, Jithesh KUYVALIL, Yu ZHAO, Yanping WANG, Marianne PREVOT et Jérôme SAUBLET. Je suis très heureux d'avoir les rencontré et travaillé avec eux. Je remercie aussi l'ensemble des personnels au laboratoire FOTON donc parmi lesquels je souhaite citer : Tony ROHEL, Nicolas CHEVALIER, Olivier DEHAESE, Karine TAVERNIER, Julie LE POULIQUEN, Julien LAPEYRE, Mickaël COQUEUX. Merci pour ces nombreuses pauses cafés, discussions, moments de Barbecue, dîners de fin d'année et de bonne humeur partagés aussi bien au sein du laboratoire qu'à l'extérieur. Vous avez rendu ces 3 années passées sur Rennes très agréable grâce à votre compagnie.

J'exprime également mes remerciements les plus sincères auprès de mes amis parmi lesquels je citerai Xuan-Quy DAO, Duc-Long-Hung NGUYEN, Cam-Tu PHAN LE, Tuan-Anh DANG, Tuan-Anh TRUONG,... et en particulier ma femme Thi-Thu-Thuy NGUYEN qui est toujours présente pour m'écouter et me partager des bons comme des mauvais moments de la vie d'un doctorant, et qui m'a aidé de préparer le pôt de thèse qui était « au niveau d'une thèse » (selon Slimane LOUALICHE – Professeur au laboratoire, après avoir goûté tous les plats préparés par ma femme).

Enfin, je tiens à remercier tout particulièrement ma famille (mes parents, mes frères Thanh-Binh et Cao-Nguyen) de m'avoir soutenue malgré la distance pendant ces 3 années. Leurs encouragements nombreux m'ont permis de prendre petit à petit confiance en moi et d'arriver au bout de ce long projet.

Un grand merci final à vous tous, et que les oubliés me pardonnent !

---

---

# TABLE OF CONTENT

---

---

REMERCIEMENTS.....	I
TABLE OF CONTENT .....	I
INTRODUCTION .....	1
REFERENCES.....	4
<b>CHAPTER 1. SILICON PHOTONICS – STATE-OF-THE-ART .....</b>	<b>5</b>
1.1    SILICON: AN INEFFICIENT LIGHT EMITTER .....	5
1.2    SILICON-BASED LIGHT EMISSION .....	7
1.2.1 <i>Erbium doping</i> .....	7
1.2.2 <i>Low dimensional structures</i> .....	7
(a)    Porous silicon.....	7
(b)    Silicon nano-crystals.....	8
(c)    Erbium coupled with silicon nano-crystals.....	8
1.2.3 <i>Raman excitation</i> .....	9
1.3    BAND-GAP ENGINEERING USING GERMANIUM .....	9
1.4    INTEGRATION OF III-V MATERIALS ON SILICON.....	12
1.4.1 <i>Hybrid silicon lasers (wafer bonding)</i> .....	12
1.4.2 <i>Monolithic growth of III-V on Si</i> .....	14
(a)    Metamorphic approach.....	15
(b)    Pseudomorphic approach.....	19
1.4.3 <i>Active areas in the pseudomorphic approach</i> .....	20
1.5    CHALLENGES OF GROWING GAP/Si .....	21
1.5.1 <i>Difference in lattice constant</i> .....	21
1.5.2 <i>Difference in thermal expansion behavior</i> .....	23
1.5.3 <i>Cross-doping</i> .....	25
1.5.4 <i>Charge neutrality of the heterointerface</i> .....	25
1.5.5 <i>Antiphase domains</i> .....	26
1.5.6 <i>Stacking faults, Microtwins</i> .....	29
1.6    CONCLUSION .....	31
REFERENCES.....	31

<b>CHAPTER 2. GAPN – NITROGEN INCORPORATION .....</b>	<b>37</b>
2.1 INTRODUCTION .....	37
2.2 SAMPLES GROWTH .....	38
2.3 PLASMA PARAMETERS OPTIMIZATION.....	39
2.4 DETERMINATION OF NITROGEN CONTENT.....	40
2.5 CONTROL OF NITROGEN CONTENT .....	44
2.5.1 <i>Nitrogen-Phosphorus competition</i> .....	44
2.5.2 <i>Growth rate and valve opening</i> .....	47
2.6 INFLUENCE OF SURFACE ROUGHNESS ON N INCORPORATION .....	49
2.6.1 <i>Samples preparation</i> .....	49
2.6.2 <i>Surface investigation</i> .....	50
2.6.3 <i>Strain induced effect investigation</i> .....	52
2.6.4 <i>Step edges incorporation mechanism</i> .....	54
2.7 SUMMARY .....	58
REFERENCES.....	58
<b>CHAPTER 3. ACTIVE AREA: (IN,GA)AS/GAP QUANTUM DOTS .....</b>	<b>61</b>
3.1 GROWTH OF (IN,GA)AS QDS ON GAP (001) SUBSTRATE .....	61
3.1.1 <i>Growth conditions and structural analysis</i> .....	61
(a) Growth by GSMBE .....	61
(b) Growth by SSMBE.....	62
(c) Structural analysis .....	62
3.1.2 <i>Growth optimization of (In,Ga)As/GaP QDs</i> .....	65
(a) Deposition thickness.....	65
(b) Growth temperature .....	66
(c) Indium composition.....	69
(d) Annealing time.....	70
3.1.3 <i>Discussion</i> .....	71
3.2 OPTICAL PROPERTIES OF (IN,GA)AS/GAP QDS .....	72
3.2.1 <i>Tight-binding calculation</i> .....	72
3.2.2 <i>Room temperature photoluminescence</i> .....	73
3.2.3 <i>Annealing effect</i> .....	76
3.3 SINGLE (IN,GA)AS/GAP QUANTUM DOT STRUCTURE .....	77
3.3.1 <i>STM transfer validation</i> .....	77
3.3.2 <i>Single QD morphology</i> .....	78
3.3.3 <i>Unusual C<sub>2</sub> symmetry of the (In,Ga)As/GaP QD</i> .....	82
3.4 SUMMARY .....	85
REFERENCES.....	86

<b>CHAPTER 4. HOMOEPITAXIAL GROWTH OF SILICON.....</b>	<b>89</b>
4.1 SURFACE CLEANING .....	89
4.2 HOMOEPITAXIAL GROWTH OF SILICON USING UHV/CVD REACTOR .....	95
4.2.1 <i>Silicon growth mechanism</i> .....	95
4.2.2 <i>Growth conditions</i> .....	97
4.2.3 <i>Control of hydrogenation on the Si (001) surface</i> .....	100
(a) Hydrogen desorption.....	100
(b) Surface passivation in-situ .....	102
4.2.4 <i>Silicon surface step doubling</i> .....	106
(a) The silicon surface.....	106
(b) RHEED monitoring.....	108
4.3 SUMMARY .....	113
REFERENCES.....	114
<b>CHAPTER 5. PLANAR DEFECTS CHARACTERIZATION AND GROWTH OPTIMIZATION OF GAP/SI .....</b>	<b>117</b>
5.1 SYNCHROTRON EXPERIMENT SETUP .....	117
5.2 ANTI-PHASE DOMAINS (APD) ANALYSIS .....	118
5.2.1 <i>Principle of APD detection using XRD</i> .....	118
5.2.2 <i>APD analysis using Synchrotron XRD</i> .....	123
(a) Samples .....	123
(b) Lateral correlation length of APD .....	124
5.3 MICROTWIN STUDY IN GAP/SI NANOLAYERS .....	132
5.3.1 <i>Detection of microtwins (MT)</i> .....	132
(a) MT detection using Synchrotron source .....	132
(b) MT detection using laboratory XRD source.....	136
5.3.2 <i>Influence of the growth temperature on the MT</i> .....	137
(a) Synchrotron XRD study.....	137
(b) TEM study.....	142
5.3.3 <i>Microtwins anisotropy: a quantitative study</i> .....	144
(a) Samples .....	144
(b) MT quantification using Synchrotron radiation and XPAD detector .....	144
(c) MT quantification using laboratory XRD .....	148
(d) Correction of measurement data .....	150
(e) Evidence of MT anisotropy .....	152
5.4 GROWTH OPTIMIZATION OF GAP/SI.....	156
5.4.1 <i>Optimization of the MEE procedure</i> .....	157
5.4.2 <i>Optimization of GaP MBE overgrowth</i> .....	159
5.5 SUMMARY .....	161
REFERENCES.....	162

<b>GENERAL CONCLUSIONS AND FUTURE WORKS .....</b>	<b>165</b>
<b>APPENDICES: DESCRIPTION OF GROWTH TECHNIQUES AND CHARACTERIZATION METHODS .....</b>	<b>169</b>
A.    MOLECULAR BEAM EPITAXY (MBE).....	169
A-1.    Growth cluster UHV/CVD - MBE .....	172
A-2.    The gas source MBE chamber.....	174
A-3.    ADDON RF plasma cell – atomic nitrogen generation .....	174
A-4.    Reflection High-Energy Electron Diffraction (RHEED).....	176
B.    ATOMIC FORCE MICROSCOPY (AFM).....	181
C.    STRUCTURAL CHARACTERIZATION BY X-RAY SCATTERING .....	184
C-1.    High resolution X-ray diffraction (HRXRD) – lab setup.....	184
C-2.    Synchrotron X-ray diffraction .....	192
REFERENCES.....	197
<b>RESUME DE THESE.....</b>	<b>199</b>
REFERENCES.....	209
<b>LIST OF PUBLICATIONS ISSUED FROM THIS THESIS .....</b>	<b>211</b>
REGULAR ARTICLES.....	211
CONFERENCE PAPERS.....	212

---

---

# INTRODUCTION

---

---

If the 20<sup>th</sup> century has been noticed by the revolution of electronics and information technology, the 21<sup>st</sup> century would be the century of photonics and communications. In the past sixty years, human society has witnessed a spectacular development of electronics based on silicon – one of the most abundant and relatively low cost materials on the Earth. Coming after the stone, iron and industrial ages, the electronic age started with the invention of transistor in 1947 by J. Bardeen, W. H. Brattain and W. Shockley.<sup>[BaBr48, Bard47]</sup> Ten years later, the first electronic integrated circuit was developed by J. S. Kilby in 1957. The first microprocessor chip (model 4004) with 2300 transistors was built by Intel in 1971. During these early days, Gordon Moore pointed out his famous empirical law: the number of transistors on an integrated circuit would double every 12 months (lately corrected to 18 months).<sup>[Moor65]</sup> Integrated circuits have grown exponentially from the very first 30-transistor devices of 1965's to today's high-end microprocessors exceeding one billion transistors integrated on a silicon chip, the size of a fingernail. Decades of research and manufacturing investment to drive the Moore's law has resulted in significant performance gains while simultaneously bringing about significant cost reductions. As an example, in 1968 the cost of a transistor was around one US dollar. By 1995, one dollar bought about 3000 transistors. Today, one dollar purchases about five million transistors.<sup>[PaLo10]</sup> It is no exaggeration to tell that silicon is a material where the extraordinary is made ordinary. It is and will be the material of future high-tech.

Nowadays, we are in the mass communications/information age enabled through the development and explosion of the internet. The evolution of the internet and of pervasive computing requires new solutions to enhance their technological foundations. Photonics and electronics are playing a fundamental role in this effort. Hence this is an age of golden opportunity to introduce and marry photonics with electronics. Indeed, most of the main semiconductor companies are aggressively addressing the telecommunications, data-communications and optoelectronics markets. The

integration of photonics with electronics has two principal driving forces that seemed unimaginable even just a decade ago:

- The requirements for smart optical networks, greater bandwidths, and lower cost are pushing the integration of electronics into photonics.
- The interconnect bottleneck for CMOS circuits operating above 10 GHz is pushing the integration of photonics into electronics for timing and possibly signal channels.

To implement these powerful technology drivers, a common platform is required that integrates both optical and electronic functionalities. This is then the next challenge: to turn silicon into the photonic material where the convergence between electronics and photonics can be realized. This raises several questions. Can photonics be 'siliconized'? Could the decades of research and manufacturing experience gained from the microelectronics industry be applied to photonics? Could silicon be used as an alternative to materials such as InP or GaAs typically used to produce optical devices? Could one monolithically integrate multiple photonic circuits on a single silicon chip to increase performance while simultaneously reducing cost? Could one implement standardization and high-volume manufacturing techniques to reduce cost? Could electronics and photonics be combined to bring new levels of integration, and possibly a derivative form of Moore's law to photonics?

These are very ambitious questions. Although it is well known that silicon is the optimal material for electronics, it is unfortunately inefficient for light emission due to its indirect band gap. Different approaches were proposed to enhance the efficiency of the light emission of Si, for example using Si-nanocrystals<sup>[PNMF00]</sup> or Er<sup>3+</sup>-doped Si nanocrystals.<sup>[FPCP94]</sup> The limitation of the indirect band gap was proposed to be evaded by using the intra valence-band transitions. Si/Ge quantum cascade lasers exploiting this effect were reported to show electroluminescence.<sup>[DDGS00]</sup> The first continuous wave (cw) all-silicon optically pumped Raman-laser was demonstrated in 2005.<sup>[LiBo10, RLJC05]</sup>

Other approach which has been intensively developed in the last ten years proposes to take advantage of the direct band gap of the compound III-V materials by using the so-called wafer bonding or chip bonding technique, onto silicon. This approach (developed by CEA-Leti or Intel laboratories for instance) is the most developed technologically, but obtaining a high density of integration and reliable devices with these solutions is still remained challenging.

The heterogeneous epitaxy of III-V semiconductors lattice-matched on Silicon has been extensively attractive during the last thirty years. This approach consists in growing direct bandgap semiconductors with high lattice mismatch on Si (metamorphic)<sup>[EHJU95]</sup> or growing quasi lattice matched materials on Si (pseudomorphic approach, as followed by FOTON-OHM laboratory, thus in the scope of this thesis).

## **Dissertation overview**

This PhD work focuses on the heterogeneous growth optimization of III-V nanostructures on Si (001) substrate displaying a miscut toward the [110] direction. The main purpose concerns the integration of efficient light sources on Si substrate for high-speed optical interconnects inter-and intra-chip, as a cornerstone for the development of optoelectronic integrated circuits (OEIC).

**In chapter 1**, state-of-the-art in the achieving of light emission on silicon substrate is introduced while highlighting the advantages and limitations of each system. Finally we present the motivation for choosing the pseudomorphic approach to monolithically integrate III-V optical sources on silicon, in parallel with challenges to be overcome.

**Chapter 2** summerizes the study of nitrogen incorporation into GaP while seeking lattice matching with Si. This study concerns the optimization of atomic nitrogen production by RF plasma, the study of growth conditions such as phosphorus flux, growth rate, etc. This study reveals a competition of P and N during GaPN growth and a strong relationship between the substrate surface roughness and nitrogen incorporation efficiency.

**Chapter 3** presents the growth of (In,Ga)As quantum dots on GaP(001) substrate because this system can be transferred in a straight forward way to Si(001) substrates.<sup>[PLRS13, SoSL10]</sup> Room temperature photoluminescence of high density and homogeneous (In,Ga)As/GaP quantum dots is demonstrated. The role of indium and the electronic band structure of these quantum dots are briefly discussed. The morphology is studied at the atomic scale by STM on single (In,Ga)As/GaP quantum dot and some structural aspects are discussed.

**In chapter 4** – homoepitaxial growth of silicon – we present the growth optimization of a silicon buffer layer on silicon substrate using the UHV/CVD chamber, including the optimization of chemical cleaning process, while seeking a smooth and

double atomic stepped surface which is suitable for subsequent growth of defects-free GaP thin films. A finally optimized Si buffer grown on 6°-off Si substrate with a flat and single domain surface is demonstrated.

**Finally**, as the main aim of this thesis, in the effort to control the structural defects (such as anti-phase domains, microtwins) at the GaP/Si interface, **chapter 5** introduces a methodology to quantify these defects by X-ray diffraction techniques using Synchrotron and laboratory setup. This study reveals a relationship between the growth temperature and the reduction of planar defects. The anisotropy of microtwins linked to the misorientation of Si substrate is demonstrated. Finally an atomically flat surface and a minimum defects level of GaP/Si pseudo-substrate are demonstrated.

**The appendices section** briefly introduces the experimental techniques used in this work. They include the growth of silicon and III-V nanostructures using the newly installed growth cluster, which is composed of a Si UHV/CVD chamber connected under UHV to a III-V MBE chamber; the use of RHEED to monitor the growth in-situ; the structural characterization by X-ray diffraction techniques using Synchrotron and laboratory sources; and the surface morphology measurement by AFM.

## REFERENCES

- [BaBr48] BARDEEN, J.; BRATTAIN, W. H.: In: *Physical Review* **74** (1948), No. 2, p. 230
- [Bard47] BARDEEN, John.: In: *Physical Review* **71** (1947), No. 10, pp. 717–727
- [DDGS00] DEHLINGER, G.; DIEHL, L.; GENNSER, U.; SIGG, H.; FAIST, J.; ENSSLIN, K.; GRÜTZMACHER, D.; MÜLLER, E.: In: *Science* **290** (2000), No. 5500, pp. 2277–2280. — PMID: 11125134
- [EHJU95] EGAWA, T.; HASEGAWA, Y.; JIMBO, T.; UMENO, M.: In: *Applied Physics Letters* **67** (1995), No. 20, pp. 2995–2997
- [FPCP94] FRANZÒ, G.; PRIOLO, F.; COFFA, S.; POLMAN, A.; CARNERA, A.: In: *Applied Physics Letters* **64** (1994), No. 17, p. 2235
- [LiBo10] LIANG, Di; BOWERS, John E.: In: *Nat Photon* **4** (2010), No. 8, pp. 511–517
- [Moor65] MOORE, GE.: In: *Electronics* **38** (1965), No. 8, pp. 114–117
- [PaLo10] PAVESI, Lorenzo; LOCKWOOD, David J.: *Silicon Photonics*. Softcover reprint of hardcover 1st ed. 2004. ed. : Springer, 2010 — ISBN 3642059090
- [PLRS13] PROHL, Christopher; LENZ, Andrea; ROY, Dominik; SCHUPPANG, Josephine; et al.: In: *Applied Physics Letters* **102** (2013), No. 12, pp. 123102–123102–4
- [PNMF00] PAVESI, L.; NEGRO, L. Dal; MAZZOLENI, C.; FRANZÒ, G.; PRIOLO, F.: In: *Nature* **408** (2000), No. 6811, pp. 440–444
- [RLJC05] RONG, Haisheng; LIU, Ansheng; JONES, Richard; COHEN, Oded; HAK, Dani; NICOLAESCU, Remus; FANG, Alexander; PANICCIA, Mario.: In: *Nature* **433** (2005), No. 7023, pp. 292–294
- [SoSL10] SONG, Yuncheng; SIMMONDS, Paul J.; LEE, Minjoo Larry.: In: *Applied Physics Letters* **97** (2010), No. 22, p. 223110

## CHAPTER 1.

### SILICON PHOTONICS – STATE-OF-THE-ART

#### 1.1 Silicon: an inefficient light emitter

Light emission occurs when an electron radiatively recombines with a hole to produce a photon. The photon energy is equal to the band-gap energy if the electron is in the conduction band and the hole in the valence band, considering a non-degenerated semiconductor. If both electron and hole are located at the same point in the Brillouin zone, the radiative recombination rate is large and the radiative lifetime  $\tau_{rad}$  is short (typically a few ns). This is the case in direct bandgap semiconductors, such as GaAs or InP (**Figure 1-1** left). In indirect bandgap semiconductors such as Si, the bottom of the conduction band is not at the same location in reciprocal space as the top of the valence band (**Figure 1-1** right), free electrons tend to locate in the X valleys of the conduction band whereas the free holes are located in the  $\Gamma$  valleys of the valence band. Radiative recombination across the band-gap thus requires the participation of a phonon, making it a second-order process. As a result, the radiative lifetime is much longer, typically in the millisecond regime and the recombination rate is less efficient.

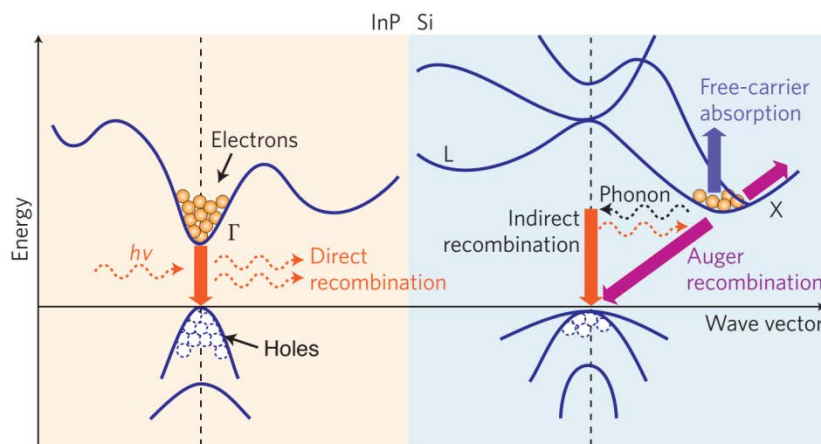


**Figure 1-1:** Energy band diagrams and major carrier transition processes in InP (left) and silicon (right).<sup>[LiBo10]</sup>

The internal quantum efficiency is given by:

$$\eta_{in} = \frac{\tau_{non-rad}}{\tau_{non-rad} + \tau_{rad}} \quad (\text{Eq. 1})$$

where  $\tau_{non-rad}$  is the lifetime for the recombination pathways that do not involve the production of photons. Non-radiative pathways include recombination at bulk or surface defects and Auger recombination. In direct bandgap semiconductors,  $\eta_{in}$  can be very large, typically of the order of 10% and may even approach 100%, because the radiative lifetime is much shorter than the non-radiative lifetime.<sup>[SYCG93]</sup> However, in indirect bandgap semiconductors such as Si, the non-radiative lifetime is usually much shorter than the radiative lifetime and  $\eta$  drops by several orders of magnitude and typically is as low as  $10^{-4}$  % to  $10^{-5}$  %.

Several approaches have been proposed to improve the quantum efficiency of silicon. These approaches can be grouped into two categories. In the first category, non-radiative recombination pathways are suppressed. To achieve this goal, bulk and surface defects must be eliminated. In bulk silicon, this can be done by carefully passivating the surface<sup>[YACG86]</sup> and by using high purity material.<sup>[GZWR01]</sup> In addition, the injected carrier concentration must remain low to eliminate Auger recombination, as the Auger rate increases with the third power of the injected carrier density.<sup>[YaGm86]</sup> In the second category, the radiative recombination rate is enhanced. This can be achieved by localizing the electron and hole wavefunctions in the same region of space, for example using quantum dots<sup>[Hybe94]</sup> or isoelectronic impurities.<sup>[BrHa97]</sup>

Other possibilities include combining silicon with another elemental semiconductor and using specific light emitting centers. Alloying is typically done with germanium, although alloys of Si with C and Ge have also shown to be promising.<sup>[OORK96]</sup> Indeed, though the Ge is also an indirect bandgap material, its indirect character is less remarked than in Si. Silicon-germanium quantum wells superlattices have been successfully employed to achieve luminescence below the band-gap energy of silicon.<sup>[Abst97]</sup> Transfer of an electron and a hole from silicon to a specific center can lead to efficient sub-band-gap luminescence. Erbium is by far the most widely used light emitting center in bulk silicon<sup>[MAMK97]</sup> as well as in nanocrystalline silicon.<sup>[LHC93]</sup> Detail state of the art about light emission on silicon will be mentioned carefully in the following paragraphs.

## 1.2 Silicon-based light emission

### 1.2.1 Erbium doping

Rare-earth ions, especially erbium, have played a significant role in the development of the optical communications network. Trivalent erbium ions ( $\text{Er}^{+3}$ ) embedded in semiconductor or dielectric materials have an incomplete 4f electronic shell, permitting intra-4f transitions when excited (or pumped) by an optical source. Further, the first excited state is at an energy of 0.8 eV, hence down-transitions following optical pumping with higher-energy photons (usually from either a 980 nm or 1480 nm laser source) can occur with the emission of photons at a wavelength of 1.54  $\mu\text{m}$ .

In the 1980s it was shown that erbium-doped optical fibers could be used as optical amplifiers when pumped by a laser source.<sup>[MRJP87]</sup> The same principle of photon emission as used in fiber amplifiers can be applied to erbium-doped silicon. Actually, electrically pumped light-emitting diode (LED) based on Er-doped silicon has been demonstrated with extremely low efficiencies at room temperature. In particular, there was a strong thermal quenching of the optical power as the temperature is raised towards 300K.<sup>[ZMRK94]</sup> In another work, Franzò et al. claimed the efficient emission from (Er+O)-doped Si LED by reverse-biasing the devices.<sup>[FCPS97]</sup>

### 1.2.2 Low dimensional structures

#### *(a) Porous silicon*

In 1990, Canham<sup>[Canh90]</sup> published a pioneering paper demonstrating efficient room-temperature luminescence from silicon samples which had been exposed to an anodization process in an HF acid electrochemical cell. The resulting structure of the samples consisted of an array of small holes that ran orthogonally to the sample surface. This so called porous silicon exhibited efficient room-temperature PL upon irradiation with Ar laser lines at 488 and 514.5 nm.

The first electroluminescent (EL) porous silicon device was demonstrated by Richter et al.<sup>[RSKL91]</sup> A small but observable emission (with the eye in a darkened environment) was recorded. Considerable progress in the fabrication of EL porous silicon LEDs is evidenced by a paper of Gelloz and Koshida.<sup>[GeKo00]</sup> Room-temperature EL with an external quantum efficiency approaching 1 % for an applied bias of 5 V is

reported, although the exact nature of the carrier excitation process is not known. These devices are the most efficient porous Si LEDs reported to date.

***(b) Silicon nano-crystals***

An approach that combines the advantages of low-dimensional silicon with robust ultra large scale integration - compatible fabrication process is the use of silicon nano-crystals (Si-nc) embedded in a dielectric SiO<sub>2</sub> matrix. A straightforward fabrication technique involves the formation of a silicon-rich, sub-stoichiometric SiO<sub>x</sub> (x<2) film on a silicon substrate, followed by a high-temperature anneal in the region of 1200°C for several minutes. The thermal energy promotes the phase separation of Si and SiO<sub>2</sub> and the final structure consists of small silicon nano-crystals whose size and distribution depend on the original film properties and the subsequent thermal anneal.

Iacona *et al.* produced silicon-rich films by plasma-enhanced chemical vapor deposition (PECVD) with x varying between 1 and 1.75.<sup>[IaFS00]</sup> Photoluminescence measurements following excitation with a 488-nm Ar laser are also reported. Devices in which the optically active medium is insulating (as is the case for SiO<sub>2</sub>) would seem incompatible with electrical excitation. Indeed the fabrication of LEDs using this medium has proven troublesome. Even so, by utilization of a current tunneling between the embedded nanocrystals, efficient EL has been demonstrated. In these devices it is likely that control of the Si-nc structure dimensions is compounded by the need for sufficient current densities (dependent on the Si-nc distribution) to create efficient EL. Irrera *et al.* fabricated a Si-nc LED using silicon PECVD-deposited SiO<sub>x</sub> and obtained room temperature EL at 850 nm.<sup>[IPMF03]</sup>

***(c) Erbium coupled with silicon nano-crystals***

Taking advantages of Si-nc and luminescence at 1.54 μm from Er<sup>+3</sup>, there is a natural extension in the coupling of these two aspects.<sup>[FPVP00, IIFM10, ZHSS01]</sup> In this system, non-radiative de-excitation processes are reduced by widening the bandgap and thus avoiding one of the most detrimental sources of Er luminescence quenching. Widening the bandgap also produces a reduction in free carrier concentration thus limiting the Auger processes. Franzò *et al.*<sup>[FPVP00]</sup> implanted Er<sup>+</sup> ions into a Si-nc matrix using PECVD. They found that not only did the Er ions produce luminescence, but the process was more efficient by a factor of 100 compared to (Er+O)-implanted bulk silicon.

EL from Er-doped SiO<sub>2</sub> as a function of concentration of Si-nc was also reported.<sup>[CCMC03]</sup> A tunneling current of 100 μA was used to induce room-temperature EL with an external quantum efficiency of 10 %. The maximum output was found to be limited only by the density of Er ions incorporated into the oxide film (approximately 1×10<sup>19</sup> cm<sup>-3</sup>). However, these devices were shown to be limited by their reliability and operating lifetime, which come from the use of a tunneling current through the thermally grown SiO<sub>2</sub> to excite the Er<sup>3+</sup> ions. Even though improvement was made, there was a compromise between the reliability and the EL efficiency, i.e. acceptable lifetime exhibited an external quantum efficiency of 1%.

### 1.2.3 Raman excitation

Experimental observation of spontaneous Raman emission from silicon waveguides was reported by the group led by Jalali at UCLA.<sup>[CDHJ02]</sup> A 1.43 μm pumping source was coupled into a silicon on-SiO<sub>2</sub> rib waveguide structure with a cross-section of approximately 20 μm<sup>2</sup>. The Raman spectra were measured for emission from both end facets of the waveguide. The 1.43 μm pump results in an emission centered at 1.542 μm which varies linearly with the pumping power. The spectral width of the frequency of the emitted light is 105 GHz. The Raman scattering efficiency for silicon was deduced as 4.1×10<sup>-7</sup>cm<sup>-1</sup>·Sr<sup>-1</sup>. In a subsequent publication the same group examined the feasibility of forming a waveguide amplifier using Raman scattering.<sup>[CIDJ02]</sup> Using a stimulated gain coefficient of 0.07 cm/MW and accounting for coupling and propagation losses and pump and signal mode mismatch, they determined that a pumping power of around 500 mW at 1.432 μm is required to provide a signal gain of 10 dB for a wavelength of 1.54 μm in a waveguide of 2 cm in length. A disadvantage of this method for the fabrication of amplifiers is the high power density introduced into the waveguide geometry, which induces nonlinear absorption effects such as two-photon absorption and amplified spontaneous emission.

## 1.3 Band-gap engineering using germanium

Bandgap engineering of III–V semiconductor structures started 30 years ago and today many commercial devices exist that use this approach. These include LEDs and lasers. It is thus reasonable to expect that band-gap engineering involving elements of

the IV column of the periodic table would produce useful devices, including light sources. The SiGe alloy system is by far the most studied system.<sup>[Abst97]</sup> Because of the large (~4%) lattice mismatch between Si and Ge, it is not possible to grow thick layers of Ge on Si without introducing dislocations. The strain present in SiGe structures is thus a limitation that does not exist in many III–V semiconductor systems. Luminescence is produced at the bandgap of the alloy, which in principle can be tuned from the bandgap of Si to that of Ge (**Figure 1-2**).<sup>[Pear94]</sup>

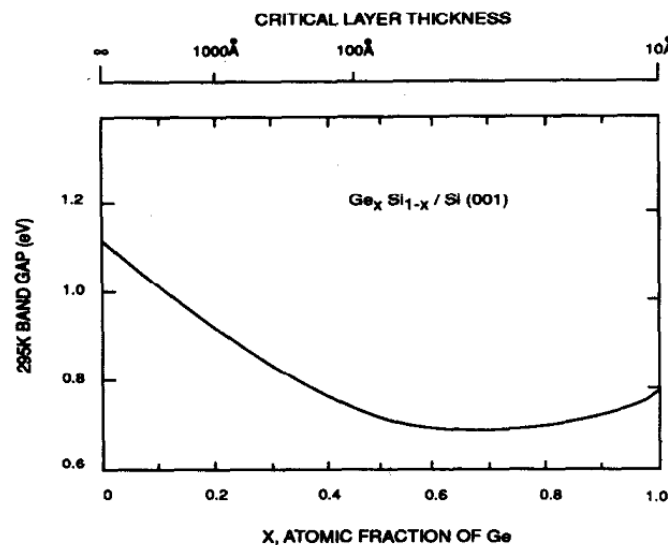


**Figure 1-2:** Calculated bandgap of SiGe strained on Si as a function of the Ge atomic fractional content. The critical thickness of the SiGe alloy decreases drastically with the Ge content.<sup>[Pear94]</sup>

SiGe layers can be grown by molecular beam epitaxy<sup>[AEFW89]</sup> or low-pressure chemical vapor deposition.<sup>[StVG98]</sup> Strain in the active layers can be managed through the use of a thick alloy layer grown directly on the silicon substrate. This thick layer is relaxed and thus subsequent layers grown on it respond to the natural lattice constant of the relaxed layer, not that of the Si substrate. However, by using small growth areas, it is possible to grow thicker SiGe layers that remain strained and do not contain dislocations.<sup>[VeSt98]</sup>

SiGe LEDs have been demonstrated using  $\text{Si}_n\text{Ge}_m$  multilayers, SiGe quantum wells, and thick SiGe layers.<sup>[SVMH03]</sup> All SiGe LEDs suffer from the same strong decrease in efficiency with increasing temperature. In fact, the best SiGe LEDs have a power efficiency that is at least one order of magnitude below that of good Si LEDs. Two main reasons explain this low efficiency. First, SiGe is still an indirect bandgap semiconductor, making it imperative to eliminate non-radiative centers. Second, the small bandgap

discontinuity between SiGe and Si (compared to that between Si and SiO<sub>2</sub> for example) makes it difficult to prevent the carriers from escaping the active layer.

Recently, the activity in this material system has moved to emission from Ge islands or quantum dots<sup>[BMSS00, Lede03]</sup> and to quantum cascade lasers that involve intraband transitions.<sup>[DMMG03, PLBI03]</sup> The first approach is related to the on-going work on III-V semiconductor quantum dot laser and EL is only starting to emerge. The second approach does not involve transitions across the fundamental bandgap, leads to light emission in the mid to far infrared. Another approach comes to emerge recently is the use of strained Ge on Si substrate, as the strain state in the strained Ge strongly modify its bandgap.<sup>[LiKM12, GEKP13]</sup> **Figure 1-3** schematically shows the bandgap modification of Ge under different strain states. One can see that the difference between the  $\Gamma$  and the L minima in the conduction band of Ge can be reduced under tensile strain and efficient direct transition can happen when the material is highly n-doped. Room temperature operation under pulsed electrically pumping laser based on bulk Ge on Si substrate (with 0.2% tensile strain thanks to the difference in thermal expansion coefficients) has been recently demonstrated by the group of L. Kimerling at the MIT. However, they have reported an extremely high threshold current density: 280 kA/cm<sup>2</sup>.<sup>[LiKM12]</sup>

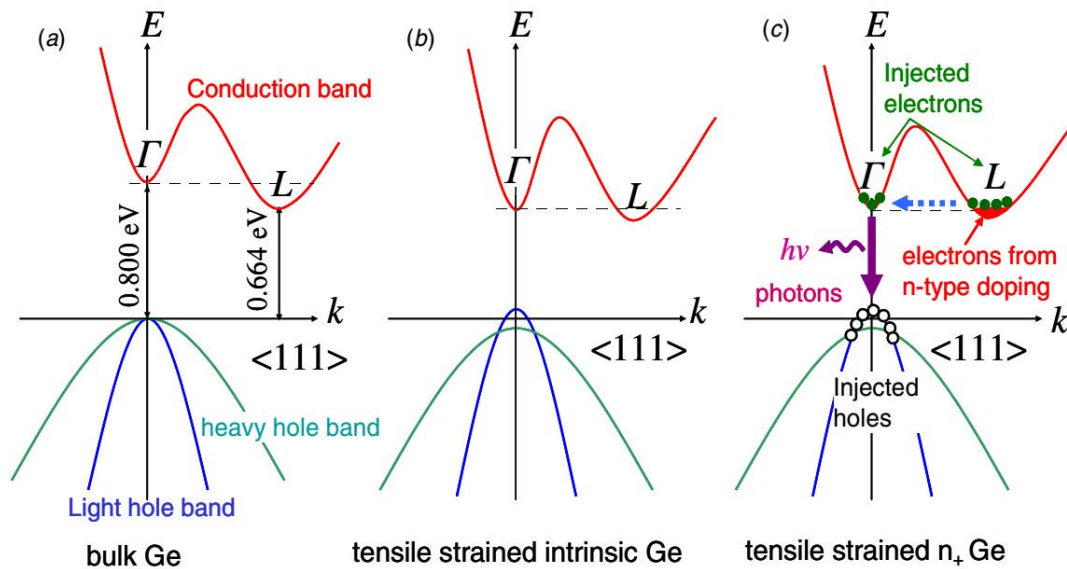


**Figure 1-3:** Germanium bandgap engineering using tensile strain. (a) bulk Ge shows indirect bandgap; (b) tensile strain reduces the difference between the  $\Gamma$  and L valley minima; (c) efficient direct transition of highly n-doped strained Ge. From Ref.<sup>[LiKM12]</sup>

## 1.4 Integration of III-V materials on silicon

Although the silicon-based light emitting has been enabled and achieved interesting results, but silicon lasers performance is by far away comparing to that of III-V family (i.e. limited at optically pumping and/or low temperature operation with high threshold current even under pulsed operation). Actually, since the first demonstrations of semiconductor laser diode in 1962 by Hall *et al.* for infrared wavelength<sup>[HFKS62]</sup> and Holonyak *et al.* for visible wavelength,<sup>[HoBe62]</sup> the major applications of semiconductor laser diodes are based on III-V direct band gap GaAs, InP, GaSb or GaN related compounds. It is therefore very interesting (but challenging) to realize photonics integrated circuits (PICs) on silicon (or to “siliconize” photonics – Intel) by combining high technology know-how of silicon-based ICs with III-V based lasers – the ultimate convergence between optics and electronics. To this end, two approaches are on the way: using hybrid silicon laser and monolithic integration of III-V materials onto silicon substrate.

### 1.4.1 Hybrid silicon lasers (wafer bonding)

Hybrid silicon lasers consist of bonding a III-V laser fabricated apart with a silicon platform. The structure of this laser is represented schematically in **Figure 1-4**. The bonding process which can be at wafer or die level is achieved by various techniques: direct bonding, using adhesive (polymer, metal), oxygen plasma-assisted, etc. The adhesion of the two structures is based on interatomic Van der Waals force and hydrogen bonding. For more detail about these techniques, reader can refer to the Ref.<sup>[PaHj02]</sup> and references therein.

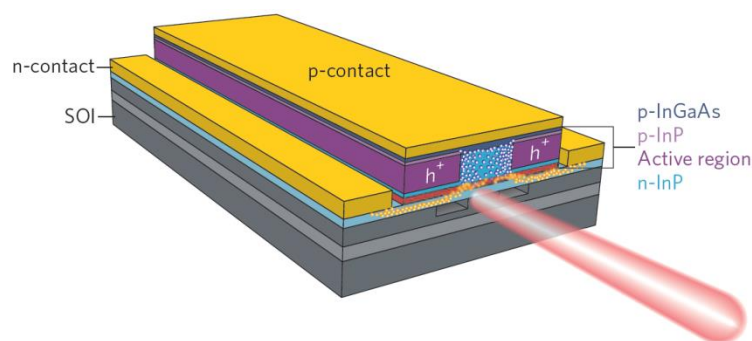


**Figure 1-4:** Sketch of a hybrid Fabry-Pérot laser bonded on a Si waveguide fabricated on SOI wafer.<sup>[LiBo10]</sup>

Such a hybrid laser was first demonstrated by Wada *et al.*<sup>[WaTK96]</sup> using direct bonding technique to join an InGaAs(P)/InP laser onto Si substrate. Room temperature lasing operation was achieved using optical pumping source at 1.49  $\mu\text{m}$ . The result showed a 1.58  $\mu\text{m}$  emission center with a threshold current density of 2  $\text{kA}/\text{cm}^2$ . Recently, electrically pumped AlGaInAs/InP laser was reported by Fang *et al.*<sup>[FPC]06]</sup> The laser was bonded on silicon waveguide fabricated on SOI substrate using low temperature  $\text{O}_2$  plasma-assisted bonding. **Figure 1-5** describes schematically this structure. Room temperature continuous wave lasing with 65 mA,  $\sim 1.8$  mW output power and overall differential quantum efficiency of  $\sim 12.7\%$  were reported. More interesting, this technique does not need laser alignment on Si waveguide which is one of the major issues for this approach and in the same time, hundreds of lasers can be bonded on a silicon die just with a single bonding step. This is very promising for large scale integration PIC fabrication on silicon using conventional technology.

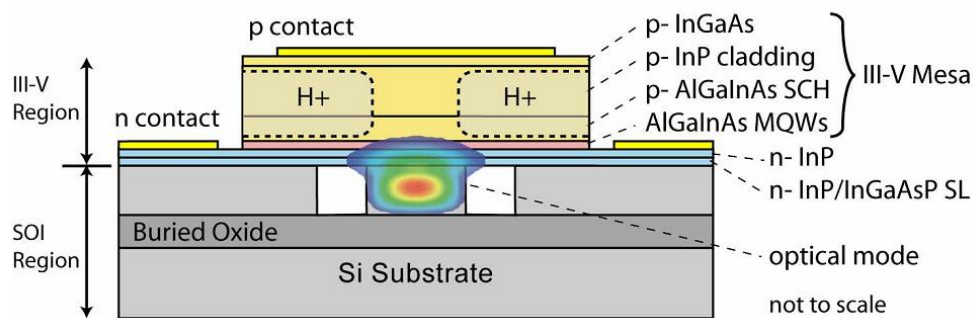


**Figure 1-5:** Schematic drawing of the hybrid laser structure with the optical mode superimposed.<sup>[FPC]06]</sup>

Hybrid silicon laser based photonics devices have already been commercialized by Intel under the name Light Peak in 2010. This Light Peak photonics link consists of a transmitter integrated circuit using 4 hybrid silicon lasers based on InP. It is capable to send data at a rate of 50 gigabits per second (Gbps) across an optical fiber to a SiGe-based receiver to convert optical data back to electrical signal (**Figure 1-6**). Recently, Intel has demonstrated a 100 Gbps silicon photonics chip at the Intel Developer Forum in Beijing – China (April 2013).

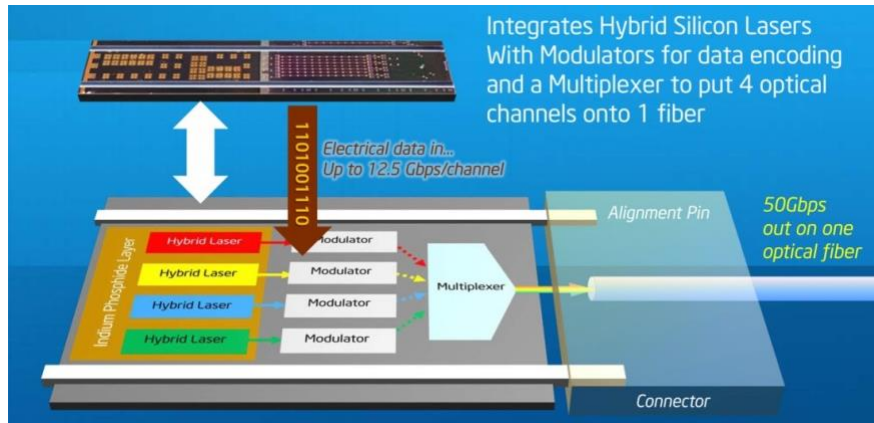


**Figure 1-6:** Integrated transmitter chip with 4 hybrid silicon lasers sending data at a rate of 50Gbps. Source: Intel.

Despite interesting results, such a hybrid approach presents a number of disadvantages in long term operation (reliability) and fabrication. Indeed, various fabrication steps are time consuming and expensive: III-V lasers fabrication, Si chips fabrication, placing and alignment of laser dies (or wafer) on Si waveguide through the bonding step. This approach also limits the integration density of laser diodes on a single silicon chip. Another concept is therefore placed in the race which promises to overcome these issues: monolithic integration of III-V materials on Si substrate.

### 1.4.2 Monolithic growth of III-V on Si

The monolithic approach consists in growing III-V semiconductor compounds directly on Si substrate. This concept avoids using high-cost III-V substrates (like GaAs, InP), without any need of bonding, thus reduces the fabrication cost and time. Furthermore, by growing III-V light emissive compounds on Si, it allows very large scale integration of devices, which cannot be achieved by hybrid approaches. The issue is that most of the well-known direct bandgap used in laser fabrication like GaAs or InP have large lattice mismatch with silicon (i.e. 4% for GaAs/Si, 8% for InP/Si). One can refer to **Figure 1-7** for a complete view of the energy gap plotted versus lattice constant of the most common III-V semiconductors in comparison with silicon.

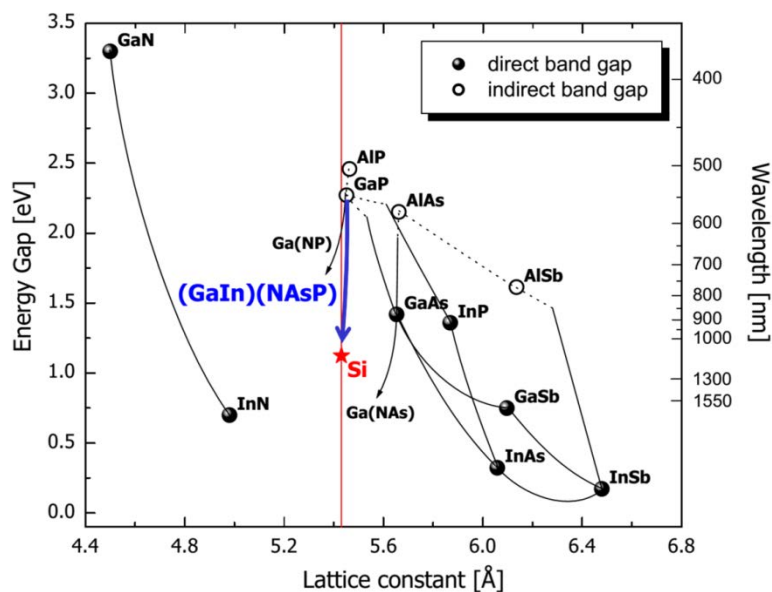


**Figure 1-7:** Bandgap energy versus lattice constant of the most common III-V semiconductors in comparison to silicon. The indirect gap semiconductor GaP has the lattice constant almost equal to that of Si which allows dislocation free growth of GaP on Si. Related semiconductor compounds (GaIn)(NAsP) lattice-matched with Si are very promising to obtain defects-free light emissive structure on Si.

The difference in lattice constant between the epitaxial layer and the substrate generate energy accumulation (strain, stress) within the layer. When the layer thickness exceeds a critical value, misfit dislocations are formed to minimize the accumulated energy.<sup>[MaBl74a]</sup> These defects act as non-radiative recombination centers in the structure. They actually add electrical resistance during the current flow through it, or limit the quantum efficiency of optical devices by decreasing the number of electrons-holes pairs recombined in photons. Dislocation density has to be minimized to fit reliable laser performance requirement ( $< 10^4 \text{ cm}^{-2}$ ). Other issues concerning the growth of III-V systems on silicon such as difference in thermal expansion coefficient, difference in lattice structure (polar and non-polar) will be detailed in the following paragraph. The main challenge in this scenario is therefore to improve crystalline quality of the grown structure on silicon, which is recently reported by several authors as detailed in the following.

### ***(a) Metamorphic approach***

The metamorphic approach uses the growth lattice mismatched III-V compounds on silicon (for example: GaAs, InP, GaSb). A direct consequence of the large mismatch is the generation of high dislocation density. **Figure 1-8** shows typical resulting

dislocations in a GaAs layer grown on Si. Although laser structures based on GaAs/AlGaAs QWs or InGaAsP/InP QWs have already been grown on Si, the very high density of dislocations ( $> 10^7 \text{ cm}^{-2}$ ) results in a more or less rapid deterioration of the devices.<sup>[RDB088, SMSI92, TYTM97, YTSM97, ZDLP87]</sup>

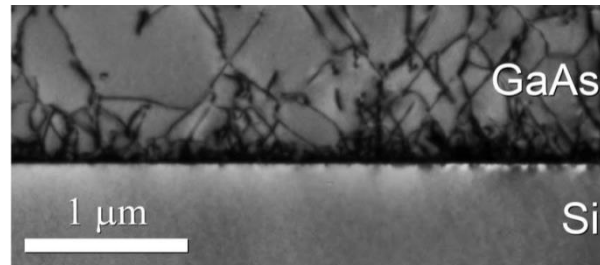


**Figure 1-8:** Cross-sectional transmission electron microscope (TEM) image highlighting the dislocations in a GaAs layer grown on a Si substrate.<sup>[LTPW13]</sup>

As these defects are unavoidable, many attempts have been tried to confine the dislocations far away from the active zone. The use of strained short-period superlattices have been demonstrated to act as a filter for dislocations<sup>[LTPW13, SYTI96]</sup> (see **Figure 1-9** (a)). On the same idea, the group of P. Bhattacharya has developed a dislocations filter buffer layer based on InAs/GaAs QDs (see **Figure 1-9** (b)). Using this technique, encouraging results have been demonstrated with lasing structures exhibiting a threshold current density of  $900 \text{ A.cm}^{-2}$  under pulsed electrical pumping at room temperature.<sup>[MYBQ09]</sup>

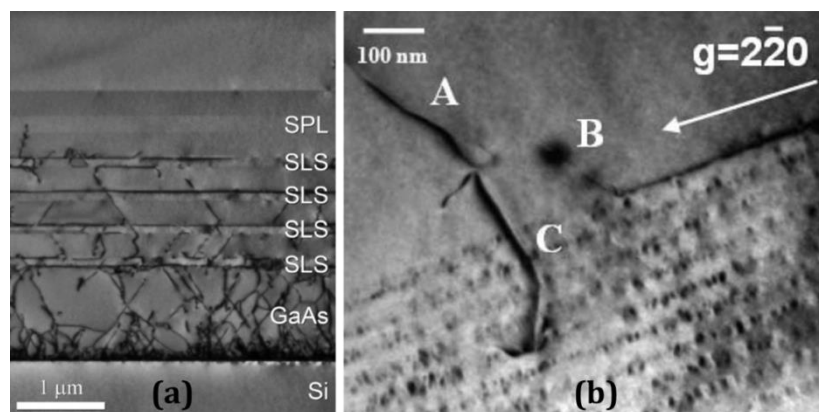


**Figure 1-9:** Cross-sectional TEM image of: (a) a threading dislocations filter based on strained-layer superlattices (SLS) and short-period superlattices (From <sup>[LTPW13]</sup>) and (b) a blocked dislocation by a QDs buffer layer (From <sup>[MYBQ09]</sup>).

Another way to deal with the lattice-mismatch issue is the growth of the III-V structure on an oxide/Si layer such as  $\text{SiO}_2/\text{Si}$  or  $\text{SrTiO}_3/\text{Si}$  template. In principle, this

technique should enable the III-V layer to immediately take its bulk lattice constant and thus prevent any threading dislocations, but only room temperature photoluminescence has been reported till date.<sup>[GPCC10, RCJV13]</sup>

Another interesting approach to confine the dislocations is the use of antimonide-based materials. As shown in **Figure 1-7**, the lattice-mismatch between Si and III-Sb compounds is very large (12% for GaSb/Si). But contrary to most of other III-V material systems, this very large lattice-mismatch is an advantage in the case of III-Sb material, since it is believed to be the main driving force for the formation of two-dimensional arrays of efficient strain-relieving misfit dislocations. **Figure 1-10** shows the relaxation of an AlSb layer by the formation of dislocations confined at the AlSb/Si hetero-interface.<sup>[HBKD08]</sup> Using this AlSb nucleation layer and a GaSb fully relaxed buffer layer, a laser diode operating at room temperature and under continuous-wave electrical pumping has been demonstrated.<sup>[RCRG11]</sup> The wavelength is 2  $\mu\text{m}$  and the threshold current density is high (1.4  $\text{kA}\cdot\text{cm}^{-2}$ ). A structure emitting at 1.55  $\mu\text{m}$  has also been achieved, but the threshold current density is still high (5  $\text{kA}\cdot\text{cm}^{-2}$ ) and only pulsed regime has been demonstrated.<sup>[CeRT10]</sup>

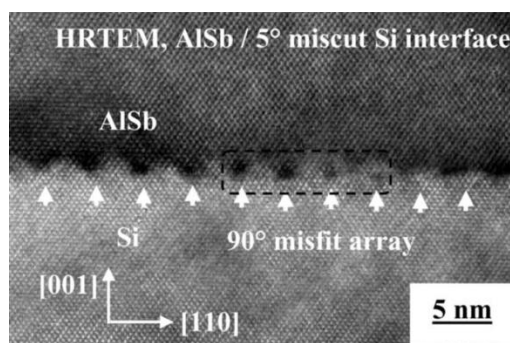


**Figure 1-10:** Cross-sectional TEM image of a two-dimensional dislocation network confined at the AlSb/Si interface.<sup>[HBKD08]</sup>

The lowest room-temperature threshold current density for any metamorphic laser on Si has been achieved by the group of A. Seeds in the University College of London. Their idea is to benefit from both low threshold InAs/GaAs QD laser structure and significant improvements in crystalline quality of Ge on Si. Indeed, as shown in **Figure 1-7** the lattice-mismatch between GaAs and Ge is small (0.08%). Moreover, their thermal expansion coefficients are also very close ( $5.7 \times 10^{-6} \text{ K}^{-1}$  for GaAs and  $5.9 \times 10^{-6} \text{ K}^{-1}$  for Ge). They have first demonstrated an InAs/GaAs QD laser on Ge substrate operating at room temperature with a low threshold current density of  $55.2 \text{ A}\cdot\text{cm}^{-2}$  under

continuous-wave electrical pumping,<sup>[LWJH11]</sup> followed by a similar structure on Ge-on-Si substrate with threshold current densities of  $163 \text{ A.cm}^{-2}$  (continuous-wave operation) and  $64.3 \text{ A.cm}^{-2}$  (pulsed operation).<sup>[LJTS12]</sup>

Nevertheless, the issue of all these approaches is that they resort on complex procedures and/or thick buffer layers which strongly limit the design flexibility for further device integration. A thick buffer layer prevents a simple coupling scheme with a photonic circuit embedded in the bottom Si chip. Moreover, driving the current through the dislocation layer is known to dramatically deteriorate the electrical performances.<sup>[RCRG11]</sup>

Another solution to manage the strain relaxation without using buffer layers is to decrease the interaction between the grown layer and the substrate. This can be done by using patterned substrates<sup>[FKIB12]</sup> or by growing self-assembled one-dimensional nanostructures such as nanowires, nanoneedles or nanopillars.<sup>[ACKN13, MSWL04, TLWH10]</sup> This approach enables the growth of lattice mismatched materials without the formation of dislocations because the large surface-to-volume ratio for one-dimensional wires allows the strain to be efficiently relaxed.<sup>[MFS]10]</sup> Interesting results have been recently achieved by the group of C. Chang-Hasnain in Berkeley.<sup>[CTNK11]</sup> They have demonstrated room temperature lasing of an InGaAs/GaAs core-shell nanopillar with helically propagating cavity modes (see **Figure 1-11**). Due to the very small laser volume ( $6.10^{-13} \text{ cm}^3$ ), this approach is exciting for ultimate integration of light source. Nevertheless, it faces various challenges. Electrically pumped laser are missing even if light-emitting diodes with complex metallic contacts technology have been shown.<sup>[CSCK11]</sup> Moreover (1 1 1) oriented Si substrate are often used to favor the vertical growth of the III-V structure. The control of the growth direction on more conventional (0 0 1) Si substrate is still challenging.

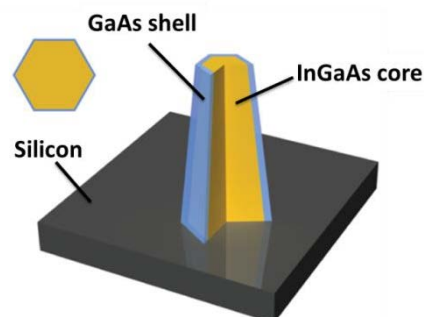


**Figure 1-11:** InGaAs/GaAs heterostructure nanopillar lasers monolithically grown on silicon. <sup>[CTNK11]</sup>

***(b) Pseudomorphic approach***

This approach which will be followed in this work consists in growing coherently (pseudomorphically) an epilayer on silicon avoiding misfit dislocation. That means the in-plane lattice constant of the epilayer has to be equal to that of the substrate. This can be done by choosing a III-V semiconductor with very close lattice constant to that of silicon below the critical thickness. Looking at **Figure 1-7**, one can see that GaP (gallium phosphide) is the best candidate as its lattice constant is almost equal to that of silicon. The lattice mismatch between GaP and Si is 0.37% at room temperature. In addition, the ternary material system Ga(NP) (gallium nitride phosphide) can be grown lattice matched to Si-substrate with a N-content of only two percent.<sup>[BiTu96]</sup> The incorporation of N into this material is believed to modify the electronic band structure of GaP via a phenomenon called bandgap bowing and thus enhances the direct bandgap character of GaPN.<sup>[BiTu96, XiTu00, XTZM00]</sup> Prof. Hiroo Yonezu and co-workers at the University of Toyohashi in Japan demonstrated the heteroepitaxial growth of Ga(NP)/GaP layer sequences on Si-substrates with high structural perfection and without the formation of any misfit dislocations and antiphase domains.<sup>[Yone02]</sup> A first double heterostructure LED based on InGaPN/GaP/Si has been demonstrated by this group in 2008.<sup>[YoFW08]</sup> The LED operation was modulated by Si MOSFET fabricated on the same Si chip and room temperature EL centered at 645 nm was reported (**Figure 1-12**).

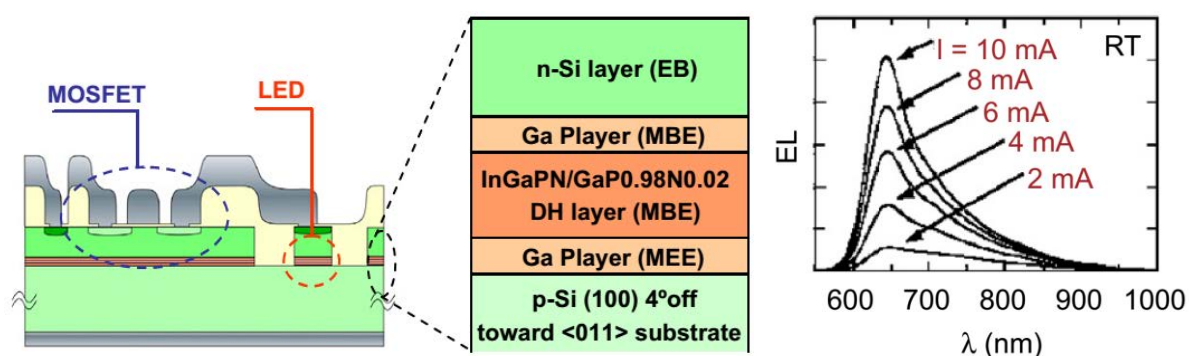


**Figure 1-12:** Sketch of the InGaPN/GaP double heterostructure LED and Si MOSFETs fabricated on Si substrate (left) and room temperature electroluminescence of the LED with respect to the feeding current (right).<sup>[YoFW08]</sup>

Based on the same concept, the Material Sciences Center of the Philipps-University Marburg (Germany) has demonstrated the integration of GaAsPN-based lasers on GaP and Si substrates.<sup>[BCKV06, KVNS06, KKR06, KRKL06, KVKS06, KuVS07, KVKS07, CASK08, KGGK09,</sup>

HHSL11, LZBL11, HJLZ12] The idea for this material system is that the incorporation of Indium (In), Arsenic (As) as well as Nitrogen (N) enables the modification of the band structure in order to change the indirect band gap to a pseudo direct one, as a basic necessity for high material gain and lasing activity. The combination of N with In and/or As allows for the essential adjustment of the lattice constant of the pentenary compound semiconductor (GaIn)(NAsP) to the lattice constant of GaP or Si, see also **Figure 1-7**. The challenge is to find the right material composition of (GaIn)(NAsP), which facilitates the pseudomorphic growth of high quality films on GaP-substrate with a good luminescence efficiency, respectively, at the same time. This group has demonstrated room temperature pulsed electrical injection lasing of the Ga(AsPN) on GaP substrate with a high threshold current density ( $4.0 \text{ kA/cm}^2$ ) in 2011.<sup>[HSR011]</sup> Recently, lasing operation of Ga(AsPN) on Si substrate under optical and electrical pumping is reported up to 150K with the emission wavelength in the region of 800 – 850 nm and a high threshold current density of  $4.4 \text{ kA/cm}^2$ <sup>[LZBL11]</sup> and optical gain has been measured up to 300K.<sup>[KBFG12]</sup>

These interesting results encourage the development of GaP/Si platform in this context. *Improvement of material quality of this system still remains challenging and is a key point of this thesis.*

### 1.4.3 Active areas in the pseudomorphic approach

Achieving an efficient light emitter on Si substrate is another challenge in the pseudomorphic approach. So far many attempts have been invested in the growth of active areas based on quantum wells (QWs) and quantum dots (QDs) on GaP(001) substrates. Ga(AsPN) and InGaPN/GaP(001) QWs are demonstrated by the Toyohashi and Marburg University groups as reported in the previous paragraph. InGaNP/GaP QWs-based yellow-red LED was also demonstrated by Odnoblyudov and Tu in 2006.<sup>[OdTu06]</sup> The use of quantum dots (QD) has also been proposed in order to allow the growth of larger lattice-mismatched nanostructures and thus to reach smaller bandgap. Moreover, due to their 0D confinement properties, such devices displaying improved optical characteristics have been reported.<sup>[LGHB00]</sup> InAs/GaP QD have already been proposed,<sup>[GBCF09, LLCW98]</sup> but the plastic relaxation due to the large lattice mismatch (11.2%) was found to be responsible for the lack of any efficient photoluminescence

(PL). InP/GaP QD have also been studied and related devices have been developed.<sup>[HLHK05]</sup> However, band lineups have been demonstrated to be borderline type-I - type-II and the QD density was low ( $10^8$ - $10^9$ cm<sup>-2</sup>).<sup>[HMST03]</sup> Gerhard *et al.* have demonstrated high density QD of In-rich Ga<sub>0.46</sub>In<sub>0.54</sub>P/GaP ( $1 \times 10^{11}$ cm<sup>-2</sup>), with, however, a low PL signal at 4K.<sup>[GBHF09]</sup> Shamirzaev *et al.* have claimed the obtaining of type-I alignment for GaAs QD on GaP, but relaxation process and indirect bandgap led to limited PL efficiency until 40K.<sup>[SAGP10]</sup> Meanwhile, Umeno *et al.* have reported the room temperature (RT) PL of 5 stacks of InGaAsN QD on GaP with a density of  $8 \times 10^{10}$  cm<sup>-2</sup>.<sup>[UFUN10]</sup> However, the large full width at half maximum (FWHM) (334 meV) was interpreted as a large inhomogeneous distribution of the QD. In a report on InGaAs/GaP QD properties, Fuchi *et al.* have measured a PL signal until 77 K and pointed out the issue of In composition.<sup>[FNMK04]</sup> Recently, Song *et al.* have reported about the growth of low density ( $1.5 \times 10^{10}$  cm<sup>-2</sup>) In<sub>0.5</sub>Ga<sub>0.5</sub>As QD on GaP and showed a PL signal up to only 80 K with a FWHM as large as 115 meV.<sup>[SoSL10]</sup> They have then developed In<sub>0.5</sub>Ga<sub>0.5</sub>As/GaP-based QDs LED and RT electroluminescence was demonstrated.<sup>[SoLa12]</sup> Calculations have been performed by Fuchi *et al.* and Fukami *et al.* showing the tremendous role of In amount in the InGaAs(N)/GaP bandlineups.<sup>[FNMK04, FUFU11, PLRS13, SGNB12]</sup> Nevertheless, efficient active area on GaP/Si still needs to be found.

## 1.5 Challenges of growing GaP/Si

### 1.5.1 Difference in lattice constant

Lattice mismatch is unavoidable for III-V on Si epitaxy, it is therefore important to consider how this mismatch will be accommodated during semiconductor crystal growth. When a semiconductor film with a lattice constant  $a_L$  is deposited on a semiconductor substrate with a lattice constant  $a_S$ , a misfit strain is developed which can be defined as:

$$f = \frac{a_S - a_L}{a_S} \quad (\text{Eq. 2})$$

For thin films with low amounts of mismatch, this misfit strain will be accommodated by an elastic deformation of the deposited film lattice. Epitaxial films

with lattice constants larger than the substrate lattice will be compressively strained, while films with smaller lattice constants will undergo tensile strain. In either case, the film material will remain coherently linked to the substrate, with each substrate atom uniquely bonded to corresponding atoms in the film above it. With higher amounts of mismatch, or thicker epitaxial films, the misfit strain at the interface will increase until it exceeds the elastic strength of the coherent semiconductor-semiconductor bonds, usually named the critical thickness. At this point, the film will undergo a plastic deformation resulting in the formation of broken bonds and non-coherent crystal defects at the substrate-film interface. A simplified cross-section showing the elastic and plastic stages of misfit strain accommodation for a compressive semiconductor film on a thick substrate is shown in **Figure 1-13**.

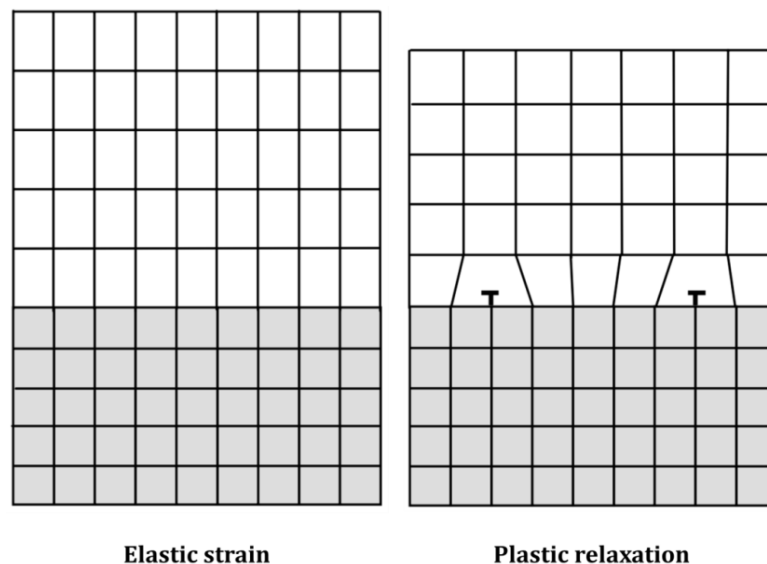


**Figure 1-13:** Elastic strain and plastic relaxation at a mismatched semiconductor interface. Note the 2 misfit dislocations at the mismatched interface after plastic relaxation (denoted by the “T” symbol).

It can be seen from the figure that the deposited film will accommodate misfit strain plastically by forming a one-dimensional line of broken atomic bonds at the substrate-film interface. This one-dimensional defect structure is known as a misfit dislocation and will extend along the interface and/or into the crystal volume.

To overcome this issue, the epilayer thickness should not exceed a critical value. The critical thickness  $h_c$  of GaP epitaxially grown on Si is predicted to be 64 nm according to Skibitzki *et al.*<sup>[SHYZ12]</sup> Experimental data have confirmed that the critical

thickness of GaP/Si is in the range of 45-95 nm.<sup>[TFWK10]</sup> Thicker layers can be grown by strain compensation of the GaP/Si system by incorporation of N. Increasing of critical thickness of Ga(PN) as a function of N content is presented in the **Figure 1-14**.<sup>[SHYZ12]</sup>

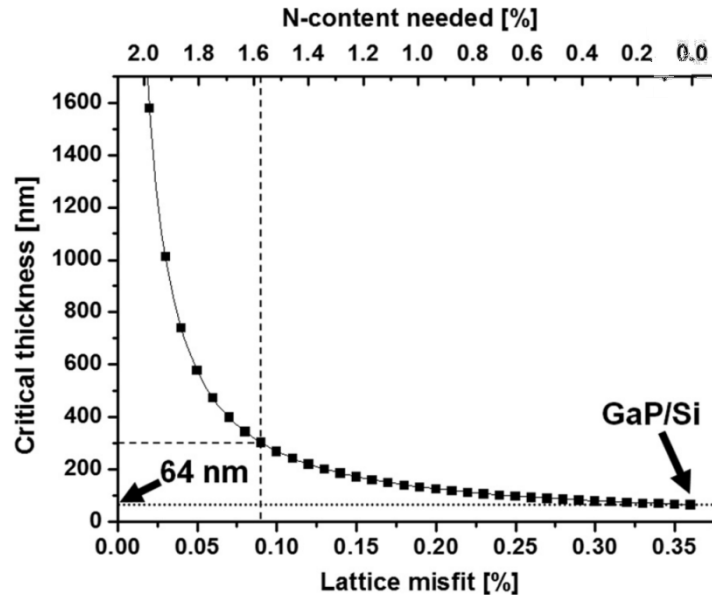


**Figure 1-14:** Critical thickness  $h_c$  vs lattice misfit as a function of N-content in GaPN (N-content varies from 0-2%) system. Vertical dotted line shows an example of  $h_c=300$  nm with 1.57% nitrogen. From Ref.<sup>[SHYZ12]</sup>

### 1.5.2 Difference in thermal expansion behavior

The thermal expansion coefficient of GaP is almost double the coefficient of Si at room temperature ( $\alpha_{\text{GaP}} = 4.65 \times 10^{-6} \text{ K}^{-1}$ ,  $\alpha_{\text{Si}} = 2.6 \times 10^{-6} \text{ K}^{-1}$ ). This causes a problem in the growth of heteroepitaxial layers, if the layer is grown at high temperature, where the actual lattice mismatch is different from the value at room temperature. The typical lattice mismatch of GaP/Si is  $\Delta a/a = 0.52\%$  at  $580^\circ\text{C}$  (typical temperature of MBE growth GaP/Si),  $0.3\%$  at  $10\text{K}$  (typical low temperature for photoluminescence measurement), and  $0.36\%$  at room temperature. One can refer to **Figure 1-15** for lattice parameters of GaP and Si as a function of temperature (a) and their lattice mismatch with respect to the temperature (b). The material system is more compressively strained at the growth temperature than at room temperature. When the material is cooled down to room temperature, a strain relief of  $0.2\%$  appears. In strained thin layers without relaxation, this effect lowers the resulting strain. Assuming a thick layer, completely relaxed at the growth temperature, this effect does not act as strain relief, but as additional tensile strain. Due to the difference between the thermal expansion coefficients, the thick wafer

material will shrink slower than the epilayer. The total amount of tensile strain accumulated upon cooling down from the growth temperature to room temperature is:

$$\varepsilon_t = \int_{T_{room}}^{T_{growth}} [\alpha_{substrate}(T) - \alpha_{epilayer}(T)] dT \quad (\text{Eq. 3})$$

This equation can be simplified for practical purpose by assuming that the thermal expansion coefficients are independent on the temperature. In this case, the accumulated tensile strain has a simple linear form:

$$\varepsilon_t = (\alpha_{substrate} - \alpha_{epilayer}) \Delta T \quad (\text{Eq. 4})$$

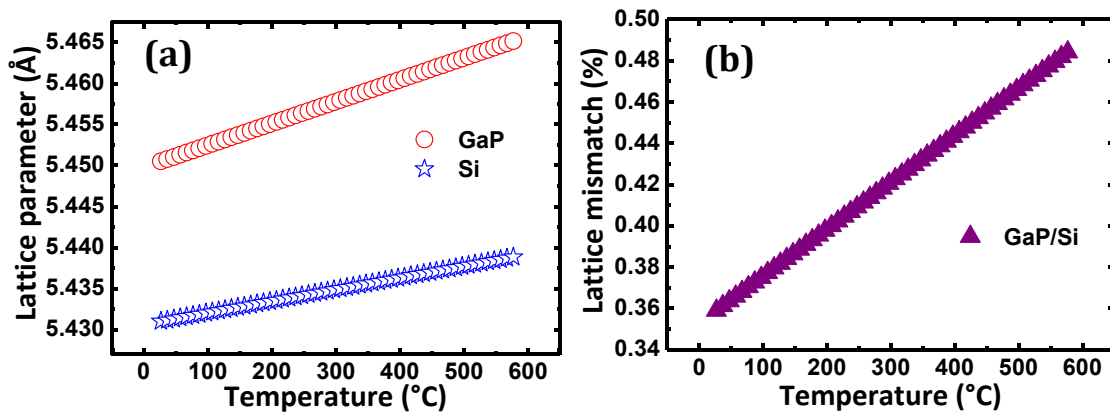


**Figure 1-15:** Lattice parameters of bulk GaP and Si with respect to temperature (a) and GaP/Si lattice mismatch as a function of temperature (b).

Since this tensile strain increases during the cooling process of the material system, the dislocation relaxation mechanisms are less efficient at relieving this strain, since the dislocation gliding processes are slower at low temperature. Reaching room temperature, only a small part of the accumulated thermal tensile strain is relieved by relaxation. The residual tensile strain can result in the appearance of microcracks in the epilayer. The critical cracking thickness of GaAs/Si system is between 3-5  $\mu\text{m}$  with lateral separation of the microcracks below 200  $\mu\text{m}$ .<sup>[HKMK91]</sup> This phenomenon also gives a thickness limitation for large wafer production and also in GaP/Si system. In the framework of this thesis, the epitaxial layer thickness is much lower than this value, microcracks could be neglected.

### 1.5.3 Cross-doping

Silicon is usually used as n-type dopant for GaP whereas Ga and P are respectively p and n-type dopants for silicon. This cross-doping is an important issue when optimizing device structure grown on Si such as laser diodes or solar cells. Indeed, silicon and GaP are mutual dopants, the autodoping can unpredictably change the doping characteristics of the interfaces, resulting in parasitic p-n junctions in devices.

Especially, growth of Si and GaP in the same chamber can cause cross-contamination during the III-V and Si crystal epitaxy. The solution could be separately growing the GaP and Si buffer, ideally by using a growth cluster composing of 2 chambers connected together under ultra-high vacuum. One chamber is devoted to the growth of III-V compounds and the other is devoted to the growth of silicon.<sup>[FYWI07, QKNP13]</sup> Such a growth cluster has been developed in our lab since 2010 which is composed of a Riber UHV-CVD chamber for silicon growth which is connected with a tunnel under vacuum to a Riber solid sources MBE chamber devoted to III-V growth. However, even with this double chamber experimental setup, thermally activated interdiffusion during or after the growth should be carefully limited.

### 1.5.4 Charge neutrality of the heterointerface

One of the concerns in MBE growth of III-V polar materials on non-polar elemental one is the problem of charge neutrality at the heterointerface. As the Si-P bond is stronger than that of Ga-Si, the first layer which bonds to Si topmost layer is predicted to be phosphorus' sublattice.<sup>[Kroe87]</sup> The Ga-Si and P-Si bonds carry a charge of  $\pm e/4$ . If the first atomic plane on the silicon surface is a continuous Ga plane (for example), the two bonds with the Si lattice would introduce a donor-like charge defect with the charge density of  $e/a^2$  which is equal to  $3 \times 10^{14} \text{ cm}^{-2}$ .<sup>[Kroe87]</sup> This huge charge would build up an electric field of  $4 \times 10^7 \text{ V/cm}$  in the epilayer. Such a large electric field could result in a rearrangement of the atoms at the topmost Si surface and also the rearrangement of III-V atoms at the heterointerface. According to Harrison's model,<sup>[HKWG78]</sup> silicon atoms are supposed to leave the topmost layer and incorporate into the first III-V layer, or leave its own crystal. This could lead to the formation of antiphase domains. However, the influence of interface charge on the structural and optical properties still remains unclear.

### 1.5.5 Antiphase domains

GaP is a non-centrosymmetric binary compound which consists of the imbrication of two FCC sublattices, each sublattice is built up from Ga or P elements. The ordering of the cationic and anionic FCC sublattices can be described by the terminology “*crystal polarity*”. Growth of a compound semiconductor on an elemental one can form crystal domains which consist of relatively reversed polarity within the compound layer. Such a crystal domain is called anti-phase domain (APD). The junction of the two consecutive APDs forms a two-dimensional structural defect called an anti-phase boundary (APB). A vertical APB is schematically represented in **Figure 1-16**.

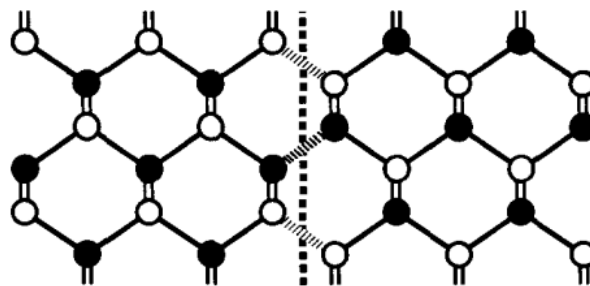


**Figure 1-16:** APB (vertical dotted line) formation in the zincblende structure, containing (in this case) both Ga-Ga and P-P bonds.<sup>[Kroe87]</sup>

The formation of such an APB during the growth of a polar semiconductor compound on a non-polar one could be taken place by two possibilities: the compound material nucleates on an atomically smooth Si surface, but not with the same initial sublattice. It can happen if two crystal domains nucleated on the Si surface are rotated by  $90^\circ$  around the  $[001]$  direction. As shown in **Figure 1-17** (a), the crystal domains on the left and right side have their local orientation perpendicular to the orientation of the middle crystal domain. This formation is assumed to occur when the first atomic plane of the compound material is locally not continuous which can happen during MBE process. In the other case, when the first deposited atomic plane is assumed to be continuous, but the Si surface has mono atomic steps, there is also a possibility to form such an anti-phase defect. The closest equal lattice planes of the diamond-structured silicon in  $[001]$  direction have a distance of  $a/4$ . This distance in the zinc-blende compounds is  $a/2$ . This means that, if a compound material is nucleated on a Si-surface, consisting of  $a/4$  – monolayer steps, the grown compound material will have a change in

the  $[001]$  lattice plane sequence – an APB above the Si monostep (as illustrated in **Figure 1-17 (b)**).

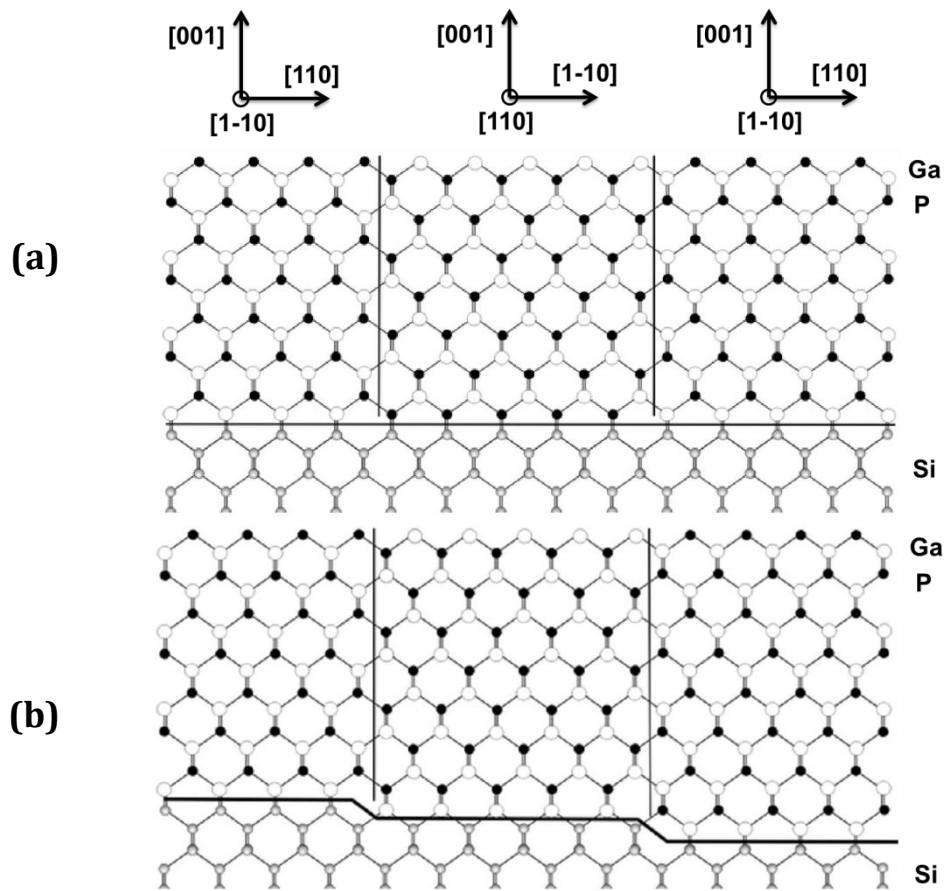


**Figure 1-17:** Anti-phase boundaries in zinc-blende structure. (a) APB lying on a  $\{110\}$  plane originated from discontinuous first GaP sublattice, (b) APB lying on a  $\{110\}$  plane, originating from a monolayer high step of the Si surface. From<sup>[Néme08]</sup>

Two APD can have their boundaries lying on various lattice planes. The possibilities are outlined in **Figure 1-18**. The APB lying on the  $(110)$  plane (between point A and B in **Figure 1-18**) is stoichiometric, i.e. it consists of an equal number of cation-cation and anion-anion antisite bonds. The total number of cations and anions is the same, as in the perfect crystal. The local bonds in the APB can be distorted because of difference of bond strength between Ga-Ga or P-P and Ga-P. There are APBs that consist of unequal number of false bonds. Such non-stoichiometric APBs are on the  $\{211\}$  (DE) and  $\{311\}$  (EF) crystallographic planes. The APBs on the  $\{111\}$  planes (BC) or on the  $\{001\}$  planes (CD) are built up of a pair of false planes of Ga-Ga or P-P.

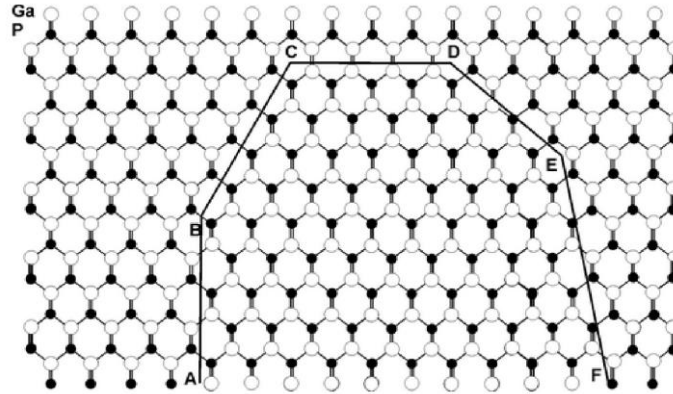


**Figure 1-18:** Anti-phase boundaries in zinc-blende structure lying on various lattice planes: AB – (110), BC – (111), CD – (001), DE – (211), EF – (311).<sup>[Néme08]</sup>

When two APBs incline towards each other, they can meet and self-annihilate, as illustrated in **Figure 1-19**. The region above the intersection of the APBs is single phase.

APBs are structural defects which can serve as a large scale trapping site to reduce minority carrier life-time in III-V layers,<sup>[LSBL96]</sup> and also act to increase majority carrier scattering in electronic circuits.<sup>[Holt69]</sup> False bonds in APBs represent electrically charged defects: A comparison of the number of bonding orbitals with the number of valence electrons available to fill them shows that Ga-Ga bonds act as acceptors, and P-P bonds as donors, with effective charges  $\pm e/2$  per bond. In general, an APB will contain roughly equal numbers of both charges, thus acting as an extremely highly compensated doping sheet with very little net doping. In the case of APBs lying on {110} planes, the situation is least bad because the equal number of Ga-Ga and P-P bonds acts as a perfect local charge compensation. This gives rise to the most stable configuration according to calculation of Rubel and Branovskii.<sup>[RuBa09]</sup> In other situations, the lack of exact local charge balance will lead to potential fluctuations that will affect the electronic properties.<sup>[Kroe87]</sup>

There were various strategies to grow APD free, single phase III-V material on elemental substrates. The main approaches of the suppression of APDs were the following:

- i) **Use of different orientation of the substrate:** this is proved by Kroemer that by using Si (211) substrate they can obtain APD free GaAs/Si layers and the heterointerface did not present the electrical charge problem. It exploited the two sublattices of the III-V crystal having a different number of back bonds to the Si substrate. The sites with the double back bonds were expected

to be occupied by the stronger bonding As-Si while the sites with the single back bonds were occupied by the weaker bonding Ga-Si. APD free structure was proved by chemical selective etching method.<sup>[Kroe87]</sup>

- ii) **Use of mis-oriented Si (001) substrates with misorientation towards the [110] direction:** the principle of this method is the suppression of monolayer high steps on Si surface and generation of even number layer high steps. It was found that a step-doubling of the misoriented Si (001) surface occurs during annealing. A detailed study of Kaplan showed that most of the surface steps on the Si surface are double steps if the Si surface is misoriented by a few degrees towards the [110] direction.<sup>[Kap80]</sup> Using this method, the growth of APDs free GaAs/Si layers<sup>[FCKM85]</sup> and GaP/Si layers were reported.<sup>[TYST98]</sup>

This thesis uses the latter method to promote the APDs annihilation. A detailed study will be discussed in chapter 4 and 5.

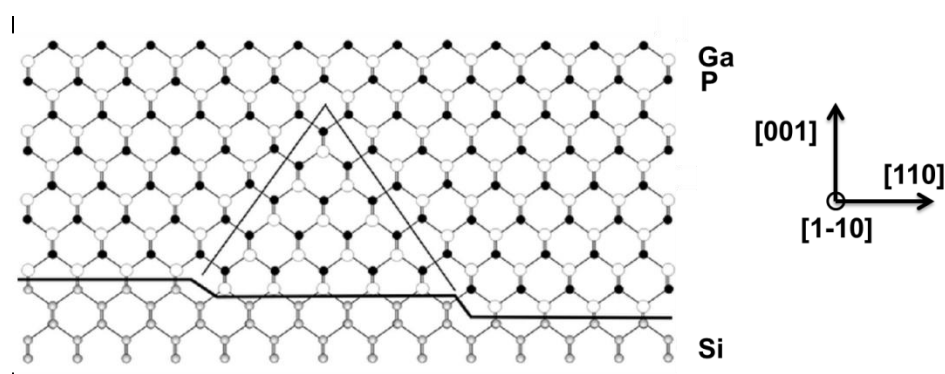


**Figure 1-19:** Self-annihilation of APBs lying on {111} planes. From <sup>[Néme08]</sup>

### 1.5.6 Stacking faults, Microtwins

The ideal stacking of (111) planes in the zinc-blende structure, ABCABC..., can be disturbed in various ways and creates area defects. This is depicted in detail by I. Németh.<sup>[Néme08]</sup> If one plane is missing, i.e. the stacking is ABCACABC, an intrinsic stacking fault is present (**Figure 1-20 (a)**). If an additional plane is present, the defect is called an extrinsic stacking fault, i.e. ABCABACABC (**Figure 1-20 (b)**). If the stacking sequence is changed so that it is mirror symmetric onto a plane, having a sequence of:

$$ABCABCABCABC \Rightarrow ABCABC|CBACBA,$$

The crystal on one side of this plane adjoins its **twin** from the other side. This is called a **microtwin** if its thickness is in the order of several atomic planes. The **microtwin** can also be understood as a rotation of the twin crystal by 180° around a

<111> direction. A model of microtwin in GaP structure is schematically represented in **Figure 1-21**, as given by Skibitzki *et al.*<sup>[SHYZ12]</sup>

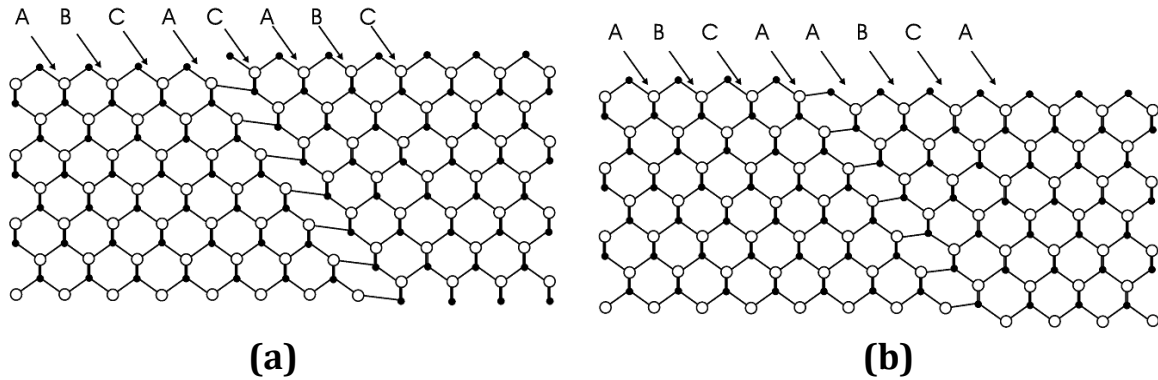


**Figure 1-20:** Planar defects of the zinc-blende crystal : (a) intrinsic stacking fault, (b) extrinsic stacking fault.<sup>[Néme08]</sup>

A stacking fault is bounded by two partial dislocations formed by the dissociation of a perfect dislocation. A perfect dislocation with Burger’s vector  $a/2 [1 1 0]$  in a III–V compound is dissociated into two Shockley partial dislocations according to Mader and Blakeslee:<sup>[MaBl74b]</sup>

$$\frac{a}{2}[0 \bar{1} \bar{1}] \rightarrow \frac{a}{6}[1 2 \bar{1}] + \frac{a}{6}[\bar{1} 1 2] \quad (\text{Eq. 5})$$

Since the dislocation energy is proportional to  $|\mathbf{b}|^2$ , the dissociation is energetically favored. The stacking-fault energies in undoped GaP films grown on Si were calculated by Cohen and Barry Carter.<sup>[CoBa99]</sup> Values of extrinsic and intrinsic stacking fault energies were equal to  $40.5 \pm 3 \text{ mJ/m}^2$  (or  $2.53 \pm 0.19 \text{ meV/\AA}^2$ ) and  $43.4 \pm 2 \text{ mJ/m}^2$  (or  $2.71 \pm 0.12 \text{ meV/\AA}^2$ ), respectively.

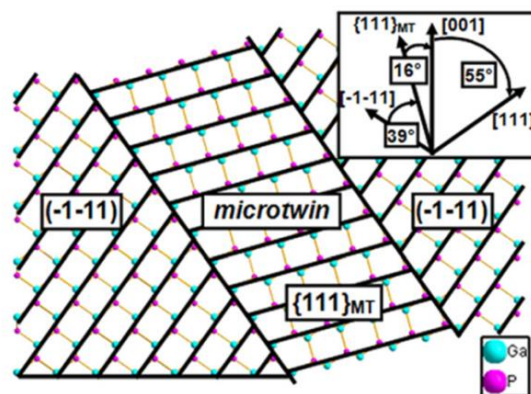


**Figure 1-21:** Schematically representation of microtwin model in zinc-blend GaP structure.<sup>[SHYZ12]</sup>

According to reports, stacking faults and microtwins are generally formed at the early growth stage of GaP/Si.<sup>[TYST98]</sup> Three dimensional growth and the coalescence of the 3D nucleation sites were attributed to be the reason for their formation. Nevertheless, the particular role of the nucleation of GaP on Si step edges cannot be neglected. Detailed study of microtwins in the GaP/Si system will be reported in chapter 5.

## 1.6 Conclusion

The dawn of the photonic age has come with the potential integration of photonic devices on silicon. Although light emission has been enabled on Si by using germanium, erbium doping, Si nanocrystal or coupling of the two later and Raman excitation, the use of III-V compound materials reveals more benefits because of their better optical and electronic properties: direct band gap, high mobility, facilitation of light emission and absorption. Hybrid silicon lasers based on InP lasers bonded on silicon platform shown their advantages in short term operation and a proof of concept for the silicon photonic routine, but long term utilization, low cost fabrication, reduced time consuming and high density integration require monolithic integration on silicon substrate. Gallium phosphide (GaP) is the best candidate for dislocation free growth of pseudomorphic heteroepitaxial GaP/Si because it is quasi lattice-matched with silicon. The inclusion of ~2.2 % of nitrogen allows the exact lattice-matching with silicon. The growth of GaP on Si substrate has to deal with the problems of growing a general polar semiconductor compound on a non-polar elemental one: the difference in lattice constant could reveal misfit dislocation, the difference in thermal expansion coefficient could generate tensile strain when cooling down from growth temperature to room temperature, the formation of anti-phase boundaries, stacking faults and microtwins which act as charge trapping and are detrimental for optical and electrical properties of the devices. In this context, one of the main challenges for the successful photonics integration is the improvement of the crystal quality of the material. Another challenge is to find an efficient light emitter on silicon substrate, in the pseudomorphic approach.

## REFERENCES

- [Abst97] ABSTREITER, Gerhard: Light Emission in Silicon: From Physics to Devices. In: DAVID J. LOCKWOOD (ed.): *Semiconductors and Semimetals*. vol. Volume 49 : Elsevier, 1997 — ISBN 0080-8784, pp. 37–76

- [ACKN13] ALOUANE, M. H. Hadj; CHAUVIN, N.; KHMISSI, H.; NAJI, K.; et al.: In: *Nanotechnology* **24** (2013), No. 3, p. 035704
- [AEFW89] ABSTREITER, G.; EBERL, K.; FRIESS, E.; WEGSCHEIDER, W.; ZACHAI, R.: In: *Journal of Crystal Growth* **95** (1989), No. 1–4, pp. 431–438
- [BCKV06] BORCK, S.; CHATTERJEE, S.; KUNERT, B.; VOLZ, K.; et al.: In: *Applied Physics Letters* **89** (2006), No. 3, p. 031102
- [BiTu96] BI, W. G.; TU, C. W.: In: *Applied Physics Letters* **69** (1996), No. 24, pp. 3710–3712
- [BMSS00] BEYER, A.; MÜLLER, E.; SIGG, H.; STUTZ, S.; GRÜTZMACHER, D.; LEIFELD, O.; ENSSLIN, K.: In: *Applied Physics Letters* **77** (2000), No. 20, pp. 3218–3220
- [BrHa97] BROWN, Thomas G.; HALL, Dennis G.: Light Emission in Silicon: From Physics to Devices. In: DAVID J. LOCKWOOD (ed.): *Semiconductors and Semimetals*. vol. Volume 49 : Elsevier, 1997 — ISBN 0080-8784, pp. 77–110
- [Canh90] CANHAM, L. T.: In: *Applied Physics Letters* **57** (1990), No. 10, pp. 1046–1048
- [CASK08] CHAMINGS, J.; ADAMS, A. R.; SWEENEY, S. J.; KUNERT, B.; VOLZ, K.; STOLZ, W.: In: *Applied Physics Letters* **93** (2008), No. 10, p. 101108
- [CCMC03] CASTAGNA, Maria Eloisa; COFFA, Salvatore; MONACO, Mariantonietta; CARISTIA, Liliana; MESSINA, Alberto; MANGANO, Rosario; BONGIORNO, Corrado: In: *Physica E: Low-dimensional Systems and Nanostructures* **16** (2003), No. 3–4, pp. 547–553
- [CDHJ02] CLAPS, Ricardo; DIMITROPOULOS, Dimitri; HAN, Yan; JALALI, Bahram.: In: *Optics Express* **10** (2002), No. 22, p. 1305
- [CeRT10] CERUTTI, L.; RODRIGUEZ, J.B.; TOURNIE, E.: In: *IEEE Photonics Technology Letters* **22** (2010), No. 8, pp. 553–555
- [CIDJ02] CLAPS, R.; DIMITROPOULOS, D.; JALALI, B.: In: *Electronics Letters* **38** (2002), No. 22, pp. 1352–1354
- [CoBa99] COHEN, Dov; BARRY CARTER, C.: In: *Philosophical Magazine A* **79** (1999), No. 8, pp. 1805–1815
- [CSCK11] CHUANG, Linus C.; SEDGWICK, Forrest G.; CHEN, Roger; KO, Wai Son; MOEWE, Michael; NG, Kar Wei; TRAN, Thai-Truong D.; CHANG-HASNAIN, Connie.: In: *Nano Letters* **11** (2011), No. 2, pp. 385–390
- [CTNK11] CHEN, Roger; TRAN, Thai-Truong D.; NG, Kar Wei; KO, Wai Son; CHUANG, Linus C.; SEDGWICK, Forrest G.; CHANG-HASNAIN, Connie.: In: *Nature Photonics* **5** (2011), No. 3, pp. 170–175
- [DMMG03] DIEHL, L.; MENTESE, S.; MÜLLER, E.; GRÜTZMACHER, D.; et al.: In: *Physica E: Low-dimensional Systems and Nanostructures* **16** (2003), No. 3–4, pp. 315–320
- [FCKM85] FISCHER, R.; CHAND, N.; KOPP, W.; MORKOÇ, H.; ERICKSON, L. P.; YOUNGMAN, R.: In: *Applied Physics Letters* **47** (1985), No. 4, pp. 397–399
- [FCPS97] FRANZÒ, Giorgia; COFFA, Salvatore; PRIOLO, Francesco; SPINELLA, Corrado.: In: *Journal of Applied Physics* **81** (1997), No. 6, pp. 2784–2793
- [FKIB12] FALUB, Claudiu V.; KÄNEL, Hans von; ISA, Fabio; BERGAMASCHINI, Roberto; et al.: In: *Science* **335** (2012), No. 6074, pp. 1330–1334
- [FNMK04] FUCHI, Shingo; NONOGAKI, Youichi; MORIYA, Hiromitsu; KOIZUMI, Atsushi; FUJIWARA, Yasufumi; TAKEDA, Yoshikazu.: In: *Physica E: Low-dimensional Systems and Nanostructures* **21** (2004), No. 1, pp. 36–44
- [FPCJ06] FANG, Alexander W.; PARK, Hyundai; COHEN, Oded; JONES, Richard; PANICCIA, Mario J.; BOWERS, John E.: In: *Optics Express* **14** (2006), No. 20, pp. 9203–9210
- [FPVP00] FRANZÒ, Giorgia; PACIFICI, Domenico; VINCIGUERRA, Vincenzo; PRIOLO, Francesco; IACONA, Fabio.: In: *Applied Physics Letters* **76** (2000), No. 16, pp. 2167–2169
- [FUFU11] FUKAMI, F.; UMENO, K.; FURUKAWA, Y.; URAKAMI, N.; MITSUYOSHI, S.; OKADA, H.; YONEZU, H.; WAKAHARA, A.: In: *physica status solidi (c)* **8** (2011), No. 2, pp. 322–324

- [FYWI07] FURUKAWA, Y.; YONEZU, H.; WAKAHARA, A.; ISHII, S.; MOON, S.Y.; MORISAKI, Y.: In: *Journal of Crystal Growth* **300** (2007), No. 1, pp. 172–176
- [GBCF09] GUO, Weiming; BONDI, Alexandre; CORNET, Charles; FOLLIOU, Hervé; et al.: In: *physica status solidi (c)* **6** (2009), No. 10, pp. 2207–2211
- [GBHF09] GERHARD, S; BAUMANN, V; HÖFLING, S; FORCHEL, A.: In: *Nanotechnology* **20** (2009), No. 43, p. 434016
- [GeKo00] GELLOZ, Bernard; KOSHIDA, Nobuyoshi.: In: *Journal of Applied Physics* **88** (2000), No. 7, pp. 4319–4324
- [GEKP13] GHRIB, A.; EL KURDI, M.; DE KERSAUSON, M.; PROST, M.; et al.: In: *Applied Physics Letters* **102** (2013), No. 22, pp. 221112–221112–4
- [GPCC10] GOBAUT, B.; PENUELAS, J.; CHENG, J.; CHETTAOUI, A.; LARGEAU, L.; HOLLINGER, G.; SAINT-GIRONS, G.: In: *Applied Physics Letters* **97** (2010), No. 20, pp. 201908–201908–3
- [GZWR01] GREEN, Martin A.; ZHAO, Jianhua; WANG, Aihua; REECE, Peter J.; GAL, Michael.: In: *Nature* **412** (2001), No. 6849, pp. 805–808
- [HBKD08] HUANG, S. H.; BALAKRISHNAN, G.; KHOSHAKHLAGH, A.; DAWSON, L. R.; HUFFAKER, D. L.: In: *Applied Physics Letters* **93** (2008), No. 7, pp. 071102–071102–3
- [Hech02] HECHT, Eugene: *Optics*. 4. ed. San Francisco : Addison-Wesley, 2002 — ISBN 9780805385663
- [HFKS62] HALL, R. N.; FENNER, G. E.; KINGSLEY, J. D.; SOLTYS, T. J.; CARLSON, R. O.: In: *Physical Review Letters* **9** (1962), No. 9, pp. 366–368
- [HHSL11] HOSSAIN, Nadir; HOSEA, T. J. C.; SWEENEY, Stephen J.; LIEBICH, Sven; ZIMPRICH, Martin; VOLZ, Kerstin; KUNERT, Bernardette; STOLZ, Wolfgang.: In: *Journal of Applied Physics* **110** (2011), p. 063101
- [HJLZ12] HOSSAIN, N.; JIN, S. R.; LIEBICH, S.; ZIMPRICH, M.; VOLZ, K.; KUNERT, B.; STOLZ, W.; SWEENEY, S. J.: In: *Applied Physics Letters* **101** (2012), No. 1, pp. 011107–011107–4
- [HKMK91] HAYAFUJI, Norio; KIZUKI, Hirotaka; MIYASHITA, Motoharu; KADOIWA, Kaoru; et al.: In: *Japanese Journal of Applied Physics* **30** (1991), No. Part 1, No. 3, pp. 459–463
- [HKWG78] HARRISON, W. A.; KRAUT, E. A.; WALDROP, J. R.; GRANT, R. W.: In: *Physical Review B* **18** (1978), No. 8, pp. 4402–4410
- [HLHK05] HATAMI, F.; LORDI, V.; HARRIS, J. S.; KOSTIAL, H.; MASSELINK, W. T.: In: *Journal of Applied Physics* **97** (2005), No. 9, p. 096106
- [HMST03] HATAMI, F.; MASSELINK, W. T.; SCHROTTKE, L.; TOMM, J. W.; TALALAEV, V.; KRISTUKAT, C.; GOÑI, A. R.: In: *Physical Review B* **67** (2003), No. 8, p. 085306
- [HoBe62] HOLONYAK, Nick; BEVACQUA, S. F.: In: *Applied Physics Letters* **1** (1962), No. 4, pp. 82–83
- [Holt69] HOLT, D.B.: In: *Journal of Physics and Chemistry of Solids* **30** (1969), No. 6, pp. 1297–1308
- [HSRO11] HOSSAIN, N.; SWEENEY, S.J.; ROGOWSKY, S.; OSTENDORF, R.; et al.: In: *Electronics Letters* **47** (2011), No. 16, pp. 931–933
- [Hybe94] HYBERTSEN, Mark S.: In: *Physical Review Letters* **72** (1994), No. 10, pp. 1514–1517
- [IaFS00] IACONA, Fabio; FRANZÒ, Giorgia; SPINELLA, Corrado.: In: *Journal of Applied Physics* **87** (2000), No. 3, pp. 1295–1303
- [IIFM10] IRRERA, Alessia; IACONA, Fabio; FRANZÒ, Giorgia; MIRITELLO, Maria; LO SAVIO, Roberto; CASTAGNA, Maria Eloisa; COFFA, Salvatore; PRIOLO, Francesco.: In: *Journal of Applied Physics* **107** (2010), No. 5, pp. 054302–054302–6
- [IPMF03] IRRERA, A.; PACIFICI, D.; MIRITELLO, M.; FRANZO, G.; et al.: In: *Physica E: Low-dimensional Systems and Nanostructures* **16** (2003), No. 3–4, pp. 395–399
- [Kapl80] KAPLAN, Ray.: In: *Surface Science Letters* **93** (1980), No. 1, p. A91
- [KBFG12] KOUKOURAKIS, N.; BÜCKERS, C.; FUNKE, D. A.; GERHARDT, N. C.; et al.: In: *Applied Physics Letters* **100** (2012), No. 9, pp. 092107–092107–3

- [KGGK09] KARCHER, C.; GRÜNING, H.; GÜNGERICH, M.; KLAR, P. J.; KUNERT, B.; VOLZ, K.; STOLZ, W.; HEIMBRODT, W.: In: *physica status solidi (c)* **6** (2009), No. 12, pp. 2638–2643
- [KKRV06] KUNERT, B.; KLEHR, A.; REINHARD, S.; VOLZ, K.; STOLZ, W.: In: *Electronics Letters* **42** (2006), No. 10, pp. 601–603
- [KRKL06] KUNERT, B.; REINHARD, S.; KOCH, J.; LAMPALZER, M.; VOLZ, K.; STOLZ, W.: In: *physica status solidi (c)* **3** (2006), No. 3, pp. 614–618
- [Kroe87] KROEMER, Herbert.: In: *Journal of Crystal Growth* **81** (1987), No. 1-4, pp. 193–204
- [KuVS07] KUNERT, B.; VOLZ, K.; STOLZ, W.: In: *physica status solidi (b)* **244** (2007), No. 8, pp. 2730–2739
- [KVKS06] KUNERT, B.; VOLZ, K.; KOCH, J.; STOLZ, W.: In: *Applied Physics Letters* **88** (2006), No. 18, p. 182108
- [KVKS07] KUNERT, B.; VOLZ, K.; KOCH, J.; STOLZ, W.: In: *Journal of Crystal Growth* **298** (2007), pp. 121–125
- [KVNS06] KUNERT, B.; VOLZ, K.; NEMETH, I.; STOLZ, W.: In: *Journal of Luminescence* **121** (2006), No. 2, pp. 361–364
- [LCHC93] LOMBARDO, S.; CAMPISANO, S. U.; VAN DEN HOVEN, G. N.; CACCIATO, A.; POLMAN, A.: In: *Applied Physics Letters* **63** (1993), No. 14, pp. 1942–1944
- [Lede03] LEDENTSOV, N. N.: Si-Ge Quantum Dot Laser. In: PAVESI, Lorenzo; GAPONENKO, Sergey; NEGRO, Luca Dal (eds.): *Towards the First Silicon Laser, NATO Science Series*: Springer Netherlands, 2003 — ISBN 978-1-4020-1194-8, 978-94-010-0149-6, pp. 281–292
- [LGHB00] LEDENTSOV, N.N.; GRUNDMANN, M.; HEINRICHSORFF, F.; BIMBERG, D.; et al.: In: *IEEE Journal of Selected Topics in Quantum Electronics* **6** (2000), No. 3, pp. 439–451
- [LiBo10] LIANG, Di; BOWERS, John E.: In: *Nat Photon* **4** (2010), No. 8, pp. 511–517
- [LiKM12] LIU, Jifeng; KIMERLING, Lionel C.; MICHEL, Jurgen.: In: *Semiconductor Science and Technology* **27** (2012), No. 9, p. 094006
- [LJTS12] LEE, Andrew; JIANG, Qi; TANG, Mingchu; SEEDS, Alwyn; LIU, Huiyun.: In: *Optics Express* **20** (2012), No. 20, pp. 22181–22187
- [LLCW98] LEON, R.; LOBO, C.; CHIN, T. P.; WOODALL, J. M.; FAFARD, S.; RUVIMOV, S.; LILIENTAL-WEBER, Z.; STEVENS KALCEFF, M. A.: In: *Applied Physics Letters* **72** (1998), No. 11, p. 1356
- [LSBL96] LI, Yuan; SALVIATI, G.; BONGERS, M.M.G.; LAZZARINI, L.; NASI, L.; GILING, L.J.: In: *Journal of Crystal Growth* **163** (1996), No. 3, pp. 195–202
- [LTPW13] LUXMOORE, I. J.; TORO, R.; POZO-ZAMUDIO, O. Del; WASLEY, N. A.; et al.: In: *Scientific Reports* **3** (2013)
- [LWJH11] LIU, Huiyun; WANG, Ting; JIANG, Qi; HOGG, Richard; TUTU, Frank; POZZI, Francesca; SEEDS, Alwyn.: In: *Nature Photonics* **5** (2011), No. 7, pp. 416–419
- [LZBL11] LIEBICH, S.; ZIMPRICH, M.; BEYER, A.; LANGE, C.; et al.: In: *Applied Physics Letters* **99** (2011), No. 7, pp. 071109–071109–3
- [MaBl74a] MATTHEWS, J.W.; BLAKESLEE, A.E.: In: *Journal of Crystal Growth* **27** (1974), pp. 118–125
- [MaBl74b] MADER, S.; BLAKESLEE, A. E.: In: *Applied Physics Letters* **25** (1974), No. 7, pp. 365–367
- [MAMK97] MICHEL, J.; ASSALI, L.V.C.; MORSE, M.T.; KIMERLING, L.C.: Light Emission in Silicon: From Physics to Devices. In: DAVID J. LOCKWOOD (ed.): *Semiconductors and Semimetals*. vol. Volume 49: Elsevier, 1997 — ISBN 0080-8784, pp. 111–156
- [MFSJ10] MONTAZERI, Mohammad; FICKENSCHER, Melodie; SMITH, Leigh M.; JACKSON, Howard E.; et al.: In: *Nano Letters* **10** (2010), No. 3, pp. 880–886
- [MRJP87] MEARS, R.J.; REEKIE, L.; JAUNCEY, I.M.; PAYNE, D.N.: In: *Electronics Letters* **23** (1987), No. 19, p. 1026
- [MSWL04] MÅRTENSSON, Thomas; SVENSSON, C. Patrik T.; WACASER, Brent A.; LARSSON, Magnus W.; et al.: In: *Nano Letters* **4** (2004), No. 10, pp. 1987–1990

- [MYBQ09] MI, Z.; YANG, Jun; BHATTACHARYA, Pallab; QIN, Guoxuan; MA, Zhenqiang. In: *Proceedings of the IEEE* **97** (2009), No. 7, pp. 1239–1249
- [Néme08] NÉMETH, Igor: Marburg (Lahn), Philipps - Universität Marburg, 2008
- [OdTu06] ODNOLYUDOV, V. A.; TU, C. W.: In: *Applied Physics Letters* **89** (2006), No. 19, pp. 191107–191107–3
- [OORK96] ORNER, B. A.; OLOWOLAFE, J.; ROE, K.; KOLODZEY, J.; LAURSEN, T.; MAYER, J. W.; SPEAR, J.: In: *Applied Physics Letters* **69** (1996), No. 17, pp. 2557–2559
- [PaHj02] PASQUARIELLO, D.; HJORT, K.: In: *IEEE Journal of Selected Topics in Quantum Electronics* **8** (2002), No. 1, pp. 118–131
- [Pear94] PEARSALL, T.P.: In: *Progress in Quantum Electronics* **18** (1994), No. 2, pp. 97–152
- [PLBI03] PAUL, D.J.; LYNCH, S.A.; BATES, R.; IKONIC, Z.; et al.: In: *Physica E: Low-dimensional Systems and Nanostructures* **16** (2003), No. 3–4, pp. 309–314
- [PLRS13] PROHL, Christopher; LENZ, Andrea; ROY, Dominik; SCHUPPANG, Josephine; et al.: In: *Applied Physics Letters* **102** (2013), No. 12, p. 123102
- [QKNP13] QUINCI, T.; KUYALIL, J.; NGUYEN THANH, T.; PING WANG, Y.; et al.: In: *Journal of Crystal Growth* **380** (2013), pp. 157–162
- [RCJV13] RENARD, C.; CHERKASIN, N.; JAFFRE, A.; VINCENT, L.; et al.: In: *Applied Physics Letters* **102** (2013), No. 19, pp. 191915–191915–4
- [RCRG11] REBOUL, J. R.; CERUTTI, L.; RODRIGUEZ, J. B.; GRECH, P.; TOURNIÉ, E.: In: *Applied Physics Letters* **99** (2011), No. 12, pp. 121113–121113–3
- [RDBO88] RAZEGHI, M.; DEFOUR, M.; BLONDEAU, R.; OMNES, F.; et al.: In: *Applied Physics Letters* **53** (1988), No. 24, pp. 2389–2390
- [RSKL91] RICHTER, A.; STEINER, P.; KOZLOWSKI, F.; LANG, W.: In: *IEEE Electron Device Letters* **12** (1991), No. 12, pp. 691–692
- [RuBa09] RUBEL, Oleg; BARANOVSKII, Sergei D.: In: *International Journal of Molecular Sciences* **10** (2009), No. 12, pp. 5104–5114.
- [SAGP10] SHAMIRZAEV, Timur S.; ABRAMKIN, Demid S.; GUTAKOVSKII, Anton K.; PUTYATO, Mikhail A.: In: *Applied Physics Letters* **97** (2010), No. 2, p. 023108
- [SGNB12] STRACKE, G.; GLACKI, A.; NOWOZIN, T.; BONATO, L.; et al.: In: *Applied Physics Letters* **101** (2012), No. 22, pp. 223110–223110–4
- [SHYZ12] SKIBITZKI, O.; HATAMI, F.; YAMAMOTO, Y.; ZAUMSEIL, P.; et al.: In: *Journal of Applied Physics* **111** (2012), No. 7, pp. 073515–073515–9
- [SMSI92] SUGO, M.; MORI, H.; SAKAI, Y.; ITOH, Y.: In: *Applied Physics Letters* **60** (1992), No. 4, pp. 472–473
- [SoLa12] SONG, Yuncheng; LARRY LEE, Minjoo.: In: *Applied Physics Letters* **100** (2012), No. 25, pp. 251904–251904–3
- [SoSL10] SONG, Yuncheng; SIMMONDS, Paul J.; LEE, Minjoo Larry.: In: *Applied Physics Letters* **97** (2010), No. 22, p. 223110
- [StVG98] STOICA, T.; VESCAN, L.; GORYLL, M.: In: *Journal of Applied Physics* **83** (1998), No. 6, pp. 3367–3373
- [SVMH03] STOICA, T.; VESCAN, L.; MÜCK, A.; HOLLÄNDER, B.; SCHÖPE, G.: In: *Physica E: Low-dimensional Systems and Nanostructures* **16** (2003), No. 3–4, pp. 359–365
- [SYCG93] SCHNITZER, I.; YABLONOVITCH, E.; CANEAU, C.; GMITTER, T. J.: In: *Applied Physics Letters* **62** (1993), No. 2, pp. 131–133
- [SYTI96] SAMONJI, K.; YONEZU, H.; TAKAGI, Y.; IWAKI, K.; OHSHIMA, N.; SHIN, J. K.; PAK, K.: In: *Applied Physics Letters* **69** (1996), No. 1, pp. 100–102
- [TFWK10] TAKAGI, Yasufumi; FURUKAWA, Yuzo; WAKAHARA, Akihiro; KAN, Hirofumi.: In: *Journal of Applied Physics* **107** (2010), No. 6, pp. 063506–063506–8

- [TLWH10] TATEBAYASHI, J.; LIN, A.; WONG, P. S.; HICK, R. F.; HUFFAKER, D. L.: In: *Journal of Applied Physics* **108** (2010), No. 3, pp. 034315–034315–5
- [TYST98] TAKAGI, Y; YONEZU, H; SAMONJI, K; TSUJI, T; OHSHIMA, N.: In: *Journal of Crystal Growth* **187** (1998), No. 1, pp. 42–50
- [TYTM97] T. EGAWA; Y. MURATA; T. JIMBO; M. UMENO.: In: *Photonics Technology Letters, IEEE* **9** (1997), No. 7, pp. 872–874
- [UFUN10] UMENO, K.; FURUKAWA, Y.; URAKAMI, N.; NOMA, R.; MITSUYOSHI, S.; WAKAHARA, A.; YONEZU, H.: In: *Physica E: Low-dimensional Systems and Nanostructures* **42** (2010), No. 10, pp. 2772–2776
- [VeSt98] VESCAN, L; STOICA, T.: In: *Journal of Luminescence* **80** (1998), No. 1–4, pp. 485–489
- [WaTK96] WADA, H.; TAKAMORI, Takeshi; KAMIJOH, Takeshi.: In: *IEEE Photonics Technology Letters* **8** (1996), No. 11, pp. 1426–1428
- [XiTu00] XIN, H. P.; TU, C. W.: In: *Applied Physics Letters* **77** (2000), p. 2180
- [XTZM00] XIN, H. P; TU, C. W; ZHANG, Yong; MASCARENHAS, A.: In: *Applied Physics Letters* **76** (2000), No. 10, pp. 1267–1269
- [YACG86] YABLONOVITCH, E.; ALLARA, D. L.; CHANG, C. C.; GMITTER, T.; BRIGHT, T. B.: In: *Physical Review Letters* **57** (1986), No. 2, pp. 249–252
- [YaGm86] YABLONOVITCH, E.; GMITTER, T.: In: *Applied Physics Letters* **49** (1986), No. 10, pp. 587–589
- [YoFW08] YONEZU, Hiroo; FURUKAWA, Yuzo; WAKAHARA, Akihiro.: In: *Journal of Crystal Growth* **310** (2008), No. 23, pp. 4757–4762
- [Yone02] YONEZU, Hiroo.: In: *Semiconductor Science and Technology* **17** (2002), No. 8, pp. 762–768
- [YTSM97] YAMADA, T.; TACHIKAWA, M.; SASAKI, T.; MORI, H.; KADOTA, Y.: In: *Applied Physics Letters* **70** (1997), No. 12, pp. 1614–1615
- [ZDLP87] VAN DER ZIEL, J. P.; DUPUIS, R. D.; LOGAN, R. A.; PINZONE, C. J.: In: *Applied Physics Letters* **51** (1987), No. 2, pp. 89–91
- [ZHSS01] ZACHARIAS, M.; HEITMANN, J.; SCHMIDT, M.; STREITENBERGER, P.: In: *Physica E: Low-dimensional Systems and Nanostructures* **11** (2001), No. 2–3, pp. 245–251
- [ZMRK94] ZHENG, B.; MICHEL, J.; REN, F. Y. G.; KIMERLING, L. C.; JACOBSON, D. C.; POATE, J. M.: In: *Applied Physics Letters* **64** (1994), No. 21, pp. 2842–2844

## CHAPTER 2.

# GAPN – NITROGEN INCORPORATION

---

---

### 2.1 Introduction

Dilute nitride III-V-N semiconductors alloys have been widely studied, because of their unusual electronic and optoelectronic properties. Various applications have been demonstrated, such as laser devices in the long-wavelength range [Harr02], in the visible (or near infra-red) range [LZBL11], and more recently highest efficiency multi-junction solar cells.[GEHW12] Among the diluted nitride materials system, the GaAs(N) is the most studied from both the optical and growth point of view.[PiTo01] GaP(N) has also created renewed interest because of its low defects pseudomorphic integration on silicon.[MYFF01] Growing such materials remains a challenge, as the epitaxial process has to overcome the extremely low solid solubility of the nitrogen in both bulk GaAs ( $[N] < 10^{14} \text{ cm}^{-3}$  at  $T = 900 \text{ K}$ ) and bulk GaP ( $[N] < 10^{16} \text{ cm}^{-3}$  at  $T = 900 \text{ K}$ ).[HoSt97] In this context, efficient incorporation of nitrogen requires far from equilibrium conditions which is the case when using Molecular Beam Epitaxy (MBE).[HULR00] At typical growth temperature used for good quality GaAs or GaP (i.e. around  $600 \text{ }^\circ\text{C}$ ), spinodal decomposition of the metastable GaAsN (and likely GaPN) alloys occur resulting in defects generation.[PiTo01] At this temperature,  $\text{N}_2$  desorption is also expected to limit the nitrogen incorporation.[FYOS02, PiTo01] At too low temperature, the photoluminescence is affected by the degradation of the material overall quality. A compromise is thus found when the growth temperature is high enough to ensure the optical quality, but low enough to ensure the stability of the alloy.[PiTo01]

With respect to the electronic and optical properties, the incorporation of nitrogen in dilute regime has two main consequences: the appearance of strongly localized state around nitrogen atoms, and the modification of the host material bandgap. The overall band structure of the whole alloy is then deduced from the hybridization of these electronic states. While for the GaAsN, localized N states

correspond to energies in the conduction band [KeZu01], the situation is different for the GaPN where energies of localized N states are located in the bandgap, below the conduction band minimum.[RBNE11, XTZM00] Electronic structure of the GaAsPN quaternary alloy is expected to have similar band structure, but with enhanced hybridization.[RPCE12] Taking advantage of the presence of localized nitrogen energy levels below the conduction band in GaPN, photoluminescence experiments revealed that the optical spectrum was composed of the optical emission from isolated N atoms, but also in a large part from N-N<sub>i</sub> clusters, being pairs of neighboring nitrogen atoms.[XTZM00] Recently, evidence of N-N<sub>i</sub> clusters inclusion in GaAsN has also been demonstrated using scanning tunneling spectroscopy.[IEVE10] These observations however raise the question of the possible stability of the N-N pair at the surface of the crystal during the growth, while N<sub>2</sub> is usually assumed to desorb from the surface.

In the framework of this thesis, we aim to introduce 2.2 % of nitrogen into GaP to elaborate lattice-matched GaPN/Si.[TFWK10] In the first step GaPN layer is grown on GaP (001) substrates. Optimized growth conditions are studied and will be applied to grow GaPN on Si (001) substrate. Various types of GaP (001) substrates are considered. The control of nitrogen content in competition with phosphorous and the influence of surface roughness on the nitrogen incorporation are studied. This work is performed in close collaboration with T. Quinci and J. Kuyyalil.

## 2.2 Samples growth

GaPN samples have been grown on GaP (001) substrates using Riber solid source MBE system. The atomic N is produced by a valved Addon radio frequency (RF) plasma cell, designed to avoid ion irradiation of the sample during the growth (see the appendices for description of the plasma cell).[RBNE11] The flow of ultrahigh purity (6N) N<sub>2</sub> gas into the plasma source is controlled and regulated by a mass flow controller. The RF plasma has been studied and optimized by means of optical spectrometer working in the [300-1100] nm wavelength range and having a resolution of 0.3 nm. A 100 nm thick GaP buffer layer is first grown at 580°C, followed by 100 nm thick GaPN layer grown under various growth rates, temperatures and phosphorus beam equivalent pressure (BEP) which will be detailed in the following paragraph. A 10 nm GaP capping layer is overgrown to avoid any annealing of the surface under nitrogen. The nitrogen content and strain relaxation are deduced from high resolution XRD  $\omega/2\theta$  scans around the

(004) Bragg reflection and by Reciprocal Space Mapping (RSM) around the (224) reflection. The growth temperature, growth rate and phosphorus BEP are varied while holding the plasma parameters constant after optimization in this study.

### 2.3 Plasma parameters optimization

As the plasma characteristics are reported to affect the N incorporation in GaPN, we firstly perform a careful study to optimize plasma parameters.<sup>[KNQA13]</sup> **Figure 2-1a)** presents the optical emission spectrum of the nitrogen plasma with a RF power of 400 W and a N<sub>2</sub> flux of 0.5 sccm. The characteristics features of atomic and broad N<sub>2</sub> molecular bands are also presented according to results reported by several authors.<sup>[CARB02, CARM03, KRRN12, WBYB05]</sup>

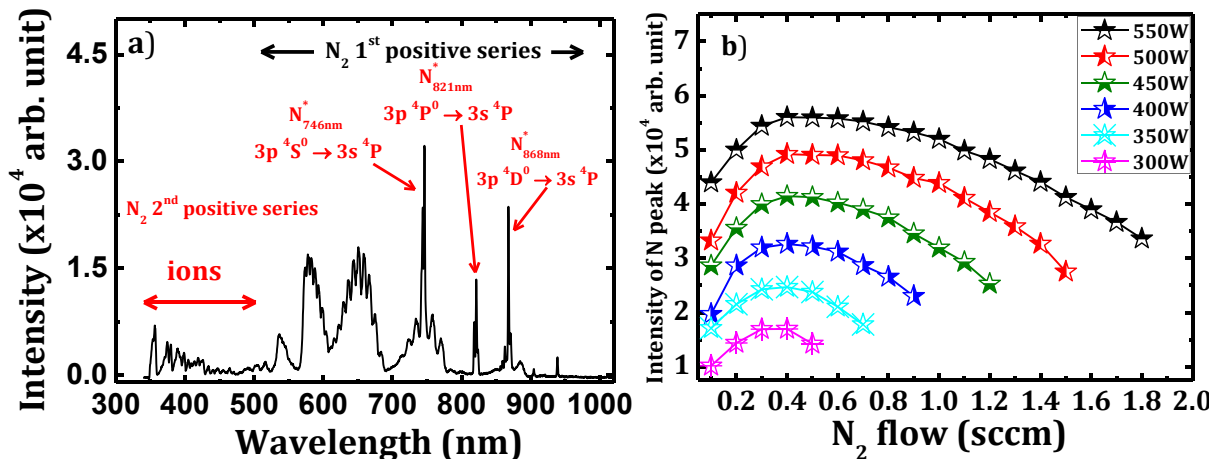


**Figure 2-1:** (a) Measured emission lines of the different atomic and molecular species in N RF plasma spectra showing the intensity of N peak versus emission wavelengths for a forward power of 400 W and flow rate of 0.5 sccm. (b) Intensity of N peak versus feeding N<sub>2</sub> flow rate for different RF powers.<sup>[KNQA13]</sup>

Three typical atomic N emission lines appear at 746, 821 and 868 nm can be distinguished from this spectrum. The legends in red denote the electron transition states corresponding to each emission line. As the main nitrogen specie which takes part in the formation of GaPN alloy is the atomic nitrogen, we have used the strongest intensity emission line appears at 746 nm in the plasma spectra (**Figure 2-1a)** to characterize and optimize the plasma conditions. We have combined the variation of RF power and N<sub>2</sub> flux to study the evolution of N<sub>2</sub> dissociation efficiency. **Figure 2-1b)** shows the integrated intensity of the atomic N line plotted as a function of RF power and N<sub>2</sub> flux. Each curve in **Figure 2-1b)** shows similar behavior of initial increase in the

intensity of N peak to reach a maximum value and a final quenching in the intensity with the flow. It can be seen from the figure that for a given flow rate the intensity of N peak increases with RF power. From the **Figure 2-1b)**, the optimum N<sub>2</sub> flow rate is deduced to be in the [0.4 – 0.5] sccm range. A 0.5 sccm input N<sub>2</sub> flux in the plasma cell will be used for the rest of the study. With respect to the RF power, a 400 W power is chosen as it allows enough nitrogen incorporation, but prevent any sample damaging from ions bombardment occurring at too high power.

## 2.4 Determination of nitrogen content

Nitrogen can be incorporated into GaP interstitial or substitutional sites. The “nitrogen content” term in this thesis concerns the total contribution of nitrogen that makes change the lattice constant. Determination of N content is performed using a simple (004)  $\omega/2\theta$  XRD diagram for perfectly biaxially strained samples. For relaxed or partially relaxed samples, strain relaxation and N content have been accurately determined using reciprocal space map (RSM) measurements around the GaP (224) asymmetric reflection. The diffractometer uses a Cu K $\alpha$  source at a wavelength of 1.54056 Å.

For the determination of N content from biaxially strained samples using (004)  $\omega/2\theta$  scan, we represent the XRD diagram in reciprocal space units (S) after correction of offset in  $2\theta$  for the substrate’s peak. The out-of-plane lattice constant of the epilayer GaPN is deduced from its diffraction peak’s position:

$$a_z = \frac{4}{S_{epi}} \quad (\text{Eq. 6})$$

The free of strain lattice constant has to be calculated in order to apply the Vegard’s law:

$$a_{FOS} = \frac{a_z - a_{sub} \cdot \alpha}{1 - \alpha} \quad (\text{Eq. 7})$$

where :

$$\alpha = \frac{e_{zz}}{e_{xx}} = -2 \frac{C_{12}}{C_{11}} \quad (\text{Eq. 8})$$

with  $C_{12}$ ,  $C_{11}$  the elastic constants of GaPN.

N content in  $\text{GaP}_{1-x}\text{N}_x$  can be calculated from the Vegard's law:

$$x = \frac{a_{\text{GaP}} - a_{\text{sub}}}{a_{\text{GaP}} - a_{\text{sub}}} \quad (\text{Eq. 9})$$

with  $a_{\text{GaP}}$  and  $a_{\text{sub}}$  respectively the free of strain lattice constant of GaP and substrate (GaP).

In the first calculation of N content we use the elastic constants of GaP because we don't know the exact elastic constants of GaPN, this result ( $x_1$ ) will be used to recalculate the  $\alpha$  term:

$$\alpha_1 = x_1 \cdot \alpha_{\text{GaP}} + (1-x_1) \alpha_{\text{GaP}} \quad (\text{Eq. 10})$$

The  $\alpha_1$  will be used to recalculate  $x$ . This loop is repeated until  $x$  is converged (i.e.  $x$  does not changed anymore).

**Figure 2-2** shows the (004)  $\omega/2\theta$  XRD diagram of a fully strained GaPN/GaP sample. The diffraction peaks of the GaP substrate and the GaPN epilayer are indicated. N content deduced from this scan is 2.95%. The well defined thickness fringes indicate very good coherence between the substrate and epilayers interfaces.

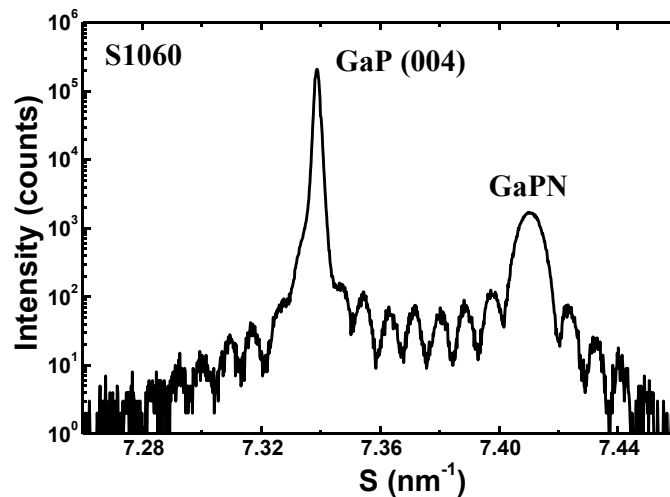


**Figure 2-2:** (004)  $\omega/2\theta$  XRD diagram of a fully strained GaPN/GaP sample. Diffraction peaks of the GaP substrate and the GaPN epilayer are indicated. Well defined thickness fringes indicate very good coherent interface between the substrate and the epilayers. N content deduced from this scan is 2.95%.

The (224) RSM has been measured for the same sample (**Figure 2-3**). One can observe very nice fringes and the vertical alignment of the epilayer and the substrate diffraction peaks which indicate fully strained epilayers on GaP (001) substrate. N content deduced from this RSM is 2.95%, the same value as determined by (004)  $\omega/2\theta$  scan. This suggests that a simple (004)  $\omega/2\theta$  scan is sufficient for N content determination in fully strained sample. The technique of N content determination from (224) RSM will be detailed in the following paragraph.

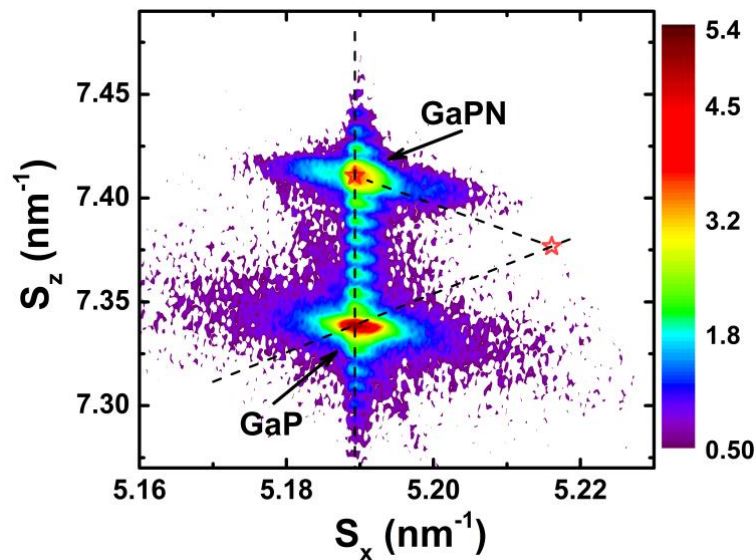


**Figure 2-3:** (224) RSM of a GaPN/GaP sample with 2.95% N and relaxation degree  $R = 1.2\%$ . Vertical alignment of the epilayer and substrate spots indicates fully strained state of the layer. Thickness fringes also indicate good coherent interfaces between the substrate and the epilayers.

**Figure 2-4** (a) shows a (004)  $\omega/2\theta$  scan of a partial relaxed GaPN/GaP sample. Its (224) RSM is presented in **Figure 2-4** (b). The axes are the reciprocal space coordinates ( $S_x$  is parallel to the surface,  $S_z$  is perpendicular to the surface).<sup>[LGCB11]</sup> The color bar presents the intensity level in log scale. The solid red dot indicates the center of the GaPN diffraction spot where we extract the  $S_x$  and  $S_z$  positions for the measurements of lattice constants. The stars present the calculated fully strained and fully relaxed positions of the GaPN spot corresponding to this N composition.

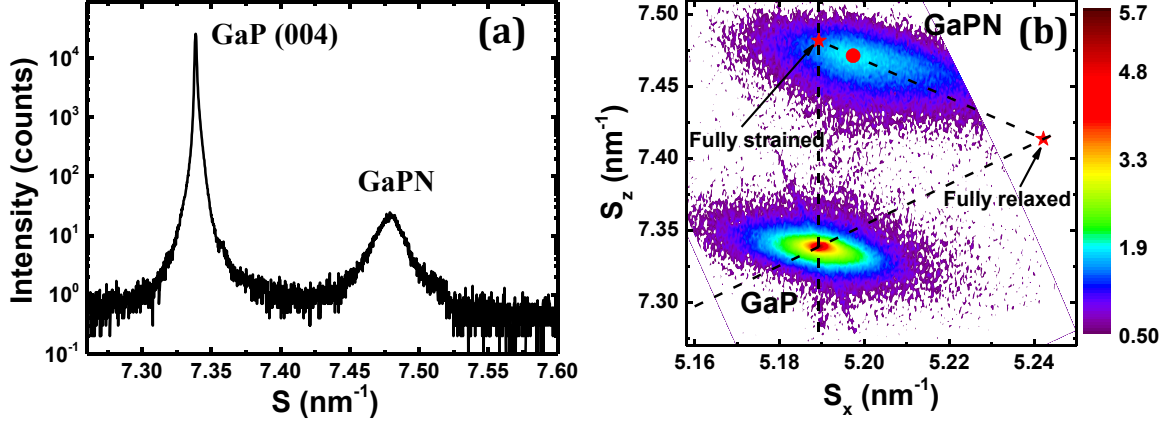


**Figure 2-4:** (a) – (004)  $\omega/2\theta$  XRD diagram of a partially relaxed GaPN/GaP sample. (b) – Its (224) RSM. The intensity (counts) is presented in log scale. Solid red dot shows the position of the GaPN spot where its coordinates  $S_x$  and  $S_z$  are extracted to calculate lattice constants. The stars indicate the calculated positions of fully strained and fully relaxed GaPN layer with the same N content.<sup>[KNQA13]</sup> The N content deduced from this RSM is 5.79 %.

Lattice constants in the in-plane and out-of-plane directions are directly deduced from the RSM:

$$a_L^{\parallel} = a_S \frac{S_{sub}^{\parallel}}{S_L^{\parallel}} \quad (\text{Eq. 11})$$

$$a_L^{\perp} = a_S \frac{S_{sub}^{\perp}}{S_L^{\perp}} \quad (\text{Eq. 12})$$

where  $a_L^{\parallel}$  and  $a_L^{\perp}$  are the lattice constants of the layer in the directions parallel and perpendicular to the surface (in-plane and out-of-plane),  $a_S$  is the lattice constant of the substrate,  $S_L^{\parallel}$ ,  $S_L^{\perp}$ ,  $S_{sub}^{\parallel}$  and  $S_{sub}^{\perp}$  are the positions of the layer and the substrate diffraction spots in the RSM in the directions parallel and perpendicular to the surface. The free of strain cubic lattice constant of the GaPN layer ( $a_L^{\infty}$ ) is then given by:

$$a_L^{\infty} = \frac{a_L^{\perp} + 2 \frac{C_{12}}{C_{11}} a_L^{\parallel}}{1 + 2 \frac{C_{12}}{C_{11}}} \quad (\text{Eq. 13})$$

where  $C_{12}$  and  $C_{11}$  the elastic constants of GaPN.<sup>[HoPB04]</sup> The N content is then deduced from the Vegard's law. The cubic lattice mismatch between the layer and the substrate ( $f_{\infty}$ ) and the relaxation degree ( $R$ ) are finally determined using:

$$f_{\infty} = \frac{a_L^{\infty} - a_S}{a_S} \quad (\text{Eq. 14})$$

$$R = \frac{a_L^{\parallel} - a_S}{a_L^{\infty} - a_S} \quad (\text{Eq. 15})$$

**Figure 2-4** (b) shows that the GaPN layer is partially relaxed. In this example, the relaxation degree is 15.27 % according to the equations above. The nitrogen content deduced from this RSM is 5.79 %.

## 2.5 Control of nitrogen content

### 2.5.1 Nitrogen-Phosphorus competition

In the growth point of view, the influence of MBE growth conditions on nitrogen sticking coefficient remains unclear. For instance, Harris *et al.* state that the sticking coefficient of N is nearly one during GaAsN growth.<sup>[HYBW05]</sup> Harmand *et al.* measured a modification of N incorporation with group V partial pressure which suggests that N is in competition with other group V elements.<sup>[HULR00]</sup>

In the GaPN alloy, recent studies presented the control of group V element flux by changing the partial pressure in Metal-Organic Vapor Phase Epitaxy (MOVPE). Studies of Wakahara *et al.* using MOVPE suggests competition of N and P during the growth of GaPN pointing out that N acts as other group V element. <sup>[WFIH07]</sup> MBE growth was also studied, by varying the RF plasma conditions, growth temperature and growth rate. In this case, the instability of the plasma source can generate problems during the growth. Varying the nitrogen flow rate or the RF power can greatly modify the plasma characteristics and change material quality.<sup>[CARB02, WBYB05]</sup> But still, the issue of nitrogen-phosphorus competition in GaPN grown by MBE remains unclear; some studies even hinting a nitrogen sticking coefficient near the unity at low growth temperature.<sup>[BiTu96, FYOS02, Yone02]</sup>

In order to get insight into the evolution of the incorporation coefficient of N in GaPN, experiments are carried out to evaluate N content for different phosphorus BEP

and temperature. In **Figure 2-5**, N content in GaPN is plotted for different phosphorus BEP at different substrate temperatures. The other parameters of the plasma cell are kept constant (400 W, 0.5 sccm, 100% valve opening). The growth rate and the Ga BEP are respectively 0.2 ML/s and  $7\pm 1\times 10^{-7}$  Torr. All these samples are performed on good surface quality substrates. Trend lines are drawn in **Figure 2-5** to aid reader's eyes.

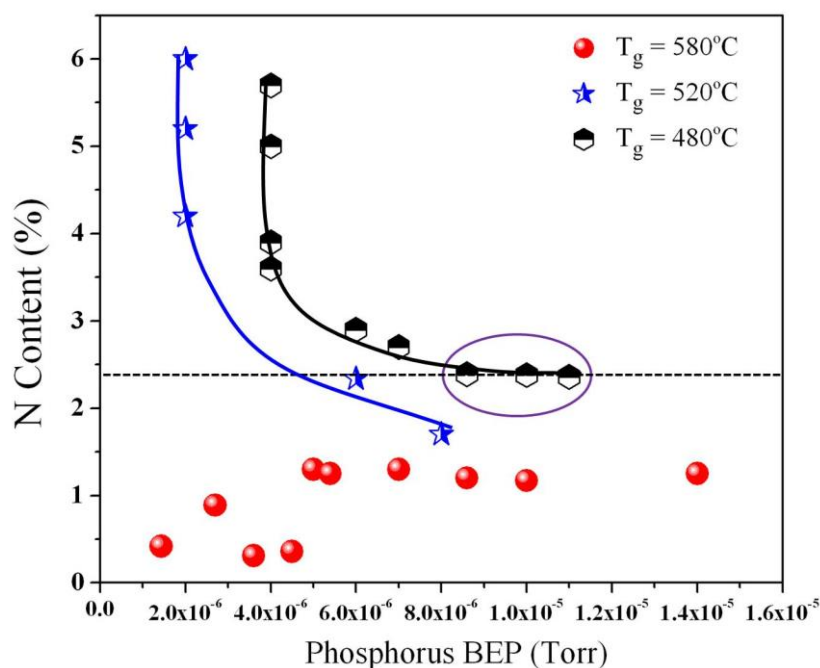


**Figure 2-5:** Evolution of N content as a function of phosphorus BEP in GaPN for different growth temperatures: 480°C (black symbols and guide to the eyes), 520°C (blue stars and guide to the eyes) and 580°C (red spheres).

These results clearly indicate that temperature and phosphorus BEP play a decisive role in determining the N content. It can be seen from the figure that at different P flux studied, N content decreases with increasing temperature, at least between 480°C and 580°C. At low temperature, the formation and desorption of  $\text{N}_2$  is limited as the mobility of nitrogen adatoms is reduced. The incorporation of nitrogen is thus enhanced at lower temperature. At higher temperature, the N content decreases (increased adatoms desorption) while the mobility of adatoms increases, which favors the  $\text{N}_2$  desorption. This is a classical behavior of diluted nitrides alloys and widely reported in the literature.<sup>[CNQA12, PiTo01]</sup> In **Figure 2-5**, the 480°C black curve clearly shows that there is a prominent effect of phosphorus BEP on the nitrogen incorporation in GaPN. At a P BEP of  $\approx 4.0\times 10^{-6}$  Torr, nitrogen content varies from  $\approx 3.5$  to 6%. Above  $4.0\times 10^{-6}$  Torr the N incorporation decreases monotonically with phosphorus flux and reaches a steady value of about  $\approx 2.3\%$ . The region above P BEP of  $\approx 8.0\times 10^{-6}$  Torr of the 480 °C curve is

encircled, and shows that N content in GaP reaches steady value independent of the P flux which also clearly brings out the fact that one can accurately control the nitrogen incorporation in GaPN showing a clear predictability of the N content. Thus in the encircled region of the 480°C the incorporation coefficient of N remains constant (incorporation coefficient is far below the unity). The low pressure range of the curve clearly brings out the competition of N and P at the growth front.

The second curve is obtained for a substrate temperature of 520°C, higher than the previous case. At a phosphorus flux of  $\approx 2 \times 10^{-6}$  Torr a variation of N content is measured which is similar to that observed for 480°C for a low P BEP of  $4 \times 10^{-6}$  Torr. Above a phosphorus BEP of  $\approx 2 \times 10^{-6}$  Torr the curve monotonically decreases. The competition of P and N in the growth front is one more time demonstrated. However at this temperature there are no growth conditions where the N content is independent of the phosphorus flux. This indicates a difficulty to control the N content, because it is always varying with phosphorus flux. At still higher substrate temperature of 580°C, a random statistical distribution of points is observed for low phosphorus BEP with low nitrogen content depicting the uncontrollable and un-predictability of the N incorporation in GaPN at high temperature. This is likely due to monoatomic and diatomic nitrogen desorption. At higher phosphorus BEP, the nitrogen content seems to be constant around 1.3%. This value is however too low to reach the lattice-matching to the silicon. Finally, the three curves indicate a stabilization of the nitrogen content when a high phosphorus BEP is used.

In the thermodynamic point of view, the GaN bond is stronger than the bond strength of GaP, the incorporation of nitrogen thus should be increased at higher temperature.<sup>[HoSt97, Stri99, ZBRF01]</sup> Secondly, the solubility limit of nitrogen in GaP at thermodynamic equilibrium is  $10^{16}$  atoms/cm<sup>3</sup> at 900K,<sup>[HoSt97]</sup> but the results obtained here clearly exceed this value (for instance: 2% of nitrogen in GaP is equivalent to  $5 \times 10^{20}$  atoms/cm<sup>3</sup>). The thermodynamic equilibrium of solid-vapor therefore cannot describe the nitrogen incorporation in this case. A possible solution can be looked into the use of kinetics models, as proposed by P. Kratzer and coworkers for homoepitaxial GaAs.<sup>[KrPS02]</sup> In this work, elemental events are discussed for every kind of atoms. For the group III atoms, adsorption, surface diffusion and incorporation are found to be important events, while for group V atoms, the As<sub>2</sub> molecule is directly adsorbed through a dimerization process (participating to the surface reconstruction), with

elemental events being only  $\text{As}_2$  adsorption and  $\text{As}_2$  desorption. In the present case, while a direct comparison can be made for Ga atoms and  $\text{P}_2$  molecules, the situation is different for nitrogen atoms, as they arrive at the surface with various physical aspects ( $\text{N}^*$  or  $\text{N}_2^*$ ). Especially, single atomic nitrogen atoms will not stabilize directly at the surface by dimerization. Thus, surface diffusion of single nitrogen atoms is expected to play an important role, if free Ga sites are available. This elemental event is thus dependent of phosphorus coverage, and governs the  $\text{N}_2$  desorption process (two single atomic nitrogen atoms should meet themselves to form a stable  $\text{N}_2$  molecule which could desorb from the surface). Adding this elemental event to the description of surface reactions, **Figure 2-5** can be fully understood: (i) in the high phosphorus BEP regime: the adsorption rate is saturated, the nitrogen content depends mainly on the  $\text{P}_2$  desorption rate which is constant at a fixed temperature. At high temperature,  $\text{P}_2$  desorption is stronger and N surface mobility is larger, which means that nitrogen can migrate more easily on the surface, and  $\text{N}_2$  desorption increases as well. (ii) in the low phosphorus BEP regime: the  $\text{P}_2$  adsorption is no longer saturated. Number of Ga sites for N incorporation increases. If the temperature is low enough, atomic nitrogen incorporates more (surface diffusion of atomic nitrogen is not significant here); at high temperature, the  $\text{P}_2$  adsorption is limited, providing free Ga sites, while the mobility of nitrogen atoms at the surface is large due to the high temperature. This leads to the largest  $\text{N}_2$  desorption, and thus to the lowest nitrogen incorporation.

Measurements presented in **Figure 2-5** demonstrate finally that the growth proceeds as a result of competition of N and P species. Effect of this competition can be avoided only in some particular growth conditions, which are for instance  $480^\circ\text{C}$  and high phosphorus BEP where the incorporation coefficient of nitrogen can be kept constant. For the growth of GaPN lattice-matched with silicon,  $480^\circ\text{C}$  and high phosphorus BEP regime can be used.

## 2.5.2 Growth rate and valve opening

In order to control the nitrogen content more accurately, influence of growth rate and valve opening is carefully studied. **Figure 2-6** shows the evolution of N content in GaPN versus growth rate for the growth temperature of  $480^\circ\text{C}$  and high phosphorus BEP ( $7 \times 10^{-6}$  Torr). It can be clearly seen from the figure that at the temperatures studied the N content decreases with the growth rate which is a classical behaviour observed in III-V-V

alloys, such as GaAsP or InAsP, where the stoichiometric incorporation of the two group V elements is reached with V/III ratio equal to one; any increasing of the V/III ratio gives rise to non- stoichiometric incorporation of the two group V elements. In the present study, lowering the growth rate leads to increase the V/III ratio, and thus modify the nitrogen/phosphorus ratio. When considering the preferential incorporation of nitrogen on atomic step edges,<sup>[RBNE11]</sup> the low growth rate may kinetically favour the migration of nitrogen atoms toward step edges, and thus increase the nitrogen incorporation. Remind that the growth rate is not modified by the phosphorus BEP.

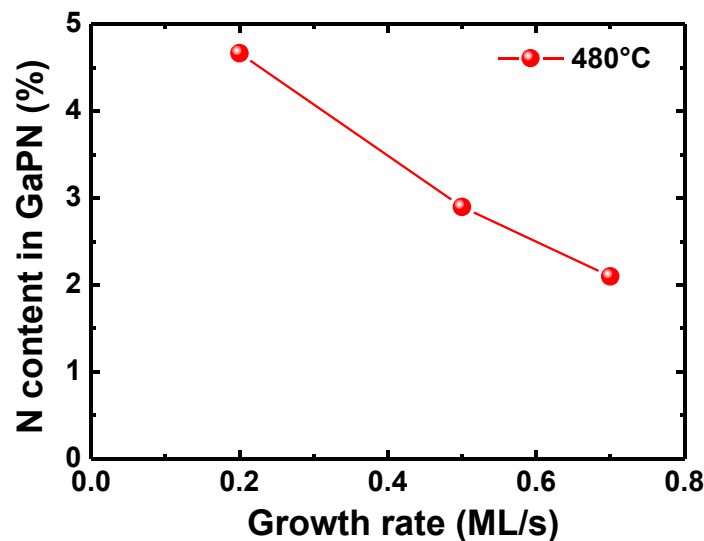


**Figure 2-6:** Evolution of N content in GaPN versus growth rate for the growth temperatures of 480°C and a phosphorus BEP of  $7 \times 10^{-6}$  Torr.

**Figure 2-7** represents the evolution of N content in GaPN as a function of the various position of the valve expressed as % opening. All the growth conditions are similar in this case, with a growth temperature of 480°C and phosphorus BEP of  $7 \times 10^{-6}$  Torr, except the valve opening. It has been checked before the experiment that no nitrogen is incorporated when the valve is closed. The trend lines are drawn in **Figure 2-7** to aid the reader's eyes. The clear trend of the curve shows the good control of the valve in our experiments, with a setting range between 20% and 50% of aperture. Finally, **Figure 2-6** and **Figure 2-7** traduce the good overall experimental control achieved in the present study.

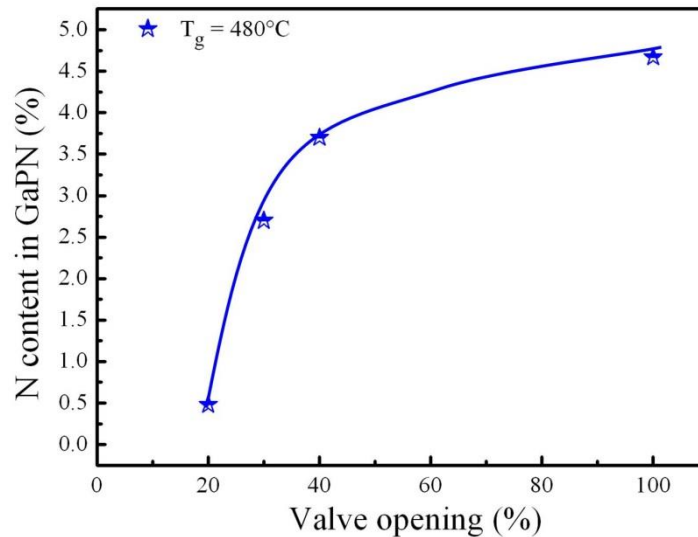


**Figure 2-7:** Evolution of N content in GaPN versus valve opening at a fixed growth temperature of 480°C and phosphorus BEP of  $7 \times 10^{-6}$  Torr.

## 2.6 Influence of surface roughness on N incorporation

By considering that nitrogen incorporation is totally governed by the surface state (and not the bulk thermodynamic), Zhang *et al.* have revealed the predominant role of the surface reconstruction in the enhancement of nitrogen solubility during the epitaxial growth.<sup>[ZhWe01]</sup> Recently, surface of GaAsN has thus been probed at the atomic level by scanning tunneling microscopy.<sup>[MBWJ05, RMYH04]</sup> In such a work, complex behavior of the surface with varying temperature is observed, with changes in roughness and reconstruction, attributed to the modification of adatoms surface mobility. But the influence of roughness on nitrogen incorporation still needs to be studied.

### 2.6.1 Samples preparation

All the samples served for this study are grown using a Riber solid source MBE system. Three different kinds of 2-inch GaP (001) substrates are used in this study. The first one (referred hereafter as “sub-A”) is high quality (etch pit density (EPD) =  $7 \times 10^4$  cm<sup>-2</sup>) epi-ready non-intentionally doped GaP substrate. The second one (“sub-B”) is high quality (EPD =  $8 \times 10^4$  cm<sup>-2</sup>) epi-ready n-doped (S) GaP substrate. The third one (“sub-C”) is a lower quality (EPD =  $3 \times 10^5$  cm<sup>-2</sup>) epi-ready n-doped (S) GaP substrate. “Lower quality” makes reference here to the defect and impurities density originating from the substrate synthesis.<sup>[Forn11]</sup> (004) RC scan of sub-A and sub-C (higher and lower quality) without any deposition reveal no difference (see **Figure 2-8**). This suggests the same

crystal quality of the substrates. When samples are grown in the same run, substrates are stuck with indium on the same molybdenum holder before loading to the growth chamber. Sample holder is continuously rotated during the growth in order to guarantee a 2-inch homogeneity of the epilayers. Homoepitaxial growth of 200 nm GaP/GaP (001) is first performed at 580°C simultaneously on substrates sub-A, sub-B and sub-C.

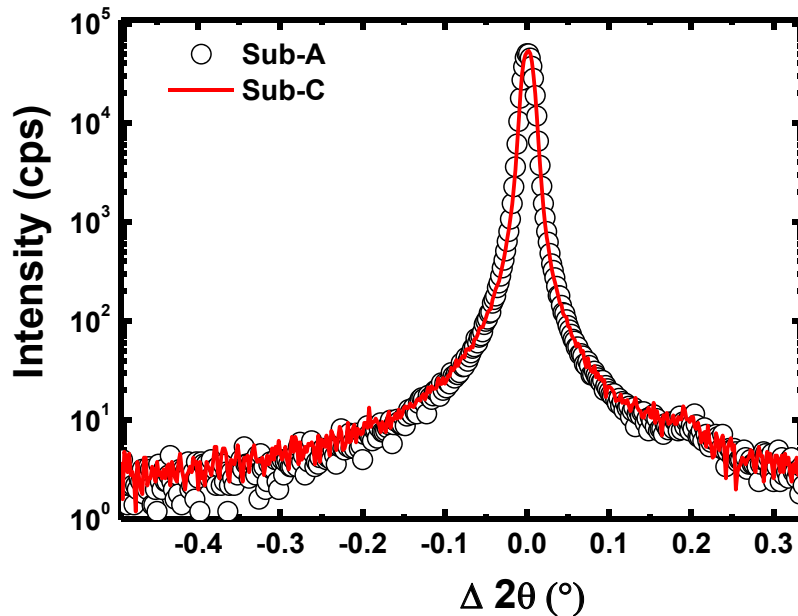


**Figure 2-8:** (004) RC performed on sub-A and sub-C without any deposition reveals no difference. This suggests the same crystal quality of the substrates.

## 2.6.2 Surface investigation

Surface morphology, as determined by AFM, is given in **Figure 2-9a**). The RMS surface roughnesses are extracted from the measurements and are equal to 0.5, 0.5 and 3.7 nm respectively. No clear difference is observed in the RMS roughness of samples grown on sub-A and sub-B, which exclude any influence of substrate doping on the overgrowth roughness. On the contrary, GaP growth on the sub-C substrate leads to very rough surface, mainly constituted of bumps of 100 nm width and 6 nm height which will be described in detail later, originating from the substrate bad quality. Few pits are also visible, but are assumed to have no statistical influence on the incorporation of substitutional N. The XRD rocking curve analysis of these homoepitaxial GaP layers reveals no differences between the three samples, within the uncertainty of our setup. In the following, the starting surface roughness is considered as the only difference between samples grown on sub-A, sub-B and sub-C substrates.

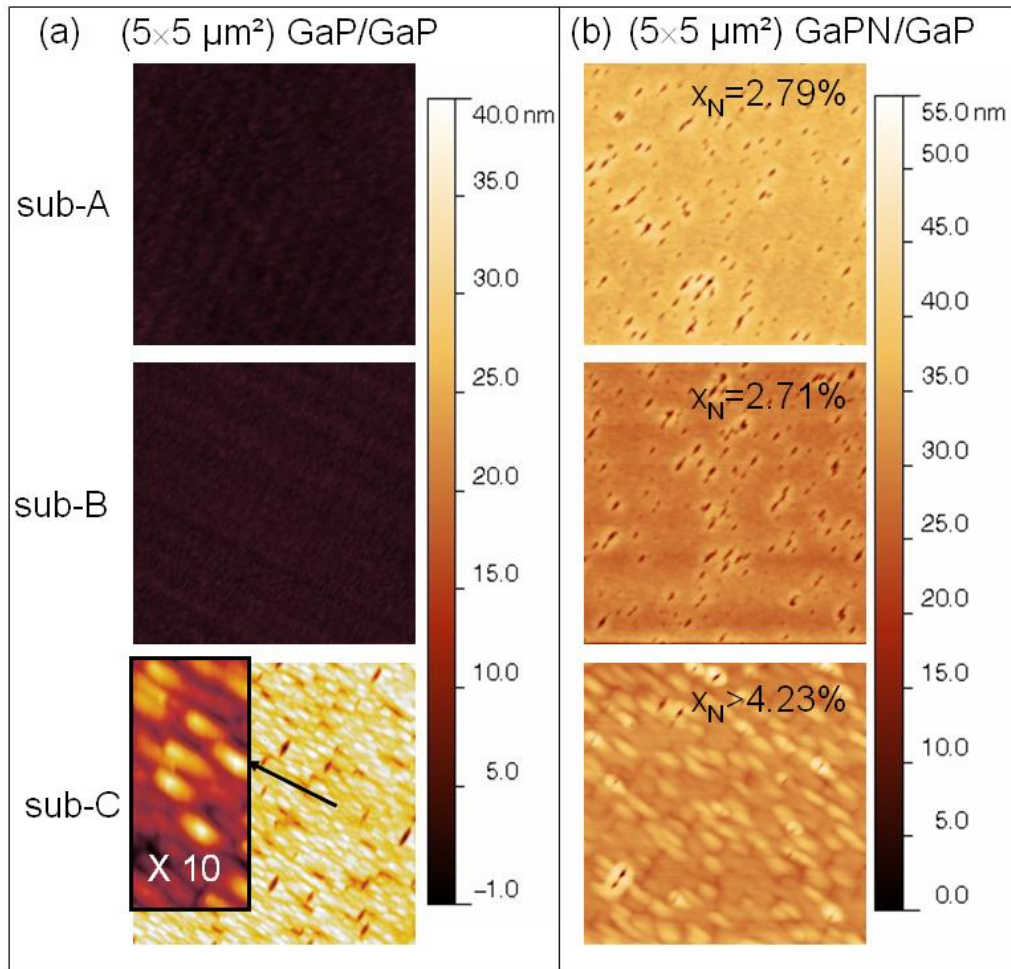


**Figure 2-9:**  $5 \times 5 \mu\text{m}^2$  AFM images of (a) homoepitaxial GaP/GaP simultaneously grown on the three different substrates: sub-A, sub-B and sub-C, inset reveals a large roughness for sub-C, (b) strained GaPN/GaP simultaneously grown on the three different substrates: sub-A, sub-B and sub-C. Very different substitutional N content, as determined by XRD, is measured for GaPN on the rough sub-C substrate.

A 100 nm thick GaPN layers have been grown simultaneously on homoepitaxial GaP on sub-A, sub-B and sub-C. **Figure 2-9b)** presents the AFM images of the three samples grown in the same run. The corresponding substitutional N compositions extracted from XRD experiments (**Figure 2-10**) are also given. The overall roughness is now governed by the pits visible on all the samples, which come from the misfit-related defects. The local RMS roughnesses (i.e. calculated without taking into account pits), are respectively 0.6, 0.8 and 2.3 nm. The local roughness of the surface for the GaPN growth performed on sub-C is much higher than for the other samples. For the growth on sub-C, a 4.23% N content is measured assuming a fully biaxially strained GaPN layer. Strain relaxation leads to underestimate the substitutional nitrogen content, which means that

$x_N > 4.23\%$ . On the contrary, for the other GaPN samples (**Figure 2-10**), the XRD profiles exhibit well-defined thickness fringes. This indicates a high degree of lattice plane coherency through the whole layer. The nitrogen contents measured for samples grown on sub-A ( $x_N = 2.79\%$ ) and sub-B ( $x_N = 2.71\%$ ) are considered as equivalent. By the consequence, substrate doping influence on nitrogen incorporation will then definitely be excluded in the following. The results clearly indicate a very large difference in substitutional N incorporation for sample on sub-C, while performed in the same run (i.e. with the same temperature, growth rate, phosphorus BEP and plasma conditions).

### 2.6.3 Strain induced effect investigation

To determine whether this effect is strain dependent or not, bulk GaAsPN layers have been grown. In this case, adding As allows to reduce the misfit. Comparison of XRD profiles of GaAsPN and GaPN layers grown on sub-A and sub-C is presented in **Figure 2-10**.

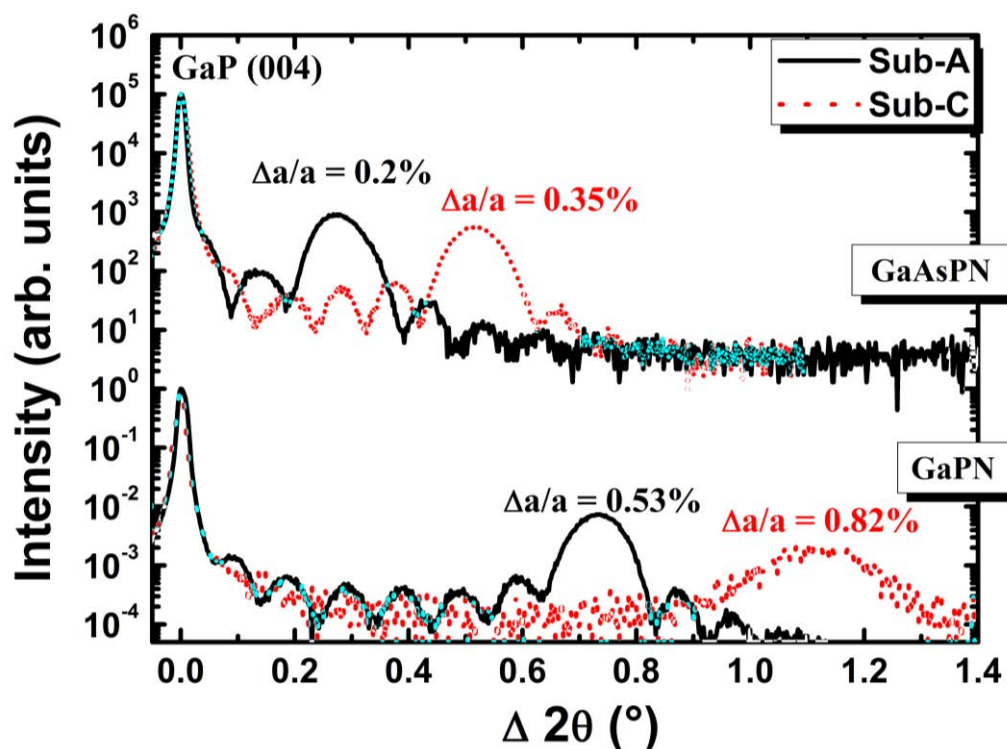


**Figure 2-10:** (004)  $\omega/2\theta$  XRD profiles are presented for both GaPN and nearly lattice-matched GaAsPN layers, grown simultaneously on sub-A (black dashed line) and on sub-C (red dotted line). Preferential incorporation of nitrogen on rough surface is independent of the strain in the volume.

Even if the GaAsPN when grown on sub-A is nearly lattice matched to GaP ( $\Delta a/a = 0.2\%$ ), the growth performed simultaneously on sub-C substrate reveals much

higher N content ( $\Delta a/a = 0.35\%$ ). Contrary to the GaPN, XRD profiles from the GaAsPN present features characteristics of high quality thin layers, with thickness fringes and thickness-limited line width diffraction peak.

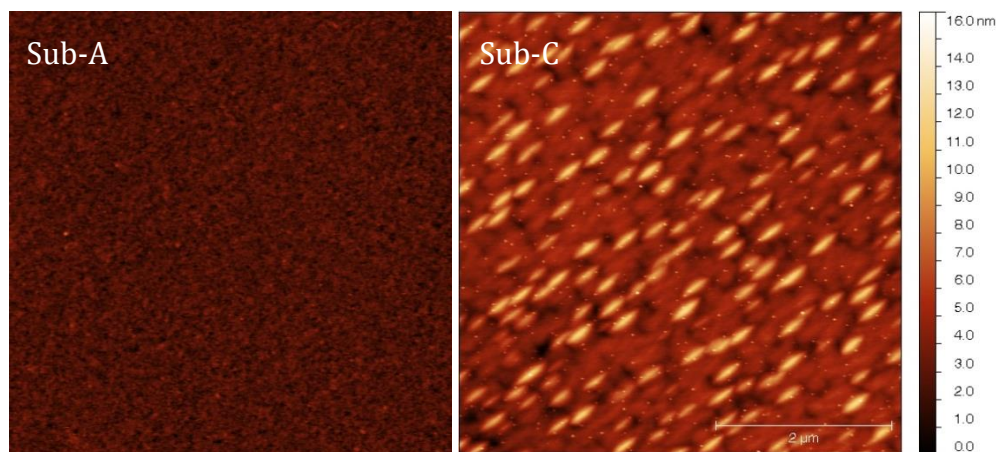


**Figure 2-11:**  $5 \times 5 \mu\text{m}^2$  AFM images of the GaAsPN samples grown simultaneously on sub-A (RMS = 0.4 nm) and sub-C (RMS = 2 nm).

**Figure 2-11** also gives the AFM images of the two GaAsPN samples. No pits are visible on these images, indicating the absence of any misfit dislocations, which reveals a much lower strain accumulation in the structure. RMS roughnesses extracted are 0.4 (sub-A) and 2 nm (sub-C), which demonstrates that the roughness is a decisive parameter for the understanding of the phenomenon, independently of the strain in the volume.

From the change of nitrogen incorporation between the two samples with a different roughness, one could argue that controlling the growth on a rough substrate leads to stochastic phenomena, which are unpredictable and by definition irreproducible which would undermine this study. **Figure 2-12** represents the evolution of the nitrogen content as a function of the phosphorus BEP in GaPN for samples performed on sub-A and sub-C (not simultaneously in this case). For both cases, a clear tendency is observed (increasing the phosphorus BEP leads to decrease the nitrogen content, as claimed on the previous paragraph), indicating a competition between phosphorus and nitrogen for the incorporation, which is a classical tendency of III-V-V alloys growth, and already observed in GaAsN-based alloys.<sup>[HULR00, JQNT99, WKWC01]</sup> However, N content of the samples grown on sub-C is clearly (and globally) shifted to higher values, which reinforces the results presented before. Inset of **Figure 2-12** presents the evolution of N content with growth rate. The linear decreasing of nitrogen

content with increasing growth rate on the sub-C, is also an indication of a good growth control (predictable, reproducible), and the absence of stochastic growth phenomena. Finally, more than 50 samples have been grown on both sub-A and sub-C, always showing the same phenomenon (increased substitutional incorporation when the surface roughness is high). It has to be noticed that the bumps at the surface of sub-C have on all the samples always the same characteristic size, aspect ratio and nearly the same density. Bumps are equivalent to misoriented surfaces, i.e. generate a local increasing of the atomic step density.

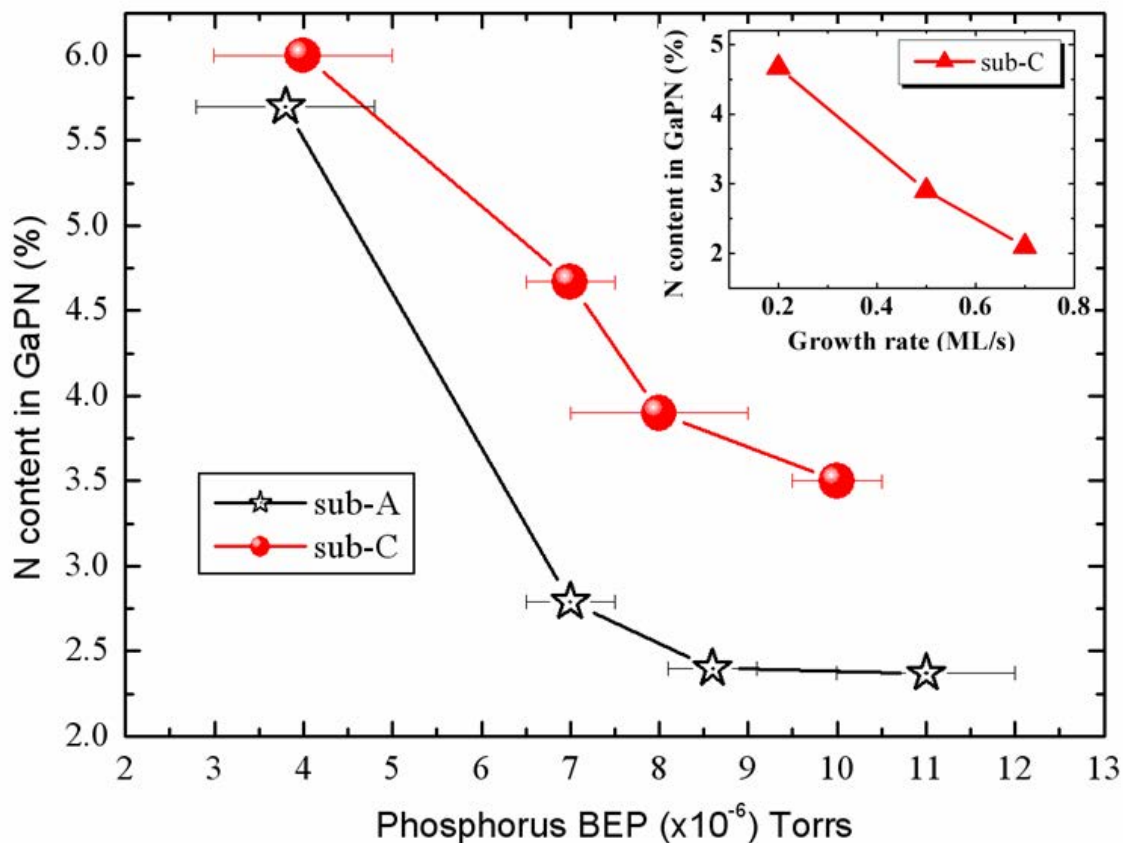


**Figure 2-12:** Evolution of nitrogen content as a function of phosphorus BEP in GaPN samples grown on sub-A (black stars) and on sub-C (red spheres). The two curves show a similar behavior, however shifted to higher N content for the rough sub-C substrate. Evolution of the N content as a function of the growth rate is given in the inset. Results indicate a well-controlled growth mode.

#### 2.6.4 Step edges incorporation mechanism

Now searching to understand the consequences of the preferential incorporation of substitutional N in the GaPN with a larger roughness, the number of atomic steps at

the surface is expected to play an important role. In other words, the properties of the nitrogen adsorption sites near the step edges seems to be different from the adsorption sites present on the 2D-plane part of the terraces between the steps. Any attempt of quantification of this mechanism is based on the precise knowledge of the surface state at the atomic scale. To this aim, a statistical study is performed on the GaP homoepitaxial layers on respectively sub-A and sub-C. **Figure 2-13** represents height profiles, as extracted from AFM images. While for homoepitaxial GaP on sub-A, the profile (black solid line) remains very flat whatever the direction considered for the profiles extraction, bumps are clearly visible on homoepitaxial GaP on sub-C.

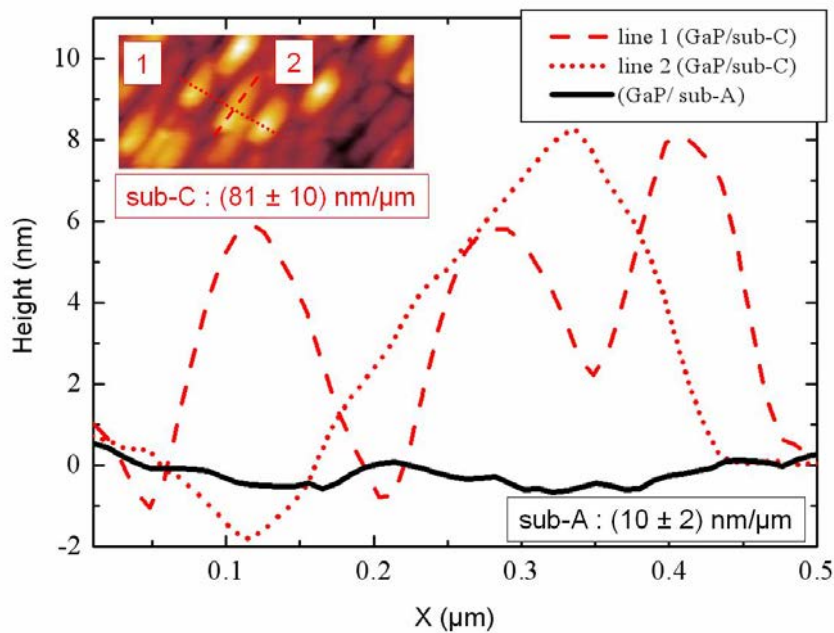


**Figure 2-13:** Height profiles of homoepitaxial GaP on the different substrates (sub-A and sub-C), extracted from AFM. Inset shows the AFM image of sub-C with characteristic bumps, which have well defined slopes at their boundaries. Average slopes for the two samples are extracted from a statistical study over 30 measurements in different crystallographic directions.

**Figure 2-13** inset presents the original AFM image with two lines (1 and 2) drawn on it. Corresponding profiles are represented with red dashed and dotted lines. From these profiles, typical slopes (height to distance ratio) can be extracted, taking into account the different crystallographic directions. Any variation below the lateral resolution of the AFM tip is not considered here. On sub-C, this analysis is possible due to the remarkable homogeneity of the size of the bumps. More than 30 slopes are calculated for both substrates. Average values are reported in **Figure 2-13**:  $(10 \pm 2)$  nm/ $\mu\text{m}$  for sub-A and  $(81 \pm 10)$  nm/ $\mu\text{m}$  for sub-C (boundaries of bumps have

clearly two different slopes; but only an average is needed here, to determine the number of steps). These average values can also be expressed in term of angle with the (001) surface, being  $0.6^\circ$  for sub-A and  $4.6^\circ$  for sub-C. The surface is thus considered as vicinal, with the (001) surface reconstruction. The 15% decreasing of the RMS surface roughness as determined by AFM during the 100 nm Ga(As)PN diluted nitride growth is neglected in this study; the difference in nitrogen incorporation being quantitatively much higher. When admitting monolayer steps, this gives respectively 37 steps/ $\mu\text{m}$  (sub-A) and 297 steps/ $\mu\text{m}$  (sub-C). Thus the average terrace width of the steps are respectively  $L_{\text{step sub-A}} = 27 \text{ nm}$  and  $L_{\text{step sub-C}} = 3.4 \text{ nm}$ . To interpret the previous results, different adsorption sites are considered: step edges adsorption sites, and 2D plane terraces adsorption sites, as depicted in **Figure 2-14**. Writing the conservation of the substitutional N content at the surface leads to:<sup>[CNQA12]</sup>

$$\xi_{\text{step edge}} \frac{a_{\text{GaP}}}{\sqrt{2}L_{\text{step sub-}i}} N_{\text{tot}} + \xi_{\text{plane}} \left( 1 - \frac{a_{\text{GaP}}}{\sqrt{2}L_{\text{step sub-}i}} \right) N_{\text{tot}} = x_{N \text{ sub-}i} N_{\text{tot}} \quad (\text{Eq. 16})$$

where  $a_{\text{GaP}}$  is the lattice parameter of bulk GaP at room temperature,  $\xi_{\text{step edge}}$  and  $\xi_{\text{plane}}$  are the occupancy rates of step edges adsorption sites and 2D plane terraces adsorption sites respectively, i.e. the percentage of different sites being occupied by a nitrogen atom,  $L_{\text{step sub-}i}$  are the step width for the different substrates (sub-A and sub-C),  $x_{N \text{ sub-}i}$  the substitutional nitrogen content for the samples grown on the sub-A and sub-C substrates, as determined by XRD, and  $N_{\text{tot}}$  the total number of adsorption sites at the surface. By taking the data extracted from GaPN samples grown on sub-A and sub-C presented in **Figure 2-9** and **Figure 2-10**, the two equations system can be solved leading to the following solutions :  $\xi_{\text{step edge}} = 0.173$  and  $\xi_{\text{plane}} = 0.026$ . While 17.3 % of step edges adsorption sites have been occupied by nitrogen during the growth, only 2.6 % of in-plane adsorption sites have been filled. The ratio of adsorption probability on step edges and on in-plane site is then given by:  $\frac{\alpha_{\text{step edge}}}{\alpha_{\text{plane}}} = \frac{\xi_{\text{step edge}}}{\xi_{\text{plane}}} = 6.7$ . The

incorporation of substitutional N on a step edge adsorption site is thus around 7 times more favorable than on an in-plane adsorption site. Of course this value is expected to change with the growth temperature and nature of the substrate (GaAs or GaP), as it is mainly governed by the adatoms migration. As described in **Figure 2-14**, this also can

explain the relative stability of nitrogen pairs at the surface. As described in many papers and in **Figure 2-14**,  $N_2$  pairs are expected to desorb from the surface (high temperature favors the mobility of nitrogen adatoms, and increase the probability to form  $N_2$ ).<sup>[Pit001]</sup>  $N-N_i$  nitrogen clusters are however often observed both in GaAsN<sup>[IEVE10]</sup> and GaPN.<sup>[XTZM00]</sup> With respect to the results found in this study, an explanation can be found in the predominant role of step edges in the nitrogen incorporation where the step edges help to stabilize the nitrogen pairs, as described in **Figure 2-14**.

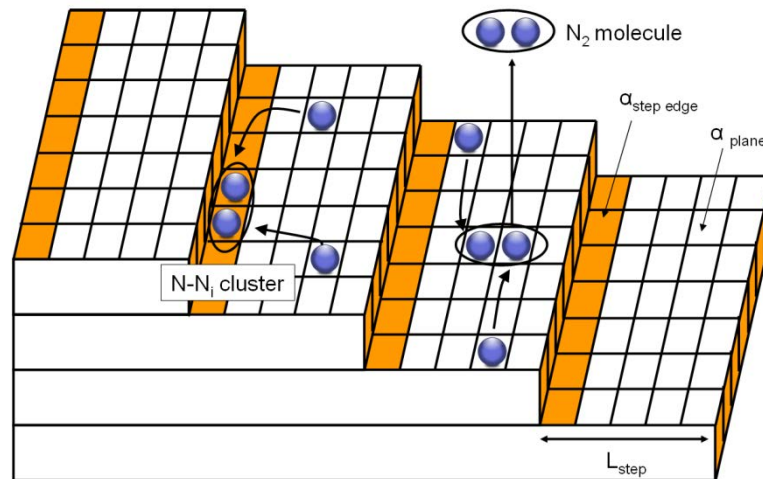


**Figure 2-14:** Substitutional nitrogen incorporation scheme at the stepped surface of the crystal. Step edges adsorption sites (in orange) and 2D-plane adsorption sites (in white) are assumed to have different incorporation probability ( $\alpha_{\text{step edge}}$  and  $\alpha_{\text{plane}}$ ). The relative stability of nitrogen cluster  $N-N_i$  at the surface is explained by enhanced step edges adsorption, as compared to the 2D plane adsorption, limited by the  $N_2$  desorption.

Note that both atomic nitrogen, and metastable  $N_2^*$  molecules coming from the plasma source can follow this scheme.<sup>[HULR00]</sup> Finally, these observations can be corroborated by the literature. Indeed, Utsumi *et al.* have noticed a different incorporation of substitutional nitrogen in GaPN grown simultaneously on GaP and Si substrate.<sup>[UFYW06]</sup> This larger nitrogen content when grown on silicon substrate may not be attributed to strain, but more likely to the roughness appearing during the deposition of the first GaP layers.<sup>[GBCL12]</sup> Moreover, Ulloa *et al.* have noticed the absence of any visible  $N-N_i$  cluster on cross-sectional STM performed on the  $[110]$  surface plane.<sup>[UIKH08]</sup> This suggests that  $[110]$  and  $[1-10]$  steps would have different adsorption probability of the clusters, which would be comprehensible, given the different nature of the atomic steps in these two directions.<sup>[ZhWe01]</sup> The preferential incorporation on step edges may be responsible for this.

## 2.7 Summary

We have systematically studied the incorporation of N in GaPN as a function of different growth determining factors. Nitrogen plasma spectroscopy has been first performed to optimize the nitrogen dissociation, and the atomic nitrogen production. The influence of growth conditions has been then clarified. Especially, the N content evolution with phosphorus BEP for different growth temperatures clearly demonstrates prominent dependence of the former on the latter. We thus demonstrate that there is a competition between N and P at the growth front, implying that N incorporation coefficient is much lower than the unity during GaPN growth. Effects of this competition on the growth control accuracy can be limited by choosing sufficiently low growth temperature (480 °C) and high phosphorus BEP ( $>8 \times 10^{-6}$  Torr). The experimental accuracy is furthermore improved as growth rate and plasma cell valve opening can be efficiently used to control quantitatively the N incorporation on a wide range of N composition. On the other hand, surface roughness has been clarified to play a decisive role in N incorporation, independently on the other growth parameters and strain effects. We have shown that substitutional nitrogen incorporation near the step edges is around 7 times more favorable than substitutional N incorporation on a 2D-plane terrace adsorption site in the growth conditions used. It is therefore important to control the surface roughness when growing diluted nitrides compounds.

## REFERENCES

- [BiTu96] BI, W. G.; TU, C. W.: In: *Applied Physics Letters* **69** (1996), No. 24, pp. 3710–3712
- [CARB02] CARRÈRE, H.; ARNOULT, A.; RICARD, A.; BEDEL-PEREIRA, E.: In: *Journal of Crystal Growth* **243** (2002), No. 2, pp. 295–301
- [CARM03] CARRÈRE, H.; ARNOULT, A.; RICARD, A.; MARIE, X.; AMAND, Th.; BEDEL-PEREIRA, E.: In: *Solid-State Electronics* **47** (2003), No. 3, pp. 419–423
- [CNQA12] CORNET, C.; NGUYEN THANH, T.; QUINCI, T.; ALMOSNI, S.; et al.: In: *Applied Physics Letters* **101** (2012), No. 25, pp. 251906–251906–4
- [Forn11] FORNARI, R.: In: EDITORS-IN-CHIEF: PALLAB BHATTACHARYA; ROBERTO FORNARI; HIROSHI KAMIMURA (eds.): *Comprehensive Semiconductor Science and Technology*. Amsterdam : Elsevier, 2011 — ISBN 978-0-444-53153-7, pp. 1–35
- [FYOS02] FURUKAWA, Y.; YONEZU, H.; OJIMA, K.; SAMONJI, K.; FUJIMOTO, Y.; MOMOSE, K.; AIKI, K.: In: *Japanese Journal of Applied Physics* **41** (2002), No. Part 1, No. 2A, pp. 528–532
- [GBCL12] GUO, W.; BONDI, A.; CORNET, C.; LÉTOUBLON, A.; et al.: In: *Applied Surface Science* **258** (2012), No. 7, pp. 2808–2815
- [GEHW12] GREEN, M. A.; EMERY, K.; HISHIKAWA, Y.; WARTA, W.; DUNLOP, E. D.: In: *Progress in Photovoltaics: Research and Applications* **20** (2012), No. 5, pp. 606–614

- [Harr02] HARRIS, J S: In: *Semiconductor Science and Technology* **17** (2002), No. 8, pp. 880–891
- [HoPB04] HOLY, V.; PIETSCH, U.; BAUMBACH, T.: In: *High-Resolution X-Ray Scattering from Thin Films and Multilayers, Springer Tracts in Modern Physics*. vol. 149. 2nd. ed. : Springer Berlin Heidelberg, 2004 — ISBN 978-3-540-62029-7, 978-3-540-49625-0, pp. 151–167
- [HoSt97] HO, I-hsiu; STRINGFELLOW, G.B.: In: *Journal of Crystal Growth* **178** (1997), No. 1–2, pp. 1–7
- [HULR00] HARMAND, J. C.; UNGARO, G.; LARGEAU, L.; LE ROUX, G.: In: *Applied Physics Letters* **77** (2000), No. 16, p. 2482
- [HYBW05] HARRIS JR., J.S.; YUEN, H.; BANK, S.; WISTEY, M.; LORDI, V.; GUGOV, T.; BAE, H.; GODDARD, L.: In: *Dilute Nitride Semiconductors*. Amsterdam : Elsevier, 2005 — ISBN 978-0-08-044502-1, pp. 1–92
- [IEVE10] IVANOVA, L.; EISELE, H.; VAUGHAN, M. P.; EBERT, Ph.; et al.: In: *Physical Review B* **82** (2010), No. 16, p. 161201
- [JQNT99] JIN, C.; QIU, Y.; NIKISHIN, S. A.; TEMKIN, H.: In: *Applied Physics Letters* **74** (1999), No. 23, pp. 3516–3518
- [KeZu01] KENT, P. R. C.; ZUNGER, Alex.: In: *Applied Physics Letters* **79** (2001), No. 15, p. 2339
- [KNQA13] KUYALIL, J.; NGUYEN THANH, T.; QUINCI, T.; ALMOSNI, S.; et al.: In: *Journal of Crystal Growth* **377** (2013), pp. 17–21
- [KrPS02] KRATZER, P.; PENEV, E.; SCHEFFLER, M.: In: *Applied Physics A* **75** (2002), No. 1, pp. 79–88
- [KRRN12] KRAMIDA, A.; RALCHENKO, Yu.; READER, J.; NIST ASD TEAM: URL <http://physics.nist.gov/asd>. — National Institute of Standards and Technology, Gaithersburg, MD
- [LGCB11] LÉTOUBLON, A.; GUO, W.; CORNET, C.; BOULLE, A.; et al.: In: *Journal of Crystal Growth* **323** (2011), No. 1, pp. 409–412
- [LZBL11] LIEBICH, S.; ZIMPRICH, M.; BEYER, A.; LANGE, C.; et al.: In: *Applied Physics Letters* **99** (2011), p. 071109
- [MBWJ05] MCGEE, W. M.; BONE, P. A.; WILLIAMS, R. S.; JONES, T. S.: In: *Applied Physics Letters* **87** (2005), No. 18, pp. 181905–181905–3
- [MYFF01] MOMOSE, Kenji; YONEZU, Hiroo; FUJIMOTO, Yasuhiro; FURUKAWA, Yuzo; MOTOMURA, Yoshifumi; AIKI, Kunio.: In: *Applied Physics Letters* **79** (2001), No. 25, p. 4151
- [PiTo01] PINAULT, M.-A.; TOURNIÉ, E.: In: *Applied Physics Letters* **79** (2001), No. 21, pp. 3404–3406
- [RBNE11] ROBERT, C.; BONDI, A.; NGUYEN THANH, T.; EVEN, J.; et al.: In: *Applied Physics Letters* **98** (2011), No. 25, pp. 251110–251110–3
- [RMYH04] REASON, M.; MCKAY, H. A.; YE, W.; HANSON, S.; GOLDMAN, R. S.; ROTBERG, V.: In: *Applied Physics Letters* **85** (2004), No. 10, pp. 1692–1694
- [RPCE12] ROBERT, C.; PERRIN, M.; CORNET, C.; EVEN, J.; JANCU, J. M.: In: *Applied Physics Letters* **100** (2012), No. 11, pp. 111901–111901–4
- [Stri99] STRINGFELLOW, Gerald B.: *Organometallic Vapor-Phase Epitaxy: Theory and Practice* : Academic Press, 1999 — ISBN 9780080538181
- [TFWK10] TAKAGI, Y.; FURUKAWA, Y.; WAKAHARA, A.; KAN, H.: In: *Journal of Applied Physics* **107** (2010), No. 6, p. 063506
- [UFYW06] UTSUMI, A.; FURUKAWA, Y.; YONEZU, H.; WAKAHARA, A.: In: *Journal of Crystal Growth* **295** (2006), No. 1, pp. 12–15
- [UIKH08] ULLOA, J. M.; KOENRAAD, P. M.; HOPKINSON, M.: In: *Applied Physics Letters* **93** (2008), No. 8, pp. 083103–083103–3
- [WBYB05] WISTEY, Mark A.; BANK, Seth R.; YUEN, Homan B.; BAE, Hopil; HARRIS JR., James S.: In: *Journal of Crystal Growth* **278** (2005), No. 1–4, pp. 229–233
- [WFIH07] WAKAHARA, A.; FURUKAWA, Y.; ITOH, S.; HATAKENAKA, S.; YONEZU, H.: In: *Journal of Crystal Growth* **300** (2007), No. 1, pp. 182–185

- [WKWC01] WANG, J S; KOVSH, A R; WEI, L; CHI, J Y; WU, Y T; WANG, P Y; USTINOV, V M.: In: *Nanotechnology* **12** (2001), No. 4, pp. 430–433
- [XTZM00] XIN, H. P.; TU, C. W.; ZHANG, Yong; MASCARENHAS, A.: In: *Applied Physics Letters* **76** (2000), No. 10, p. 1267
- [Yone02] YONEZU, Hiroo.: In: *Semiconductor Science and Technology* **17** (2002), No. 8, pp. 762–768
- [ZBRF01] ZORODDU, Agostino; BERNARDINI, Fabio; RUGGERONE, Paolo; FIORENTINI, Vincenzo. In: *Physical Review B* **64** (2001), No. 4, p. 045208
- [ZhWe01] ZHANG, S. B.; WEI, Su-Huai: In: *Physical Review Letters* **86** (2001), No. 9, pp. 1789–1792

## **CHAPTER 3.**

### **ACTIVE AREA: (IN,GA)AS/GAP QUANTUM DOTS**

---

---

*In this chapter, we present the growth of (In,Ga)As quantum dots (QDs) on GaP(001) substrate by MBE. As this material system offers several advantages over both InP/GaP and InAs/GaP QDs systems: i) The bandgap of bulk InGaAs is lower than that of bulk InP for In content higher than 5%, meaning stronger confinement; ii) Lower lattice mismatch than that of InAs/GaP (4%-7% for In content from 7% - 50%), allowing wider window for dislocation-free three-dimensional growth and greater emission wavelength tunable range.<sup>[SoSL10]</sup> Various growth parameters have been considered: nominal indium content, QDs thickness and growth temperature. Structural and RT optical characterizations of high density (In,Ga)As QDs are then discussed. The role of indium composition in the QDs is also discussed from atomistic calculations. Structural study of single (In,Ga)As/GaP QD is finally mentioned.*

### **3.1 Growth of (In,Ga)As QDs on GaP (001) substrate**

#### **3.1.1 Growth conditions and structural analysis**

The growth of (In,Ga)As QDs has been studied using the gas sources MBE (GSMBE) and solid sources MBE (SSMBE) apparatus. The QDs are self-assembled via the Stranski-Krastanov mechanism. The structural analysis of these QDs has been performed using the SPM Image Magic software. This analysis concerns the statistic measurement of QDs density, the average height, radius, surface area and volume of QDs.

##### ***(a) Growth by GSMBE***

The GaP (001) substrate is subjected to a thermal treatment at 650°C (pyrometer) under phosphine overpressure for cleaning. The substrate's temperature is

then ramped down to 580°C and the growth of a 450 nm thick GaP buffer layer is started. After the growth of GaP buffer layer, the PH<sub>3</sub> flux is switched to AsH<sub>3</sub> for the growth of (In,Ga)As QDs layer and the growth is followed by 30 seconds annealing under AsH<sub>3</sub> overpressure. A 30 nm thick GaP capping layer is deposited for photoluminescence study. The growth sequences are depicted in **Figure 3-1**.

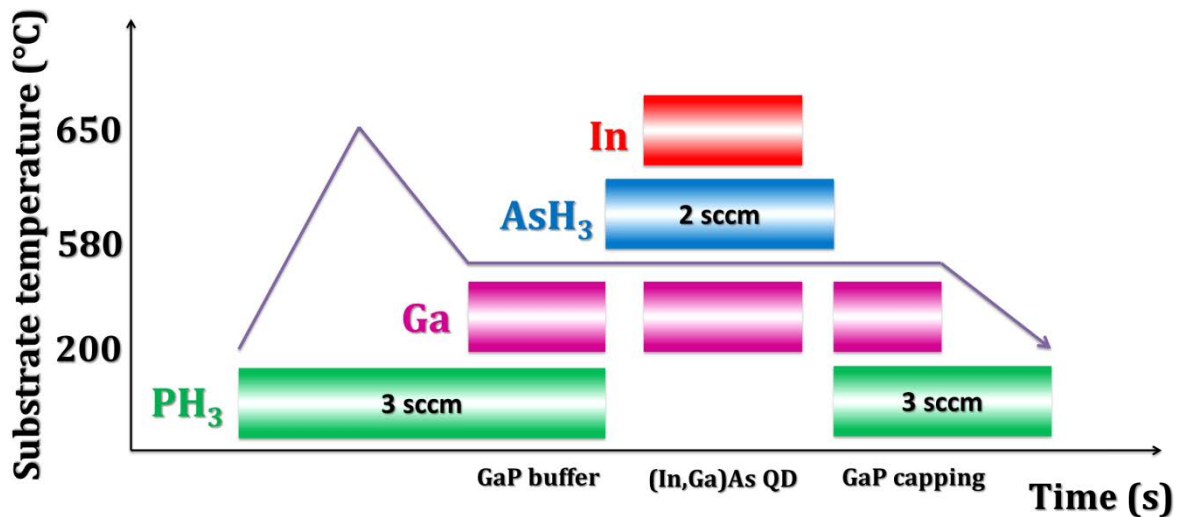


**Figure 3-1:** Growth sequences for (In,Ga)As QDs on GaP substrate using GSMBE.

### ***(b) Growth by SSMBE***

The same growth sequences as described above are used to grow (In, Ga)As QDs using the SSMBE chamber. The difference is that the SSMBE uses all-solid sources for Ga, In, As and P (see the appendices section for more description). The beam equivalent pressure (BEP) of the V and III elements are measured by Bayard Alpert pressure gauges. The growth rate is fixed at 0.37 ML/s and the V/III ratio at 3.

### ***(c) Structural analysis***

For this study, AFM images will be used to perform the structural analysis. **Figure 3-2** shows an AFM image of a (In,Ga)As/GaP QDs sample grown by SSMBE with an In nominal content of 60% (In<sub>0.6</sub>Ga<sub>0.4</sub>As/GaP) and 3 ML thick. The growth temperature has been set at 580°C, without a capping layer. The undulation observed on the surface may be attributed to the elastic relaxation of GaAs during the growth, as observed earlier in the thesis of A. Bondi. The undulation is always oriented in the

[1-10] direction. This helps to determine the crystallographic directions on the samples presenting the similar undulation. **Figure 3-3** shows the report sheet obtained from statistical analysis on this (In,Ga)As QDs sample. This report sheet gives the number of QDs counted from the AFM image ( $698 \text{ QDs}/\mu\text{m}^2$ ), the average height ( $3.56 \pm 2.569 \text{ nm}$ ), radius ( $15.64 \pm 4.641 \text{ nm}$ ), area ( $900.1 \pm 513.1 \text{ nm}^2$ ), volume ( $1649 \pm 2393 \text{ nm}^3$ ) and the repartition histograms of QDs. The QDs density deduced from this measurement is  $6.98 \times 10^{10} \text{ cm}^{-2}$ .

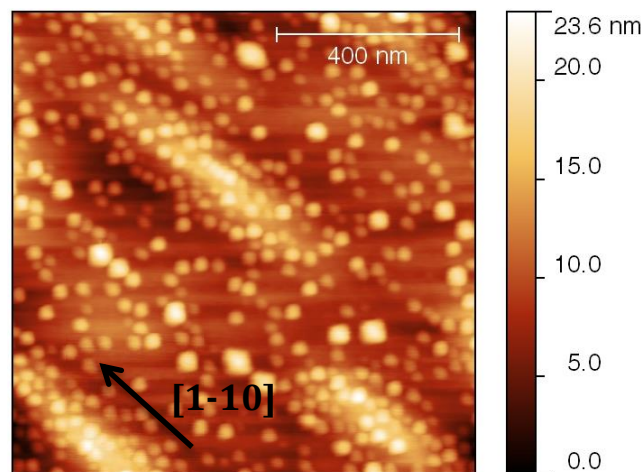


**Figure 3-2:**  $1 \times 1 \mu\text{m}^2$  AFM image on a (In,Ga)As/GaP QDs sample grown by SSMBE with an In nominal content of 60% ( $\text{In}_{0.6}\text{Ga}_{0.4}\text{As}/\text{GaP}$ ).

The AFM image above reveals a low QDs density and the QDs sizes are visually non-homogeneous. This drives us to a systematic study of growth optimization in order to achieve high density and high uniformity of QDs. The In sticking coefficient is also studied with the growth temperature. Indeed the growth temperature reported here ( $580^\circ\text{C}$ ) is very high for In deposition; a question is thus naturally raised: is there any In in the QDs material? If yes, what is the In content and how about its distribution inside a QD? These issues are addressed in the next paragraph.

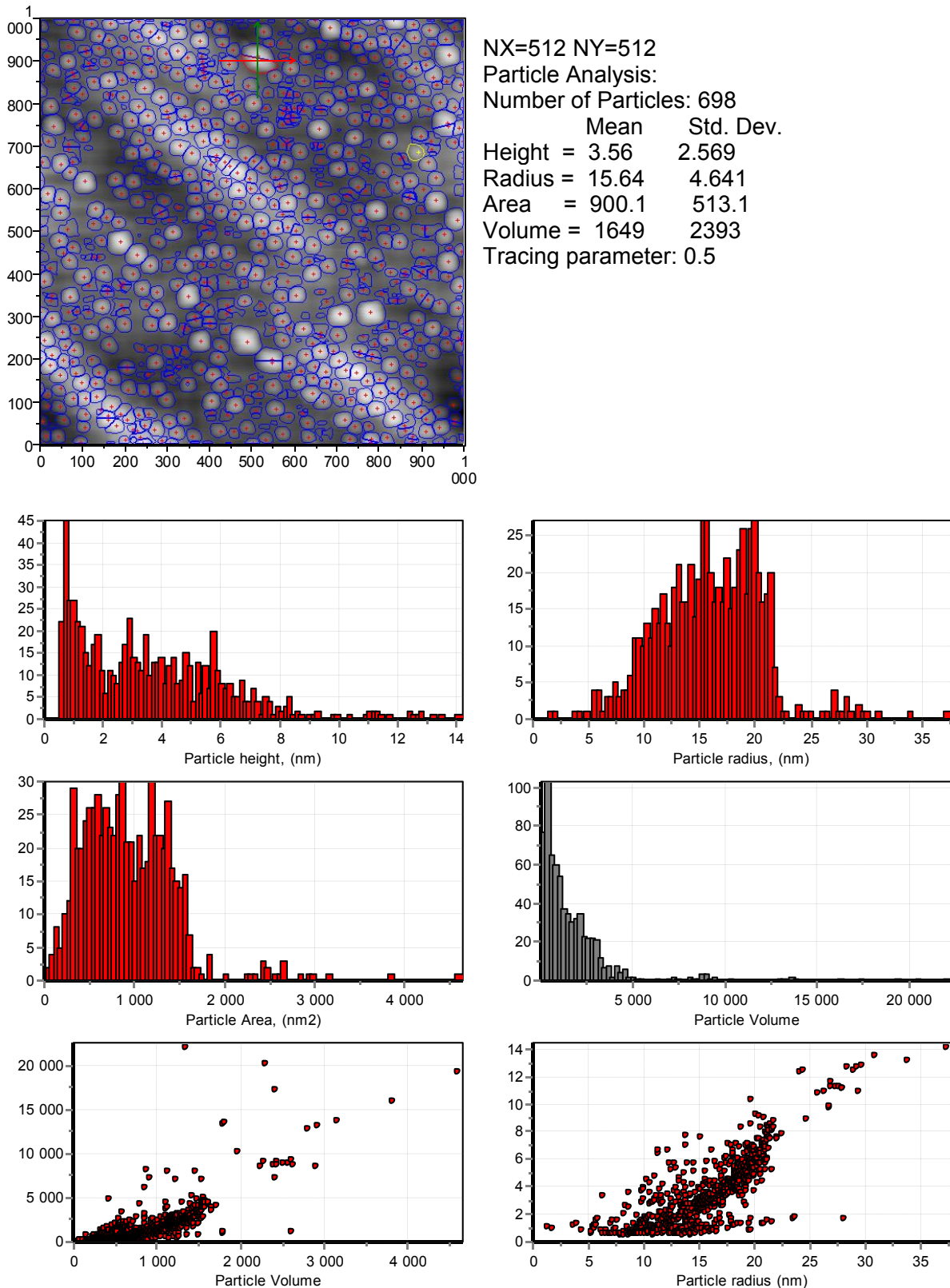


**Figure 3-3:** Report sheet of the statistical analysis on (In,Ga)As QDs sample. This sheet reports the number of QDs counted on the AFM image, the average height, radius, area, volume together with their standard deviation and the repartition histograms of the QDs.

### 3.1.2 Growth optimization of (In,Ga)As/GaP QDs

#### *(a) Deposition thickness*

This study has been performed on the SSMBE apparatus. The nominal thickness of the (In,Ga)As layer is varied in the range of 1 – 4 ML. The growth temperature is set at 580°C and the growth rate is 0.37 ML/s. Nominal In content is calibrated to 30%.

**Figure 3-4** reports  $1 \times 1 \mu\text{m}^2$  AFM images obtained from these samples. From these images, one can see that low thickness ( $< 3$  ML) cannot form QDs but wetting layer should be formed, as the critical thickness of the (In,Ga)As wetting layer is observed for 1.9 ML in the  $\text{In}_{0.5}\text{Ga}_{0.5}\text{As}/\text{GaP}$  QDs system.<sup>[SoSL10]</sup> Evidence of the existence of such a wetting layer will be discussed in the next section. 3 ML is an optimal thickness enough to form high density QDs ( $1.8 \times 10^{11} \text{ cm}^{-2}$  as shown in **Figure 3-4** (c)). Some kind of dashes is formed for higher thickness (4 ML). This can be explained by the coalescence of the QDs due to the excess of the material. The visible undulation on the surface of every sample may be due to the typical elastic relaxation of GaAs on GaP substrate. This point was already discussed in the thesis of Alexandre Bondi in 2010 where the GaAs (without indium) was grown with different thicknesses and temperatures on GaP (001) substrats but it did not form the QDs.<sup>[Bond10]</sup>

**Caution:** The optimal deposition thickness of (In,Ga)As is different when using the GSMBE apparatus. We have observed that 4 ML is an optimal thickness to achieve high density and uniform QDs by using the GSMBE chamber but at 3 ML the QDs could not be formed. This could be attributed to the difference in the cells calibration between the GSMBE and the SSMBE apparatus. More generally, growth parameters of both GSMBE and SSMBE cannot be compared directly because of the difference in the temperature, gas flux, cell calibration, etc.

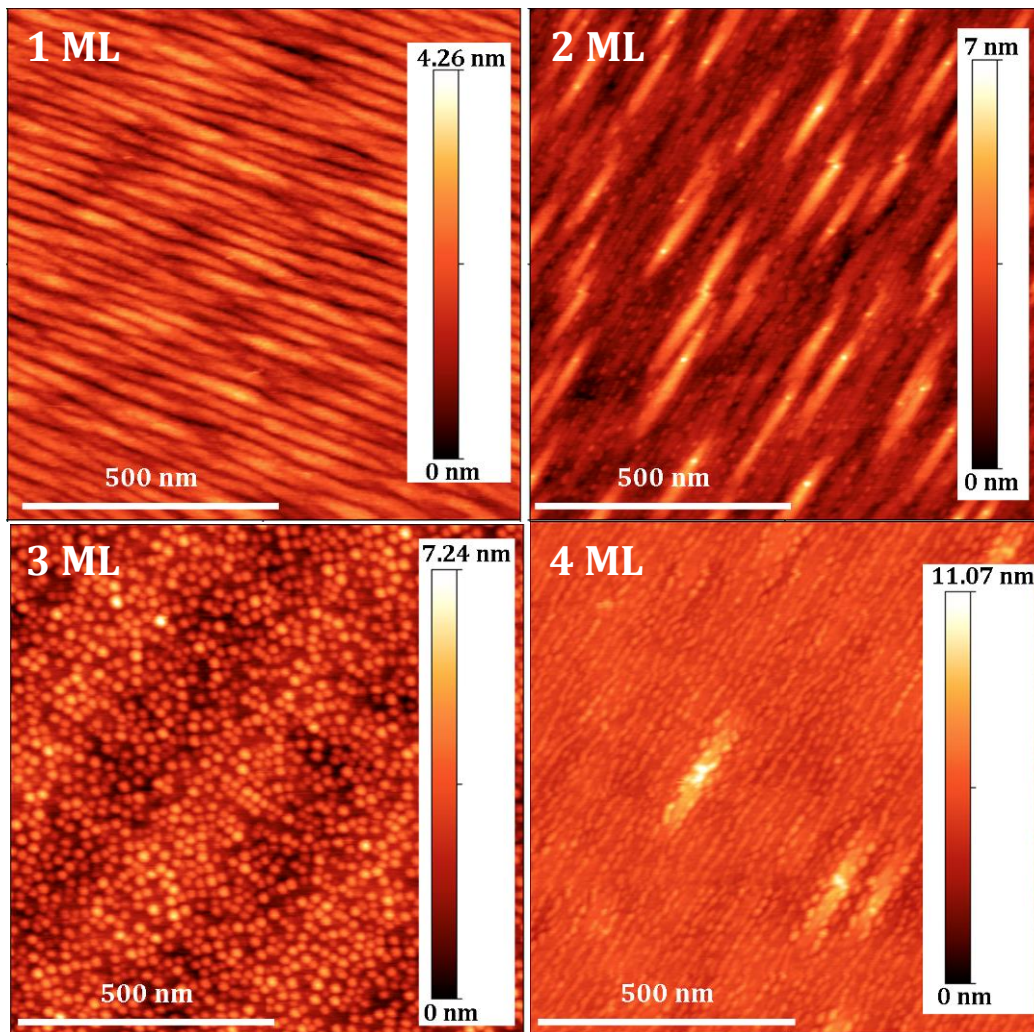


**Figure 3-4:**  $1 \times 1 \mu\text{m}^2$  AFM images of (In,Ga)As/GaP samples with 30% indium and various thickness. Low thickness ( $< 3$  ML) is not sufficient to form QDs but wetting layer should be formed. High thickness ( $> 3$  ML) does not give birth to QDs but they coalesce together to form some kind of dashes. 3 ML is an optimal thickness to achieve high density ( $1.8 \times 10^{11} \text{ cm}^{-2}$ ) and homogeneous QDs (average height =  $1.9 \pm 0.7$  nm, average radius =  $10.6 \pm 2.1$  nm). The visible undulation on the surface may be due to the typical elastic relaxation of GaAs on GaP substrate along the  $[1-10]$  direction.

### ***(b) Growth temperature***

The main motivation for this study is to understand the role of In sticking coefficient, because the effective In composition depends on In segregation, In desorption, or surface energies, which remains challenging and require specific investigations.<sup>[GKHH11]</sup> The growth temperature ( $T_g$ ) has been studied in the range of  $500 - 620^\circ\text{C}$ . Nominal In composition and QDs layer thickness is respectively set to 30% and 3 ML. The results are reported in **Figure 3-5**. As one can see, the appearance of QDs

is not evident at  $T_g$  higher than  $580^\circ\text{C}$ . This might be due to the complete desorption of In at such a high temperature and the remaining material is composed of two dimensional GaAs. From the structural point of view,  $T_g = 580^\circ\text{C}$  is found to be the optimal temperature that can provide high density and good homogeneity (In,Ga)As/GaP QDs. Lower  $T_g$  seems to result in rougher surface with lower QDs density.

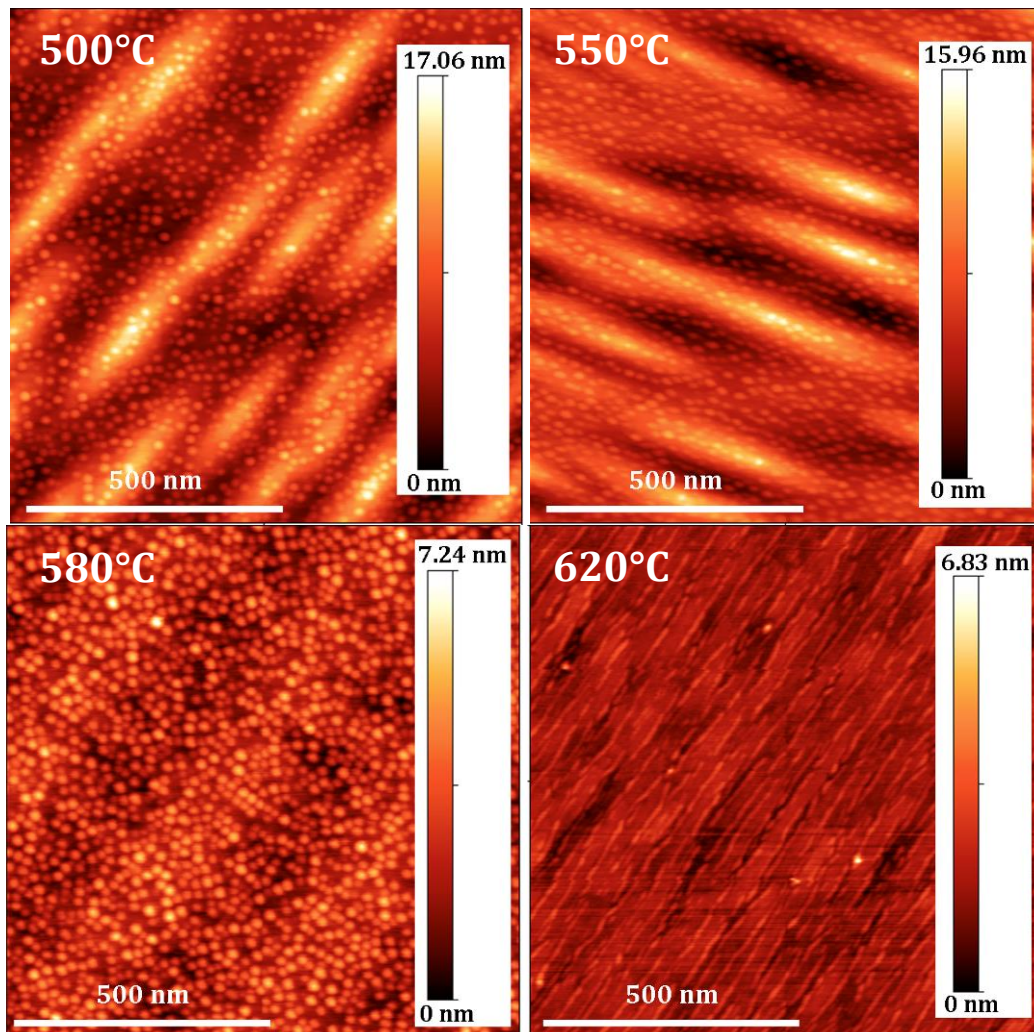


**Figure 3-5:**  $1 \times 1 \mu\text{m}^2$  AFM images of (In,Ga)As/GaP samples with 30% indium, 3 ML thick and various growth temperature ( $500^\circ\text{C}$  –  $620^\circ\text{C}$ ).

Structural analysis of the optimal sample is reported in **Figure 3-6**. This report reveals very high density ( $1.8 \times 10^{11} \text{ cm}^{-2}$ ) and good uniformity of (In,Ga)As/GaP QDs.

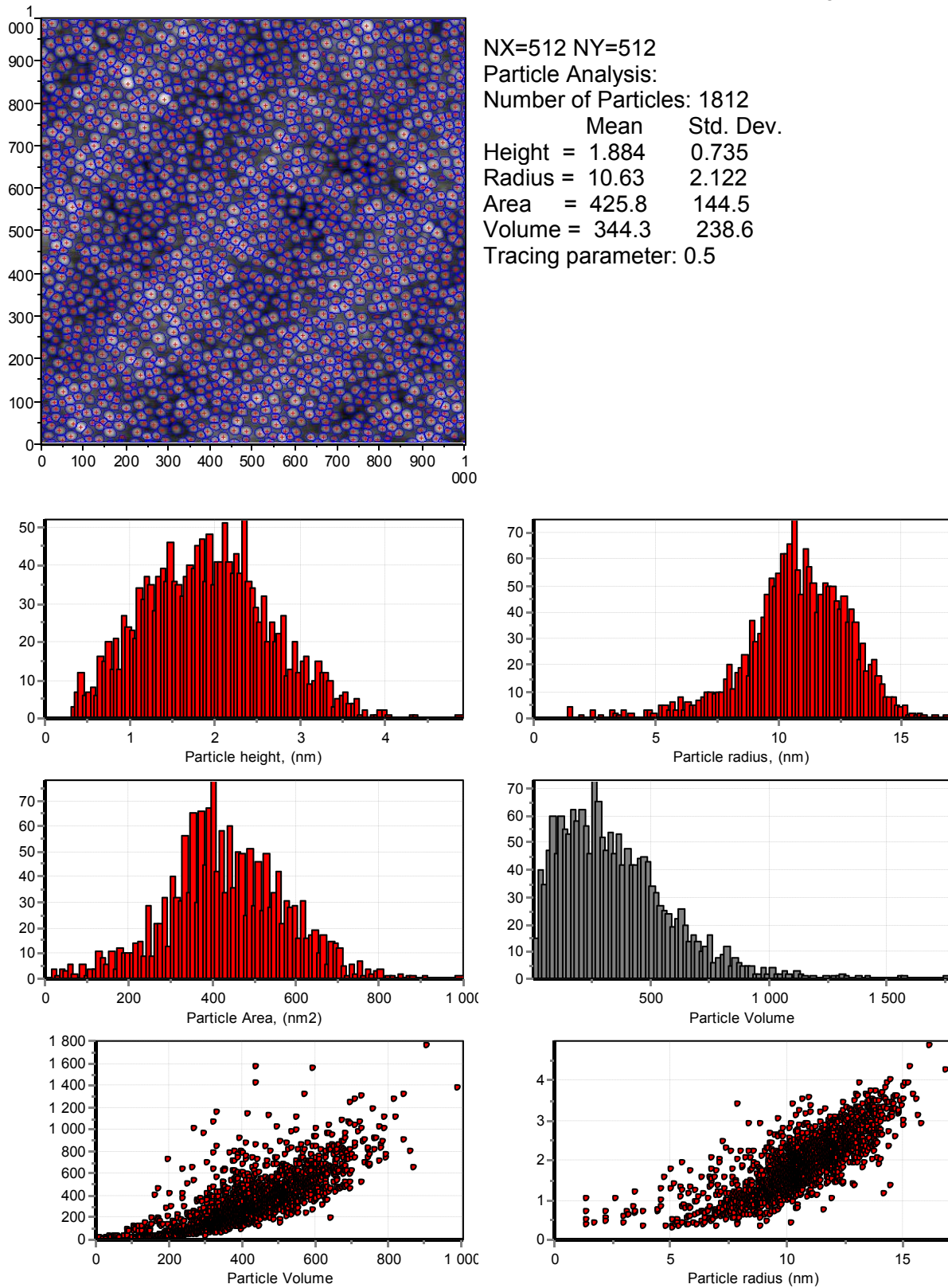


**Figure 3-6:** Structural analysis of the optimal sample reveals very high density ( $1.8 \times 10^{11} \text{ cm}^{-2}$ ) and good homogeneity.

***(c) Indium composition***

The influence of In content on the formation of QDs is studied using both of the GSMBE and SSMBE apparatus. It is reminded that the optimal thickness is found 4 ML and 3 ML respectively for the growth using the GSMBE and the SSMBE chamber.

**Figure 3-7** compares both samples grown with different In content by SSMBE. The In nominal content for the sample reported in **Figure 3-7** (a) is 60% and (b) is 30%. Their density and homogeneity is already reported previously (the reader can refer to **Figure 3-3** and **Figure 3-6** respectively for statistical analysis of sample (a) and (b)).

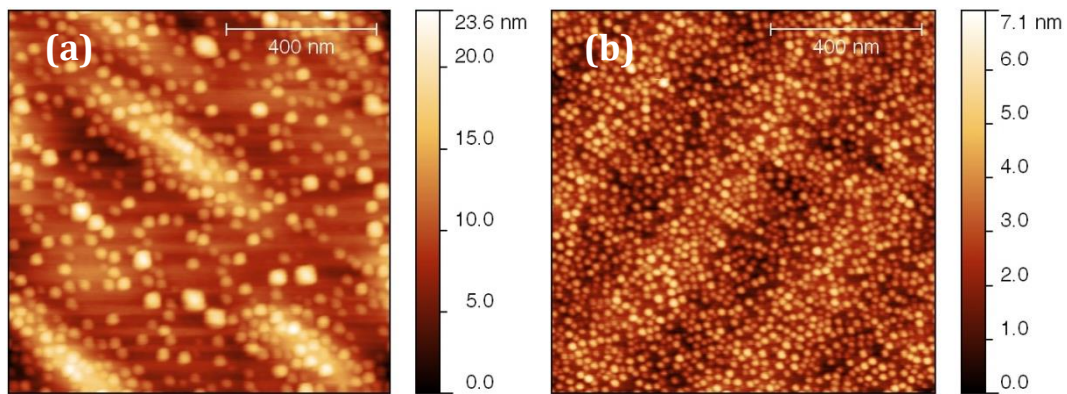


**Figure 3-7:** AFM images of 3 ML (In, Ga)As/GaP QDs grown by SSMBE – (a) 60% In, (b) 30% In.

In content has also been studied using GSMBE (problem of unavailability of the SSMBE for some time). In this study, we have varied the nominal In content from 10 – 30% while fixing the growth temperature and deposition thickness at 580°C and 4 ML, respectively. As reported in **Figure 3-8**, QDs cannot be formed for an In content lower than 30%. Statistical analysis is performed on the sample with 30% In.

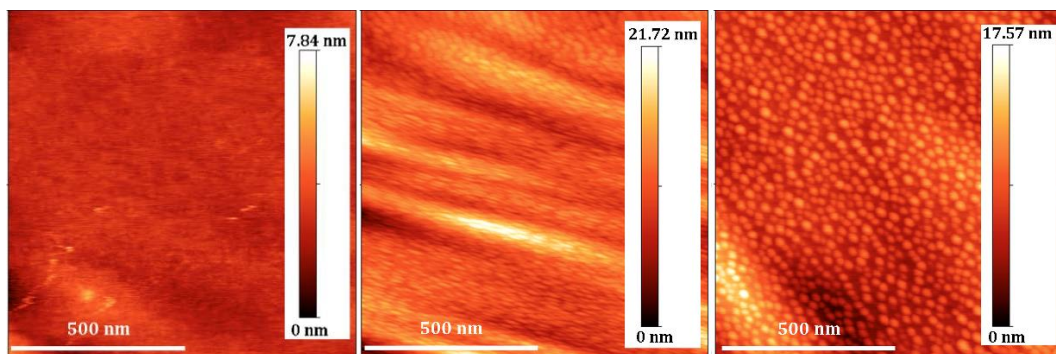


**Figure 3-8:** 1x1 $\mu\text{m}^2$  AFM image from (In,Ga)As QDs grown on GaP substrate using GSMBE with In content of 10% (a), 20% (b) and 30% (c).

The QDs average size and density in the both studies are summarized in **Table 3-1**. From this table, one can see that higher In content results in lower QDs density and larger QDs size. The sample with 30% In grown by GSMBE reveals a similar characteristic as the optimal sample grown by SSMBE. A slight difference between these two samples may be due to the difference in deposition thickness.

**Table 3-1:** Summary of average size and density of (In,Ga)As/GaP QDs grown by SSMBE and GSMBE with different In content.

Sample	Density (cm <sup>-2</sup> )	Height (nm)	Radius (nm)
60% In (SSMBE)	$6.98 \times 10^{10}$	$3.56 \pm 2.57$	$15.64 \pm 4.64$
30% In (SSMBE)	$1.81 \times 10^{11}$	$1.88 \pm 0.74$	$10.63 \pm 2.12$
30% In (GSMBE)	$1.37 \times 10^{11}$	$2.71 \pm 1.16$	$12.41 \pm 3.12$

#### **(d) Annealing time**

In this preliminary study (using GSMBE), the QDs layer is subjected to an annealing under arsine overpressure at 580°C. We have tried with 3 minutes annealing and without annealing at all. AFM measurement of the two samples is presented in **Figure 3-9**. The sample presented in (a) is without annealing and (b) is with 3 minutes annealing. A clear difference between these two samples can be noticed: the sample with annealing has lower QDs density with larger QDs lateral size (see **Table 3-2** for a summary of statistical analysis).

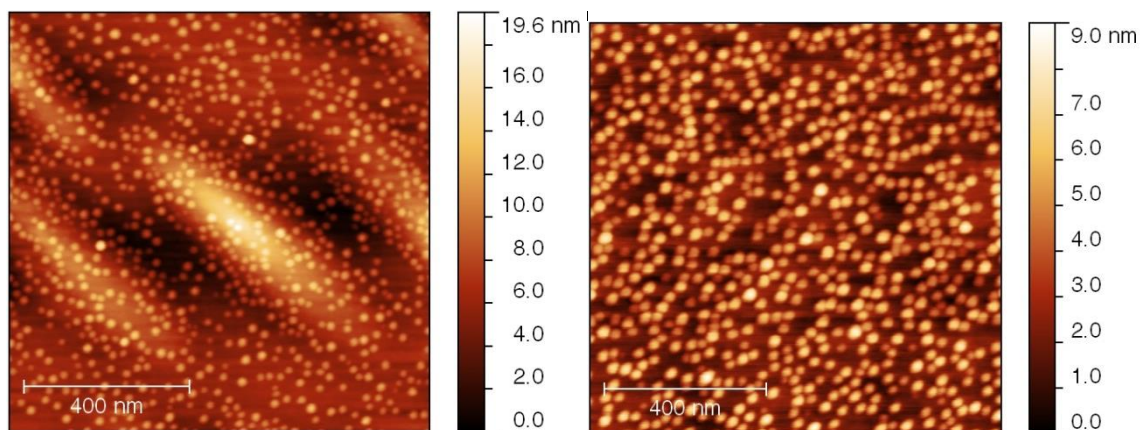


**Figure 3-9:** AFM measurement on (In,Ga)As/GaP QDs samples without annealing (a) and with 3 minutes annealing under AsH<sub>3</sub> overpressure (b).

**Table 3-2:** Influence of annealing time on the density and size of (In,Ga)As/GaP QDs.

Annealing time (s)	Density (cm <sup>-2</sup> )	Height (nm)	Radius (nm)
0	$9.47 \times 10^{10}$	$3.65 \pm 1.50$	$11.57 \pm 2.09$
180	$7.70 \times 10^{10}$	$3.26 \pm 1.17$	$15.71 \pm 3.05$

The change of QDs size due to longer annealing time is not studied in detail in the framework of this thesis, but the preliminary result is interesting. This aspect could be exploited further in order to tune the emission wavelength by changing the QDs size via annealing, likely playing with the reduction of the difference between the  $\Gamma$  and X valleys.

### 3.1.3 Discussion

The growth optimization of (In,Ga)As QDs on GaP substrate reveals high density and good homogeneity of QDs. It is well known that In is desorbed for temperature higher than 520°C by the segregation effect.<sup>[LDBS04]</sup> The growth temperature (580°C) in our case is thus too high for indium incorporation. In order to verify if the indium plays a role in the formation of the QDs, we have applied the optimal growth conditions for (In,Ga)As/GaP QDs to grow GaAs/GaP but the sample has revealed flat surface with no evidence of QDs, as presented in **Figure 3-10** (a). This suggests that In plays an important role in the QDs nucleation. The question is: how much is it incorporated?

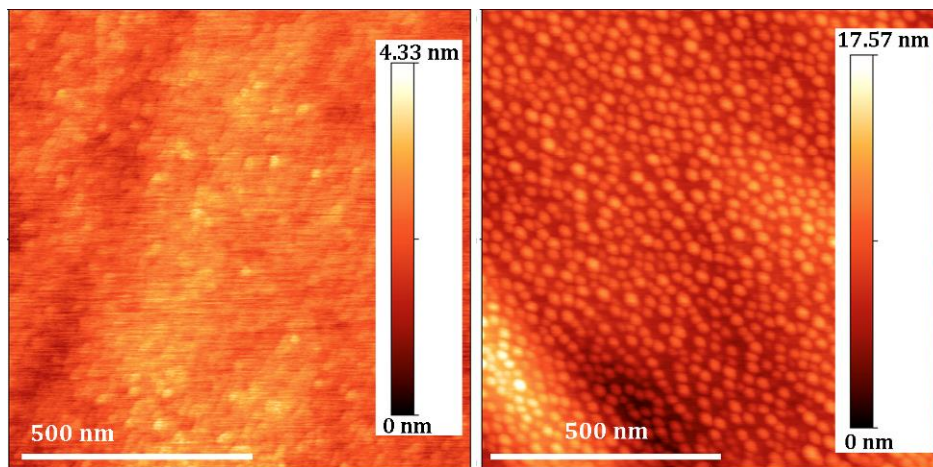


**Figure 3-10:** (a)  $1 \times 1 \mu\text{m}^2$  AFM scan of GaAs/GaP (4 ML, 580°C) reveals flat surface with RMS roughness = 0.27 nm, (b) (In,Ga)As/GaP shows high density QDs with the same growth conditions. Both samples are grown by GSMBE.

Despite the desorption of In atoms which arises when the temperature is higher than 520°C, In incorporation has been reported even at 595°C during (In,Ga)As/GaAs deposition.<sup>[LDBS04]</sup> Moreover, the In incorporation coefficient in InGaAs/GaAs epilayers at this temperature has been measured to be around 40-50%,<sup>[FMDB97, MHAK00, RRSW91, TuMa87]</sup> depending on growth conditions. Considering that the In incorporation is dependent on the strain,<sup>[MbTM88, TuMa87]</sup> In incorporation coefficient in our case (i.e. on GaP substrate) is thus even lower, which would lead to an In effective composition below or equal to 15% for a nominal content of 30%.

In order to evaluate the potentiality of these QDs for laser devices, a comparison can be made with well-known QDs materials systems such as InAs/InP or InAs/GaAs which are currently used in high performance laser devices.<sup>[CBCD05, HMMH99]</sup> The size distribution is evaluated in terms of the dispersion in height  $\frac{\Delta h}{h}$  and radius  $\frac{\Delta r}{r}$  which are respectively 42.80% and 25.14% for the optimized sample grown by GSMBE; 39.36% and 19.94% respectively for the optimized sample grown by SSMBE. In the case of InAs/InP QDs, good laser devices are obtained with density around  $1.6 \times 10^{11} \text{ cm}^{-2}$ . In this case, the dispersion in height and radius are 21% and 16 % respectively.<sup>[CBCD05]</sup> In the InAs/GaAs material systems, good laser performances are reached with a maximum density around  $10^{11} \text{ cm}^{-2}$ , and the dispersion in height and radius equal to 24% and 11%, respectively.<sup>[HMMH99]</sup> Thus, the measured size homogeneity of our (In,Ga)As/GaP QDs system is not far from the state-of-the-art QDs in other reference materials systems.

## 3.2 Optical properties of (In,Ga)As/GaP QDs

### 3.2.1 Tight-binding calculation

The motivation for choosing InGaAs/GaP materials system and the role of indium composition in strained InGaAs/GaP heterostructures is discussed in the context of the band-edge alignments using the tight-binding (TB) approach and *ab initio* calculations of the valence-band offsets.<sup>[LWCY09]</sup> This study is in the framework of C. Robert's thesis. To this end, we consider the extended-basis *spds*\_ TB model which provides a band-structure description with unique sub-millielectron volt precision throughout the Brillouin zone.<sup>[SCLS04]</sup> Strain effects are taken into account in the same way of smaller TB models known to be reliable for strained GaInAs QWs.<sup>[BJGB92]</sup> **Figure 3-11** represents the band alignment of biaxially strained  $\text{In}_x\text{Ga}_{1-x}\text{As}$  and InP on GaP. We observe a clear

localization of the holes states in the alloy whatever the In content. Electron behavior is more complex because of the proximity in energy of  $\Gamma$ , L, and  $X_{XY}$  conduction states of InGaAs and the X conduction band minimum of GaP at low concentration. In particular, for strained GaAs, all these states are located in a window of 150 meV. Consequently there is no hope to achieve a realistic  $\Gamma$ -like conduction band minimum in GaAs/GaP nanostructures. For 30% In, the energy difference between the  $\Gamma$  and  $X_{XY}$  bands of the alloy is about 200 meV. We thus expect the QDs structure to keep a type-I carrier confinement and a direct transition in k-space despite quantum confinement effects. Moreover, if we compare the band alignments of InP/GaP and In<sub>0.53</sub>Ga<sub>0.47</sub>As/GaP which has exactly the same lattice mismatch with GaP, this latter presents a better confinement as indicated by arrows in **Figure 3-11**, showing the high potential of the (In,Ga)As system.

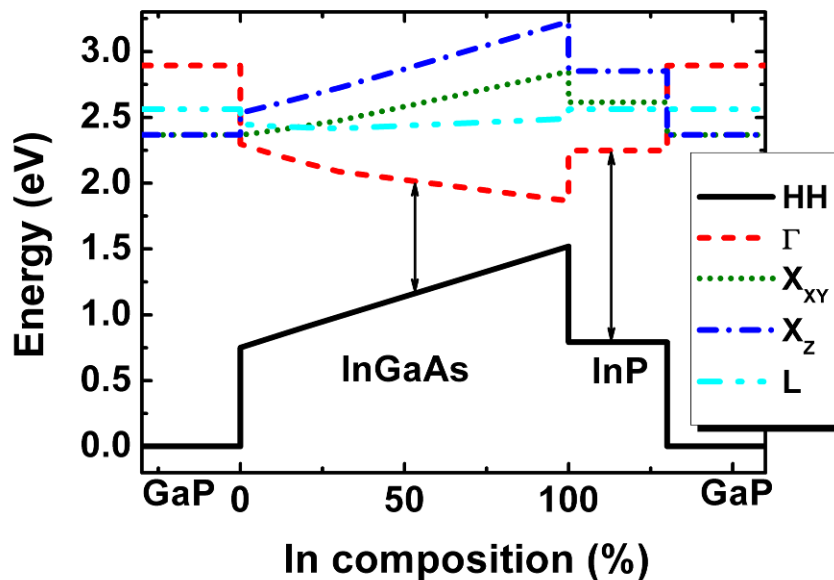


**Figure 3-11:** Tight-binding calculation of conduction and valence band alignment and band structure of In<sub>x</sub>Ga<sub>1-x</sub>As and InP strained to GaP as a function of indium composition.<sup>[NRCP11]</sup>

### 3.2.2 Room temperature photoluminescence

Samples used for PL experiments were covered by a 30 nm thick GaP capping layer. Both GaAs/GaP and (In,Ga)As/GaP have been grown in the same conditions (4 ML, 580°C) to confirm the existence of In in our material system. Since the AFM image of GaAs/GaP sample shows a flat surface (RMS roughness = 0.26 nm), as reported in **Figure 3-10**, the structure is thus expected to behave as a quantum well after deposition of the GaP capping layer. PL experiments were carried out by exciting the samples with a

continuous 405 nm wavelength laser with a  $630 \text{ W/cm}^2$  incident power. Temperature dependent PL characterization of the samples was performed in a Helium closed-cycle cryostat from 12 K to RT.

**Figure 3-12** shows a comparison between the RT PL spectra of both the (In,Ga)As/GaP and GaAs/GaP nanostructures. Moreover, the weak RT PL signal from GaP substrate deep centers is also reported.<sup>[GBCF09, GBHF09, LLCW98]</sup> Therefore, a significant contribution of optically active nanostructures is clearly observed as compared to the GaP substrate. For the GaAs/GaP sample, the emission energy is  $E_{\text{GaAs}}=1.78 \text{ eV}$  (this energy is typically higher than the bulk GaAs because of strain and vertical quantum confinement when grow on GaP substrate),<sup>[RPCE12]</sup> while for the (In,Ga)As/GaP sample, the energy emission is redshifted toward  $E_{(\text{In,Ga})\text{As}}=1.74 \text{ eV}$ . Different PL peaks shapes are also observed. While for the GaAs case where the PL spectrum is composed of one peak, the (In,Ga)As PL spectrum reveals a double peak. A fitting of both peaks with Gaussian functions yields 1.74 eV for the main contribution (ground state) and 1.82 eV attributed to an excited state transition of the system (**Figure 3-13**). These differences in the optical properties (energy shift and double peak) between both material systems can be understood by looking at the nanostructure shape (QW or QD) and the indium incorporation.

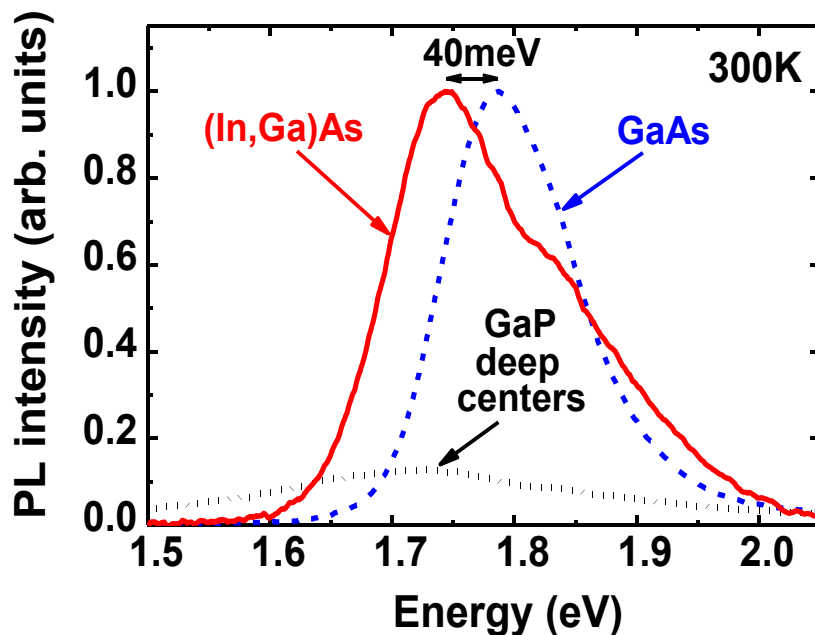


**Figure 3-12:** Room temperature photoluminescence of (In,Ga)As/GaP QDs (red solid curve), GaAs/GaP (blue dashed curve) and GaP deep centers (black dotted curve).<sup>[NRCP11]</sup>

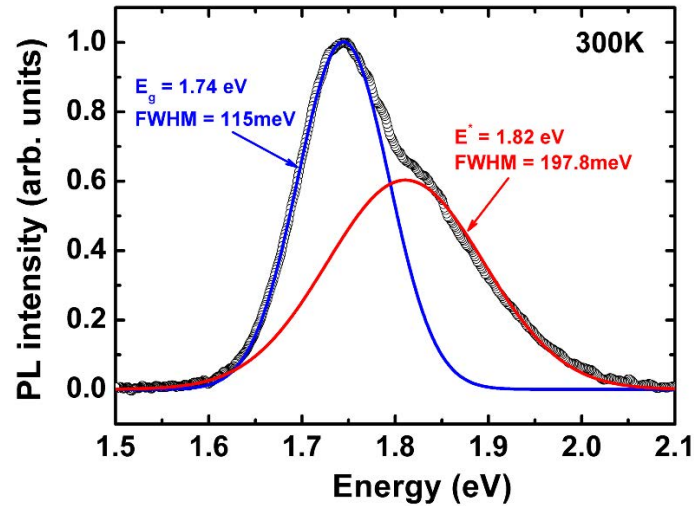


**Figure 3-13:** Gaussian fit of the ground state and excited state of the (In,Ga)As/GaP QDs PL signal at room temperature.

**Figure 3-14** presents the PL spectra of a single layer of (In,Ga)As/GaP QDs at RT (red dashed curve) and 12K (black solid curve). The double peak observed in PL experiments at RT being attributed to any excited state from the whole system (wetting layer, QDs excited state transitions, participation of other valleys in the conduction band ...), the inhomogeneous broadening in this system is thus characterized by the low energy half width at half maximum (HWHM) of the ground state transition peak, measured to be 54 meV. This value, much smaller than the one obtained on InGaAsN/GaP QDs (167 meV), [UFUN10] is not far from those measured in the InAs/InP (28 meV) [CBCD05] and InAs/GaAs reference systems (38 meV). [HMMH99]

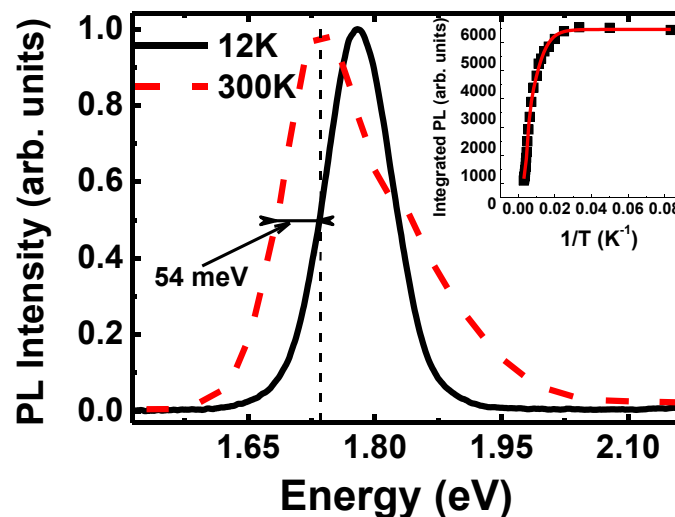


**Figure 3-14:** Photoluminescence of (In,Ga)As/GaP QDs at 12K (black solid curve) and room temperature (red dashed curve). Inset shows the integrated photoluminescence intensity versus inverse temperature. This curve is fitted by an Arrhenius equation over two localized states. [NRCP11]

Carrier confinement properties are studied by means of the temperature dependent PL analysis. From 12 K to RT, the PL energy peak follows the so-called Varshni's law. The appearance of the second PL peak at RT is related to the thermal filling of excited states. Also the evolution of the PL integrated intensity of (In,Ga)As/GaP QDs is shown in the inset of **Figure 3-14**. The PL integrated intensity ratio between low temperature and RT is equal to 25. This ratio is the signature of a better carrier confinement than the one in usual QWs (factor 100 – C. Netzel *et al.*)<sup>[NHWK10]</sup> but maybe a lower confinement compared to high efficiency QDs systems (factor 10 – Kim *et al.*)<sup>[KPPS07]</sup> By taking into account an Arrhenius distribution over 2 energy levels (biexponential fitting presented in **Figure 3-14** inset), activation energies can be calculated.<sup>[HMMH99]</sup> The integrated intensity is almost constant from 12 K to 40 K, then it quenches slightly to 210 K with an activation energy of 20 meV and finally quenches dramatically with an activation energy of 134 meV. The first activation energy shows a clear proximity of excited states to the barrier while the second activation energy confirms reasonable electrons confinement of QDs.

### 3.2.3 Annealing effect

As presented in the first section, we have observed an increase in lateral size of QDs with an annealing time of 3 minutes. RT PL of the sample with 3 minutes annealing and the sample with 30 seconds annealing is compared in **Figure 3-15**. We found that the sample with 3 minutes annealing reveals an increase of the integrated intensity by a factor of 10 comparing to the sample annealed in 30 seconds. The emission peak is slightly shifted toward higher energy which may be explained as lower In content due to longer annealing time.

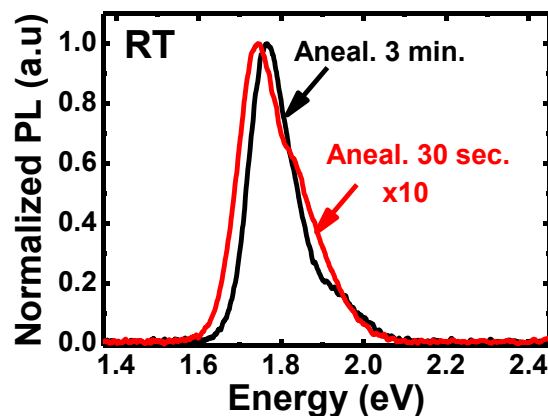


**Figure 3-15:** Influence of annealing time on RT PL. 3 minutes annealing increases PL integrated intensity by a factor of 10, with respect to 30 seconds annealing.

### 3.3 Single (In,Ga)As/GaP quantum dot structure

Single (In,Ga)As/GaP QD structure has been studied using AFM and scanning tunneling microscopy (STM) in collaboration with P. Turban at the Institut de Physique de Rennes – Université de Rennes 1. The samples have been grown by SSMBE system using n-doped GaP(001) substrate.<sup>[RCTN12]</sup> The growth temperature is fixed at 580°C with a nominal thickness and indium content of 3 ML and 30%, respectively. For STM study, 500 nm thick n-doped GaP buffer layer is grown using silicon as dopant with a doping level of  $10^{17} \text{ cm}^{-3}$ . It is followed by 10 nm undoped GaP layer on which (In,Ga)As QDs will be formed. As we have to bring out the sample to the STM system which is not near from our lab, the sample surface is protected by an amorphous arsenic capping layer which is deposited at 10°C during 6 hours ( $\text{BEP}_{\text{As}} = 5 \times 10^{-6} \text{ Torr}$ ). This protective layer is then removed in-situ by thermal heating at 430°C in the STM UHV chamber. All of STM images were scanned in constant-current mode operation. In the following, the tunnel voltage between the STM tip and the sample surface is denoted  $U_t$  and the tunnel current  $I_t$ . All images shown are filled-states images.

#### 3.3.1 STM transfer validation

In order to check if the QDs remain unchanged during the amorphous As deposition and removal, and thus the validity of the STM measurements, preliminary experiments have to be conducted. Particularly, the QDs ripening during this stage should be avoided. For this purpose, structural properties have been first compared on two similar samples in **Figure 3-16**. The first  $800 \times 800 \text{ nm}^2$  image on the left (**Figure 3-16 (a)**) is directly obtained by AFM right after the growth. The second one on the right (**Figure 3-16 (b)**) is obtained by STM after amorphous As capping and removal. The QDs density is measured to be  $(1.5 \pm 0.2 \times 10^{11}) \text{ cm}^{-2}$  in **Figure 3-16 (a)** and  $(1.3 \pm 0.2 \times 10^{11}) \text{ cm}^{-2}$  in **Figure 3-16 (b)**. A ripening of the QDs would clearly lower the QDs density, which is not observed here.

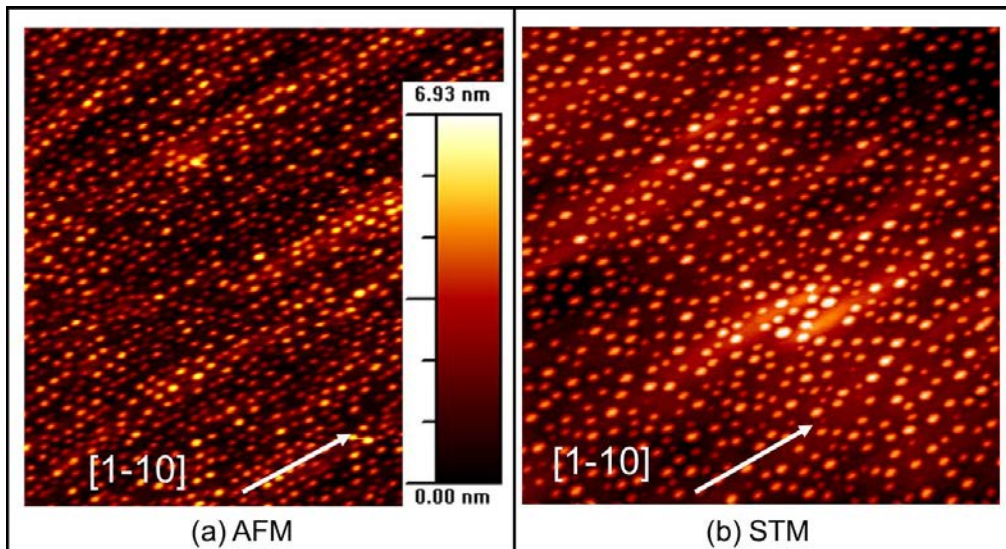


**Figure 3-16:** (a) 800x800 nm<sup>2</sup> AFM image of uncapped (In,Ga)As/GaP QDs, and (b) 800x800 nm<sup>2</sup> STM image ( $U_t = -3.27$  V;  $I_t = 0.04$  nA) of (In,Ga)As/GaP QDs, transferred to the STM chamber with amorphous As capping layer. The QD morphology was not changed during the transfer.

Statistical analysis of heights and radii distributions is also performed. The mean QDs height is equal to  $(3.0 \pm 1.0)$  nm in **Figure 3-16** (a) and  $(3.5 \pm 1.2)$  nm in **Figure 3-16** (b). The slight discrepancy may come from the underestimated height due to high QDs density in the AFM scan. The measured mean radius is  $(11 \pm 2)$  nm in **Figure 3-16** (a) and  $(9.0 \pm 1.8)$  nm in **Figure 3-16** (b). This gives a typical aspect ratio (height to diameter ratio) of 0.2. The lateral extent of the QDs is thus measured to be different. This slight discrepancy can be mainly attributed to the convolution between real surface and the probing tip, which is known to be more important in AFM than in STM. Accurate to within the uncertainty, the two sets of QDs parameters can be considered identical. In conclusion, QDs morphology is found to be the same before and after the amorphous As capping and decapping.<sup>[RCTN12]</sup>

### 3.3.2 Single QD morphology

**Figure 3-17** (a) presents a 60x60 nm<sup>2</sup> STM high resolution image of the surface with a few QDs. Surface topography was derivated to enhance contrast. Surface reconstruction of the planar areas allows to unambiguously identify the [1-10] crystallographic direction of the substrate. Atomic sites with high electronic density are observed on top of the QDs as well as on the base planar surface and are fingerprints of an In-rich surface. Presence of In reveals the existence of a wetting layer, and thus demonstrates the Stranski-Krastanov growth mode of these QDs. Given the relatively

low In content in the structure due to the In desorption at high growth temperature (580 °C), the (In,Ga)As alloy composition is thus likely inhomogeneous. It has been shown in the well-known (In,Ga)As/GaAs, (In,Al)As/GaAs or (Ga,Al)As/GaAs systems, that group III elements with lower bond strength (i.e. indium here) tend to float on the growth surface, leading to the so-called In segregation [INAN90, MTSC87, TuMa87]. This mechanism is expected to occur in our sample. In the extreme borderline case, the total amount of In is located at the surface, and the QDs are exclusively composed of GaAs (**Figure 3-17** (b)). In this situation, the predominant role of In in the QDs nucleation is to increase the lattice mismatch, it is the QDs nucleation driving force. The In-rich (In,Ga)As islands are expected to be precursors of the SK transition when the In concentration is high enough.[CNWM02, TeLe94] Actually, indium can be considered here as a catalyst for the QDs nucleation. Very recent X-STM result from the TU Berlin indicates that the wetting layer does not contain indium after capping by GaP, all the indium are located at the upper part of the QD.[PLRS13]

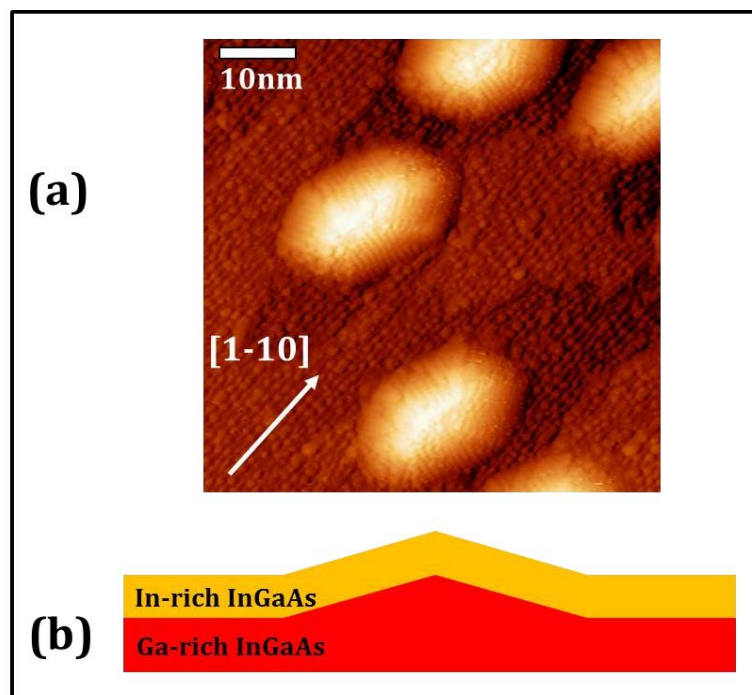


**Figure 3-17:** (a) 60x60 nm<sup>2</sup> STM plane view ( $U_t = -2.87$  V;  $I_t = 0.01$  nA) of typical (In,Ga)As QDs. (b) Structure model of a single (In,Ga)As QD with an In-rich InGaAs layer on the top and Ga-rich InGaAs layer underneath.

A careful observation of these QDs reveals the appearance of few ripened QDs (QDs that accumulate atoms to enlarge their size). **Figure 3-18** (a) shows a 75x75 nm<sup>2</sup>

STM image on which we can observe this kind of QDs among typical ones (i.e. QDs whose size is mostly found on the whole surface).

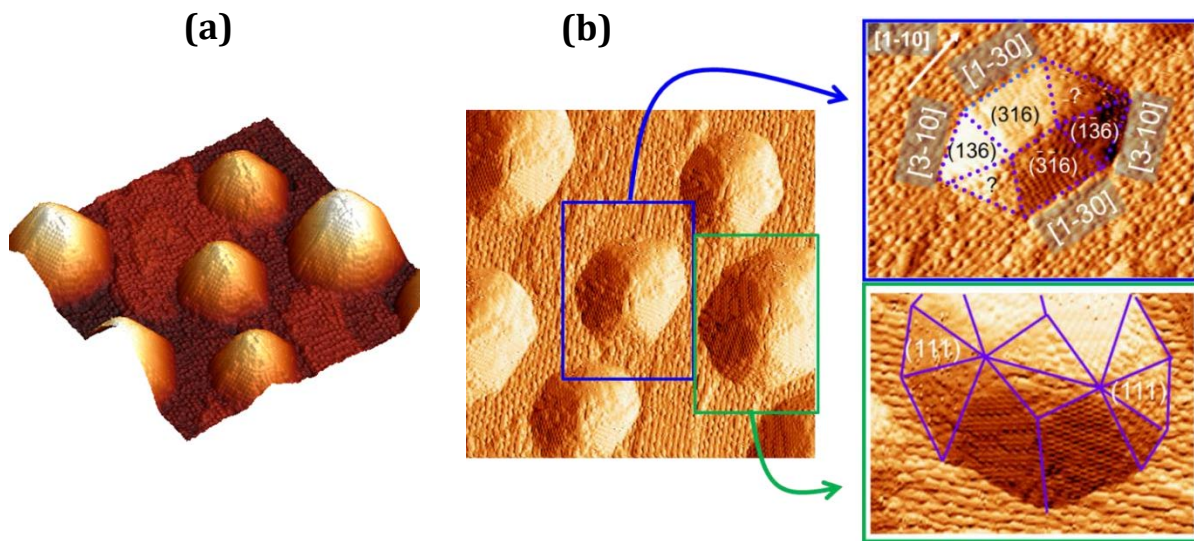


**Figure 3-18:** (a)  $75 \times 75 \text{ nm}^2$  STM 3D plane view of (In,Ga)As QDs showing ripened QDs among typical ones. (b)  $60 \times 60 \text{ nm}^2$  STM plane view ( $U_t = -2.87 \text{ V}$ ,  $I_t = 0.01 \text{ nA}$ ) of (In,Ga)As/GaP QDs (image on the left). A detailed angle analysis of the image allows the identification of facets in typical QD (image on the upper right). Facets analysis for ripened QD reveals the appearance of low index facets (image on the lower right).

**Figure 3-18** (b) presents the morphology of a single typical QD and a larger QD. The in-plane anisotropic ratio (between length and width) is reduced from 1.5 (small QD) to nearly 1 (large QD). These values show the relatively low in-plane anisotropy of the QD. Facets were thus determined by measuring angles between facets and the base plane, combined with angle measurements between facets intersections with the base plane and the  $[1 \ -1 \ 0]$  direction. Small QD (**Figure 3-18** (b) upper right) exhibit 6 main facets, including  $(3 \ 1 \ 6)$ ,  $(1 \ 3 \ 6)$ ,  $(-1 \ -3 \ 6)$  and  $(-3 \ -1 \ 6)$  well-defined planes, and 2 other facets with a more diffuse aspect; for these two facets, the dispersion on the measured angles is too large to unambiguously conclude. Directions of the QDs edges under the  $(1 \ 3 \ 6)$  facets are  $[1 \ -3 \ 0]$  and  $[3 \ -1 \ 0]$ . These high-index surfaces observed can be compared to other studies performed on In(Ga)As/GaAs QDs, where the stability of  $(1 \ 3 \ 7)$  [CRMA06, Jaco03, KCLS09, KLAM06, MagJ01],  $(1 \ 3 \ 6)$  [LLYS98],  $(1 \ 2 \ 5)$  [HKXS98], and even  $(2 \ 5 \ 11)$  planes [GTMK02, Jaco03] were already discussed. In the case of InAs/InP  $(0 \ 0 \ 1)$  QD,  $(1 \ 3 \ 6)$  facets were also observed. [MSPB06]

Note that all the previously cited high-index planes are very close in the stereographic triangle (**Figure 3-19**); [Jaco03] the measurement accuracy does not allow to

choose between these high index-planes (the (1 3 6) choice is the direct result of the angle measurement). Our measurement confirms the thermodynamic stability of these high-index facets with the common InAs material system composing the QDs on GaP, GaAs and InP substrates.

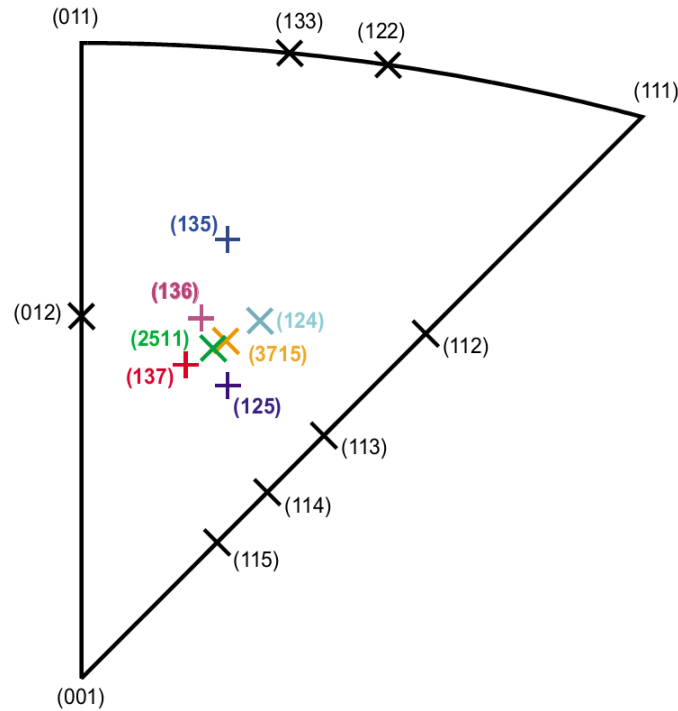


**Figure 3-19:** Stereographic triangle for FCC III-V compound semiconductor surfaces exhibiting the low-index corner points, the  $[-1\ 1\ 0]$ -zone borderline connecting the  $(0\ 0\ 1)$  and  $(1\ 1\ 1)$  corner points, and the different high-index surface orientations touched upon in this contribution.<sup>[Jaco03]</sup>

In the larger QD (**Figure 3-18** (b) - lower right), the QD presents additional facets, and especially well-defined low-index  $(1\ 1\ 1)$  facets. Considering that large QD are formed by the ripening process (increasing amount of atoms in the QD), this observation is in total agreement with observations performed on InAs/GaAs QDs.<sup>[CRMA06, KLAM06]</sup> This has also been observed in the SiGe materials system.<sup>[RSTK05]</sup> The energy gain  $E_{\text{tot}}$  associated with the formation of three-dimensional islands on the wetting layer is given by <sup>[KLAM06]</sup>:

$$E_{\text{tot}} = E_{\text{relax}} + E_{\text{surf}} + E_{\text{edge}} \quad (\text{Eq. 17})$$

where  $E_{\text{relax}}$  is the contribution originating from bulk strain relaxation,  $E_{\text{surf}}$  the additional formation of facets, and  $E_{\text{edge}}$  the contribution of QD edges formation on the

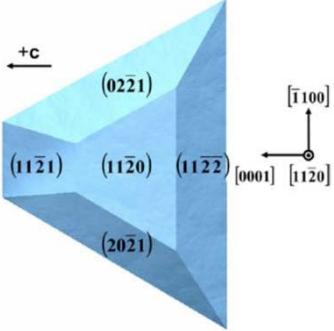
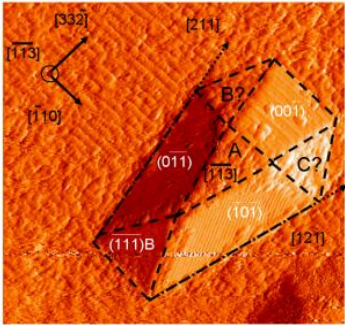
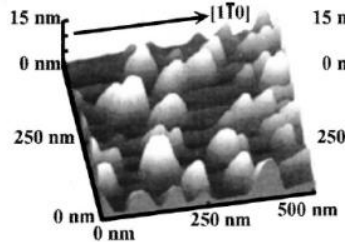
reconstructed surface. It is then shown that, considering a single QD at the thermodynamic equilibrium, its shape depends on its number of indium atoms. In accordance with our results, high index facets are present for small atoms content, because the  $E_{\text{surf}}$  has a predominant role. Note that (1 3 6) and (3 1 6) planes are not reconstructed in the same way, and thus do not have in this case the same energy. When the QD ripens, the increasing amount of atoms leads to the predominance of the  $E_{\text{relax}}$  contribution, which implies low index facets, and to the increase of the number of facets. In Ref. [KLAM06], the third term  $E_{\text{edge}}$  is neglected, because the detailed atomic structure near the edges is not known. This approximation is not valid for too small islands, and shouldn't be neglected here.

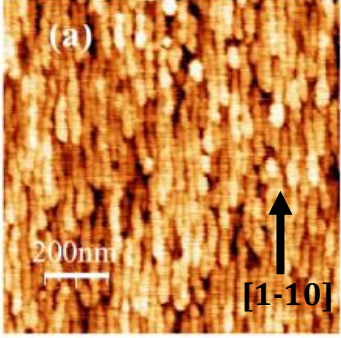
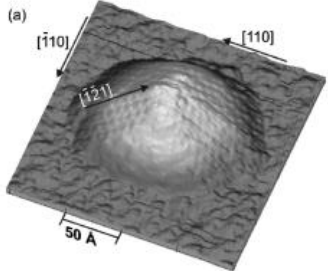
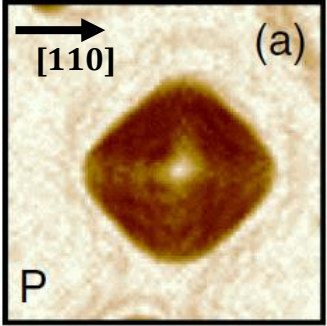
### 3.3.3 Unusual $C_2$ symmetry of the (In,Ga)As/GaP QD

The STM study on single QD reveals an unusual  $C_2$  symmetry. Let's take a look at different nanostructures and their corresponding crystal structures as reported in **Table 3-3**. The first two groups (GaN/AlN - wurzite, InAs/InP (113)B – Zinc Blende) do not have a  $C_2$   $\pi$  rotation axis but have a  $\sigma(1-10)$  symmetric plane. The next three groups (CdTe/ZnTe QDs – Zinc Blende, InAs/InP (001) quantum dashes – Zinc Blende, InGaAs/GaAs (001) QDs – Zinc Blende) have a  $C_2$   $\pi$  rotation axis, a  $\sigma(110)$  and a  $\sigma(1-10)$  symmetric planes. Finally the SiGe/Si (001) QDs (diamond crystal) have the highest symmetric order. One can remark that higher symmetry of the crystal structures leads to higher symmetry of the nanostructures, and secondly, the  $\sigma(1-10)$  symmetric plane always presents in most of the structures.

Turning back to our case, as one can see in **Figure 3-20**, the (In,Ga)As/GaP (001) QDs does not possess any  $\sigma$  symmetric plane, but does present a  $C_2$   $\pi$  rotation axis. **Figure 3-20** (c) is rotated by 180 degree with respect to its original one (b) to prove the  $C_2$  rotation axis. The same phenomena have been observed in the work of Michon *et al* [MSPB06], for the InAs/InP (001) QDs system, or in the work of Mano *et al* [MNHE03], for the InGaAs/GaAs (001) QDs system.

**Table 3-3:** Bibliographic study of symmetry in different nanostructures with different crystal structures.

	$C_2$ ( $\pi$ rotation)	$\sigma(110)$ (Mirror)	$\sigma(1-10)$ (Mirror)	Nanostructure symmetry	Crystal symmetry
 <p><b>GaN/AIN</b> <b>(Wurzite)</b><sup>[FBMD07]</sup></p>	NO	NO	YES	$C_s$	$C_{6v}$
 <p><b>InAs/InP (113)B</b> <b>(Zinc-Blende)</b><sup>[CTBT11]</sup></p>	NO	NO	YES	$C_s$	$T_d$
 <p><b>CdTe/ZnTe</b> <b>(Zinc-Blende)</b><sup>[TGMK03]</sup></p>	YES	YES	YES	$C_{2v}$	$T_d$

 <p><b>InAs/InP (001)</b> <b>(Zinc-Blende)</b><sup>[LPLN09]</sup></p>	YES	YES	YES	$C_{2v}$	$T_d$
 <p><b>InGaAs/GaAs (001)</b> <b>(Zinc-Blende)</b><sup>[MáGJ01]</sup></p>	YES	YES	YES	$C_{2v}$	$T_d$
 <p><b>SiGe/Si (001)</b> <b>(Diamond)</b><sup>[RSTK05]</sup></p>	YES	YES	YES	$C_{4v}/C_{2v}$	$O_h$

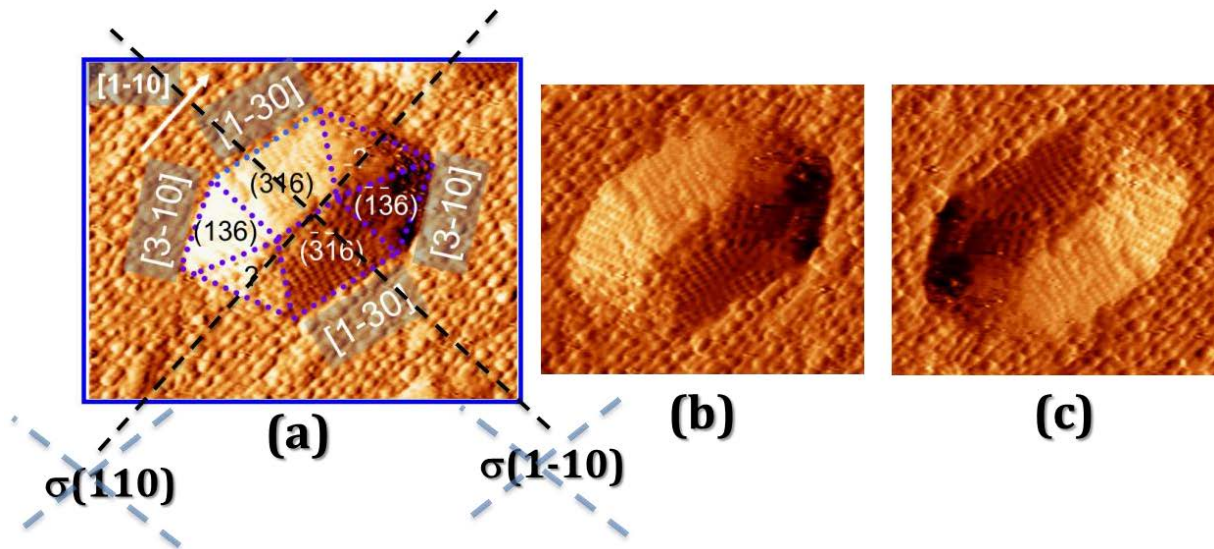


**Figure 3-20:**  $C_2$  symmetry of regular (small and medium size) (In,Ga)As/GaP QD. (a) reveals neither  $\sigma(110)$  nor  $\sigma(1-10)$  symmetric plane; (c) is rotated by 180 degree with respect to its origin presented in (b).

This observation is found on regular QDs (small and medium size). For ripened QDs (large size), a  $\sigma(1-10)$  symmetric plane is easily found (see **Figure 3-18** (b) for example). Although the origin of these phenomena is unclear till date, it seems that  $C_2$  symmetry is a property of small size InAs-based QDs, with a non-negligible contribution of  $E_{\text{surf}}$  and  $E_{\text{edge}}$ .

### 3.4 Summary

We have achieved high density (In,Ga)As QDs ( $10^{11} \text{ cm}^{-2}$ ) on GaP substrate. Electronic structure and bandlineups in the (In,Ga)As/GaP material system have been determined from advanced atomistic calculations. The RT PL and homogeneous size distribution of these QDs reveal good structural quality and electronic properties leading to an efficient optical emission. Complete temperature dependent photoluminescence analysis shows promising confinement properties. In this regard, (In,Ga)As/GaP QDs seem to address all requirements (high density, type-I bandlineup, efficient carrier confinement, good structural quality) for the development of laser applications in the field of optoelectronic integration on silicon.

Morphological analyses of single QDs using STM reveal the appearance of ripened QDs. The contribution to the QDs formation energy is found to switch from surface to

volume with the progressive ripening of the dot. This has consequences on the morphology properties: small dots exhibit high {1 3 6} index facets whereas low index {1 1 1} facets are observed for larger dots. A  $C_2$  unusual symmetry is found on regular (small and medium size) QDs while ripened QDs present a  $\sigma(1-10)$  symmetric plane. The origin of this phenomenon is unclear till date and it requires further study.

## REFERENCES

- [BJGB92] BORING, Philippe; JANCU, Jean-Marc; GIL, Bernard; BERTHO, Denis; JOUANIN, Christian; MOORE, Karen J.: In: *Physical Review B* **46** (1992), No. 8, p. 4764
- [Bond10] BONDI, Alexandre: Rennes, INSA de Rennes, 2010
- [CBCD05] CAROFF, P.; BERTRU, N.; LE CORRE, A.; DEHAESE, O.; ROHEL, T.; ALGHORAIBI, I.; FOLLIOU, H.; LOUALICHE, S.: In: *Japanese Journal of Applied Physics* **44** (2005), No. No. 34, pp. L1069–L1071
- [CNWM02] CULLIS, A.G.; NORRIS, D.J.; WALTHER, T.; MIGLIORATO, M.A.; HOPKINSON, M.: In: *Physical Review B* **66** (2002), No. 8, p. 081305
- [CRMA06] COSTANTINI, G.; RASTELLI, A.; MANZANO, C.; ACOSTA-DIAZ, P.; SONGMUANG, R.; KATSAROS, G.; SCHMIDT, O. G.; KERN, K.: In: *Physical Review Letters* **96** (2006), No. 22, p. 226106
- [CTBT11] CORNET, C.; TURBAN, P.; BERTRU, N.; TRICOT, S.; et al.: In: *Euro-MBE conference (2011) – Alpe d’Huez, France*.
- [FBMD07] FOUNTA, S.; BOUGEROL, C.; MARIETTE, H.; DAUDIN, B.; VENNÉGUÈS, P.: In: *Journal of Applied Physics* **102** (2007), No. 7, pp. 074304–074304–6
- [FMDB97] FOURNIER, Françoise; METZGER, Robert A.; DOOLITTLE, Alan; BROWN, April S.; CARTER-COMAN, Carrie; JOKERST, Nan Marie; BICKNELL-TASSIUS, Robert.: In: *Journal of Crystal Growth* **175–176, Part 1** (1997), pp. 203–210
- [GBCF09] GUO, Weiming; BONDI, Alexandre; CORNET, Charles; FOLLIOU, Hervé; et al.: In: *physica status solidi (c)* **6** (2009), No. 10, pp. 2207–2211
- [GBHF09] GERHARD, S; BAUMANN, V; HÖFLING, S; FORCHEL, A.: In: *Nanotechnology* **20** (2009), No. 43, p. 434016
- [GKHH11] GIDDINGS, A. D.; KEIZER, J. G.; HARA, M.; HAMHUIS, G. J.; YUASA, H.; FUKUZAWA, H.; KOENRAAD, P. M.: In: *Physical Review B* **83** (2011), No. 20, p. 205308
- [GTMK02] GEELHAAR, L.; TEMKO, Y.; MÁRQUEZ, J.; KRATZER, P.; JACOBI, K.: In: *Physical Review B* **65** (2002), No. 15, p. 155308
- [HKXS98] HASEGAWA, Y.; KIYAMA, H.; XUE, Q. K; SAKURAI, T.: In: *Applied Physics Letters* **72** (1998), No. 18, pp. 2265–2267
- [HMMH99] HEITZ, R.; MUKHAMETZHANOV, I.; MADHUKAR, A.; HOFFMANN, A.; BIMBERG, D.: In: *Journal of Electronic Materials* **28** (1999), No. 5, pp. 520–527
- [INAN90] IIMURA, Y.; NAGATA, K.; AOYAGI, Y.; NAMBA, S.: In: *Journal of Crystal Growth* **105** (1990), No. 1–4, pp. 230–233
- [Jaco03] JACOBI, K.: In: *Progress in Surface Science* **71** (2003), No. 5–8, pp. 185–215
- [KCLS09] KRATZER, Peter; CHAKRABARTI, Aparna; LIU, Quincy K K; SCHEFFLER, Matthias.: In: *New Journal of Physics* **11** (2009), No. 7, p. 073018
- [KLAM06] KRATZER, P.; LIU, Q. K. K.; ACOSTA-DIAZ, P.; MANZANO, C.; et al.: In: *Physical Review B* **73** (2006), No. 20, p. 205347

- [KPPS07] KIM, J.H.; PARK, Y.J.; PARK, Y.M.; SONG, J.D.; LEE, J.I.; KIM, T.W.: In: *Applied Surface Science* **253** (2007), No. 7, pp. 3503–3507
- [LDBS04] LEE, S. C.; DAWSON, L. R.; BRUECK, S. R. J.; STINTZ, A.: In: *Journal of Applied Physics* **96** (2004), No. 9, pp. 4856–4865
- [LLCW98] LEON, R.; LOBO, C.; CHIN, T. P.; WOODALL, J. M.; FAFARD, S.; RUVIMOV, S.; LILIENTAL-WEBER, Z.; STEVENS KALCEFF, M. A.: In: *Applied Physics Letters* **72** (1998), No. 11, p. 1356
- [LLYS98] LEE, Hao; LOWE-WEBB, Roger; YANG, Weidong; SERCEL, Peter C.: In: *Applied Physics Letters* **72** (1998), No. 7, pp. 812–814
- [LPLN09] LAMY, J. M.; PARANTHOEN, C.; LEVALLOIS, C.; NAKKAR, A.; et al.: In: *Applied Physics Letters* **95** (2009), No. 1, pp. 011117–011117–3
- [LWCY09] LI, Yong-Hua; WALSH, Aron; CHEN, Shiyu; YIN, Wan-Jian; et al.: In: *Applied Physics Letters* **94** (2009), No. 21, p. 212109
- [MÁGJ01] MÁRQUEZ, J.; GEELHAAR, L.; JACOBI, K.: In: *Applied Physics Letters* **78** (2001), No. 16, pp. 2309–2311
- [MbTM88] MBAYE, A. A.; TURCO, F.; MASSIES, J.: In: *Physical Review B* **37** (1988), No. 17, pp. 10419–10422
- [MHAK00] MASHITA, Masao; HIYAMA, Yoshihito; ARAI, Kenta; KOO, Bon-Heun; YAO, Takafumi.: In: *Japanese Journal of Applied Physics* **39** (2000), pp. 4435–4437
- [MNHE03] MANO, T.; NÖTZEL, R.; HAMHUIS, G.J.; EIJKEMANS, T.J.; WOLTER, J.H.: In: *Journal of Crystal Growth* **251** (2003), No. 1–4, pp. 264–268
- [MSPB06] MICHON, A.; SAGNES, I.; PATRIARCHE, G.; BEAUDOIN, G.; MÉRAT-COMBES, M. N.; SAINT-GIRONS, G.: In: *Physical Review B* **73** (2006), No. 16, p. 165321
- [MTSC87] MASSIES, J.; TURCO, F.; SALETES, A.; CONTOUR, J.P.: In: *Journal of Crystal Growth* **80** (1987), No. 2, pp. 307–314
- [NHWK10] NETZEL, C.; HOFFMANN, V.; WERNICKE, T.; KNAUER, A.; WEYERS, M.; KNEISSL, M.; SZABO, N.: In: *Journal of Applied Physics* **107** (2010), No. 3, p. 033510
- [NRCP11] NGUYEN THANH, T.; ROBERT, C.; CORNET, C.; PERRIN, M.; et al.: In: *Applied Physics Letters* **99** (2011), No. 14, pp. 143123–143123–3
- [PLRS13] PROHL, Christopher; LENZ, Andrea; ROY, Dominik; SCHUPPANG, Josephine; et al.: In: *Applied Physics Letters* **102** (2013), No. 12, pp. 123102–123102–4
- [RCTN12] ROBERT, C.; CORNET, C.; TURBAN, P.; NGUYEN THANH, T.; et al.: In: *Physical Review B* **86** (2012), No. 20, p. 205316
- [RPCE12] ROBERT, C.; PERRIN, M.; CORNET, C.; EVEN, J.; JANCU, J. M.: In: *Applied Physics Letters* **100** (2012), No. 11, pp. 111901–111901–4
- [RRSW91] REITHMAIER, J.-P.; RIECHERT, H.; SCHLÖTTERER, H.; WEIMANN, G.: In: *Journal of Crystal Growth* **111** (1991), No. 1–4, pp. 407–412
- [RSTK05] RASTELLI, A.; STOFFEL, M.; TERSOFF, J.; KAR, G. S.; SCHMIDT, O. G.: In: *Physical Review Letters* **95** (2005), No. 2, p. 026103
- [SCLS04] SACCONI, F.; DI CARLO, A.; LUGLI, P.; STADELE, M.; JANCU, J. -M.: In: *IEEE Transactions on Electron Devices* **51** (2004), No. 5, pp. 741–748
- [SoSL10] SONG, Yuncheng; SIMMONDS, Paul J.; LEE, Minjoo Larry.: In: *Applied Physics Letters* **97** (2010), No. 22, p. 223110
- [TeLe94] TERSOFF, J.; LEGOUES, F. K.: In: *Physical Review Letters* **72** (1994), No. 22, pp. 3570–3573
- [TGMK03] TINJOD, F.; GILLES, B.; MOEHL, S.; KHENG, K.; MARIETTE, H.: In: *Applied Physics Letters* **82** (2003), No. 24, pp. 4340–4342
- [TuMa87] TURCO, F.; MASSIES, J.: In: *Applied Physics Letters* **51** (1987), No. 24, pp. 1989–1991
- [UFUN10] UMENO, K.; FURUKAWA, Y.; URAKAMI, N.; NOMA, R.; MITSUYOSHI, S.; WAKAHARA, A.; YONEZU, H.: In: *Physica E: Low-dimensional Systems and Nanostructures* **42** (2010), No. 10, pp. 2772–2776



## CHAPTER 4.

# HOMOEPITAXIAL GROWTH OF SILICON

---

---

*As mentioned previously, a single domain, biatomic stepped Si surface is expected to avoid the APB formation. The Si surface after growth can be free from recontamination by transferring to the MBE chamber using a ultrahigh vacuum tunnel. To this end, an MBE-UHV/CVD cluster is equipped in our lab since 2010. Description of this cluster is presented in the appendices. This chapter will discuss some of the epitaxial optimization steps and the results obtained on smooth, contaminant-free and biatomic stepped Si surface. This work is performed in close collaboration with J. Kuyyalil and T. Quinci.*

### 4.1 Surface cleaning

An oxygen- and carbon-free substrate surface is essential for smooth, single-crystalline, and defect-free epitaxy. As much as one monolayer of residual surface oxide can cause polycrystalline or amorphous rather than single-crystalline film growth. Interface contamination gives rise to increased film surface roughness and various crystal defects. Nayak *et al.* have argued that surface contamination reduces the diffusivity of adsorbed  $\text{SiH}_x$  species,<sup>[NSCL95]</sup> thus resulting in an increased initial three-dimensional growth or localized deposition. Boron surface contamination commonly occurs as a result of wafer handling in air, while oxide forms by reacting with oxygen and  $\text{H}_2\text{O}$  vapor during transport in air and water rinses. Carbon is found as contamination in native oxide and processing liquids, such as hydrofluoric acid or DI-water. “Backstreaming” hydrocarbons originating from hot and turbulent pump oils can cause significant accumulation of carbon on silicon substrates processed in vacuum equipment. Other organic and metal impurities are typically found on the wafer surface after polishing steps, lithography, storage in plastic containers, and handling in air.<sup>[Ha0t01]</sup>

In a production environment, the ex-situ wet chemical cleaning typically employs an RCA-based procedure (Radio Corporation of America)<sup>[KePu70]</sup> or a Shiraki-based procedure.<sup>[IsSh86]</sup> Briefly, the RCA-based method consists of a solvating and oxidizing base mixture which removes organic, particles, and some metals contamination. It is followed by an oxidizing acid-based solution in which metal contaminants are converted to soluble complexes. After rinsing, the wafers are then immersed in an HF solution to remove the surface oxide and terminate dangling silicon bonds with atomic hydrogen. This procedure has proven to result in a surface that is stable in air against re-oxidation for several minutes,<sup>[Meye92]</sup> with less than 1% coverage with residual oxygen, carbon, and boron (typical interface doses in the mid- $10^{12}$  cm<sup>-2</sup>). The surface can be purified further employing in-situ cleans. The Shiraki-based process consists of a wet chemical treatment to remove hydrocarbon and metal contamination, and forms a thin protective oxide layer. After several chemical cleaning steps, the final oxide layer is grown in a boiling solution of HCl:H<sub>2</sub>O<sub>2</sub>:H<sub>2</sub>O (3:1:1) at 90°C for 10 minutes. This oxide layer is removed under UHV by thermal annealing below 900°C. The removing of the oxide consists of the diffusion of silicon atoms into the oxide layer. The reaction of Si and SiO<sub>2</sub> forms 2 molecules SiO which are volatile and thus escape into the vacuum:



Ishizaka and Shiraki demonstrated that the thin oxide layer is completely removed after 40 minutes treatment at 710°C or removed in 15 minutes at 785°C.<sup>[IsSh86]</sup>

Beside these two usually used methods, numerous other ones have also been tried. Hydrogen bakes have been reported to be effective only at temperatures above 750°C for durations of 30 seconds to several minutes to reduce SiO<sub>2</sub> into SiO and water.<sup>[AHHS04, BoMR97]</sup> HCl-based etching produces clean and smooth surfaces employing comparable temperatures.<sup>[GiGW85]</sup> Clean and damage-free Si surface was obtained by Wright and Kroemer using gallium molecular beam exposure at temperature as low as 800°C to reduce SiO<sub>2</sub> into a volatile mixed-oxide compound (Ga<sub>2</sub>O, SiO).<sup>[WrKr80]</sup> Morar *et al.* have shown that a submonolayer coverage of germanium yielded nonstoichiometric germanium-oxides, which desorbed at temperatures as low as 625°C and proposed a low-temperature CVD batch-compatible oxide removal based on brief germane exposures.<sup>[MMKH87]</sup> Similarly, the addition of small amounts of disilane during

thermal annealing accelerates the surface oxide decomposition, and annealing temperatures as low as 780°C were successfully demonstrated.<sup>[NKKS99]</sup> Hydrogen ECR (electron cyclotron resonance) cleaning was demonstrated to be effective in reducing interfacial contaminants at temperatures between room temperature and 600°C, whereas low-energy argon and argon-hydrogen ion bombardment at temperatures below 300°C and 100°C, respectively, yielded defect-free crystalline growth and proved successful in removing molecular contamination.<sup>[Cres06]</sup> However, higher ion energies, though more effective in removing contamination, resulted in increased surface roughness and argon incorporation.<sup>[BBPS77]</sup>

As the CVD growth technique is highly sensitive to surface contamination, very few contaminants at the surface would result in a rough and holed surface after growth. In this regard, UHV/CVD growth quality gives a direct evaluation of surface preparation by looking at the surface roughness. In order to study the cleaning process optimization, we have applied in the first time a modified RCA cleaning method which is detailed in **Table 4-1**. RCA cleaning method is widely used in microelectronic fabrication for long time and has proven its efficiency.<sup>[KePu70]</sup> This process consists of many chemical attacks to remove in the first time organics, then oxides and metal particles. It is terminated by dipping the sample in a diluted HF (2.25 %) bath for transferring to CVD. **Figure 4-1** (left) shows the Si surface measured by AFM after 1 hour 20 minutes growth at 800°C (pyrometer) in the low pressure mode. Growth details will be given in the next part. The very high RMS surface roughness (48.2 nm) evidences the presence of contaminants at the surface prior to grow. This can be explained by the re-contamination of carbon due to repeated dipping in chemical and water for long time.

**Table 4-1:** Modified RCA silicon surface preparation

Step	Chemical	T (°C)	Time	Effect
Degrease	Trichloroethane	80	3 min	Remove heavy organic contamination
	Acetone	60	3 min	
	Ethanol	70	3 min	
	Cooling down in ethanol then put under ultrasonic bath	RT	1 min	
	DI water	RT	20 min	
Modified RCA clean	NH <sub>4</sub> OH : H <sub>2</sub> O <sub>2</sub> : H <sub>2</sub> O 10 : 30 : 200	70	10 min	Remove particles, small organic residues (1-2 nm) and metallic impurities (Cu, Ag, Ni, Co and Cd); introduce other metallic contamination (Fe and Al)
	DI water	RT	20 min	
	HF : H <sub>2</sub> O 12.5 : 237.5	RT	1 min	Remove oxide, introduce Carbon and small amount of ions (especially Cu) Remove residues of the metallic contamination; form Oxide layer at surface
	HCl : H <sub>2</sub> O <sub>2</sub> : H <sub>2</sub> O 30 : 30 : 150	80	10 min	
	DI water	RT	10 min	
	HF : H <sub>2</sub> O 12.5 : 237.5	RT	1 min	
	DI water	RT	10 min	Remove the oxide layer
	Oxydation in UV/O <sub>3</sub>	RT	2 min	
	DI water	RT	3 min	Remove C, S at the surface
	HF : H <sub>2</sub> O 12.5 : 237.5	RT	1 min	
	DI water	RT	3 min	
	Repeated 5 times the 4 steps above using new HF solution with the same concentration in the last 3 cycles. After this step, the wafer is immersed in a new HF bath and is loaded to the reactor.			

A cross-sectional SEM (scanning electron microscopy) image of this sample is shown in **Figure 4-1** (on the right). It reveals a flat bottom in a groove and (113) type plane edges which are typical signatures of residual carbon related contaminants or oxide. This also indicates the bad quality of the chemical preparation that has to be optimized.

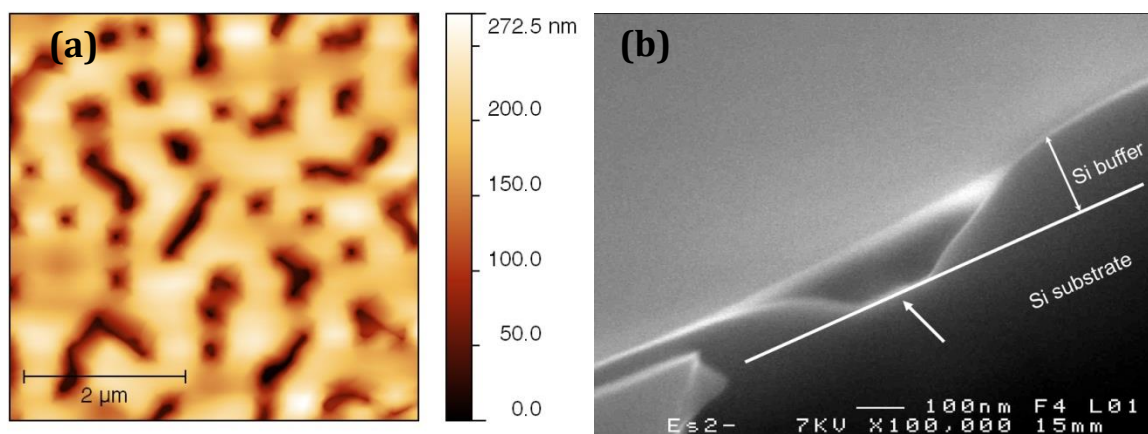


**Figure 4-1:** (a)  $5 \times 5 \mu\text{m}^2$  AFM image of silicon surface grown using the cleaning process described in **Table 4-1**. High RMS surface roughness (**48.2 nm**) is a clear indicator of bad chemical preparation. (b) Cross-sectional SEM image of this sample. A flat surface at the bottom of the groove is indicated by the arrow. The inclined angle of the edges is about  $25^\circ$  which is corresponding to (113) crystal planes. The groove depth corresponds to the homoepitaxial layer thickness which is estimated to about 150 nm.

This feature has been observed for various chemical preparation conditions, with the RCA and Shiraki modified procedures repeated between 1 to 10 times. Surface roughness of the grown layers was not improved significantly and statistically. We attribute this to the lack of purity of the chemical products used in the lab environment. Thus optimization of the chemical preparation was performed by using AFM post-growth analysis and trying to limit the exposure of silicon wafer to chemical solutions. The optimized recipe of the chemical preparation is described in **Table 4-2**. This cleaning process is similar to the process reported by Takahagi *et al.* who claimed successful achievement of clean and carbon-free silicon surface.<sup>[TNIK88]</sup> It consists in removing the native oxide layer on the substrate by a first HF dipping in 90 seconds. Organics and metal particles are oxidized and removed under UV/O<sub>3</sub> exposure in 10 minutes. This step also forms a thin SiO<sub>2</sub> layer on the surface which is removed by a last HF dipping just before loading into the load lock chamber. We have diluted the commercial concentrated HF solution at a concentration as low as 1% and the reaction time in HF is reduced to 90 seconds in order to avoid the surface roughening due to concentrated acid solution and long reaction time.

**Table 4-2:** Optimized surface preparation: HF-last cleaning process

Solution	Time	Description
HF 1%	90 sec.	Remove native oxide
UV/O3	10 min.	Remove C, organics, small particles; re-oxidation at surface
HF 1%	90 sec.	New HF bath; remove oxide layer + passivation of surface with hydrogen → Loading to the reactor.

**Figure 4-2** (a) shows an AFM image of a sample grown with this optimized cleaning process. This sample has been grown for 2 hours at 800°C (pyrometer) in the low pressure mode (the same growth conditions as reported in the previous sample for comparison). Contrary to the previous case, this AFM image reveals a very smooth surface which indicates a clean substrate prior to grow. The growth with this chemical preparation is repeated several times to prove the reproducibility of the cleaning process. After each growth, AFM measurements confirm the smoothness of the surface with the RMS around 2 Å which is in the noise uncertainty of the AFM measurement. Cross-sectional SEM images have been carefully taken on these samples and no defects (pits, holes, grooves) have been found (**Figure 4-2** (b)).

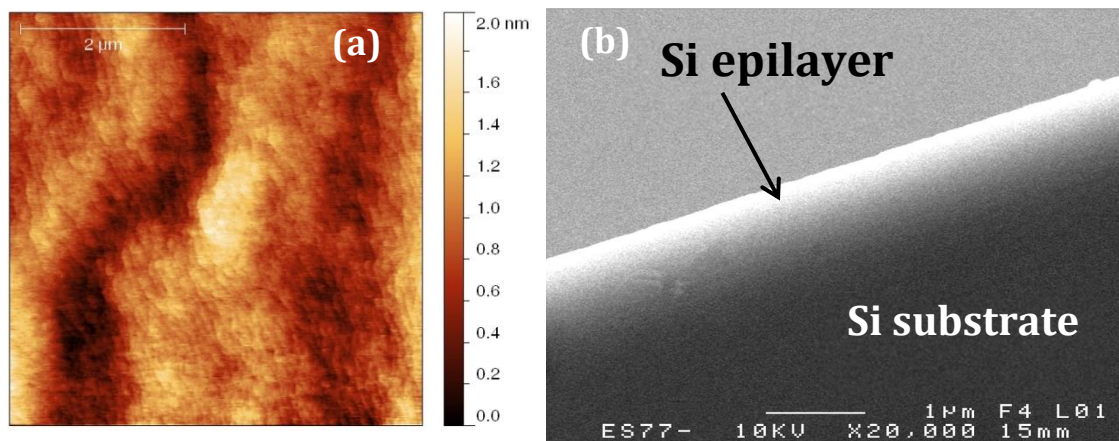


**Figure 4-2:** (a)  $5 \times 5 \mu\text{m}^2$  AFM image shows the surface of Silicon sample grown after the HF last cleaning process. RMS roughness is measured to be 0.3 nm. (b) Cross-sectional SEM image of the sample with the optimized cleaning process. The interface between the substrate and the epilayer is not visible. Especially, defects and holes were not found at the surface and interface.

## 4.2 Homoepitaxial growth of silicon using UHV/CVD reactor

### 4.2.1 Silicon growth mechanism

The deposition of silicon from chemical vapors is based on the thermal decomposition of silane ( $\text{SiH}_4$ ) at the substrate's surface. The silicon growth rate depends strongly on the adsorption of hydride species and hydrogen desorption. These very complex processes had been studied carefully by many authors.<sup>[BHBC88, GaGB90, GaKu91, Meye86, SFPR97, ShTK07, SSLW89, WuLi98]</sup> At low temperature ( $< 500^\circ\text{C}$ ), the growth rate is limited by the availability of dangling bonds which depends on the hydrogen desorption rate; at sufficiently high temperature ( $> 700^\circ\text{C}$ ) where hydrogen is completely desorbed, the growth rate is dependent on the adsorption rate of precursors (silane flux). At intermediate temperatures, the growth rate is controlled by the combination of hydrogen desorption and precursor chemisorption rates. These three regimes can be schematized as an Arrhenius plot in **Figure 4-3**. Experimental measurements of silicon growth rate as a function of temperature and silane flux had been demonstrated in the literature and confirmed this tendency.<sup>[BHBC88, GaKu91, LGK090]</sup>

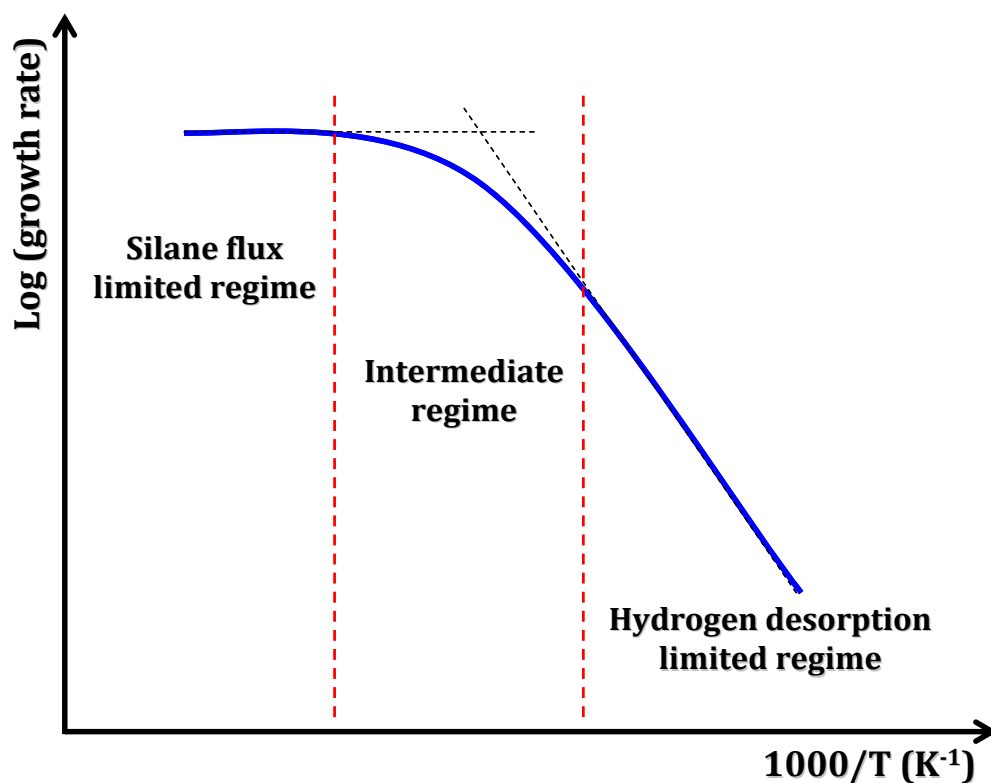
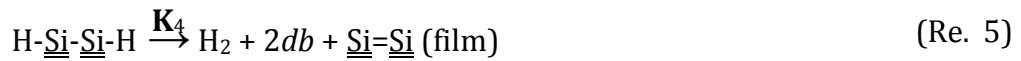


**Figure 4-3:** Three distinct regimes of silicon deposition rate under silane exposure in UHV/CVD conditions.

The silicon deposition kinetics is modelled by Gates *et al.* via a system of decomposition reactions:[GaGB90, GaKu91]



The reaction constant  $\mathbf{K}_i$  is defined as:

$$K_i = A_i e^{\frac{E_{ai}}{RT}} \quad (\text{Eq. 18})$$

where  $A_i$  is the pre-exponential term,  $E_{ai}$  the activation energy and  $R=8.314 \text{ JK}^{-1}\text{mol}^{-1}$  the gas constant. The last two reactions are assumed to happen in the same rate, with the same reaction constant  $K_4$ . These parameters can be found in the Ref. [GaGB90, GaKu91, SFPR97]. The symbol  $db$  is used for a dangling bond of a Si surface atom, and the number of surface bonds of a Si or H atom is indicated by single and double underlining, respectively. Based on these reactions, the silicon growth rate (GR) is expressed as follow:[GaKu91]

$$\text{GR} = 2K_1[\text{SiH}_4][db]^2 \quad (\text{Eq. 19})$$

Our calculation for the growth rate using equations and constants in Ref. [GaGB90, GaKu91, GuCG88, SFPR97] shows the same curves tendency with three regimes as explained above (see **Figure 4-4**). The given experimental measurements of the growth rate for a silane pressure of  $1.98 \times 10^{-4}$  Torr and  $6 \times 10^{-3}$  Torr in this figure show a good agreement with the simulation.

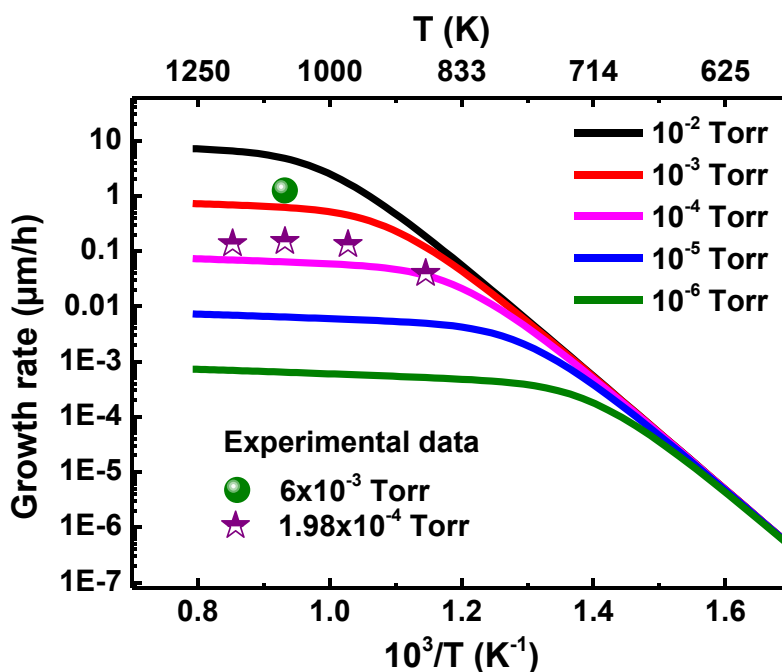


**Figure 4-4:** Simulation of silicon growth rate with different silane flux as a function of reversed temperature. At high temperature regime, growth rate is saturated and will be governed by silane flux. Higher flux gives faster growth.

#### 4.2.2 Growth conditions

The silicon growth sequence in our study is illustrated in **Figure 4-5**. The as-cleaned substrate is loaded to the growth chamber and is heated to 435°C (pyrometer). At this temperature, hydrogen starts to desorb and they leave dangling bonds behind (see the next paragraph for hydrogen desorption study). The surface is now reactive and risks to be recontaminated. The substrate is thus exposed under a very low flux of silane to prevent recontamination. The substrate is continued to be heated to the growth temperature  $T_g$ , silane flux is now regulated to a wanted flux and maintained constant during the growth. Extractor gauge is carefully turned off before sending silane so that it is not damaged by high gas pressure. Baratron gauge is used to monitor the chamber pressure during the growth. The growth temperature and pressure will be studied based on the simulated curve shown on **Figure 4-4**. After growth the temperature is quickly ramped down and the silane flux is immediately sent to the VENT (outgassing). The gas line will be purged for several minutes before resetting the silane flux back to zero.

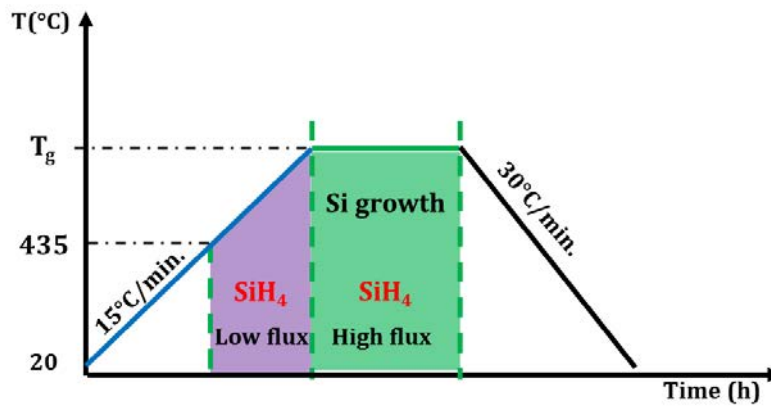


**Figure 4-5:** Silicon growth sequences.

Silicon growth using Riber UHV/CVD chamber can be operated in low pressure mode and high pressure mode, as the high pressure mode allows higher growth rate (see **Figure 4-4**). Switching between low pressure mode and high pressure mode can be done by using the by-pass of the turbo molecular pump as described in **Figure 4-6**. Big valve  $V_2$  allows high pumping capacity to keep high vacuum level in the growth chamber. Small valve  $V_1$  is connected to a by-pass system which allows weaker pumping capacity so that the pressure inside the chamber is high. Low pressure mode is set by closing  $V_1$  and opening  $V_2$  whereas high pressure mode is in operation when  $V_1$  is opened and  $V_2$  is closed.

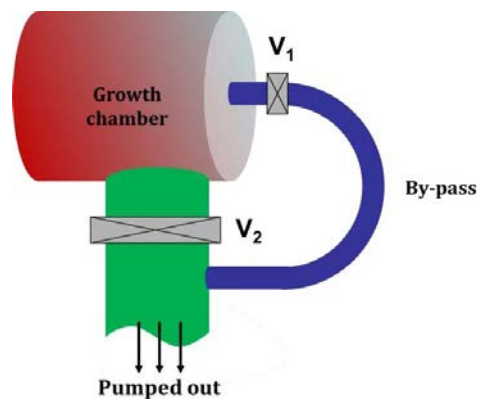


**Figure 4-6:** By-pass control for switching from low to high pressure mode. Low pressure mode:  $V_1$  closed and  $V_2$  opened, high pressure mode:  $V_1$  opened and  $V_2$  closed.

In the low pressure mode, the chamber pressure during the growth is maintained at  $1.98 \times 10^{-4}$  Torr. The growth temperature  $T_g$  has been studied from 600-800°C. **Figure 4-7** shows AFM images of the three 150 nm thick samples grown at 600 (a), 700 (b) and 800°C (c). The surface roughnesses measured in term of RMS are 6.05 nm, 0.16 nm and 0.30 nm, respectively. Silicon growth at 700°C is repeated several times and

we found that the surface flatness is reproducible, i.e. RMS around 2 Å. This RMS value is in the limit resolution of AFM and indicates a very smooth surface.

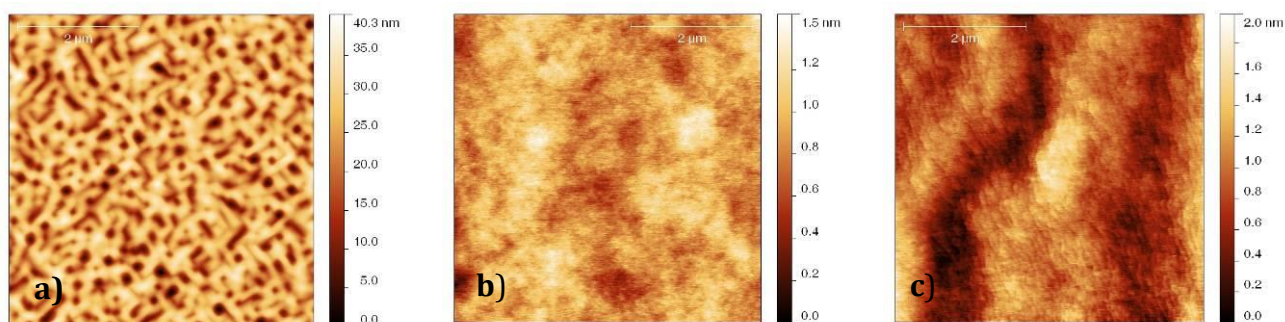


**Figure 4-7:**  $5 \times 5 \mu\text{m}^2$  AFM images of silicon homoepitaxial layers at  $T_g = 600^\circ\text{C}$  (a),  $700^\circ\text{C}$  (b),  $800^\circ\text{C}$  (c). RMS surface flatnesses are 6.05 nm (a), 0.16 nm (b) and 0.30 nm (c), respectively.

Passing to the high pressure mode, the silane pressure is set to  $6 \times 10^{-3}$  Torr, giving a streaky RHEED pattern. The streaky pattern is slightly changed to spotty when the temperature is reduced to  $700^\circ\text{C}$  which indicates rough surface. The growth conditions are then fixed at  $800^\circ\text{C}$  (pyro) and under a silane pressure of  $6 \times 10^{-3}$  Torr for the high pressure mode. **Figure 4-8** shows a comparison of the two samples grown at high pressure mode, sample (a) is grown at  $700^\circ\text{C}$  (pyrometer) and the (b) one is grown at  $800^\circ\text{C}$ . Surface RMS roughness is measured to be 10.78 nm (a) and 0.13 nm (b). A significant improve of the surface roughness is observed for the sample growth at  $800^\circ\text{C}$ .

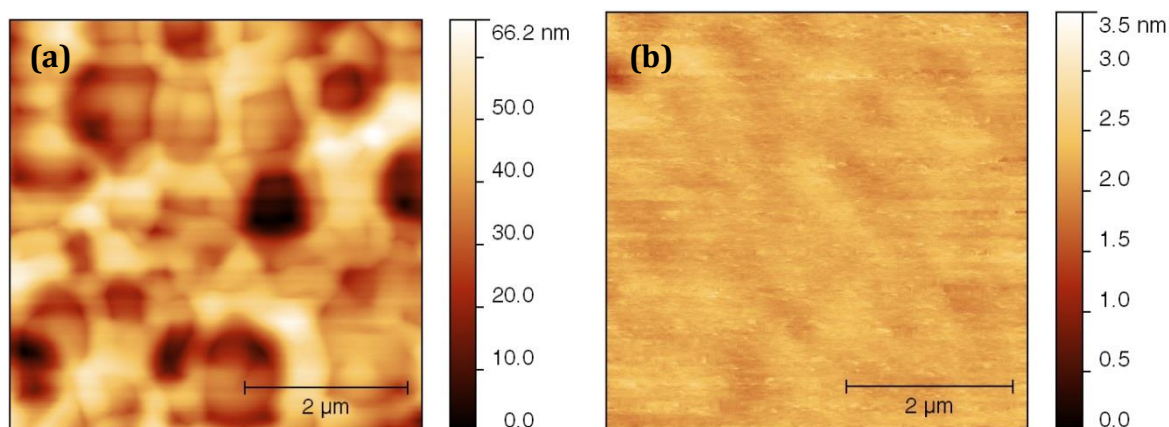


**Figure 4-8:**  $5 \times 5 \mu\text{m}^2$  AFM images of homoepitaxial Si growth at high pressure mode and growth temperature  $T_g = 700^\circ\text{C}$  (a) and  $800^\circ\text{C}$  (b). RMS surface roughness is measured to be 10.78 nm (a) and 0.13 nm (b).

For sample grown at 800°C (high pressure mode), AFM local scan (5x5  $\mu\text{m}^2$ ) gives a surface roughness of 0.13 nm which is in the limit uncertainty of AFM measurement and the observation at a larger region (20x20  $\mu\text{m}^2$ ) gives an RSM roughness of 0.15 nm (**Figure 4-9**). It confirms the perfect smoothness of the Si surface under this growth condition.

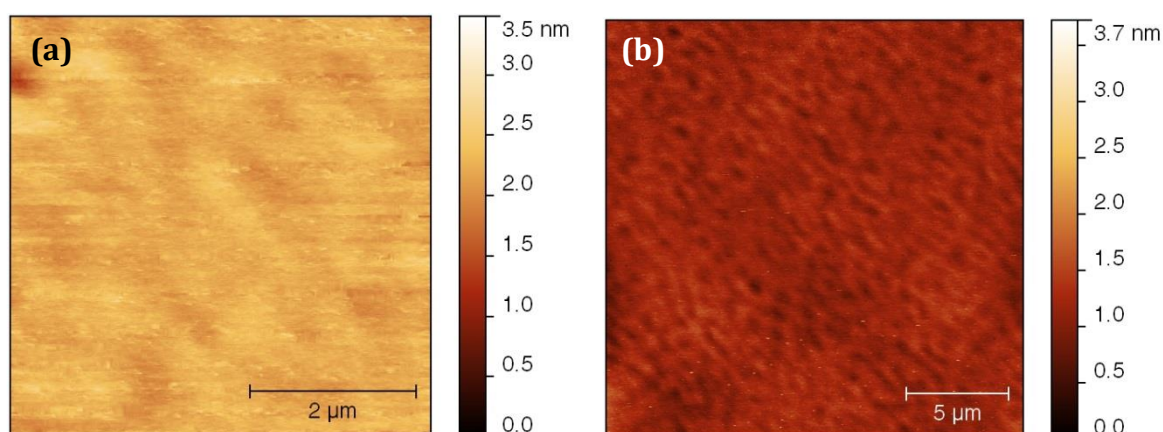


**Figure 4-9:** AFM images of silicon sample grown at high pressure mode (800°C pyro), (a) 5x5  $\mu\text{m}^2$ , RMS = 0.13 nm, (b) 20x20  $\mu\text{m}^2$ , RMS = 0.15 nm.

### 4.2.3 Control of hydrogenation on the Si (001) surface

#### *(a) Hydrogen desorption*

The desorption kinetics of hydrogen from Si (001) surface has been extensively studied by several authors.<sup>[GuCG88, KiBe89, Nami06, OrSm05, RGRA03, SSLW89]</sup> The detection of H<sub>2</sub> desorption from different hydride species (SiH<sub>x</sub>) is mainly based on Fourier-transform infrared spectroscopy and temperature-programmed desorption. Gupta *et al.* have claimed the desorption activation barriers of hydrogen from SiH and SiH<sub>2</sub> respectively are 65 kCal/mol (2.82 eV) and 43 kCal/mol (1.86 eV). Consequently, hydrogen from SiH<sub>2</sub> species desorbs between 640 and 700 K (367 – 427°C, this desorption peak is denoted as  $\beta_2$ ), whereas desorption of H<sub>2</sub> from SiH species takes place between 720 and 800 K (447 – 527°C, this desorption peak is denoted  $\beta_1$ ).<sup>[GuCG88]</sup> Very few studies were performed about the hydrogen desorption from SiH<sub>3</sub> species on Si (001) surface because it's very close to  $\beta_2$ . However, this later have been studied by several authors on Si (111) 7x7 reconstructed surface.<sup>[KMAC88, MoMT95, ScHe83]</sup> According to the measurement results of Schulze *et al.* on Si (111) surface, the desorption peak of H<sub>2</sub> from SiH species ( $\beta_1$ ) begins

at 450°C and completely desorbed at 630°C, whereas the H<sub>2</sub> desorption from SiH<sub>2</sub> and SiH<sub>3</sub> ( $\beta_2$  and  $\beta_3$ ) takes place between 300 – 500°C. For temperature below 200°C one can observe a wide desorption peak of the sample holder.<sup>[ScHe83]</sup>

Coming back to our studies, 2-inch silicon wafers are prepared using HF-last process to cover the surface with a mono atomic layer of hydrogen. After loading into the reactor chamber on a molybdenum holder, the substrate is heated by a PBN oven which works in the [50°C – 1300°C] range (thermal couple temperature). The wafer degassing is studied using mass spectrometer and Extractor gauge (which works in the pressure range of 10<sup>-10</sup> – 10<sup>-3</sup> Torr) inside the reactor chamber. The temperature is measured by a near infrared pyrometer working in the range of 575 – 1000°C with the silicon emissivity setting up to be  $\epsilon \approx 0.65$  and a Eurotherm thermal couple installed near the oven. **Figure 4-10** shows the partial pressures as determined by the mass spectrometer's measurement during the substrate degassing from room temperature to 700°C. Three main contributions are identified, namely H<sub>2</sub>, (OH, H<sub>2</sub>O) compounds and CO. Water is first desorbed around 100°C, hydrogen is continuously desorbed from RT to 700°C; carbon starts to desorb from 570°C in the form of CO.

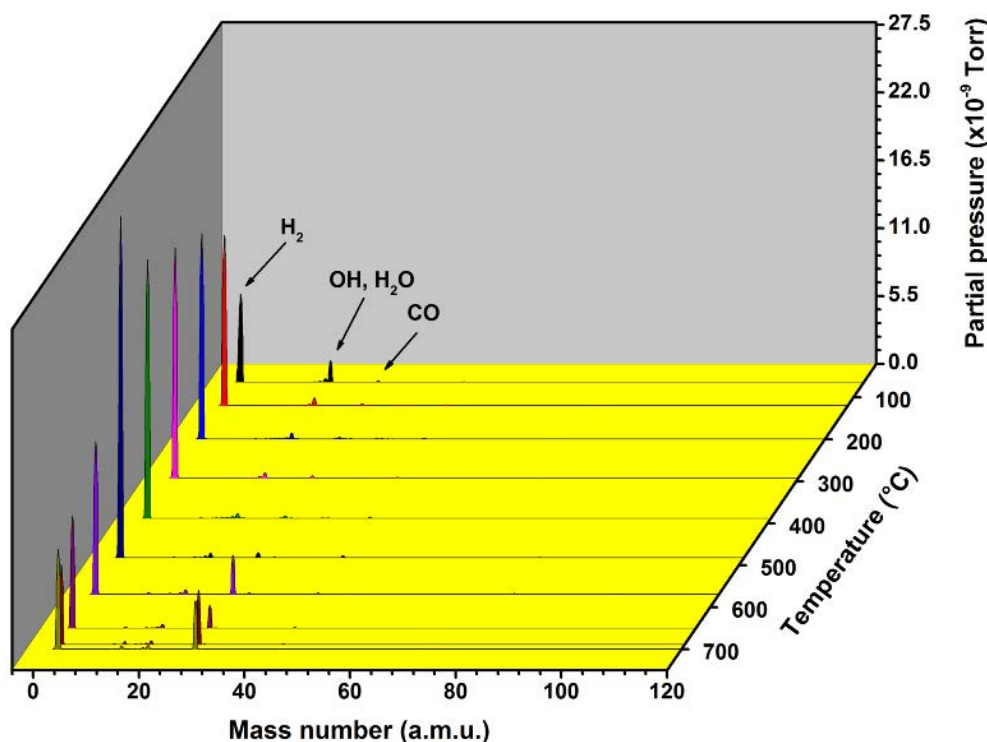


**Figure 4-10:** Mass spectrometer monitoring of {substrate + molybdenum holder} degassing prior to grow.

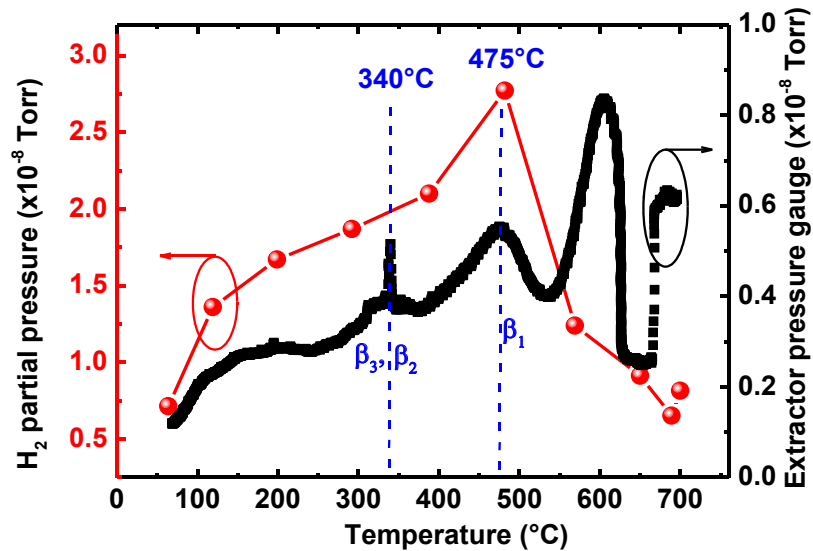


**Figure 4-11:** Degassing curves of clean - hydrogen terminated silicon surface. The red curve presents the H<sub>2</sub> desorption (in its partial pressure, recorded by mass spectrometer), the black curve shows the total pressure in the growth chamber, recorded by Extractor gauge. Two desorption peaks  $\beta_1$  and  $\beta_2$  correspond to the hydrogen desorption from mono- and di-hydride (SiH, SiH<sub>2</sub>) respectively.  $\beta_3$  corresponds to the desorption of hydrogen from SiH<sub>3</sub>. This peak is usually overlapped by the  $\beta_2$ .

The substrate degassing is monitored in the same time using the Extractor gauge. **Figure 4-11** shows the evolution of H<sub>2</sub> partial pressure measured by the mass spectrometer (red spherical connect curve) and the Extractor gauge pressure (black curve) with respect to degassing temperature (pyrometer). The two distinct desorption peaks  $\beta_1$  (475°C) and  $\beta_2$  (340°C) as mentioned previously are clearly identified on this figure. These peaks are in good agreement with the literature. The third peak in the Extractor gauge curve may be due to the sum of total pressure of different species that are desorbed at higher temperature (CO, CO<sub>2</sub> ...). The origin of these contaminants is not clarified in this work. Both Si wafer and molybdenum holder can be responsible for this degassing. In order to limit the effects of this carbon related emission on silicon nucleation, molybdenum holders were regularly heated at high temperature before Si growth, and a low pressure of silane is sent in the chamber at 435°C (pyrometer) before each growth (as explained in the previous section).

### ***(b) Surface passivation in-situ***

The motivation of this study is to protect the silicon homoepitaxial layer surface by hydrogen during the transfer to the MBE chamber to limit the possible

recontamination. In the constant effort to control the initial Si surface, the aim of this part is to evaluate the possibility to passivate in-situ the Si surface with hydrogen before the UHV transfer. In this study we have used silane to produce atomic hydrogen coverage for the passivation because molecular hydrogen  $H_2$  has an extremely low sticking coefficient and it requires very high temperature to be cracked.<sup>[BrKH96]</sup> The surface passivation sequence is presented in **Figure 4-12**.

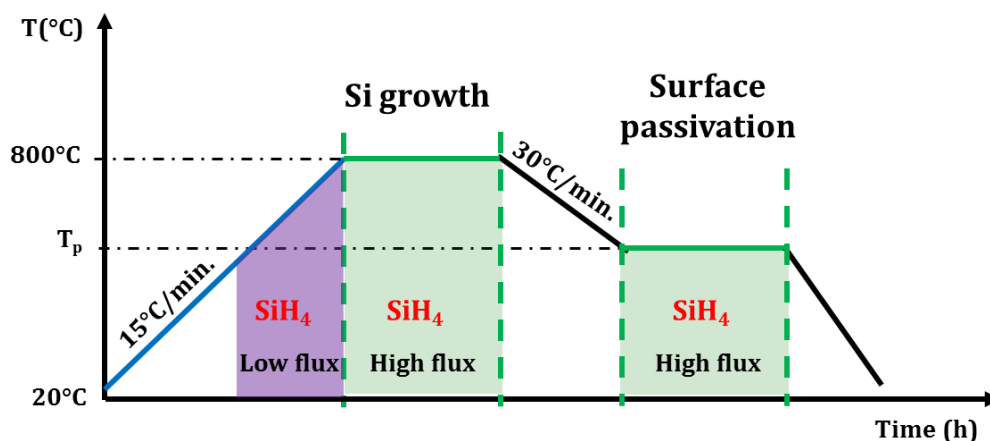


**Figure 4-12:** Silicon surface passivation sequences.

Both low pressure mode and high pressure mode experiments have been studied using the same sequences as described in **Figure 4-12**. After deposition, silane flux is switched off and the temperature is ramped down to the passivation temperature. Three passivation temperatures ( $T_p$ ) have been chosen in this study: before the hydrogen desorption peak, right at the peak and after the peak (240°C, 340°C and 440°C, respectively). The hydrogen desorption peak mentioned here corresponds to the  $\beta_2$  in **Figure 4-11**. The silane flux is opened again at  $T_p$  during 1 hour and the silane pressure is the same as in the growth stage. At this low temperature regime, silicon deposition rate is extremely low (see the growth rate curve in **Figure 4-4**), but  $SiH_x$  species are cracked to provide atomic hydrogen to cover the surface.<sup>[SFPR97]</sup> After passivation the temperature is quickly quenched to room temperature. To make sure that the surface is well covered with hydrogen, the substrate's temperature is once again ramped to 700°C for degassing. Mass spectroscopy observation records the desorption of  $H_2$  as presented in **Figure 4-13**. For this sample, the passivation temperature is 240°C.

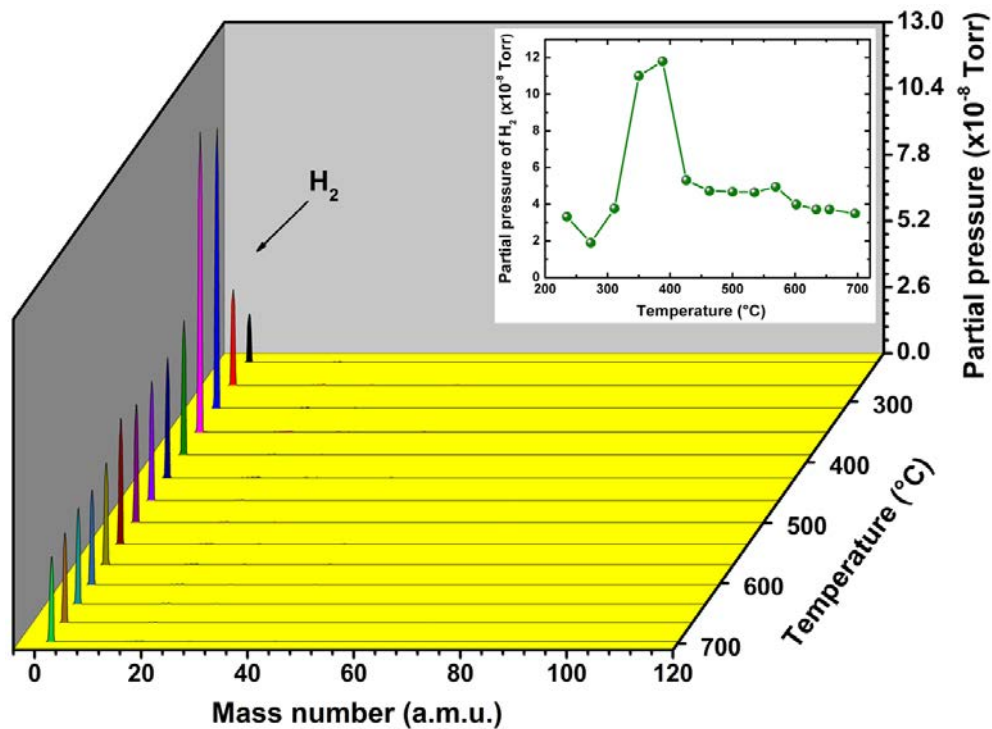


**Figure 4-13:** Degassing of hydrogen terminated surface – recorded by mass spectrometer. Inset figure (green curve) shows the evolution of the  $H_2$  peak with respect to the temperature. The desorption peak around  $360^\circ\text{C}$  corresponds to the  $\beta_2$  which is the desorption peak of hydrogen from  $\text{SiH}_2$ .

**Figure 4-13** inset shows only the evolution of  $H_2$  peak with respect to temperature (pyrometer). From this graph we can observe a clear desorption peak of hydrogen around  $360^\circ\text{C}$ . This temperature corresponds to the desorption of hydrogen from  $\text{SiH}_2$  ( $\beta_2$ ), as observed in **Figure 4-11**. Notice that the activation energy of the formation of available adsorption sites during CVD growth of silicon using silane on a  $2\times 1$  reconstructed surface, covered by  $\text{H-Si-Si-H}$ , is around 2.1-2.2 eV, which is very close to the activation energy of hydrogen desorption from  $\text{SiH}_2$ . That means the above observed hydrogen desorption probably results from a surface covered by  $\text{SiH}_2$  or  $\text{Si}_2\text{H}_2$ . In this figure, one can see that hydrogen is the only specie found from the degassing. Carbon and oxide traces are not found even at very high temperature, due to the previous thermal heating before the Si growth.

**Figure 4-14** (a, b and c) show AFM scans of the three samples after growth at  $700^\circ\text{C}$  (low pressure mode) and then passivated at  $T_P = 240^\circ\text{C}$ ,  $340^\circ\text{C}$  and  $440^\circ\text{C}$ , respectively. The sample with the passivation temperature before the hydrogen desorption peak ( $240^\circ\text{C}$ ) reveals a very smooth surface (RMS roughness = 0.25 nm), whereas the other 2 samples reveal significantly rough surface. At low temperature,

hydrogen is directly stuck to the surface and therefore inhibits the growth. At higher temperature, the hydrogen desorption allows the growth of Si which is 3D at this growth temperature (far from the ideal one).

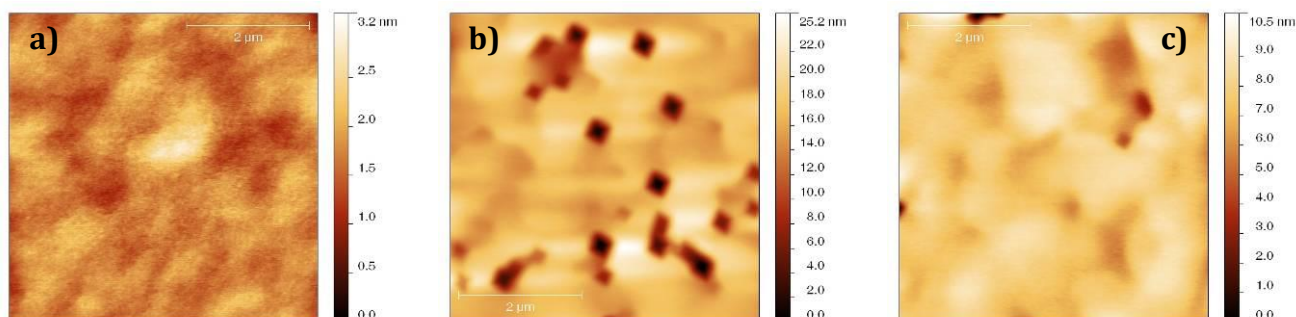


**Figure 4-14:** AFM images ( $5 \times 5 \mu\text{m}^2$ ) of samples passivated by hydrogen at  $T_p = 240^\circ\text{C}$  (a),  $340^\circ\text{C}$  (b) and  $440^\circ\text{C}$  (c). The RMS surface roughness is measured to be 0.25 nm (a), 3.06 nm (b) and 0.87 nm (c), respectively.

High pressure mode growth and passivation have also been studied. **Figure 4-15** shows AFM image of a silicon sample grown at  $800^\circ\text{C}$  (high pressure mode) and hydrogen passivated at  $240^\circ\text{C}$  (pyrometer). RMS surface roughness is measured to be 0.21 nm. These observations confirm the good hydrogenation of the surface preparation and surface passivation, which can be used for further defects-free growth of III-V compounds since stacking faults related defects in III-V epilayers are generally originated from contaminants on the Si surface. For the annihilation of anti-phase domains, it is of paramount importance to get double-height atomic steps on the Si surface. Next paragraph will mention the Si surface study using RHEED patterns.

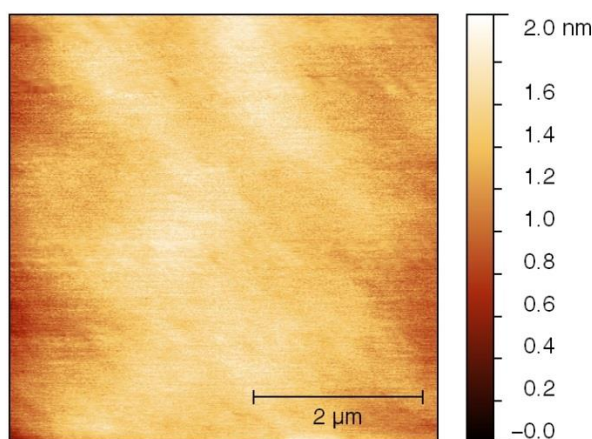


**Figure 4-15:**  $5 \times 5 \mu\text{m}^2$  AFM image of silicon grown at  $800^\circ\text{C}$  (high pressure mode) and hydrogen passivated at  $240^\circ\text{C}$  (pyrometer). RMS roughness is measured to be 0.21 nm.

#### 4.2.4 Silicon surface step doubling

##### *(a) The silicon surface*

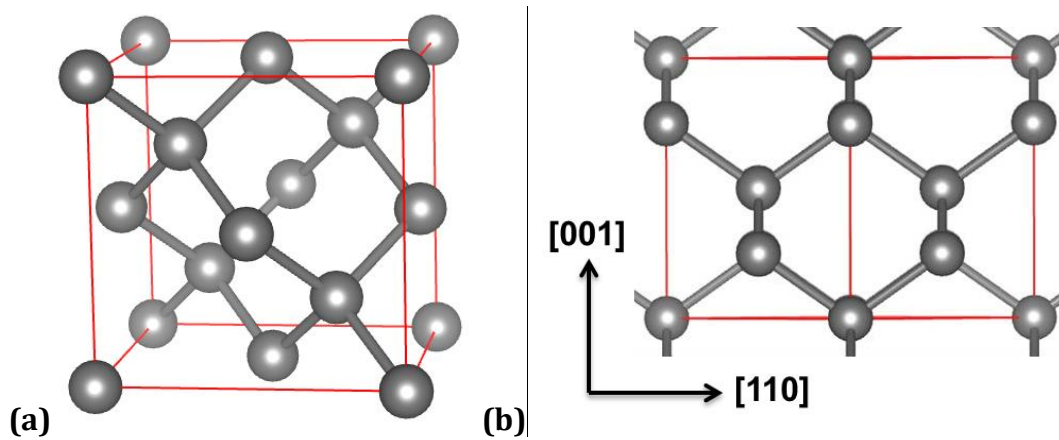


**Figure 4-16:** Sketch of a crystal unit cell of silicon diamond structure, (a) bird-eye view, (b) [110] direction projection.

The silicon crystals have their atoms arranged in diamond cubic structure and can be imagined as two equivalent interpenetrating FCC unit cells, shifted by  $(\frac{1}{4}, \frac{1}{4}, \frac{1}{4})$  from one to another (see **Figure 4-16**). The Si (001) surface always presents an unintentional miscut which leads to the presence of numerous atomic steps. When the wafer is cut, the Si-Si bonds at the cutting plan are broken. These Si atoms are now at the top surface of the wafer and present dangling bonds. The wafer cleaning process described in the first paragraph cover these dangling bonds with hydrogen atoms which should be thermally desorbed in-situ and let the dangling bonds behind (see **Figure 4-17** (a)). The reduction of surface energy encourages the top silicon atoms to rearrange themselves by dimerization to minimize the number of dangling bonds. This procedure is called the surface reconstruction. The type of surface reconstruction of the top atoms depends on the arrangement of dangling bonds. A clean surface of a Si (001) wafer consists of wide planar terraces of Si-Si dimer pairs separated by irregularly spaced monoatomic steps. The dimerization axis of the Si-Si bonds can be parallel or perpendicular to the step edges depending on the orientation of the unit cells directly below them. By each single atomic step transition, the dimerization axis will rotate by 90 degrees, forming alternating terraces of parallel and perpendicular Si-Si dimers. **Figure 4-17** (b) represents such a silicon surface reconstruction with alternating dimer axis. We denote type-A terraces for the dimers parallel to the step edges and type-B terraces for those perpendicular to the step edges (Kroemer's terminology).<sup>[Kroe87]</sup>

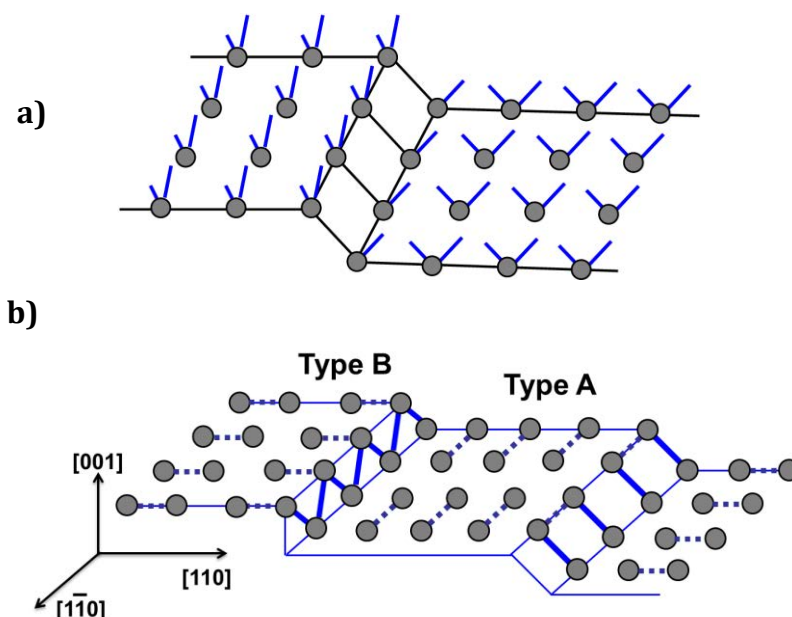


**Figure 4-17:** Schema of single atomic steps on a Si (001) surface. a) Dangling bonds on top Si atoms b) Si surface reconstruction by dimer pairing. The dimerization axis is rotated by  $90^\circ$  after each single step transition.<sup>[SSMN89]</sup>

Such a silicon surface with alternating terraces of perpendicular and parallel dimers is called double domain surface and is characteristic by the coexistence of  $2 \times 1$  (type-A terraces) and  $1 \times 2$  (type-B terraces) reconstructions. Any surface with an odd number of monolayer height (one monolayer height of a single element crystal cell =  $a_0/4$ ) presents the same characteristic. On the contrary, a double-atomic height stepped silicon surface has only one type of terrace (single domain) which is represented by the dimer parallel or perpendicular to the step edges (**Figure 4-18**). It is reported by Kroemer that biatomic stepped surface with Si dimers parallel to the step edges is more energetically favorable than the one with the dimerization axis perpendicular to the edges <sup>[Kroe87]</sup>. According to Kroemer, such a single domain surface can be achieved by heating the substrate at very high temperature (over  $1000^\circ\text{C}$ ) and in a long time (typically 20 minutes). At such a high temperature, atoms from B-type edges would diffuse toward A-type edges until forming a double step which is bounded by type-A edges. Chadi had also calculated the formation energies of the single and double layer (for both type A and B) by semi-empirical tight-binding-based total-energy calculations and found that on a vicinal surface with miscut towards  $[110]$  or  $[1-10]$  direction, double layer of type A is more favorable than type B because of its lower formation energy.<sup>[Chad87]</sup> Calculations performed by Chadi gave the formation energies per unit length of single and double steps of both type A and B as follow (note: Chadi's notation

of type-A, type-B is different from the notation of Kroemer, here we use the Kroemer's convention to denote type-A and type-B steps, with A-type dimers parallel to the step edges and B-type perpendicular to the step edges):

$$E(S_A) \approx (0.15 \pm 0.03 \text{ eV})/a \quad (\text{Eq. 20})$$

$$E(S_B) \approx (0.01 \pm 0.01 \text{ eV})/a \quad (\text{Eq. 21})$$

$$E(D_A) \approx (0.05 \pm 0.02 \text{ eV})/a \quad (\text{Eq. 22})$$

$$E(D_B) \approx (0.54 \pm 0.10 \text{ eV})/a \quad (\text{Eq. 23})$$

where  $E(S_A)$ ,  $E(S_B)$  respectively the formation energies per unit length of type-A and type-B single layers;  $E(D_A)$ ,  $E(D_B)$  respectively the formation energies per unit length of type-A and type-B double layers; and  $a \approx 3.85 \text{ \AA}$  the  $1 \times 1$  surface lattice constant.

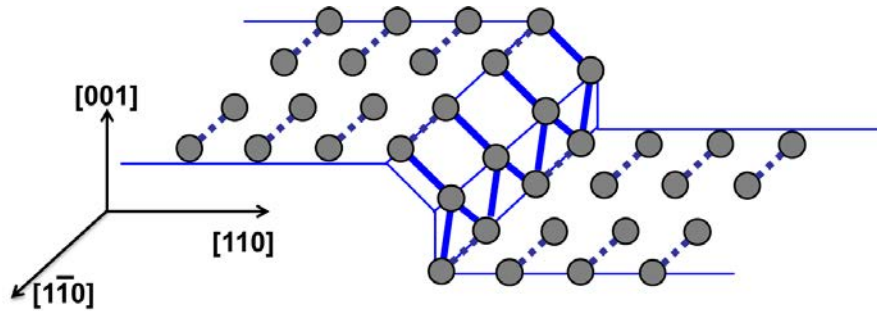


**Figure 4-18:**  $2 \times 1$  reconstruction of Si (001) double atomic step surface with dimerization axis parallel to the step edges.

At thermal equilibrium and room temperature, the Si (001) surface is composed of equivalent contribution of type-A and type-B terraces (surface coverage about 50%) as reported by Alerhand *et al.*<sup>[ABJ<sup>V</sup>90]</sup> They claimed a phase transition from a double domain to single domain surface dependant on the anneal temperature and miscut angle. Many other authors also reported the achievement of step doubling by thermal treatment.<sup>[Aslh86, Dolc89, INZI92, Kapl80, PeTe91, SKNH87]</sup>

### ***(b) RHEED monitoring***

Experiments have been performed on Si (001) substrates with different miscut angle ( $0.15 \pm 0.5^\circ$ ,  $1^\circ$ ,  $2^\circ$ ,  $4^\circ$  and  $6^\circ$ ) toward the [110] direction. A RHEED system with electron beam incident angle of about  $0.3^\circ$  with respect to the horizontal direction and working at 25-29 kV and 1.5 A is setup to monitor the real-time growth. The RHEED patterns have been recorded before, during and after growth via a CMOS high definition

camera. Note that the intensity of the specular spot during the growth is limited by the electron diffusion due to the high pressure.

On nominal substrates, before heating, the Si surface presents  $1\times 1$  RHEED patterns which indicate a clean and hydrogenated surface (**Figure 4-19**). After heated up to  $900^{\circ}\text{C}$ , the surface was reconstructing to  $2\times 1$  for the first pack of 25 wafers (as reported in **Figure 4-20** a) and b). For the other packs of wafers, we could not observe the  $2\times 1$  reconstruction but a mixture of  $2\times 1$  and  $1\times 2$  is regularly present which indicates double domain surface (as shown in **Figure 4-20** c and d). This suggests that a selection of nominal substrates with an appropriate residual miscut is possible for the formation of single domain surface. The streaky patterns confirm a clean and smooth surface. This is one of indicators to evaluate the chemical cleaning process.

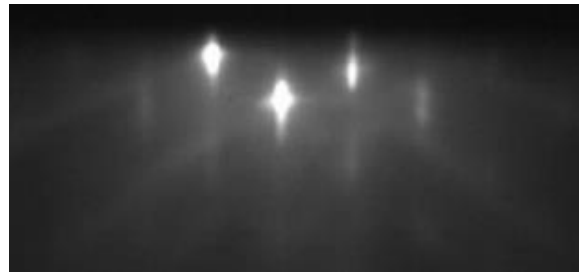


**Figure 4-19:**  $1\times 1$  RHEED pattern of the as-prepared Si (001) surface.

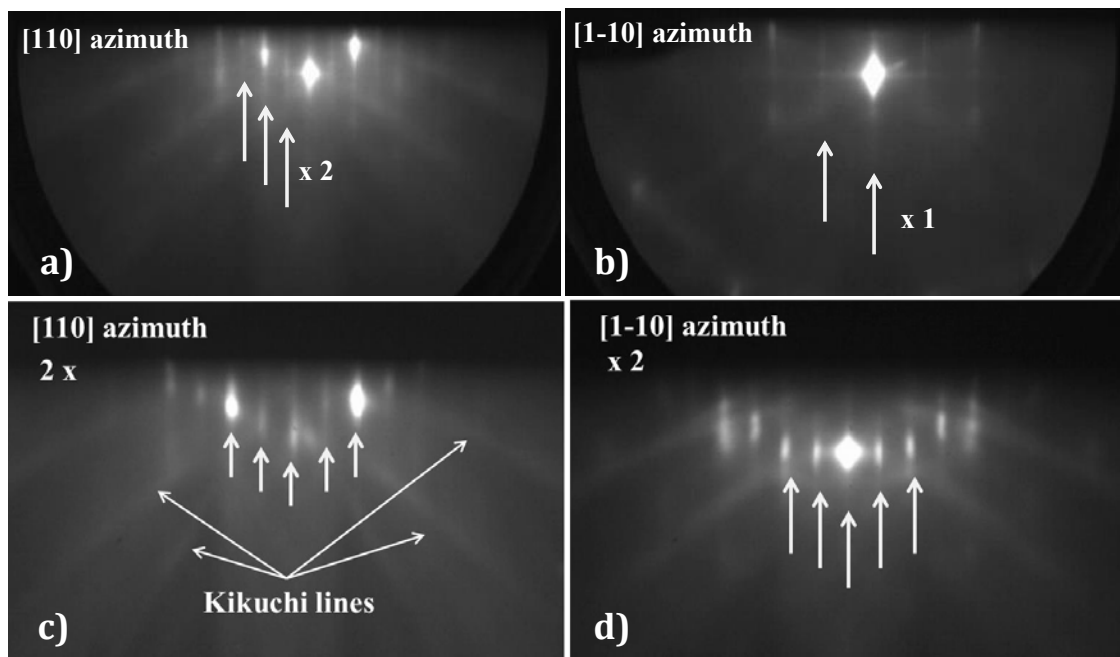


**Figure 4-20:**  $2\times 1$  reconstruction surface after heated to  $900^{\circ}\text{C}$  for the first pack of 25 wafers (a and b). For other packs, a mixture of  $2\times 1$  and  $1\times 2$  reconstructions is present which is characteristic of a double domain surface (c and d).

Considering the RHEED patterns for  $6^\circ$ -off substrates, we observed a  $2 \times n$  pattern instead of  $2 \times 1$ , with  $n \approx 7$  (**Figure 4-21**). The calculation of  $n$  is reported in **Figure 4-22** with  $n = L/l$ . Average value of  $l$  and  $L$  are measured to be 8.13 and 57.42 (arbitrary units) respectively. This is typically found on vicinal surfaces with bi-atomic high steps as reported by Zhu *et al.* [ZhBA99]. The  $2 \times$  pattern is observed when the electron beam is parallel to the  $[110]$  direction (perpendicular to the step edges) while the  $\times n$  pattern is observed in the  $[1-10]$  direction (parallel to the step edges) (**Figure 4-23**). The  $\times n$  pattern is the result of the diffraction from the grating like staircase steps, as explained by Zhu *et al.* [ZhBA99]

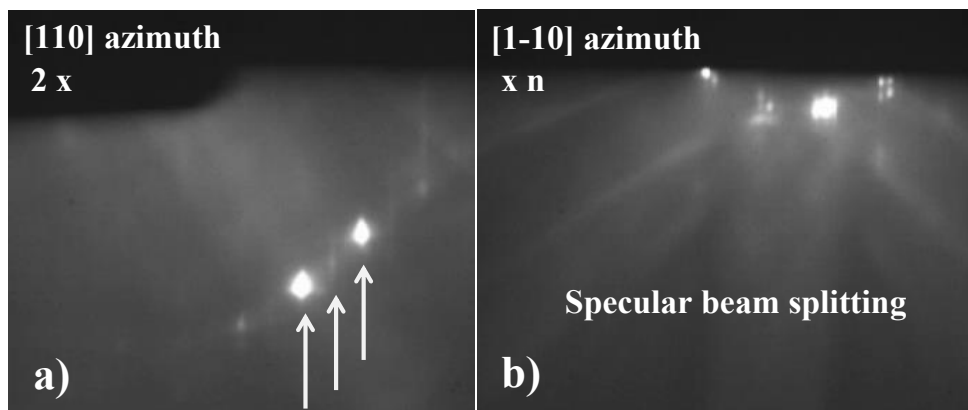


**Figure 4-21:**  $2 \times n$  RHEED patterns from a single domain composed from bi-atomic height stepped Si surface. Fig. (b) shows the splitting of the diffraction spot which is due to the grating like steps on the surface.

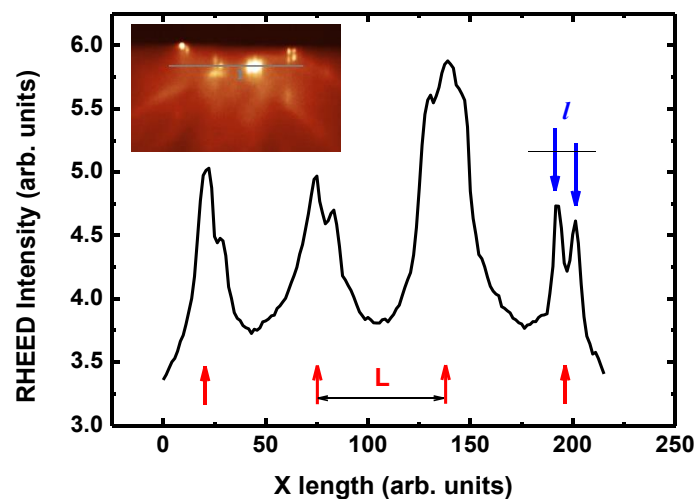


**Figure 4-22 :** Cross profile analysis of the RHEED pattern. Red arrows indicate the diffraction spots from the surface lattice along  $[110]$  direction, blue arrows indicate the diffraction spots from the steps length (grating like). Calculation from average  $l$  and  $L$  gives  $n=L/l=7.06$ . Inset shows the RHEED pattern in which the profile is extracted.

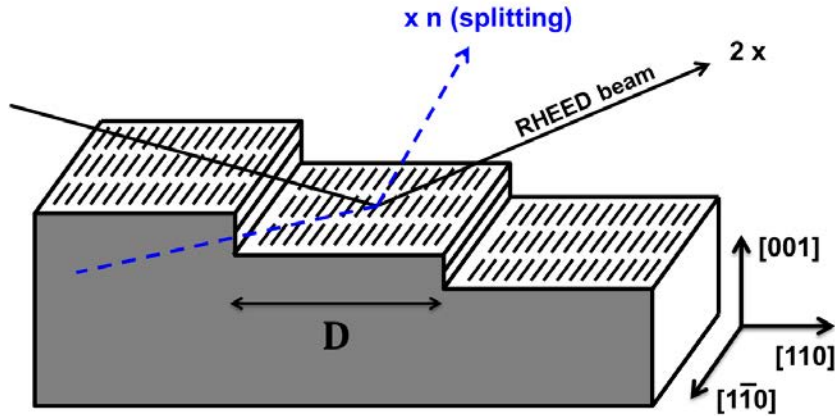


**Figure 4-23:** Schema of a perfect grating like staircase double atomic stepped surface.

Since  $l$  is proportional to  $2\pi/D$  where  $D$  is the terraces length, and  $L$  is proportional to  $2\pi/d$  where  $d$  is the lattice parameter of silicon in the direction  $[110]$ , that means  $d = a_{\text{Si}[110]} = a_0 / \sqrt{2} = 0.384$  nm. A simple relation  $d/D = l/L$  allows us to calculate the terraces length between atomic steps:  $D = \frac{d \times L}{l} = d \times n = 2.69$  nm. This length corresponds to a double-height atomic stepped surface which is very close to the theoretical value calculated by the equation (Eq. 24). Calculated terrace lengths on double and mono atomic stepped surface are reported in the **Table 4-3**.

$$\tan \theta_{\text{miscut}} = \frac{\text{step\_height}}{\text{step\_length}} \quad (\text{Eq. 24})$$

**Table 4-3:** Terraces length on double stepped and mono-stepped silicon surface for different miscut angle.

	0.15°	1°	2°	4°	6°
<b>Mono step</b>	51.86 nm	7.78 nm	3.89 nm	1.94 nm	1.29 nm
<b>Double step</b>	103.72 nm	15.56 nm	7.78 nm	3.88 nm	<b>2.58 nm</b>

As mentioned before, a bi-stepped and smooth surface is expected for further growth of defects-free GaP nanolayers. Different mis-oriented angle substrates (from 0.15° to 6°) are subjected to study but 6°-off substrate is the only one who evidences both of our two criteria. Other substrates reveal always a mixture of 2×1 and 1×2 (or 2×2 as language abuse) RHEED patterns which is the signature of double domain surface. As presented in **Figure 4-24**, AFM RMS surface roughness is plotted with

respect to substrate's miscut angle. The green spherical connected curve and the black starred connected curve present the RMS measurement on large scan  $50 \times 50 \mu\text{m}^2$  and small scan  $5 \times 5 \mu\text{m}^2$ , respectively ( $1 \times 1 \mu\text{m}^2$  AFM images show RMS roughness around  $2 \text{ \AA}$  for all samples).

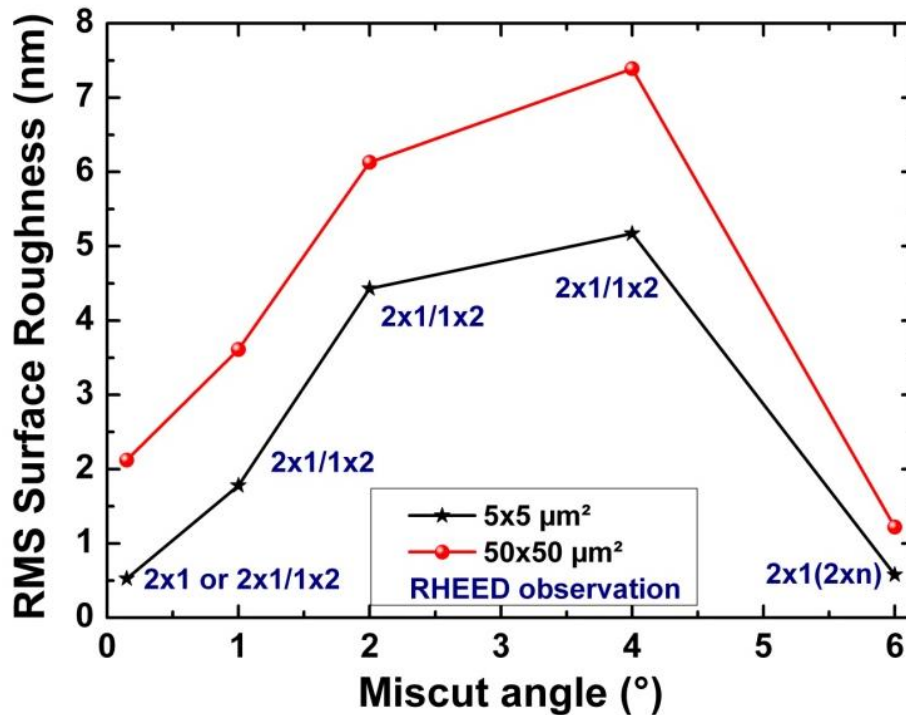


**Figure 4-24** : AFM RMS roughness versus miscut angle. The  $6^\circ$  off substrates reveal a smooth and bi-stepped surface. Other substrates present mono stepped surface as characterized by the presence of  $2 \times 1$  and  $1 \times 2$  mix reconstructions.

Highly rough surface is observed for substrates with 4 degrees off-cut. Nominal substrate ( $0.15^\circ$  off-cut) reveals a smooth surface but ' $2 \times 2$ ' RHEED pattern is obtained showing bi-domain surface which is not suitable for APD-free growth of GaP.

AFM images of these samples are presented in **Figure 4-25**. The misorientation angle is noted on each image. **Figure 4-25** (b) is a derivation of the figure (a) which shows the atomic steps contrast on the surface. Height measurement of these steps reveals monoatomic high steps. Atomic steps are not visible on other samples because the terraces length is shorter than the AFM tip diameter ( $\sim 20 \text{ nm}$ ) (see **Table 4-3**). The  $6^\circ$ -off surface (f) presents a similar surface roughness as on nominal one. Some visible pits are believed to be suppressed by annealing. Works are in progress to clarify this point and will be carefully described in the thesis of T. Quinci.

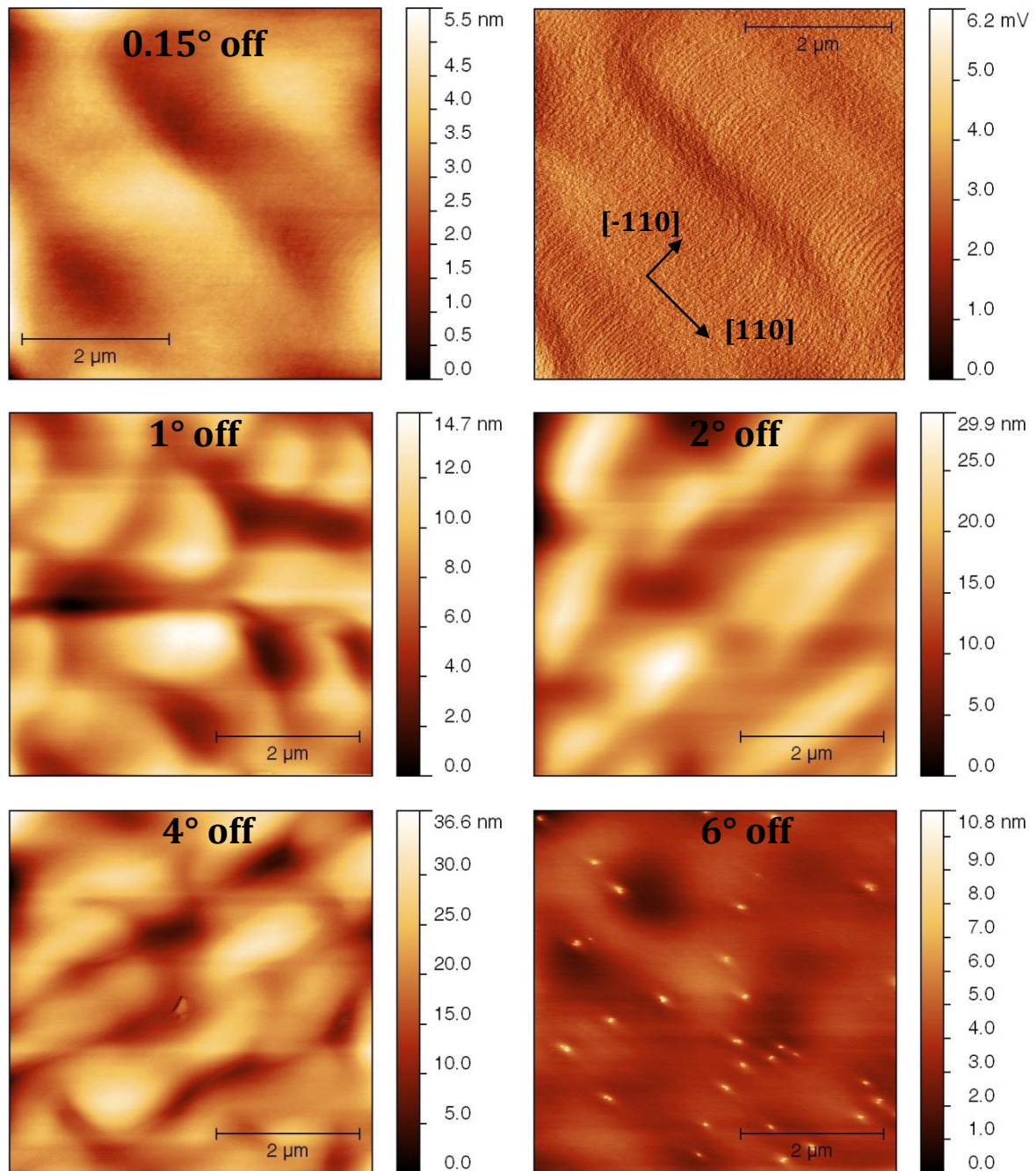


**Figure 4-25:**  $5 \times 5 \mu\text{m}^2$  AFM images of silicon homoepitaxial growth at high pressure mode, with different misorientation angle ( $0.15^\circ$  -  $6^\circ$  off towards  $[110]$  direction). Figure (b) is a derivation of the figure (a) to show the contrast of atomic steps on this surface. RMS roughness for (a), (c), (d), (e) and (f) are 0.7 nm, 2.4 nm, 4.4 nm, 5.4 nm and 0.67 nm, respectively.

### 4.3 Summary

We have successfully optimized the silicon cleaning process which consists in dilute HF dipping and UV/O<sub>3</sub> oxidation. This new cleaning method is very simple and

reproducible. Comparing to RCA like method which is very time consumed (several hours), this efficient process requires a very short time to prepare (1 hour maximum).

Smooth, single domain surface and defect-free Si homoepitaxial layer have been demonstrated on 6° off-cut substrates as observed by RHEED patterns. This is important for further growth of high structural perfection GaP(N) nanolayers (free from planar defects such as anti-phase domains and micro-twins).

Smooth and passivated surface after silicon deposition is successfully obtained. Silicon surface is covered with hydrogen in the form of SiH<sub>2</sub> and no traces of carbon or oxide can be found from mass spectrometer monitoring.

## REFERENCES

- [ABJV90] ALERHAND, O. L.; BERKER, A. Nihat; JOANNOPOULOS, J. D.; VANDERBILT, David; HAMERS, R. J.; DEMUTH, J. E.: In: *Physical Review Letters* **64** (1990), No. 20, pp. 2406–2409
- [AHHS04] ABBADIE, A.; HARTMANN, J.M.; HOLLIGER, P.; SÉMÉRIA, M.N.; BESSON, P.; GENTILE, P.: In: *Applied Surface Science* **225** (2004), No. 1–4, pp. 256–266
- [Aslh86] ASPNES, D. E.; IHM, J.: In: *Physical Review Letters* **57** (1986), No. 24, pp. 3054–3057
- [BBPS77] BEAN, J. C.; BECKER, G. E.; PETROFF, P. M.; SEIDEL, T. E.: In: *Journal of Applied Physics* **48** (1977), No. 3, pp. 907–913
- [BHBC88] BUSS, Richard J.; HO, Pauline; BREILAND, William G.; COLTRIN, Michael E.: In: *Journal of Applied Physics* **63** (1988), No. 8, pp. 2808–2819
- [BoMR97] BODNAR, S.; MORIN, C.; REGOLINI, J.L.: In: *Thin Solid Films* **294** (1997), No. 1–2, pp. 11–14
- [BrKH96] BRATU, P.; KOMPA, K.L.; HÖFER, U.: In: *Chemical Physics Letters* **251** (1996), No. 1–2, pp. 1–7
- [Chad87] CHADI, D. J.: In: *Physical Review Letters* **59** (1987), No. 15, pp. 1691–1694
- [Cres06] CRESSLER, John D.: *Silicon Heterostructure Handbook: Materials, Fabrication, Devices, Circuits and Applications of SiGe and Si Strained-Layer Epitaxy*: CRC Press, 2006 — ISBN 9781420026580
- [DoIc89] DOI, Takahisa; ICHIKAWA, Masakazu.: In: *Journal of Crystal Growth* **95** (1989), No. 1–4, pp. 468–471
- [GaGB90] GATES, S. M.; GREENLIEF, C. M.; BEACH, D. B.: In: *The Journal of Chemical Physics* **93** (1990), No. 10, pp. 7493–7503
- [GaKu91] GATES, S. M.; KULKARNI, S. K.: In: *Applied Physics Letters* **58** (1991), No. 25, pp. 2963–2965
- [GiGW85] GIBBONS, J. F.; GRONET, C. M.; WILLIAMS, K. E.: In: *Applied Physics Letters* **47** (1985), No. 7, pp. 721–723
- [GuCG88] GUPTA, P.; COLVIN, V. L.; GEORGE, S. M.: In: *Physical Review B* **37** (1988), No. 14, pp. 8234–8243
- [HaOt01] HABUKA, Hitoshi; OTSUKA, Toru: U.S. Patent.
- [INZI92] ITOH, H.; NARUI, S.; ZHANG, Z.; ICHONOKAWA, T.: In: *Surface Science* **277** (1992), No. 3, pp. L70–L76
- [IsSh86] ISHIZAKA, Akitoshi; SHIRAKI, Yasuhiro.: In: *Journal of The Electrochemical Society* **133** (1986), No. 4, pp. 666–671
- [Kapl80] KAPLAN, Ray.: In: *Surface Science Letters* **93** (1980), No. 1, p. A91

- [KePu70] KERN, W.; PUOTINEN, D.A.: In: *RCA Review* **31** (1970), pp. 187–206
- [KiBe89] KISIELOWSKI-KEMMERICH, C.; BEYER, W.: In: *Journal of Applied Physics* **66** (1989), No. 2, pp. 552–558
- [KMAC88] KOEHLER, B. G.; MAK, C. H.; ARTHUR, D. A.; COON, P. A.; GEORGE, S. M.: In: *The Journal of Chemical Physics* **89** (1988), No. 3, pp. 1709–1718
- [Kroe87] KROEMER, Herbert.: In: *Journal of Crystal Growth* **81** (1987), No. 1-4, pp. 193–204
- [LGKO90] LIEHR, M.; GREENLIEF, C. M.; KASI, S. R.; OFFENBERG, M.: In: *Applied Physics Letters* **56** (1990), No. 7, pp. 629–631
- [Meye86] MEYERSON, B. S.: In: *Applied Physics Letters* **48** (1986), No. 12, pp. 797–799
- [Meye92] MEYERSON, B.S.: UHV/CVD growth of Si and Si. In: *Proceedings of the IEEE* **80** (1992), No. 10, pp. 1592–1608
- [MMKH87] MORAR, J. F.; MEYERSON, B. S.; KARLSSON, U. O.; HIMPSEL, F. J.; McFEELY, F. R.; RIEGER, D.; TALEB-IBRAHIMI, A.; YARMOFF, J. A.: In: *Applied Physics Letters* **50** (1987), No. 8, pp. 463–465
- [MoMT95] MORITA, Yukinori; MIKI, Kazushi; TOKUMOTO, Hiroshi.: In: *Surface Science* **325** (1995), No. 1–2, pp. 21–32
- [Nami06] NAMIKI, A.: In: *Progress in Surface Science* **81** (2006), No. 8–9, pp. 337–366
- [NKKS99] NOZAWA, K.; KATAYAMA, K.; KANZAWA, Y.; SUGAHARA, Q.; SAITOH, T.; KUBO, M.: In: *MRS Online Proceedings Library* **569** (1999), p. 83
- [NSCL95] NAYAK, S.; SAVAGE, D.E.; CHU, H.-N.; LAGALLY, M.G.; KUECH, T.F.: In: *Journal of Crystal Growth* **157** (1995), No. 1–4, pp. 168–171
- [OrSm05] ORLOV, L.; SMYSLOVA, T.: In: *Semiconductors* **39** (2005), No. 11, pp. 1275–1279
- [PeTe91] PEHLKE, E.; TERSOFF, J.: In: *Physical Review Letters* **67** (1991), No. 10, pp. 1290–1293
- [RGRA03] RIVOLO, P.; GEOBALDO, F.; ROCCHIA, M.; AMATO, G.; ROSSI, A. M.; GARRONE, E.: In: *physica status solidi (a)* **197** (2003), No. 1, pp. 217–221
- [ScHe83] SCHULZE, G.; HENZLER, M.: In: *Surface Science* **124** (1983), No. 2–3, pp. 336–350
- [SFPR97] SPITZMÜLLER, J.; FEHRENBACHER, M.; PITZER, M.; RAUSCHER, H.; BEHM, R. J.: In: *Physical Review B* **55** (1997), No. 7, pp. 4659–4664
- [ShTK07] SHI, J.; TOK, E. S.; KANG, H. Chuan.: In: *The Journal of Chemical Physics* **127** (2007), No. 16, pp. 164713–164713–12
- [SKNH87] SAKAMOTO, T.; KAWAMURA, T.; NAGO, S.; HASHIGUCHI, G.; SAKAMOTO, K.; KUNIYOSHI, K.: In: *Journal of Crystal Growth* **81** (1987), No. 1–4, pp. 59–64
- [SSLW89] SINNIAH, Kumar; SHERMAN, Michael G.; LEWIS, Lias B.; WEINBERG, W. Henry; YATES, John T.; JANDA, Kenneth C.: In: *Physical Review Letters* **62** (1989), No. 5, pp. 567–570
- [SSMN89] SAKAMOTO, K.; SAKAMOTO, T.; MIKI, K.; NAGAO, S.: In: *Journal of The Electrochemical Society* **136** (1989), No. 9, pp. 2705–2710
- [TNIK88] TAKAHAGI, T.; NAGAI, I.; ISHITANI, A.; KURODA, H.; NAGASAWA, Y.: In: *Journal of Applied Physics* **64** (1988), No. 7, pp. 3516–3521
- [WrKr80] WRIGHT, Steve; KROEMER, Herbert.: In: *Applied Physics Letters* **36** (1980), No. 3, pp. 210–211
- [WuLi98] WU, Perng-Hung; LIN, Deng-Sung.: In: *Physical Review B* **57** (1998), No. 19, pp. 12421–12427
- [ZhBA99] ZHU, Jian-hong; BRUNNER, K.; ABSTREITER, G.: In: *Applied Surface Science* **137** (1999), No. 1–4, pp. 191–196



---

## CHAPTER 5.

# PLANAR DEFECTS CHARACTERIZATION AND GROWTH OPTIMIZATION OF GaP/Si

---

*In chapter 1 we have described different challenges to be overcome when growing GaP/Si nanolayers. Among them, planar defects such as anti-phase boundaries (APB), stacking faults (SF) and microtwins (MT) are detrimental for both electronic and optical properties of devices and have to be eliminated.<sup>[NRGL12a]</sup> This effort has been spent during the last thirty years but it still lacks a complete and rapid analysis methodology in order to optimize growth conditions.<sup>[ErPi88, Kroe87]</sup> This chapter will give a detail defects analysis using mainly non-destructive X-ray diffraction (XRD) performed on Synchrotron and laboratory sources. Transmission electron microscopy (TEM) and atomic force microscopy (AFM) analysis confirm the results obtained using XRD analysis.*

### 5.1 Synchrotron experiment setup

X-ray measurements were performed on the D2AM (BM2) CRG beam line at the ESRF. In the framework of this thesis, two experiments were carried out with different sets of samples but with similar measurement conditions. A large hybrid pixels detector<sup>[BBBC09]</sup> has been used to allow a much faster data collection than with traditional point detector. This is a crucial point for the acquisition of diffuse signal from crystal defects. The size of each pixel is  $p = 130 \mu\text{m}$ . The photon energy has been set at 16 keV in order to reach the (008) GaP and Si reflections. This energy corresponds to a wavelength of  $\lambda = 0.7749 \text{ \AA}$ . Measurement setup is schematically represented in **Figure 5-1** (a). The distance from the sample to the detector is  $D = 484.2 \text{ mm}$ . The analysis was carried out on fixed exposure images taken on the four  $(00l)$  GaP reflections ( $l = 2, 4, 6, 8$ ). The azimuth  $\phi=90^\circ$  of the sample was set in order to have the horizontal direction of the detector parallel to the  $[110]$  direction of the crystal. For  $\phi=0^\circ$  the horizontal direction of the detector is then parallel to  $[-110]$  (see **Figure 5-1**(b)). In

these conditions,  $\chi$  ( $\chi$  rotation axis is parallel to the X-ray beam when  $\omega=0^\circ$ ) is rotated by  $4^\circ$  to maintain the Bragg reflection spots at the center of the detector.

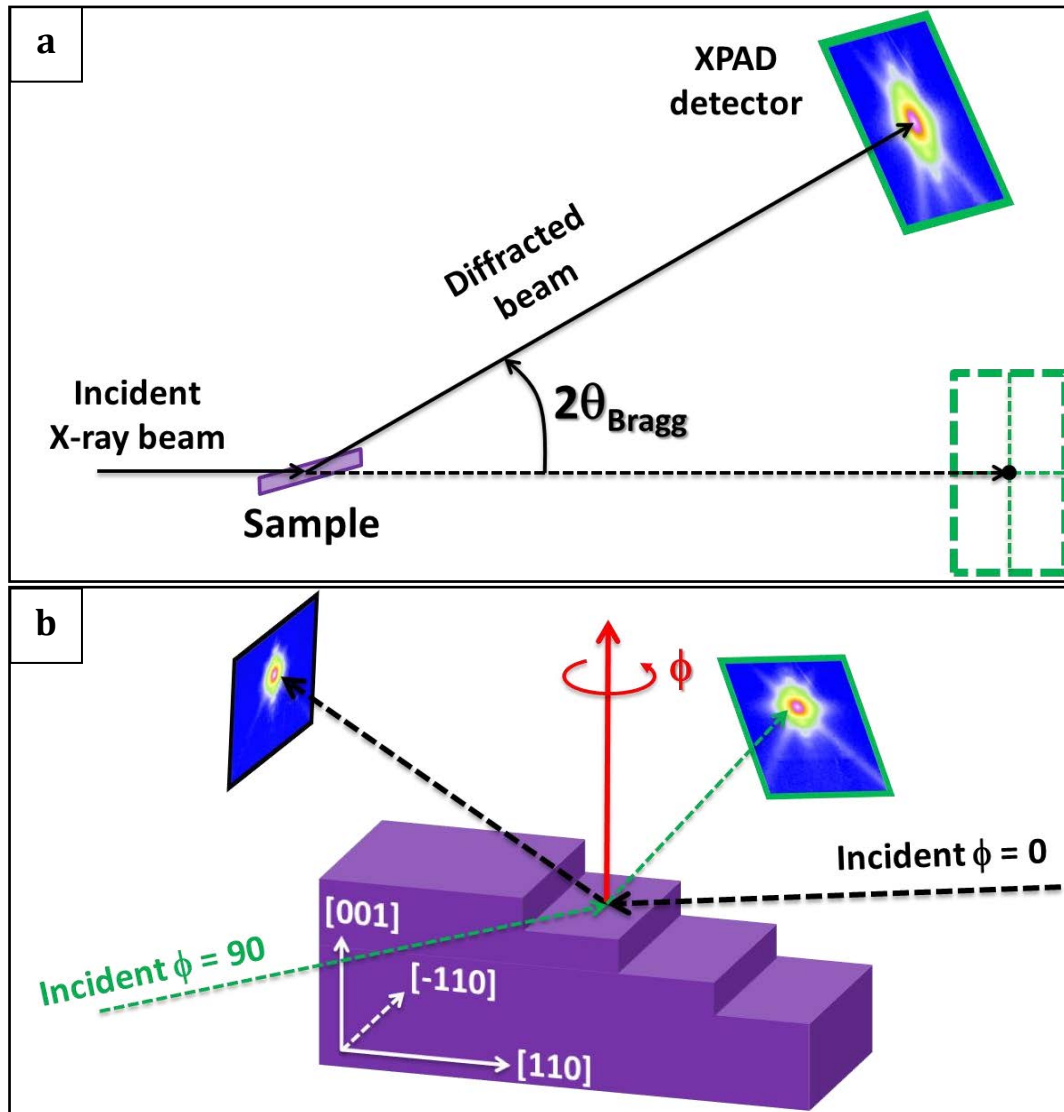


**Figure 5-1:** Schematic representation of Synchrotron measurement setup (a) and sample alignment with respect to the incident beam and surface azimuth (b).

## 5.2 Anti-phase domains (APD) analysis

### 5.2.1 Principle of APD detection using XRD

As described in chapter 1, APD can be formed for instance when growing GaP on monoatomic steps on the silicon surface while the surface is covered by continuous layer of Ga or P (see **Figure 5-2**). These domains are limited by the so-called anti-phase boundaries (APB) which are composed of Ga-Ga and P-P bonds instead of normal zinc-

blende Ga-P bonds. Strain accommodation at these wrong bonds results in relaxation of atoms' positions at the APB boundary. In addition, such defects are expected to be electrically active and are a concern in device operation.<sup>[Kroe87, NMBW02a]</sup> APB can be laid on different lattice plane families: {110}, {111}, {112} or {113} (see chapter 1). According to calculation results of Rubel and Baranovskii, APB {111} has highest formation energy ( $53 \text{ meV}/\text{\AA}^2$ ) while APB {110} has lowest formation energy ( $33.6 \text{ meV}/\text{\AA}^2$ ).<sup>[RuBa09]</sup> This suggests that APB {111} is hard to be formed but once appeared they can be easily self-annihilated within the epilayer. The problem remains for APB {110} because of their lowest formation energy and the fact that they can propagate through the entire GaP layer to the surface that can damage the active layer grown above it. The sketch of such an emergent APD is presented in **Figure 5-2**.

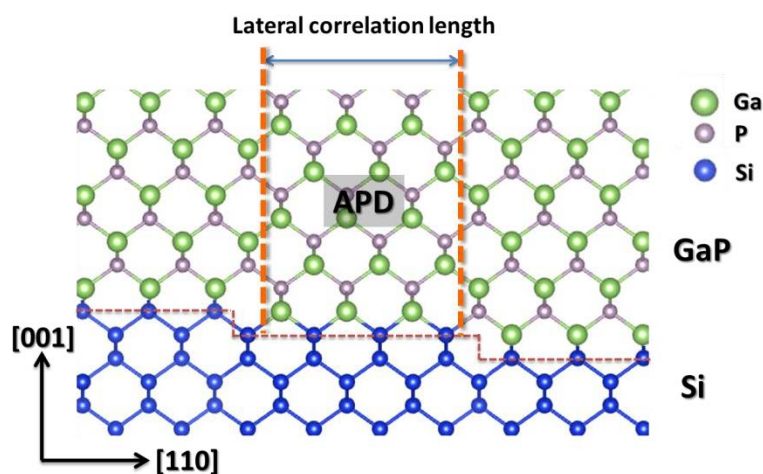


**Figure 5-2:** Schematic representation of APB {110} in GaP grown on monoatomic stepped Si (001).

APD characterization using XRD has been long ago presented (see also Ref [NKSV08a] for a review) and has been also applied in thin films for AlGaIn on sapphire,<sup>[KPMPO5]</sup> GaAs on Si<sup>[NZFM87]</sup> and GaP on Si.<sup>[DGSS08, LGCB11]</sup> The idea is that weak “anti-phase” reflections (APR) act as APD sensors. Indeed Ga and P scatter in anti-phase around weak reflections and in phase around strong reflections (SR). Ga and P positions are just exchanged in an APD when compared to the surrounding main phase matrix.<sup>[GBCL12]</sup> The APD doesn't break the lateral long range order given by epitaxy but gives a broad peak around anti-phase reflections with a weaker peak maximum intensity. The broad peak profile is characteristic of the APD width (i.e. lateral correlation length). This result can be explained by simple consideration on shape and

structure factors.<sup>[NRGL12a]</sup> When looking at scattered amplitudes and intensities near Bragg reflections, all structure and shape factors can be considered as real numbers and can be simply added. Then, in the vicinity of a strong reflection ((004) for instance) the scattered amplitude is roughly proportional to:

$$A_{Total}(\mathbf{S}) \approx \{F_{MP}(\mathbf{S}) + F_{APD}(\mathbf{S})\} F_{SR}(\mathbf{S}) \quad (\text{Eq. 25})$$

We call  $F_{Total}(\mathbf{S})$  the shape factor of the whole layer (main phase and APD) whereas  $F_{APD}(\mathbf{S})$  and  $F_{MP}(\mathbf{S})$  are respectively the APD and main phase shape factors. The zinc-blende cell structure factor on strong reflections is  $F_{SR}(\mathbf{S}) = 4 \cdot (f_{Ga}(\mathbf{S}) + f_P(\mathbf{S}))$ .

The equation (Eq. 25) rewrites:

$$A_{Total}(\mathbf{S}) \approx F_{Total}(\mathbf{S}) \cdot F_{SR}(\mathbf{S}) \quad (\text{Eq. 26})$$

with  $F_{MP}(\mathbf{S}) + F_{APD}(\mathbf{S}) = F_{Total}(\mathbf{S})$ . Similarly, for weak reflections ((002) and (006)), the scattered amplitude is roughly proportional to:  $A_{Total}(\mathbf{S}) \approx \{F_{MP}(\mathbf{S}) - F_{APD}(\mathbf{S})\} \cdot F_{WR}(\mathbf{S})$  and the zinc-blende cell structure factor for weak reflection is:  $F_{WR}(\mathbf{S}) = 4 \cdot \{f_{Ga}(\mathbf{S}) - f_P(\mathbf{S})\}$ . Indeed, because of Ga/P positions exchange and of  $f_{Ga}(\mathbf{S}) - f_P(\mathbf{S})$  term, the cell structure factor takes an opposite value when going from the main phase to the APD. The equation (Eq. 26) rewrites:

$$A_{Total}(\mathbf{S}) \approx \{F_{Total}(\mathbf{S}) - 2F_{APD}(\mathbf{S})\} \cdot F_{WR}(\mathbf{S}) \quad (\text{Eq. 27})$$

Finally from these equations, the scattered intensity around strong reflections is proportional to:

$$|A_{Total}(\mathbf{S})|^2 \approx F_{Total}^2(\mathbf{S}) \cdot (F_{SR}(\mathbf{S}))^2 \quad (\text{Eq. 28})$$

and around weak reflections, it is proportional to:

$$|A_{Total}(\mathbf{S})|^2 \approx (F_{Total}^2 + 4F_{APD}^2 - 4F_{Total} \cdot F_{APD}) \cdot (F_{WR})^2 \quad (\text{Eq. 29})$$

The dependence with  $\mathbf{S}$  is omitted for concision in the last equation.

Both equations (Eq. 28) and (Eq. 29) help to understand the following features: i) APD brightly appears on APR with a factor 4 enhancement when compared to the contribution of a void of the same shape ( $4F_{APD}^2$  term in (Eq. 29)); ii) APD contribution remains hidden in SR; iii) the long range lateral coherence (thin peak) remains even on APR (when APD density is not too large) with the term  $F_{Total}^2$ . These features can also be illustrated by a simple simulation. In this simulation, a single one dimensional APD with APB lying on the (110) planes has been inserted in a GaP layer as presented in the **Figure 5-3** (left hand side).<sup>[NRGL12a]</sup>

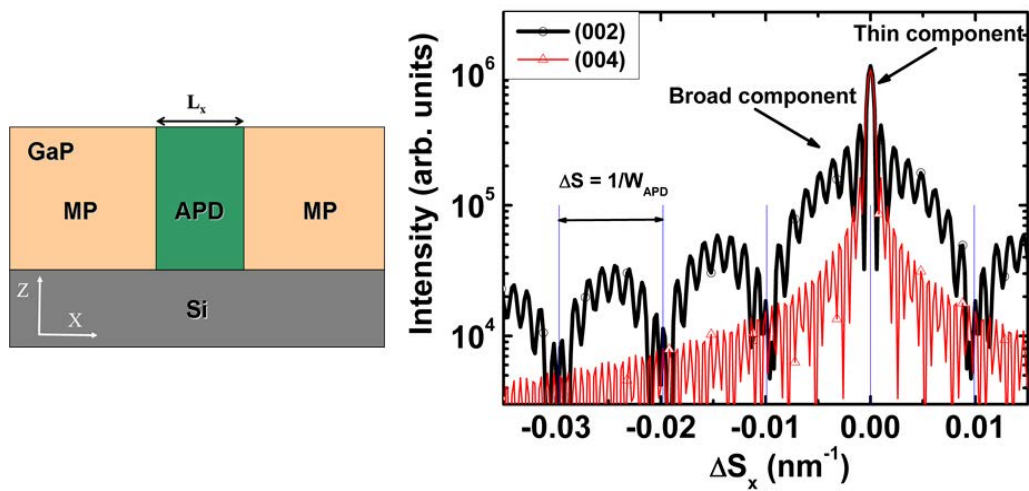


**Figure 5-3:** Simulation model of an APD with the lateral length  $L_x$  and (110) boundaries inserted in the main phase (MP) GaP layer on Si substrate (left) and transverse-scan simulations through (002) and (004) GaP reflections (right).

The intensity is calculated by using the Fourier transform of the whole structure. The scattered intensity simulation on transverse-scans through (002) and (004) GaP reflections, along the [110] direction, is presented on the right. The (004) transverse-scan shows a very sharp peak of which the integral breadth corresponds to  $1/W_{Box}$ ,  $W_{Box}$  being the width of the simulation box in the [110] direction. In the (002) pattern, one can observe two components: a narrow Bragg peak (usually with a resolution limited width in real measurement) is attributed to long-range structural correlations (thin component) due to the epitaxial character of the thin GaP film on the Si substrate, while a broad base is attributed to diffuse scattering of shorter-range defects-induced correlation lengths (broad component). More explanation of these two components can be found in the Ref.<sup>[DLRH11]</sup> Two sets of fringes are also observed: thinner fringes correspond to the lateral correlation length of the whole box, whereas the larger fringes

correspond to the lateral correlation length of the APD. These fringes are usually not observed in real measurement due to large size distribution of APD. It has also been checked that the inter fringes distance gives the APD lateral size in the [110] direction:  $W_{APD} = 1/\Delta S$ . Moreover different defects can contribute to the broad component of the Bragg peaks: micromosaicity, size effect (APD, microtwins, voids), strain... The micromosaic term  $\Delta M$  and the short correlation length can be disentangled using a Halder-Wagner parabolic analysis (derived from a well-known Williamson-Hall plot analysis), adapted to transverse-scans using the following equation:<sup>[DLRH11]</sup>

$$\left(\frac{IB}{S}\right)^2 = \Delta M^2 + \frac{1}{CL} \frac{IB}{S^2} \quad (\text{Eq. 30})$$

where  $IB$  is the integral breadth of the broad component,  $CL$  the correlation length and  $S$  the total scattering vector length of the corresponding reflections.<sup>[DLRH11, JNHL12]</sup> This plot will be called hereafter the “Williamson – Hall like” plot (WHL).

The broadening on the weak reflections is experimentally observed as presented in **Figure 5-4**.<sup>[NRLC12]</sup> Detail about the sample and measurement conditions will be mentioned in the following paragraph. From this figure, one can observe an intense and sharp peak at the center of the Bragg reflection and a diffused component around the (002) Bragg center. Therefore, a transverse-scan performed over the (002) and (006) reflections through the Bragg center (along the broadening direction) gives diffraction patterns composed of a thin and a broad component as explained earlier in which the integral breadth of the broad component is inversely proportional to APD average lateral correlation length. Fitting these patterns with a Pseudo-Voigt function allows separating the two components (**Figure 5-5**). The micromosaicity and APD lateral correlation lengths will then be deduced from a WHL plot using (Eq. 30) with the information obtained from fitted patterns.<sup>[DLRH11]</sup>

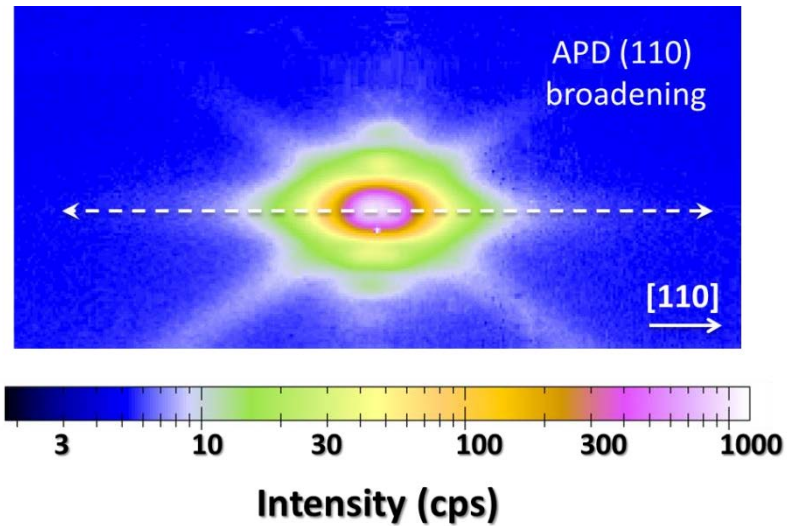


**Figure 5-4:** GaP (002) reflection recorded by a 2D XPAD hybrid pixel detector (see the appendices section for description of XPAD detector). Broadening along the [110] direction is due to APD (110) contribution.<sup>[NRLC12]</sup>

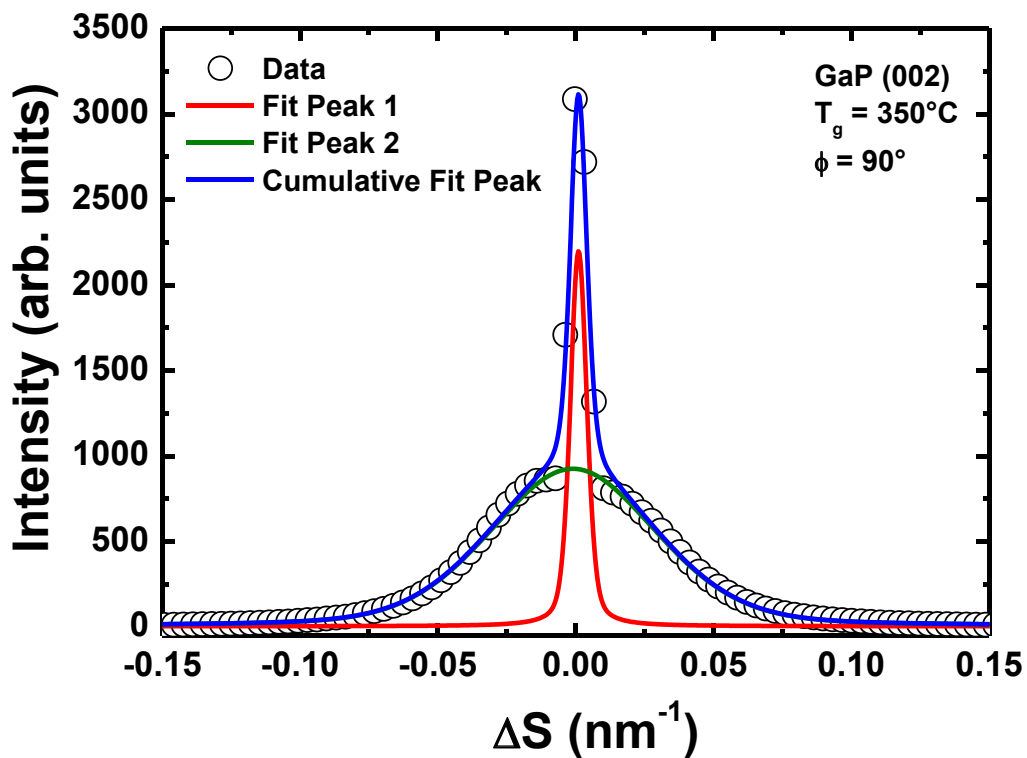


**Figure 5-5:** Pseudo-Voigt fitting of the transverse-scan from GaP (002) reflection.

## 5.2.2 APD analysis using Synchrotron XRD

### (a) Samples

The samples in this study have been grown on 2" Si (001) substrates with a  $4^\circ$  offcut toward [110]. The Si substrates have been prepared by a modified Radio

Corporation of America (RCA) cleaning process and in-situ thermal treatment at 900°C in 10 minutes prior to grow the GaP layers.<sup>[GBCL12, NRLC12]</sup> 20 nm GaP thin layers have been grown without any Si buffer layer, using Migration Enhanced Epitaxy (MEE) technique which consists in alternative growth of Ga and P atomic layers and aims to limit the density of planar defects originating from island-like nucleation.<sup>[GBCF09, GBCL12, LGCB11]</sup> The growth temperature was varied from 350°C to 580°C. Notice that for the sample grown at 350°C, the substrate cleaning process was different from the 3 other samples (cf. Weiming Guo thesis).<sup>[Guo10]</sup> This sample is therefore considered separately.

***(b) Lateral correlation length of APD***

For the WHL analysis, GaP (00l) images are recorded and a transverse-scan is performed on each image ( $l = 2, 4, 6, 8$ ). The abscissa of the transverse-scan patterns are converted to the reciprocal space units ( $\Delta S$ ) using the following equations:

$$\Delta S = (2/\lambda)\sin(2\theta_H/2) \quad (\text{Eq. 31})$$

$$2\theta_H = \tan^{-1}((X - X_o)p/D) \quad (\text{Eq. 32})$$

where  $\theta_H$  is the angular difference between the center of the detector and the studied point,  $X_o$  is the detector center abscissa,  $p$  is the pixel size (130  $\mu\text{m}$ ) and  $D$  is the goniometer to detector center distance (484.2 mm).

**Figure 5-6** shows the images of the 4 GaP (00l) reflections for the sample grown at 350°C. Several features can be observed from these images. Figure (a) and (b) are the (002) reflections with the surface azimuth  $\phi = 90^\circ$  and  $\phi = 0^\circ$  respectively (see **Figure 5-1** (b) for azimuthal alignment). The broadening of the Bragg reflections along the  $\langle 110 \rangle$  directions is characteristic of APB  $\{110\}$  contribution as explained earlier. Streaky pattern in the  $\langle 111 \rangle$  directions is a signature of microtwins that will be discussed later. Black dotted lines indicate the crystal truncation rods (CTR) which are normal to the sample surface. In our experiment, sample surface has been rotated by  $4^\circ$  in  $\chi$  to place the Bragg spot in the detector's center. This rotation results in a clockwise rotation of the CTR as presented in **Figure 5-6** (a). The figures (c) and (d) present the (004) and (008) strong reflections of GaP and Si. In figures (c) and (d), the larger peak indicates the Si reflection whereas the smaller peak underneath corresponds to the GaP reflection. The GaP (006) reflection is reported in the **Figure 5-6** (e). One can observe on

this figure some thin streaky reflections. The exact nature of these reflections is still unknown at the moment. All of these images are presented in the same scale (size and intensity range). The  $0^\circ$  azimuthal images will be used for APD analysis. The exposure time for the weak reflections (002) and (006) is 300 seconds whereas (004) and (008) reflections are recorded for 10 seconds with a strong attenuation coefficient (to not damage the detector due to strong diffraction intensity of Si (004) and (008)). This results in a difference in color scale but is not detrimental for the broadening analysis.

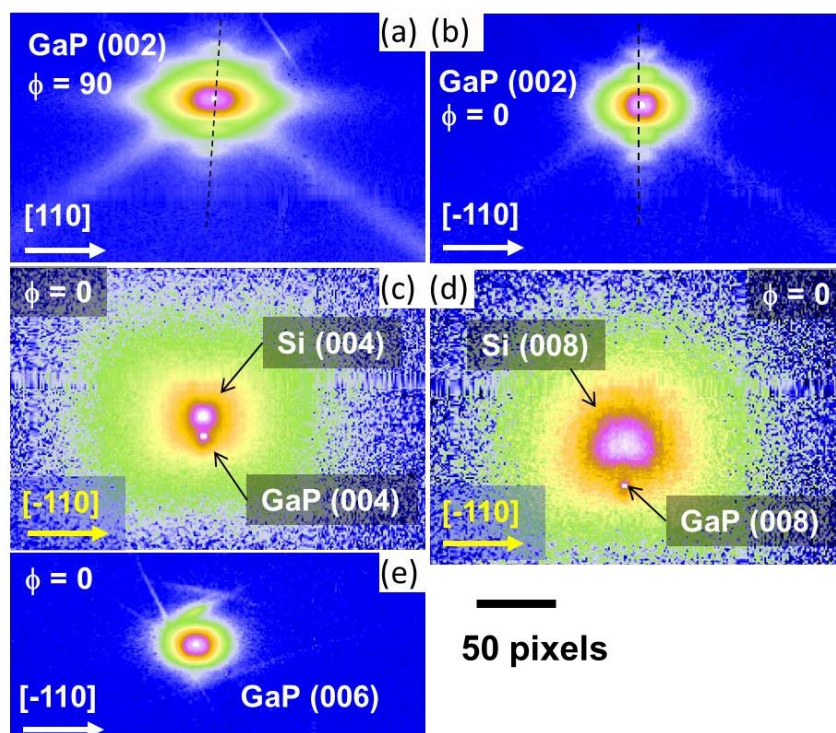


**Figure 5-6:** XPAD images centred on the 4 different nearly specular GaP reflections for the azimuth  $\phi=0^\circ$  (b, c, d and e). For this azimuth, the  $[1-10]$  direction of the sample is normal to the main scattering plane which means that planar defect with boundaries lying on  $(1-10)$  planes would produce scattering along the horizontal direction of the 2D image.  $\phi$  is rotated of  $90^\circ$  for (a).<sup>[NRLC12]</sup>

Transverse-scans extracted from the GaP  $(00l)$  reflections are reported in **Figure 5-7**. The (002) and (006) weak reflections are reported on the figure (a) which shows up a thin component and a broad component. The transverse cuts through the (004) and (008) GaP reflections are respectively reported on the figure (b) and (c). As observed in **Figure 5-6**, an important part of the broad component on the strong reflections can be actually attributed to the substrate. In order to subtract this contribution, a second cutline was performed at a position above the Si diffuse

maximum, symmetric to the GaP cutline. The original GaP cut lines (“GaP (00*l*)” with *l*=4 or 8) and the Si diffuse (“Si dif”) as well as the subtraction of the substrate contribution (“GaP-Si dif”) are reported in **Figure 5-7 b)** and **c)**.

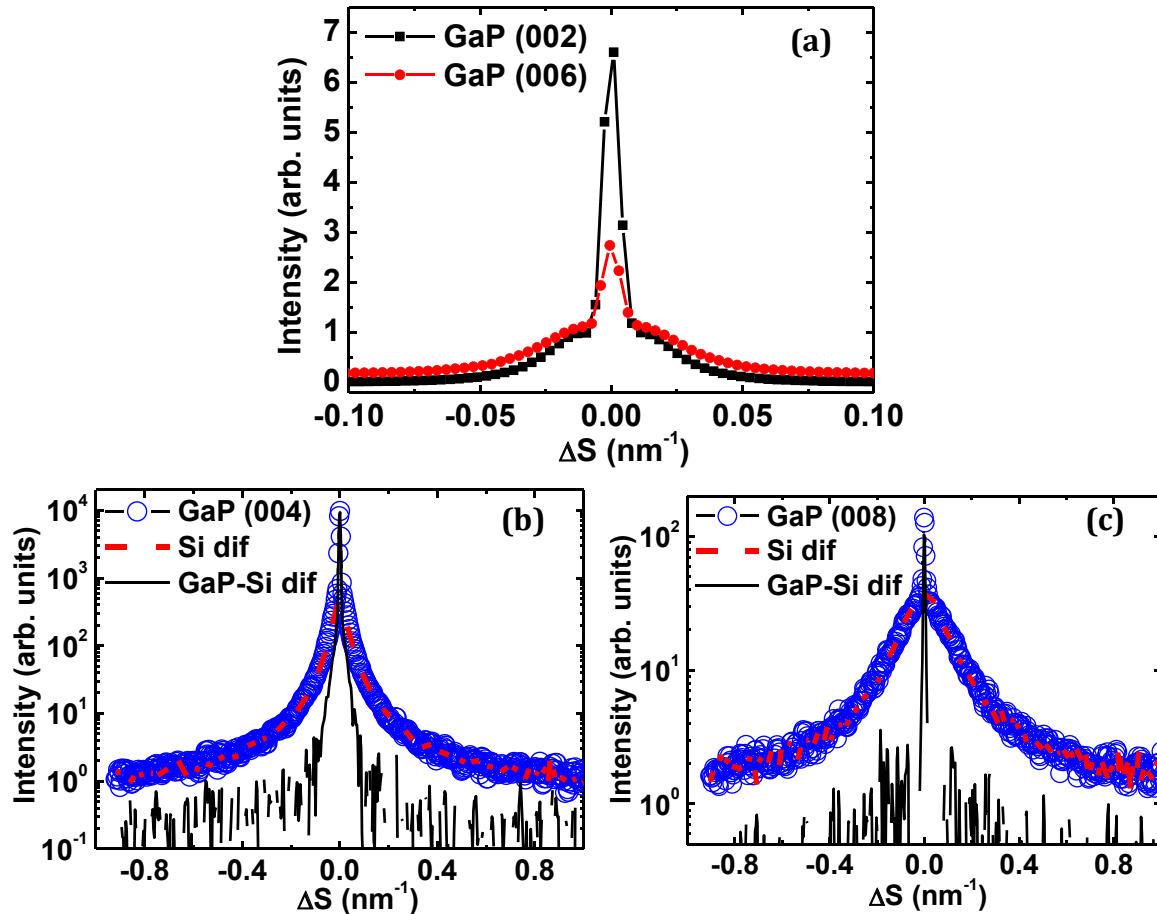


**Figure 5-7:** Transverse-scan patterns extracted from the GaP (002) and (006) reflections (a). A thin and a broad component can be observed for both patterns. Figures (b) and (c) present the transverse-scans on the (004) and (008) GaP reflections, respectively. The both later images also present a cutline taken on the Si diffused part and the subtraction of this part from the GaP Bragg transverse cuts.

Two simple parameters are extracted from these plots: the integral breadth of the broad contribution (IB) and the quality factor (QF) which is defined as the area ratio of the thin versus the broad contribution:  $QF = \frac{A_{thin}}{A_{broad}}$ . In the case of GaP (008) reflection,

there is an important contribution of the silicon thermal diffuse scattering (TDS - proportional to  $S^2$ ), and because of high incident X-ray beam (38-39°), the contribution of the GaP epilayer is less significant. The GaP (008) profile after subtraction of Si TDS does not present the broad component; it is therefore excluded from analysis here after.

**Figure 5-8** shows a synthetic view of the extracted results. **Figure 5-8 (a)** presents IB

and QF for the 3 reflections (002), (004) and (006). This shows a non-monotonic evolution of QF with the scattering vector  $S$  (proportional to the  $l$  index) which is very illustrative for the particular role played by the weak reflections, i.e. (002) and (006) reflections. This is the signature of APD whose contribution only appears on anti-phase reflections (see Guo *et al.*<sup>[GBCL12]</sup> and references therein). Moreover, the fact that very high QF for the (004) strong reflection implies that APD contribution is dominant on weak reflections and these reflections can be treated separately in the defect-induced correlation length (also named crystallite size) analysis. To this end, WHL analysis has been performed on the transverse-scans. The WHL plot presented in **Figure 5-8 b)** using both the (002) and (006) weak reflections allows the extraction of the micromosaicity  $\Delta M$  and the lateral correlation lengths.<sup>[DLRH11, HaWa66]</sup> The slope given by the two APR reflections gives then a correlation length of  $17.4 \pm 1.0$  nm and a micromosaicity of  $0.137 \pm 0.01^\circ$ . This correlation length is attributed to all kind of defects included the APDs. Since the (004) diffraction planes belongs to the  $(00l)$  planes, their micromosaicity is necessarily the same as the one of (002) and (006) planes. Therefore we join the (004) point in the WHL plot to the intercept given by APR reflections. This gives an estimation of the defect-induced lateral correlation length except the APD.<sup>[NRGL12a]</sup> As the QF of the (004) reflection is very high with respect to the QF of the (002) and (006) reflections, which indicates the effect of APDs contribution, we can tell that the correlation length extracted from the (002) and (006) (see **Figure 5-8b)** is attributed to the APDs only. In the other words, the correlation length extracted from the (002)-(006) line represents the average distance between APBs.

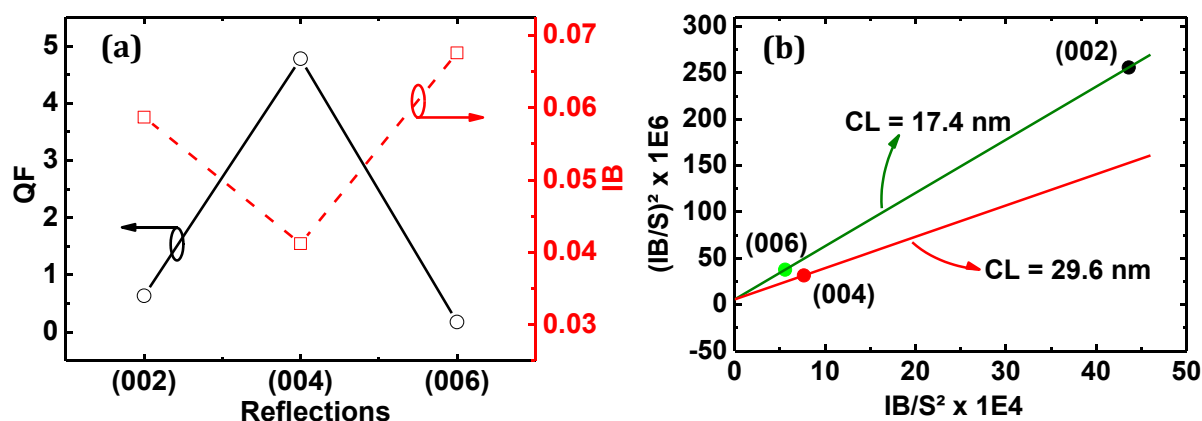


**Figure 5-8:** WHL analysis from transverse-scans with (a) Quality Factor (QF) & Integral Breadth (IB) and (b) WHL plot for lateral correlation lengths extraction. APD lateral correlation length (CL) of 17.4 nm and a mosaicity of  $0.137^\circ$  is deduced from this analysis.

Finally for this sample (GaP/Si – 4° miscut towards [110] – 20 nm MEE at 350°C), a transverse-scan analysis carried out on (002) for  $\phi = 90^\circ$  gives a broader IB than in the  $\phi = 0^\circ$  azimuth (0.0844 nm<sup>-1</sup> versus 0.0587 nm<sup>-1</sup>, see **Figure 5-9**). In other words the broadening along the [110] direction is larger than the broadening in the [-110] direction. That means the lateral correlation length from the APBs in the [110] direction is shorter than in the [-110] direction. As the IB of the (002) and (006) are very close, we can estimate the correlation length by a first order approximation using the Scherrer relation:  $CL \cong 1/IB$ . This gives a correlation length of 11.8 nm. This is coherent with our previous analysis using lab setup XRD in which the WHL plot gave the APD correlation length of  $11 \pm 1$  nm with a lower QF.<sup>[NRGL12a]</sup> This means that there are more APD with the boundaries lying on (110) planes than the APD with the boundaries lying on the (-110) planes. This anisotropy is probably linked to the miscut orientation of the substrate (4° off toward [110]). The anti phase boundaries are longer in the direction parallel to the step edges and shorter in the direction of the steps.

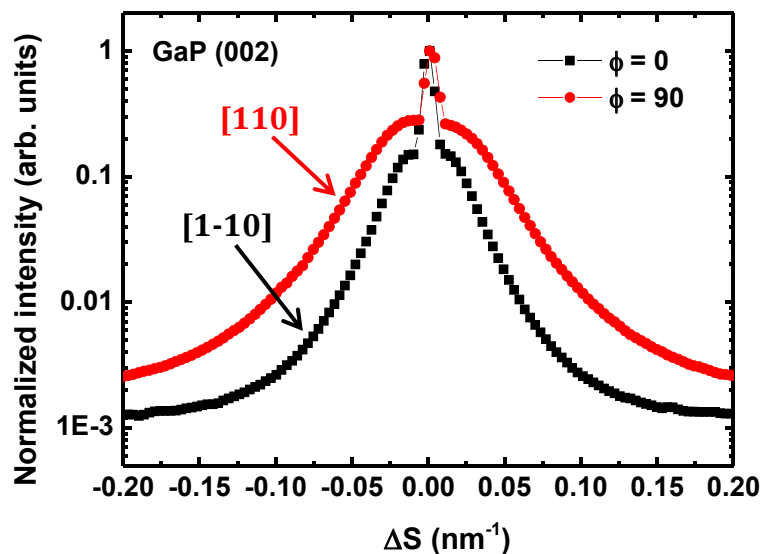


**Figure 5-9:** Transverse-scans of GaP (002) for the two azimuths  $\phi = 0$  and  $\phi = 90$ .

The anisotropy of APD is evidenced by TEM observation in plan-view mode. TEM measurements have been done in collaboration with A. Ponchet and J. Stodolna at the CEMES group in Toulouse. The micrographs have been recorded using a Philips CM30 in high resolution and conventional modes, with an acceleration voltage of 300 kV. The zone axis [1-10] has been selected for imaging. Thin plates have been prepared by mechanical polishing and ion thinning. **Figure 5-10** shows a TEM micrograph in plan-

view mode, with the projection closed to the  $[001]$  direction. In dark field imaging mode, the dark lines visible on this image indicate the APB. Crystallographic directions are also indicated in the figure. As one can observe in this figure, a preferential orientation of these dark lines can be noticed along  $[110]$  and  $[-110]$  directions. We can also notice shorter ABP to APB distances along  $[110]$  than along  $[-110]$  that confirms the results obtained by XRD.

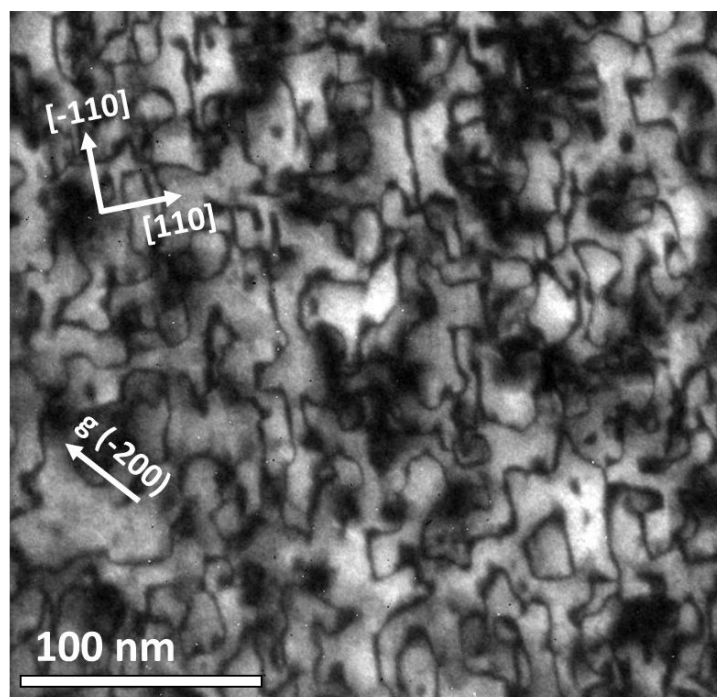


**Figure 5-10:** Plan view TEM micrograph selecting the  $(-200)$  reflection (sample: 20 nm GaP/Si, MEE 350°C). In this view mode, the dark lines indicate anti-phase boundaries. Anisotropy of the boundaries can be observed on this image.

The WHL method has been applied to characterize the lateral correlation length of APD in the  $[-110]$  direction for the last 3 samples ( $T_g = 400, 450$  and  $580^\circ\text{C}$ ). **Figure 5-11** presents RSM obtained on the GaP  $(00l)$  reflections for these 3 samples ( $l = 2, 4, 6$ ). These images reveal different features from one sample to another. The first remark that can be withdrawn is the difference in the lateral broadening of the weak reflections (i.e.  $(002)$  and  $(006)$ ). Secondly, the  $(002)$  Bragg spot's shape is also different from one sample to another. The difference in weak reflections broadening indicate the difference in APB correlation length and their density, whereas the difference in the  $(002)$  Bragg spot's shape may be due to the difference in layer morphology (such as roughness) and/or other planar defects (such as microtwins).

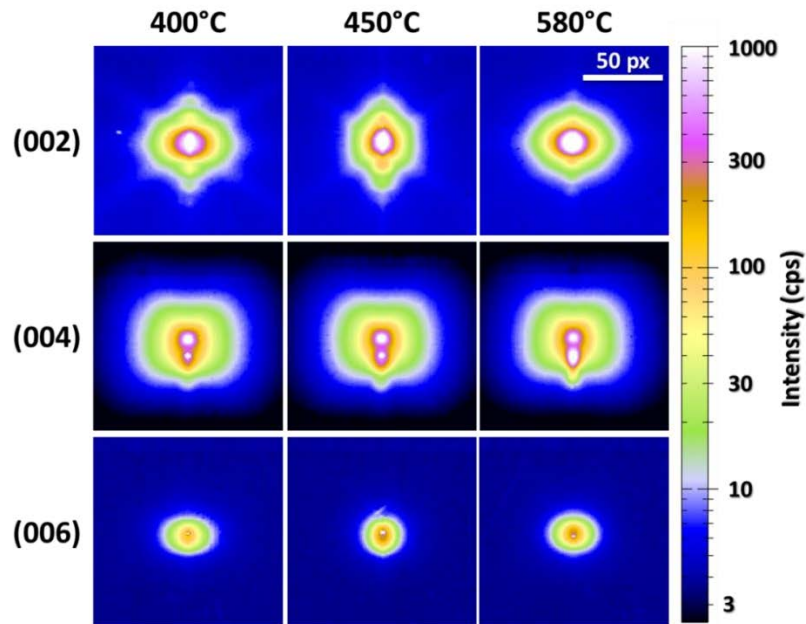


**Figure 5-11:** Synthetic of GaP ( $00l$ ) reflections ( $l = 2, 4, 6$ ) for 3 GaP/Si samples with  $T_g = 400, 450$  and  $580^\circ\text{C}$ .

Practically we can use two points (002) and (006) to apply the WHL plot (as presented in **Figure 5-8b**), we have therefore extracted the transverse-scans on the (002) and (006) RSM. Integral breadths obtained from these transverse-scan profiles are presented in **Figure 5-12** (left) and the lateral correlation lengths of APB (-110) deduced from the WHL plots are presented in **Figure 5-12** (right).

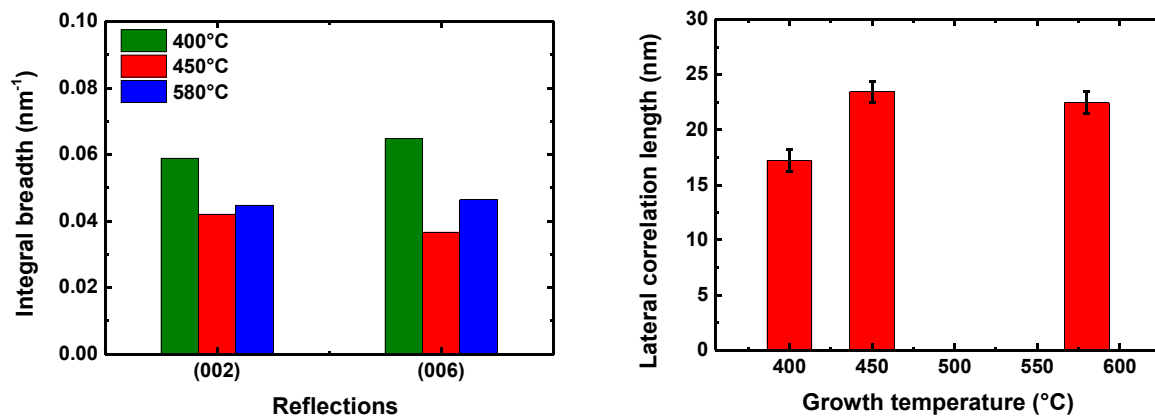


**Figure 5-12:** Integral breadth and lateral correlation length of APB (-110) are deduced from WHL analysis on the 3 GaP/Si samples ( $T_g = 400, 450$  and  $580^\circ\text{C}$ ).

These results show up the evolution of APD lateral correlation lengths, thus related to their density (number of domain per surface unity), with respect to the growth temperature. Low growth temperature results in higher APD density (i.e. larger

broadening in the weak reflections and shorter lateral correlation length); whereas high growth temperature reveals lower APD density. This can be explained by the fact that at high temperature the APBs  $\{110\}$  tend to kink to the APB adjacent and self-annihilate on  $\{111\}$  or  $\{112\}$  planes.<sup>[NKS08b, NKS08a, VBW011, WBG12]</sup>

A more complete APD quantification can be done combining TEM characterization with XRD analysis. The methodology development is still in progress in collaboration with CEMES. Preliminary results of APD quantification by TEM in the plan-view mode are reported in the **Figure 5-13**. APBs are evidenced by dark solid lines. One can observe many small dark solid spots among the lines. These dark solid spots correspond to the projection of self-annihilated APD which do not contribute to the broadening along  $\langle 110 \rangle$  directions in both XRD (002) and (006) reflections. Binary image (i.e. image in which the contrast difference of the main phase and APD are given as 1 and 0) in (e) is generated from (d) for domains quantification, where APD appear in black. The images presented in (a), (b) and (c) reveal the increase of the APD size (or correlation lengths) which confirms the XRD analysis results.

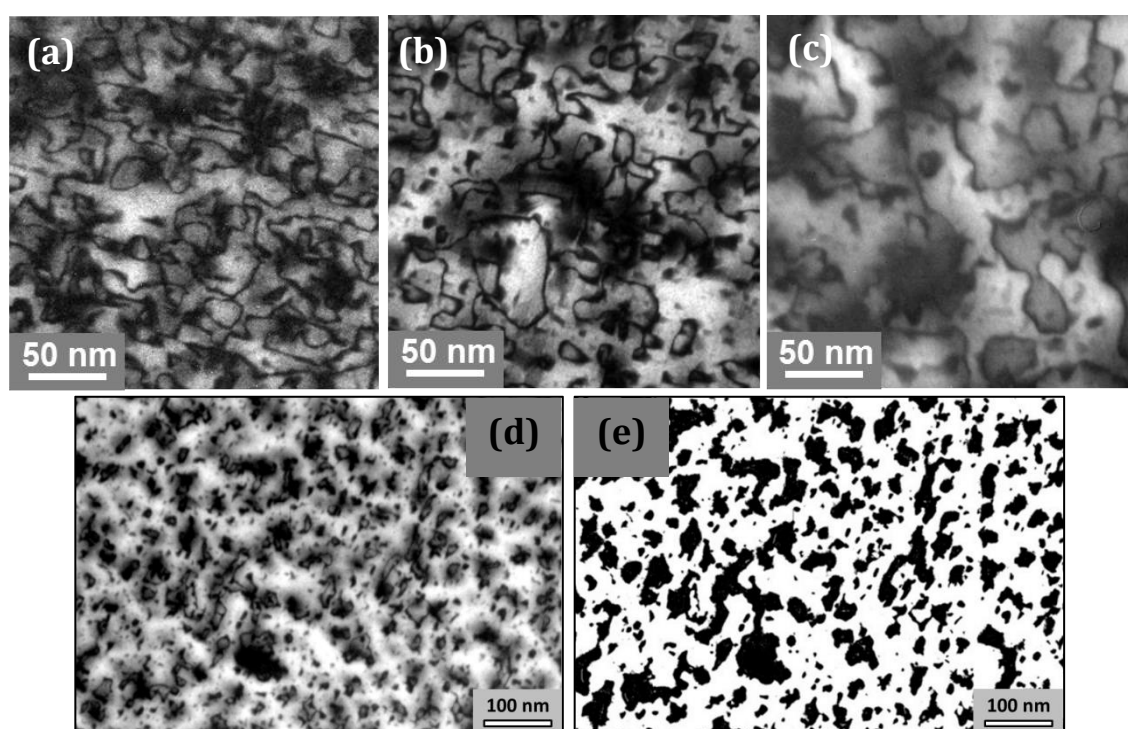


**Figure 5-13:** Plan-view TEM micrographs reveal APB in GaP/Si samples grown by MEE at  $T_g = 350$  (a), 400 (b) and 580°C (c). (d) is a smaller scale picture taken on the sample grown at 450°C, (e) is a color contrast deduced from (d) for domains quantification, APD appear in black in this image.

### 5.3 Microtwins study in GaP/Si nanolayers

In the previous section, we can notice the presence of diagonal streaks in the GaP (002) Bragg reflection which is signature of microtwins. This section gives more details about the study of microtwins as well as the influence of the growth conditions on microtwins behavior.

#### 5.3.1 Detection of microtwins (MT)

##### *(a) MT detection using Synchrotron source*

In chapter 1 we have described what a microtwin (MT) is. **Figure 5-14** reminds the structure of a MT in a GaP matrix. MT generally observed in zinc-blende compounds actually correspond to a sequence of stacking faults lying on  $\{111\}$  planes. They can be imagined as a  $180^\circ$  rotation of the nominal crystal around a  $\langle 111 \rangle$  axis.

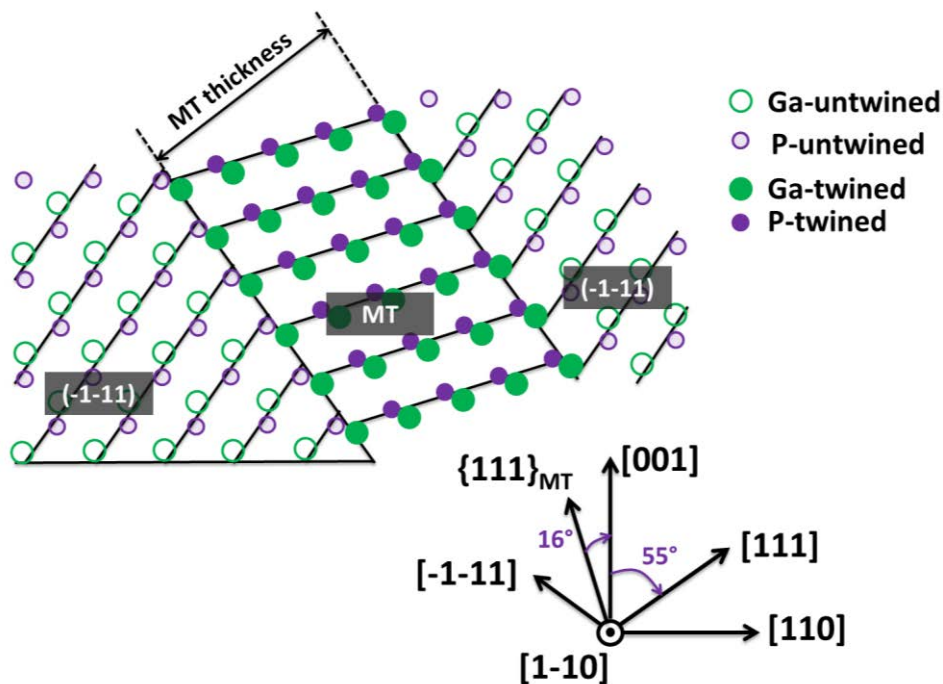


**Figure 5-14:** Sketch of a MT  $\{111\}$  in a GaP matrix.

As a direct consequence of the 4-fold symmetry of the cubic structure, 4 variants of MT can be formed, lying on  $\{111\}$  planes. Their name is given by assignment of their boundaries planes. For example: **Figure 5-14** depicts a MT (111) as their boundaries lie on (111) planes. These MT have been observed by several authors using mainly TEM, as reported by Hiruma *et al.*<sup>[HYK095]</sup> They showed that the  $180^\circ$  rotation of the crystal

planes produces new reflection positions as described schematically on the **Figure 5-15**. The transversal width of the MT in the direct space will produce streaks in the reciprocal space which are elongated in the direction perpendicular to their boundaries.

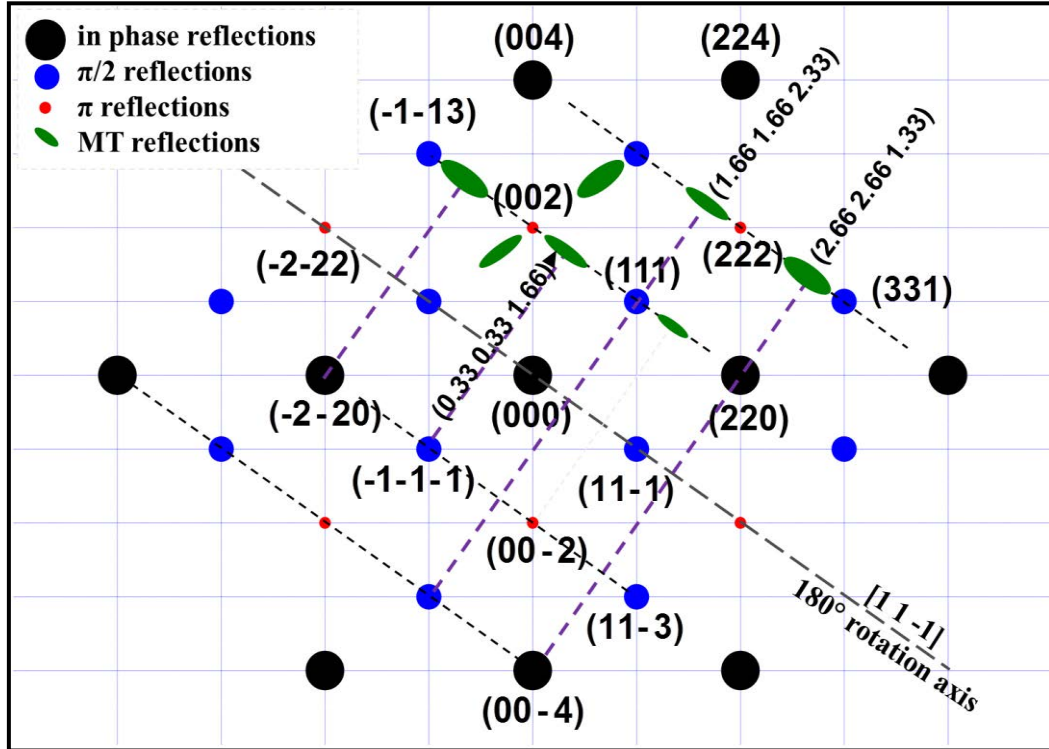


**Figure 5-15:** Reciprocal lattice points of GaP. The black, blue and red solid circles represent strong, medium and weak reflections. The green ellipsoid shapes indicate the diffraction spots of MT. This schema presents 1 out of the 4 MT variants.

In the direct space, these 4 MT variants are schematically depicted in the **Figure 5-16**. The convention ABCD was introduced by Skibitzki *et al.*<sup>[SHYZ12]</sup> and will be used instead of MT {111} in this thesis. In this convention, MT A, C, D, B correspond respectively to MT (-1-11), (111), (-111) and (1-11).

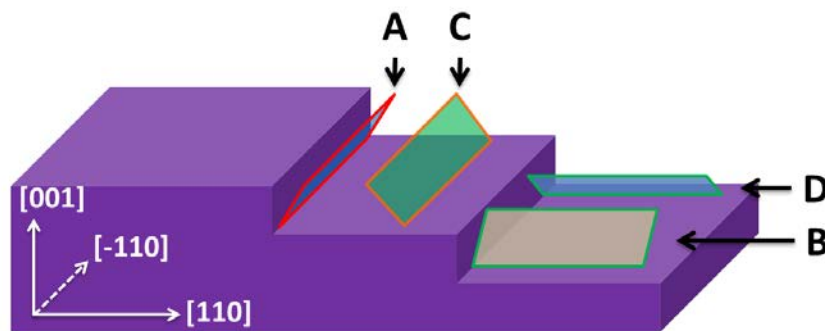


**Figure 5-16:** Schematic presentation of the 4 MT variants in the real space. The ABCD convention was introduced by Skibitzki *et al.*<sup>[SHYZ12]</sup>

MT are generally initiated from the step edges, contaminants or 3D nucleation sites in the early growth stages and formed by stacking error of the III-V atoms on the {111} lattice planes. Ernst *et al.* have investigated the formation of MT in GaP/Si and suggested that the growth should be performed at high substrate temperature and low growth rate to reduce the formation of planar defects.<sup>[ErPi88]</sup> Narayanan *et al.* have also claimed that MT could be eliminated at high growth temperature because atoms are sufficiently mobile to arrange themselves into low energy configurations.<sup>[NSBM99, NMBW02b]</sup> In this study, high growth temperature leads unfortunately to rough surface. By investigating the variation of the GaP film thickness grown by metal organic vapor phase epitaxy on Si(001) substrate with an intentional miscut of  $0.1 \pm 0.5^\circ$  towards [110], Beyer *et al.* believed that MT can be suppressed if the integrated strain of the III-V layer does not exceed a certain critical value which corresponds to a film thickness of about 70 nm.<sup>[BNLO11]</sup>

In the next paragraph we will discuss about the influence of growth temperature on the reduction of MT density. Samples in this study are the same as presented in the previous paragraph (20 nm thin GaP/Si – Si (001)  $4^\circ$  miscut towards [110] – MEE at  $T_g = 350, 400, 450$  and  $580^\circ\text{C}$ ). MT are evidenced by taking reciprocal space map (RSM) around GaP (002) reflection as depicted in **Figure 5-17**. They are clearly shown up in the form of some additional reflections beside the conventional (002) Bragg reflections.

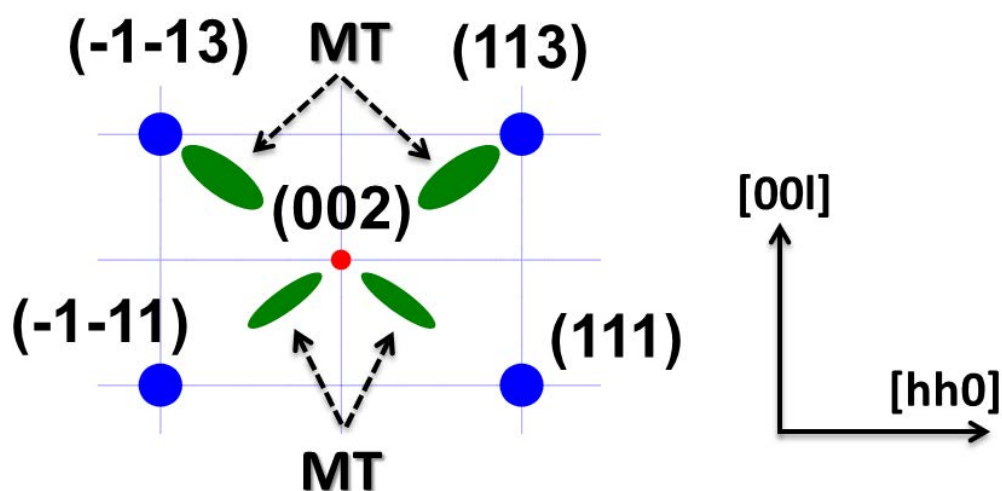


**Figure 5-17:** Reciprocal lattice points of GaP around (002) reflections including MT reflections.

**Figure 5-18** (left) depicts a measurement of such a RSM around GaP (002) reflection. This image has been recorded by XPAD detector (Synchrotron XRD) and the sample azimuth was set at  $\phi = 90^\circ$  (i.e. the X-ray incident beam along the  $[-110]$  direction - see **Figure 5-1** (b) for description of azimuthal sample alignment). MT reflections are evidenced by streaky patterns elongated along  $[-1-11]$  (right) and  $[111]$  (left), which correspond to MT A and C, respectively. **Figure 5-18** (right) presents a cross-section TEM micrograph showing a stacking fault and a pack of C-type MT which consists in a band of close-packed MT for the same sample. This image reveals the distance between each single MT in the order of 2 nm. In the direct space, the distance between single MT will be called hereafter the transversal correlation length and the length of MT along the  $\langle 111 \rangle$  direction will be called the longitudinal correlation length.

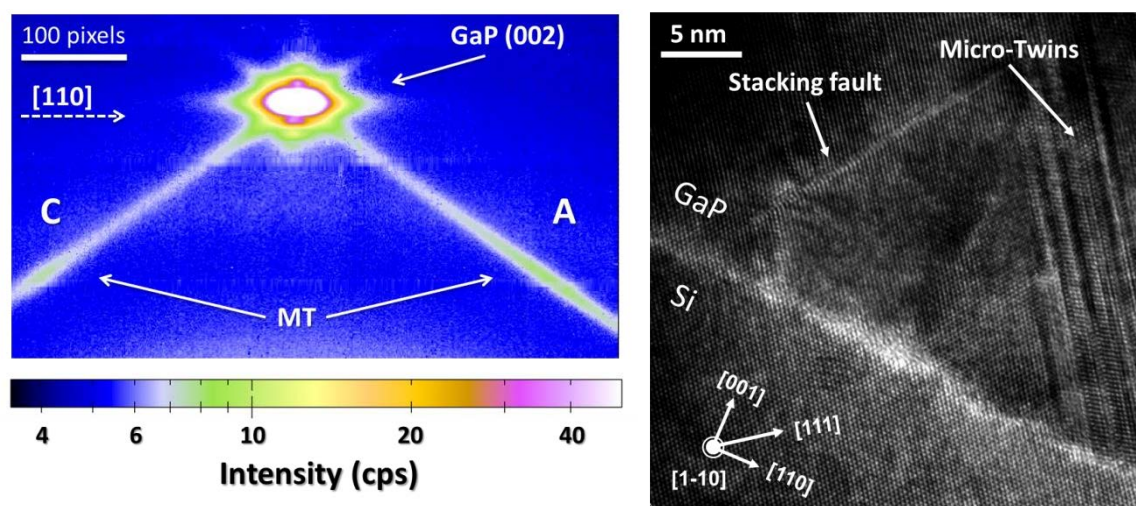


**Figure 5-18:** Left: RSM around GaP (002) reflection reveals appearance of MT reflections (for sample grown at  $T_g = 350^\circ\text{C}$ ). This image is recorded setting  $\phi = 90^\circ$  and evidences the appearance of MT A and C. Right: Cross-section TEM micrograph of the same sample showing MT-C and a stacking fault.

For a complete study of the MT, we need to measure the entire MT streaks. The measurement consists in changing  $\omega$  (or Eta motor in the notion of the beamline goniometer) and  $\phi$  (azimuthal rotation – normal to the surface) in order to maximize the diffraction intensity of the MT streaks. The detector is then moved horizontally to place the entire MT streaks in the center (**Figure 5-19**).

In order to estimate the MT correlation lengths (transversal and longitudinal), we have extracted a cut along the MT streak or perpendicular to the MT streak, as indicated by dashed double head arrows in **Figure 5-19**. Fitting the cut patterns by a Pseudo-Voigt

function gives us the integral breadth which is proportional to the inverse of the corresponding correlation length, as suggested by the Scherrer relation.<sup>[YiMN09]</sup> In this example, the average longitudinal and transversal correlation length of MT-A is estimated to be  $16.5 \pm 1$  nm and  $1.9 \pm 0.1$  nm, respectively.<sup>[NRGL12b]</sup>

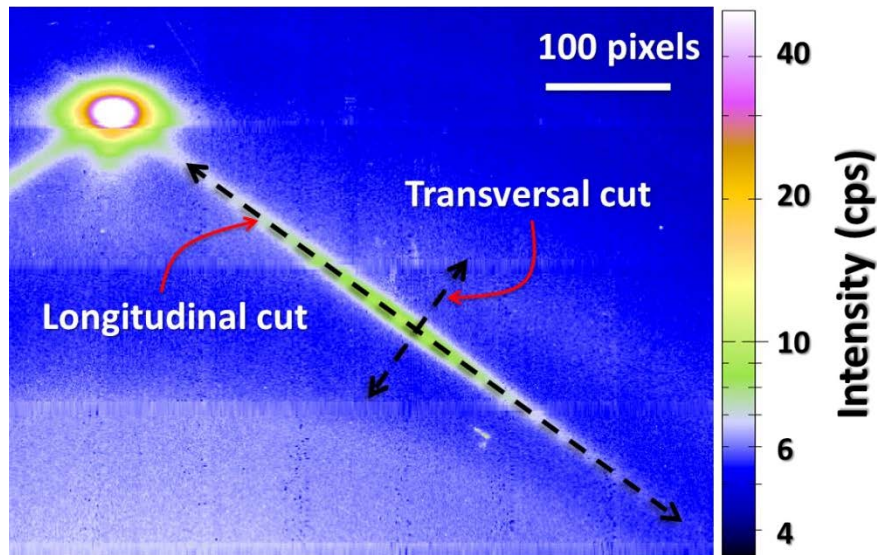


**Figure 5-19:** MT streak measurement on the GaP/Si sample grown at 350°C. Longitudinal and transversal cuts through the MT streak are indicated by double head arrows.

### ***(b) MT detection using laboratory XRD source***

For a laboratory XRD study, MT can be detected using pole figures (see the appendices for a description of the pole figure technique). As depicted in **Figure 5-14**, MT formation inside a GaP (001) matrix create additional MT {111} planes that are inclined by  $39^\circ$  from the original GaP {111}. They are therefore inclined by  $16^\circ$  from the (001) planes – according to the observation of Zaumseil and Schroeder in 2008 <sup>[ZaSc08]</sup> or J. Cheng *et al.* in 2009 for the InP/SrTiO<sub>3</sub>(001) system.<sup>[CLPR09]</sup> MT reflections thus can be found in the vicinity of the GaP {111} reflections with an inclination in  $\chi$  by  $16^\circ$  from surface normal, whereas GaP {111} can be found with  $\chi$  inclination about  $55^\circ$  from the surface normal.<sup>[SHYZ12]</sup> After alignment of  $2\theta$  (detector) and  $\omega$  (sample rocking) to the Bragg position corresponding to GaP (111) planes, we fix the  $\omega$  and  $2\theta$  angles and perform a circular scan in  $\phi$  ( $0^\circ - 360^\circ$ ) after every offset in  $\chi$  (remind that the  $\chi$  axis is

parallel to the X-ray beam when  $\omega=0$  – see the appendices section for the description). **Figure 5-20** presents a pole figure performed on a GaP/Si sample while fixing GaP (111) Bragg position. The silicon (001) substrate is miscut by  $6^\circ$  toward [110] direction. Due to the fourfold symmetry, 4 symmetric GaP {111} Bragg peaks at  $\chi \approx 55^\circ$  are measured. Note that the 4 GaP {111} spots are overlapped by the four corresponding Si {111} spots because of the large opening of the detector. The four lower intensity peaks at  $\chi \approx 16^\circ$  correspond to the MT reflections. The 4 MT variants (A, B, C, D) are indicated in the figure. Note that the MT-A and MT-C are shifted in  $\chi$  by  $\pm 6^\circ$  due to the substrate miscut. The inset depicts sample alignment at initial position corresponding to  $\phi=0^\circ$ . The positive direction movement of the motor  $\phi$  is also indicated.

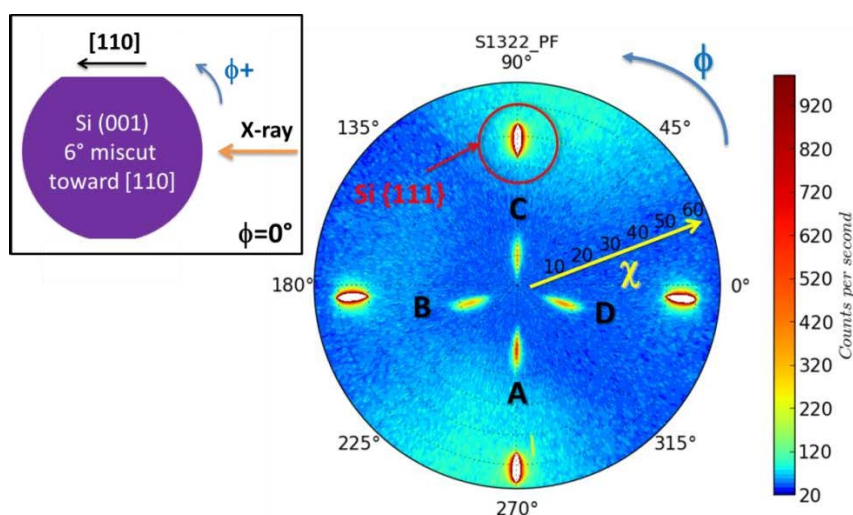


**Figure 5-20:** Pole figure measured on a GaP/Si sample ( $6^\circ$  off Si substrate). The 4 larger and brighter peaks at  $\chi \approx 55^\circ$  correspond to GaP {111} reflections (which are overlapped by Si {111} reflections because of their vicinity and wide opening detector), the 4 weaker peaks at  $\chi \approx 16^\circ$  correspond to MT reflections. The four MT variants are named by ABCD convention as indicated on the figure. Intensity in counts per second is represented in log scale. Inset depicts sample alignment at initial position corresponding to  $\phi=0^\circ$  and the positive direction movement of  $\phi$  motor is also indicated.

### 5.3.2 Influence of the growth temperature on the MT

#### (a) Synchrotron XRD study

This study has been performed using Synchrotron source for the samples grown by MEE at different temperature (i.e. the same samples as described in the APD study).

In order to qualitatively compare the MT density in the different samples corresponding to different growth temperatures ( $T_g$ ), we have measured the MT reflections around GaP (002) reflection. Special care has been taken in order to get the highest intensity of the MT streaks. This is done by finding GaP (002) reflection followed by a  $\phi$  scan around  $\phi_0 \pm 5^\circ$ , with  $\phi_0$  the initial azimuth. **Figure 5-21** depicts a synthetic report of the MT reflections for the 3 samples ( $T_g = 400, 450$  and  $580^\circ\text{C}$ ). One can observe a progressive reduction of MT intensity when  $T_g$  increases. They could not be detected for the sample grown at  $580^\circ\text{C}$ .

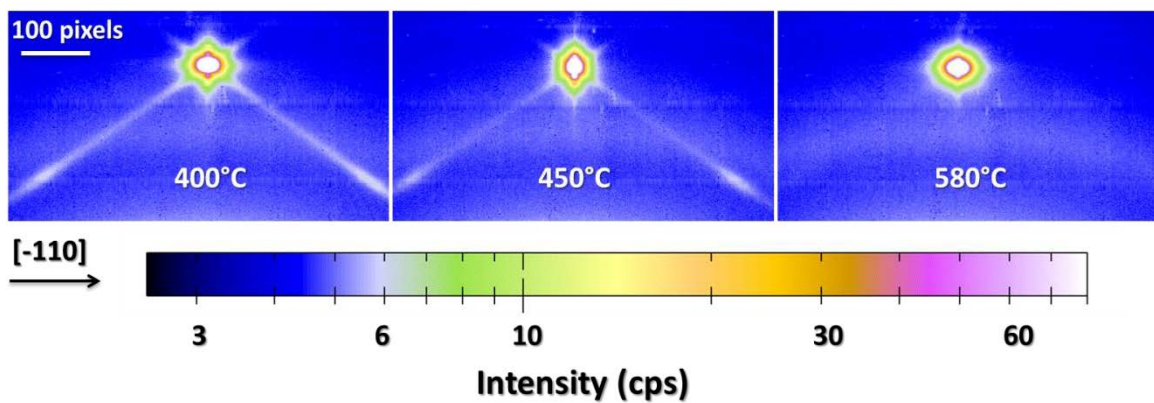


**Figure 5-21:** Synthetic of MT detection for the 3 samples GaP/Si grown at  $T_g = 400, 450$  and  $580^\circ\text{C}$ . Progressively reduction of MT intensity is visible.

No MT reflections have been observed on the sample grown at  $580^\circ\text{C}$  neither in the azimuth  $\phi = 0^\circ$  nor in the azimuth  $\phi = 90^\circ$  (**Figure 5-22**).

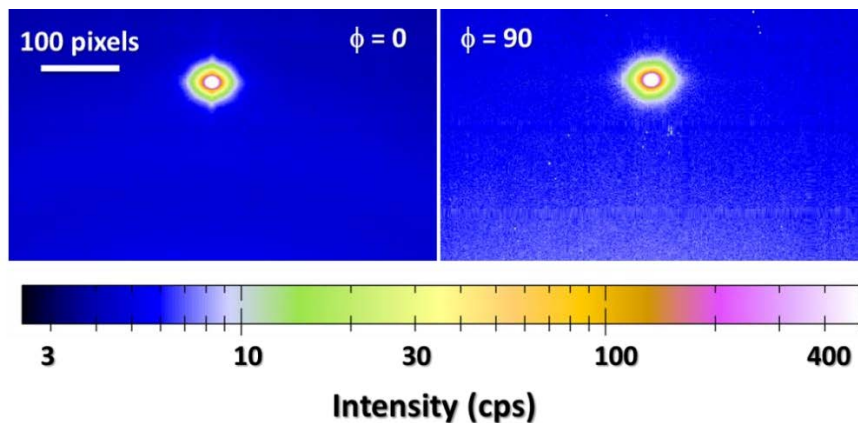


**Figure 5-22:** MT reflections are not visible in the sample grown at  $580^\circ\text{C}$ , for both azimuth  $0^\circ$  and  $90^\circ$ .

The absence of MT at such a high growth temperature was observed by Lin *et al.*<sup>[LiHS03]</sup> for the TmP/GaAs system which is in agreement with the prediction of Ernst and Pirouz.<sup>[ErPi88]</sup> Narayanan *et al.* have also observed the reduction of MT in GaP grown on Si (001) at high growth temperature (560°C).<sup>[NSBM99]</sup>

The correlation lengths of MT are estimated using the method depicted in **Figure 5-19**. **Table 5-1** resumes the measurement results for the longitudinal and transversal correlation lengths of MT in the 3 samples in which MT streaks are found. The results suggest that MT correlation lengths increase with increasing growth temperature. As the thickness of the GaP epilayer is 20 nm, the average length of MT found in the sample grown at 450°C is  $\approx 22$  nm meaning that most of MT propagate to the surface.<sup>[NRGL12b, NRGL12a, NRLC12]</sup>

**Table 5-1:** Longitudinal and transversal correlation lengths of MT estimated from MT streaks for the 3 GaP/Si samples grown at different temperature.<sup>[NRGL12b]</sup>

$T_g$ (°C)	350	400	450
Longitudinal CL (nm)	$16.5 \pm 1.0$	$20.03 \pm 1.0$	$21.86 \pm 1.0$
Transversal CL (nm)	$1.90 \pm 0.1$	$2.13 \pm 0.1$	$3.27 \pm 0.1$

Assuming that the MT volume density is proportional to their integrated intensity, one can relatively compare the MT volume density in each sample by measuring the corresponding integrated intensity of MT reflections. To this end, one of the four MT variants on each sample has been measured. The integrated intensity of this MT reflection is measured as follow (see **Figure 5-23**): an ROI (region of interest) is defined to measure the integrated intensity of the MT reflection (ROI<sub>2</sub> in the figure). This region counts the MT intensity and the background noise. To subtract the noise, two other ROI are defined: one upper and one under the MT region (ROI<sub>1</sub> and ROI<sub>3</sub>) whose size is equal to a half of the size of the ROI<sub>2</sub>. The sum of (ROI<sub>1</sub> + ROI<sub>3</sub>) is considered as equivalent to the total noise inside the ROI<sub>2</sub>. The final integrated intensity of this MT reflection is calculated as:  $I_{MT} = ROI_2 - (ROI_1 + ROI_3)$ .

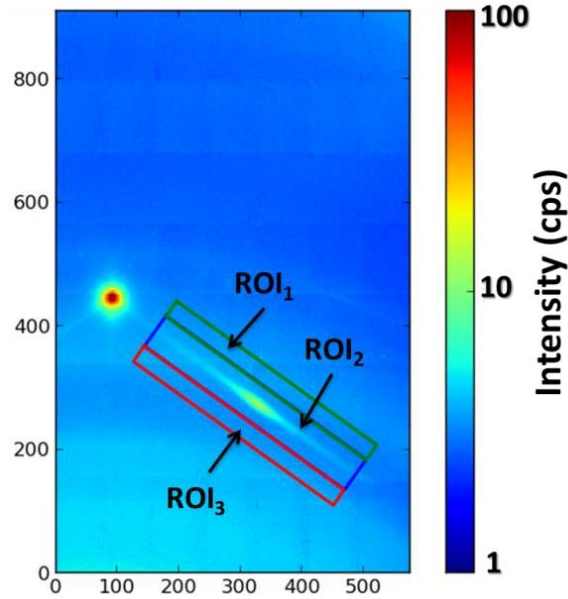


**Figure 5-23:** Measurement of integrated intensity of MT reflection. ROI<sub>1</sub> and ROI<sub>3</sub> measure the background noise, ROI<sub>2</sub> measures the sum of MT integrated intensity and noise. MT integrated intensity is deduced from  $I_{MT} = ROI_2 - (ROI_1 + ROI_3)$ .

Since the sample grown at 580°C does not reveal any MT reflection, we have considered its MT integrated intensity is zero. The MT integrated intensity is plotted as a function of the growth temperature (**Figure 5-24**). Assuming a thermally activated process, the data have been fitted with the function:

$$I = \frac{I_0}{1 + Ce^{-\frac{E}{k_B T}}} \quad (\text{Eq. 33})$$

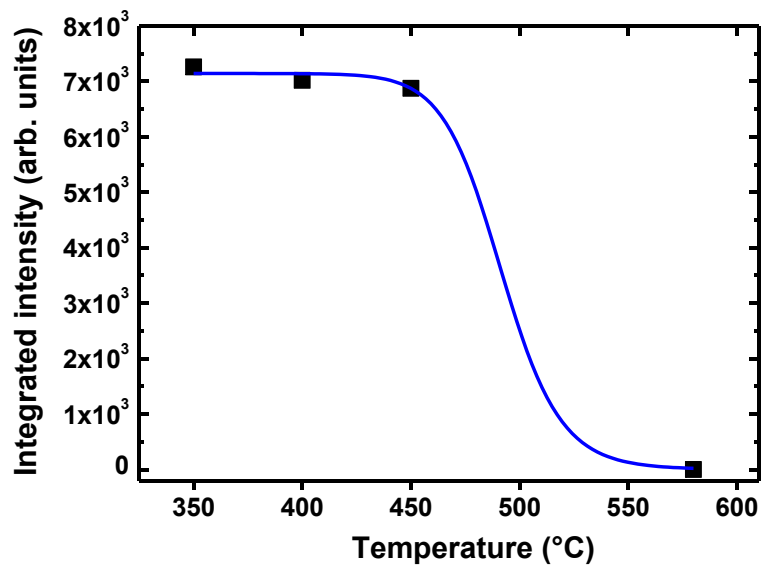


**Figure 5-24:** MT integrated intensity versus growth temperature.

The activation energy  $E$  issued from the fitting is  $3.7 \pm 1$  eV. This high activation energy requires high growth temperature so that atoms can gain sufficient mobility to arrange themselves into correct positions. This energy may be attributed to the activation energy of the self-diffusion of gallium on silicon surface. The activation energy for the self-diffusion of Ga in several mediums is reported in **Table 5-2**.

**Table 5-2:** Activation energy of Ga self-diffusion in different mediums.

	Activation energy (eV)	References
Ga self-diffusion in GaAs	4.24	[WHHE96]
Ga self-diffusion in GaP	4.5	[WWHH97]
Ga diffusion in undoped Si	3.5	[Hull99]
Ga diffusion in B-doped Si	3.85	[Hull99]

As explained earlier, MT are directly related to stacking error of III-V atoms on {111} lattice planes. These planes are formed during the early deposition stage of GaP on Si substrate from the step edges, contaminants or from the 3D nucleation of GaP themselves. At low temperature, atoms are not sufficiently mobile to arrange themselves into correct positions, they tend to stay where they arrive and may occupy incorrect positions, leading to the formation of stacking accident. At higher growth temperature, the higher mobility allows atoms to move to stable positions and reduces stacking error leading to a lower MT density. However, high growth temperature also leads to rough surface, as reported in **Figure 5-25**, which is not suitable for subsequent optical device development.

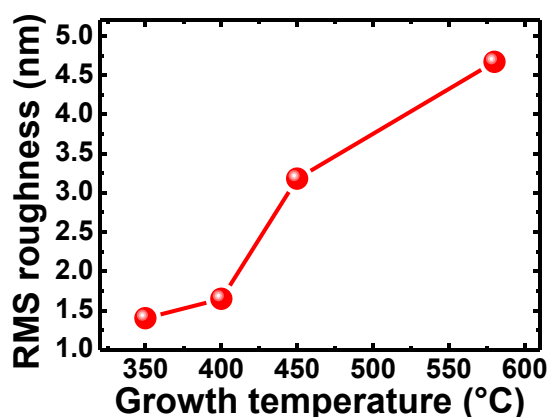


**Figure 5-25:** RMS surface roughness of the GaP/Si samples grown on 4°-off Si (001) substrate with different growth temperature. High temperature leads to high surface roughness. Connected line serves for the eyes guiding.

The increase of MT correlation lengths with  $T_g$  as reported in **Table 5-1** can be explained by the larger diffusion length of adatoms at higher temperature. Recent result in our laboratory shows that MT density is very sensitive to the quality of the initial Si surface. Works are in progress to verify this observation.

**(b) TEM study**

TEM images have been performed on these samples in cross-section and plan-view modes. Cross-section images are obtained by projecting the electron beam along the  $[-110]$  direction. **Figure 5-26** shows high resolution TEM images of the sample grown at 350°C (a) and 580°C (b). One can see that MT and SF are originated from the GaP-Si interface in the sample grown at 350°C. They propagate through the epilayer and emerge to the surface. For the sample grown at 580°C, the GaP-Si interface is difficult to be distinguished; the growth is thus very coherent. SF and MT are not observed in this image.

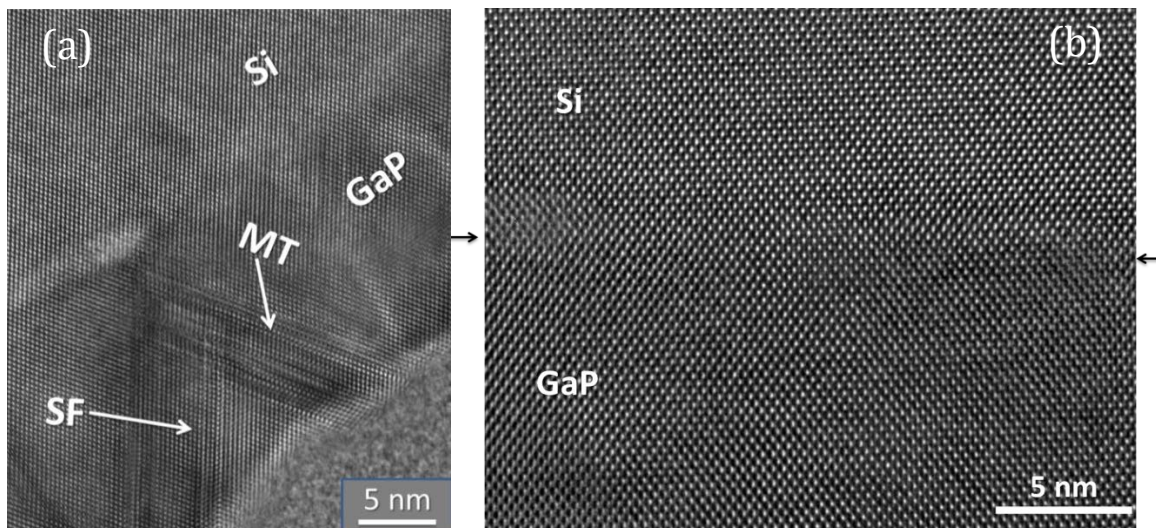


**Figure 5-26:** Cross-section high resolution TEM images of 20 nm thin GaP/Si samples grown at 350°C (a) and 580°C (b).

For a statistic analysis, plan-view TEM images have been performed selecting the  $\{111\}$  diffraction spots. Preliminary measurements are performed on the samples grown at 350, 450 and 580°C. **Figure 5-27** shows the results of these measurements in which MT appear in white. As one can observe on these images, MT density is progressively reduced in increasing the growth temperature. The preliminary results of MT quantification using the plan-view technique are reported in **Table 5-3**. These results indicate a strong reduction of MT for the sample grown at 580°C with respect to the case

of samples grown at lower temperature. Secondly, there is a slight enlargement of the MT surface with the increasing of the growth temperature. This confirms the results previously observed by XRD analysis.

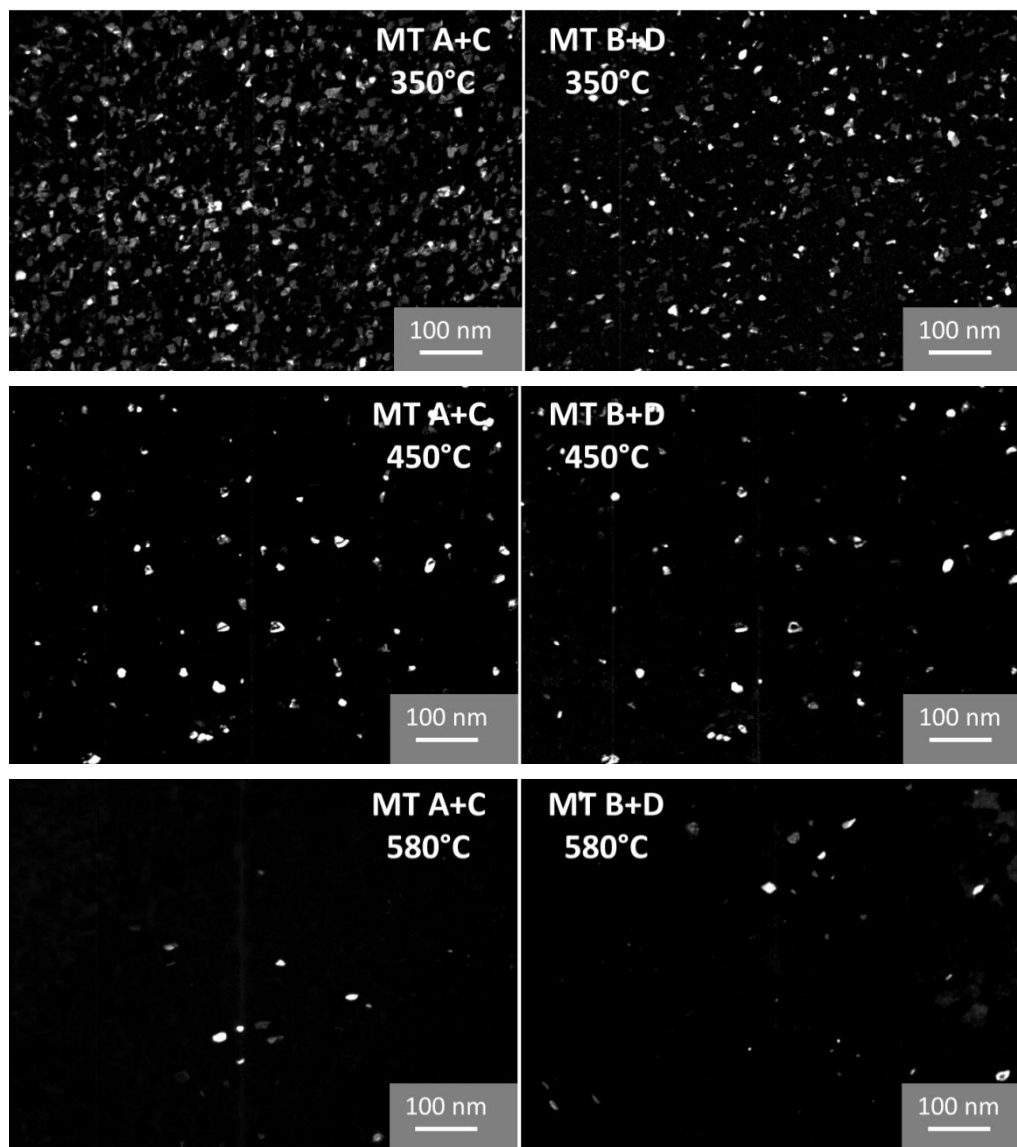


**Figure 5-27:** Plan-view TEM images obtained selecting the {111} diffraction spots. White spots in these images correspond to MT.

**Table 5-3:** Measurement of the MT average surface and surface density from TEM plan-view technique.

$T_g$ (°C)	MT A+C		MT B+D	
	Average surface	Surface density	Average surface	Surface density
350	~65 nm <sup>2</sup>	~12 %	~55 nm <sup>2</sup>	~8 %
450	~80 nm <sup>2</sup>	~1.5 %	~75 nm <sup>2</sup>	~1.5 %
580	~80 nm <sup>2</sup>	~0.5%	~70 nm <sup>2</sup>	~0.5 %

### 5.3.3 Microtwins anisotropy: a quantitative study

#### (a) Samples

The aim of the present part consists in quantitatively studying the influence of the first monolayer (ML) and the Si buffer layer on the behavior of MT. The samples consist in non-optimized 45 nm thin GaP layer grown by MBE on Si (001) substrate with or without a silicon buffer layer. The silicon substrates are cleaned by our optimized ex-situ chemical cleaning process and a 2.5  $\mu\text{m}$  thick silicon buffer layer is grown at 800°C and high pressure mode (see chapter 4 – silicon homoepitaxy). The growth is initiated by changing the chemical nature of the first atomic layer (Ga, P, Sb, Al). The GaP layers have been grown in a two-step procedure: the first 5 nm is grown at 350°C and the second layer is grown at 480°C. This two-step growth is believed to improve structural properties of the epilayer.<sup>[BiMT96, DGSS08, GBRU09, LiHF11, VBWO11]</sup> **Figure 5-28** schematically depicts the sample structure for this study. Note that these samples were grown without MEE due to technical issues.

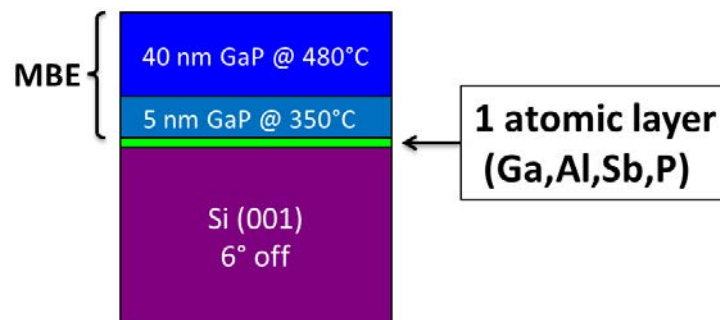


**Figure 5-28:** Sketch of GaP/Si samples with or without Si buffer layer grown on Si (001) 6° off substrate.

#### (b) MT quantification using Synchrotron radiation and XPAD detector

##### Attention for 6° off substrates

Since the Bragg angle for GaP (002) reflection is 8.1735° ( $\lambda = 0.7749 \text{ \AA}$ , GaP lattice constant 5.4505  $\text{\AA}$ ), if we take into account the substrate miscut (6°), the incident angle ( $\omega$ ) for the Bragg GaP (002) in the azimuth [110] (down stair of the steps) is in the order of 2° (**Figure 5-29 a**). For the MT (0.33 0.33 1.66),  $\omega$  is in the order of 1°. This very grazing incident angle highly increases the effective diffraction volume (**Figure 5-29 c**) and gives significant noise signal, thus decreases the efficiency of defects quantification.

To avoid this effect, we have chosen to measure MT spots above the GaP (002) spot (i.e. MT (1.66 1.66 2.66) – see **Figure 5-17**). Special attention has also been paid to not damage the detector when scanning close to the {113} silicon spots.

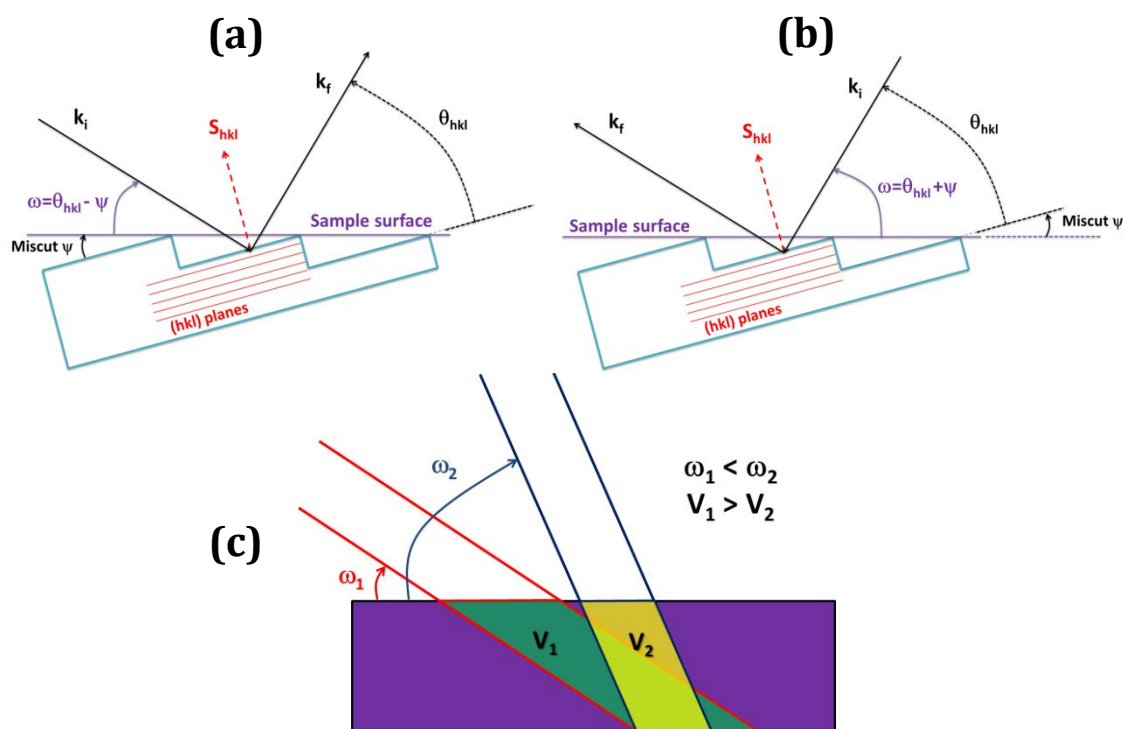


**Figure 5-29:** (a) Incident beam goes down stairs: decrease  $\omega$  (b) Incident beam goes up stairs: increase  $\omega$  (c) high incident angle decreases the effective diffraction volume.

### Quantification procedure:<sup>1</sup>

The quantification consists in measuring the entire three dimensional MT streaks. Let's imagine the MT streaks in reciprocal space as depicted in **Figure 5-30**. The intersection of the streaks with the Ewald's sphere is recorded by XPAD detector and this represents a slice cut of the MT streaks. We can perform a rocking scan (scanning in  $\omega$  by rocking the sample) around a MT reflection to move the MT streak towards the Ewald's sphere in order to integrate the entire streak volume (see **Figure 5-30**).

<sup>1</sup> In this section we will show the results of one sample to demonstrate the measurement method.

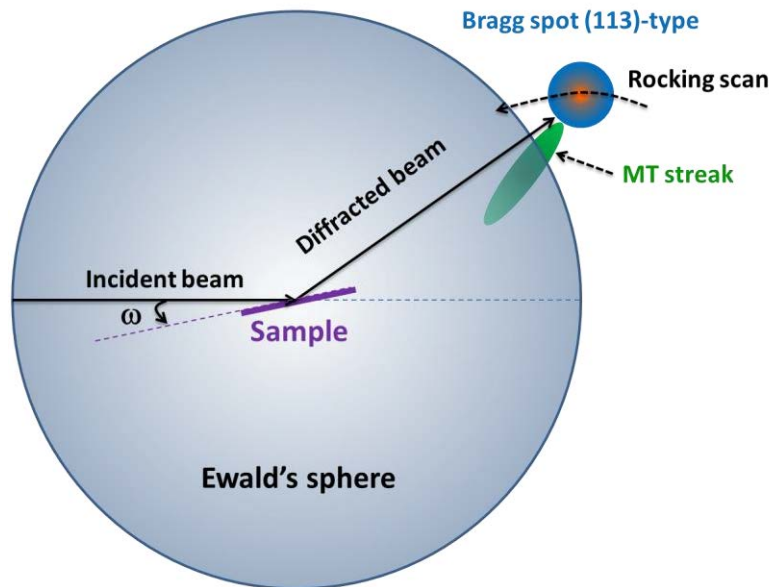


**Figure 5-30:**  $\omega$  scan (or rocking scan) of MT reflections – each scan corresponds to an intersection of the MT streaks with the Ewald's sphere. The intersection gives a slice of the MT streaks. This slice is captured by the XPAD detector.

We can capture 2 MT streaks for one azimuth. It is therefore necessary to perform the measurement on the two perpendicular azimuths to record the 4 MT variants. **Figure 5-31** depicts the azimuthal alignment of the X-ray beam with respect to the crystallographic directions of the sample and the recorded MT variants for each azimuth. The paper's plane represents the surface of the XPAD detector. Looking at this figure, we can identify the corresponding MT variants.

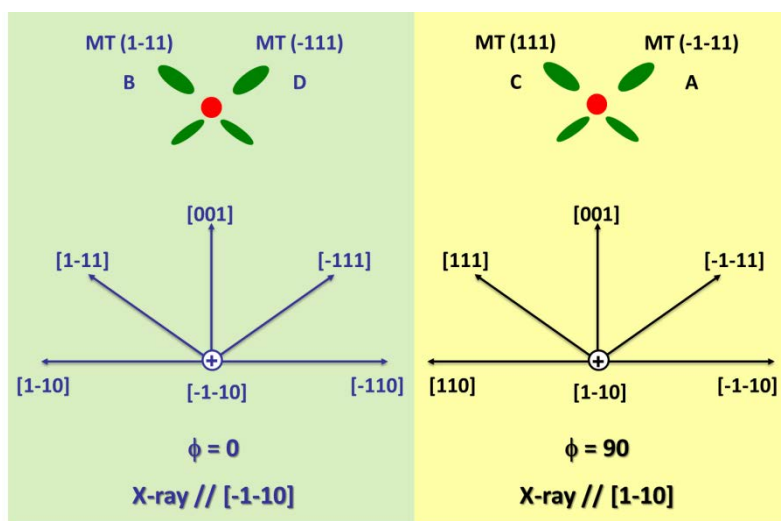


**Figure 5-31:** Azimuthal alignment and the corresponding MT variants to be captured for each azimuth. The paper plane represents the surface of the XPAD detector.

For each MT variant, 11 images have been captured around its center position with a step size of  $0.25^\circ$  in  $\omega$  (or Eta in the notion of the beamline's goniometer). **Figure 5-32** shows the rocking scan images of MT-B (left) and MT-D (right) at the azimuth  $\phi = 0$  for the sample S1180 (GaP/Si with  $6^\circ$  off substrate,  $2.5 \mu\text{m}$  thick Si buffer layer, Ga-prelayer). The MT-A and MT-C (not shown here) are measured the same way in the azimuth  $\phi = 90$ .

From these images, we can perform the measurement of the MT integrated intensity for each variant. The measurement principle which consists in defining 3 ROI is the same as described in the previous section (see **Figure 5-23** for explanation). **Figure 5-33** gives an example for the measurement of MT-B and MT-D. Measurement from each image gives one data point. The 11 images give 11 data points for the “rocking curve” presented in **Figure 5-34**. We have then fitted these data points with a Pseudo-Voigt function and calculated the area under the fitted curve. That means we have entirely integrated the 3D MT streaks. The calculated area under the fitted curve represents the integrated intensity of the corresponding MT which is proportional to their overall volume.<sup>[QKNP13]</sup>

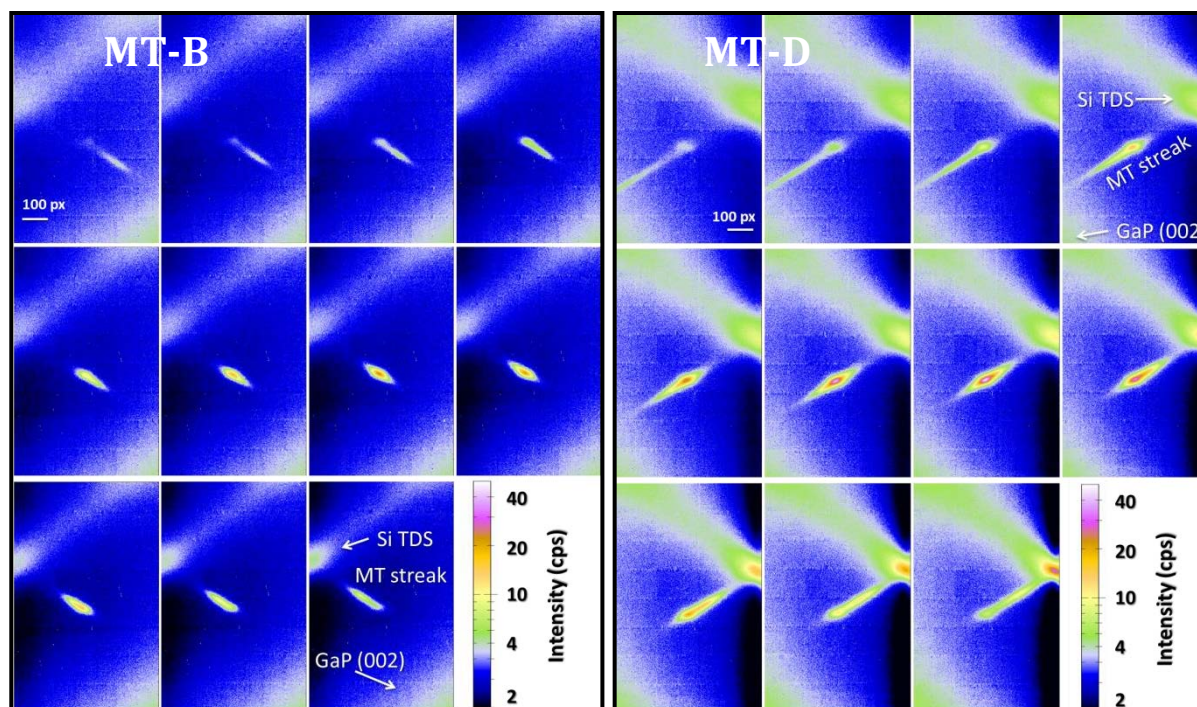


**Figure 5-32:** ( $\phi=0$ ) Rocking scan around the MT-B (left) and MT-D (right) reflection for the sample S1180 (GaP/Si with a silicon buffer layer,  $6^\circ$  off substrate, Ga-prelayer). Each image corresponds to a  $0.25^\circ$  increment in  $\omega$ . The upper spot in every image is the Si (1-13) thermal diffuse scattering (TDS) signal and the lower spot is the GaP (002) reflection – as indicated in each figure.

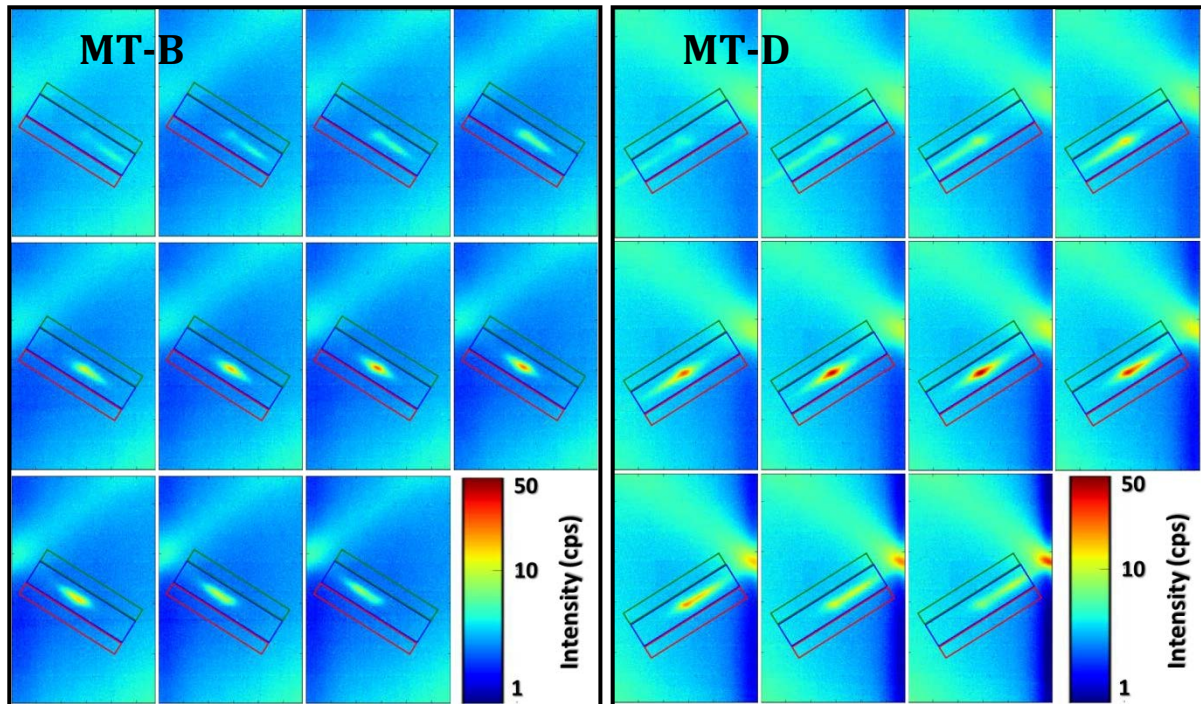


**Figure 5-33:** Integrated intensity measurement of MT-B (left) and MT-D (right) for the sample S1180.

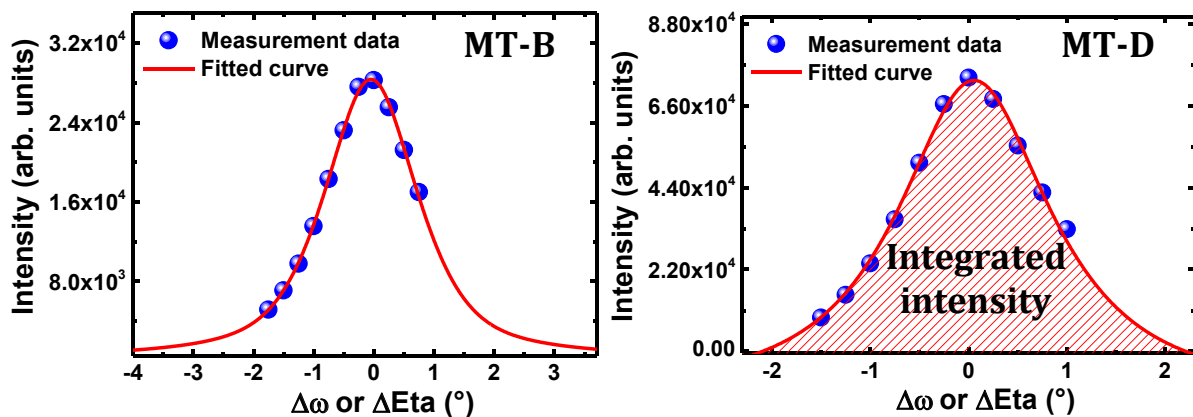


**Figure 5-34:** Sample S1180 – MT-B and MT-D. Measurement from each image gives one data point. Integrated intensity of each variant is obtained by calculating the area under the fitted curve. This means a 3D integration of the entire MT streaks.

### ***(c) MT quantification using laboratory XRD***

Synchrotron high flux source and large area XPAD detector offer ideal conditions to study planar defects in a fast and efficient way, but such a large instrument is not always available (in the framework of this thesis we have obtained 5 days per year to do experiments on the beamline D2AM - ESRF). It is therefore important for us to develop a methodology using laboratory source to study the MT. Pole figure method is found to be efficient for MT quick evaluation. In order to obtain a quick evaluation of MT density, we

have measured the integrated intensity of the 4 MT variants and the integrated intensity of the Si (111). The normalization of the integrated intensity of MT with Si(111) gives an indicator to relatively evaluate MT density from one sample to another. To this end, we have represented the pole figure data in a 2D plot instead of a polar plot. The measurement principle of MT integrated intensity from pole figures is presented in **Figure 5-35**. In this figure, the 4 strong reflections in the upper part correspond to Si {111} reflections; whereas the other 4 weaker reflections in the lower part correspond to the 4 MT variants. The background noise is considered homogeneous around the diffraction spots. **Figure 5-35** demonstrates the measurement of the Si(111) spot for example. The integrated intensity of the studied spot is measured by subtracting average noise inside the ROI1:

$$\text{Average noise/pixel: } N_{pp} = \frac{ROI2 - ROI1}{Area_{ROI2} - Area_{ROI1}} \quad (\text{Eq. 34})$$

$$\text{Integrated intensity of the spot} = ROI1 - N_{pp} * Area_{ROI1} \quad (\text{Eq. 35})$$

The fractional volume density of each MT variant can be evaluated by normalizing their integrated intensity with the intensity of the Si(111). Note that this is a relative indicator to evaluate MT density from one sample to another:

$$\%MT = \frac{I_{MT}}{I_{Si}} \times 100 \quad (\text{Eq. 36})$$

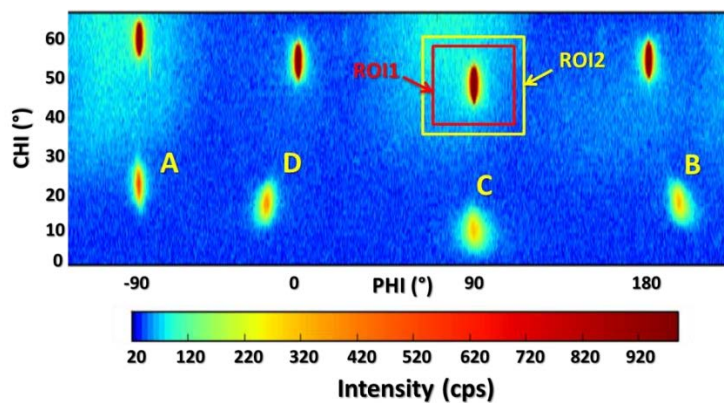


**Figure 5-35:** Sample S1322 – Demonstration of measurement of integrated intensity from pole figure. The 4 strong reflections in the upper part correspond to Si (111) reflection; the other 4 weaker reflections in the lower part correspond to the 4 MT variants. The integrated intensity of each spot is measured by two ROI as indicated in the figure. (ROI2 - ROI1) represents background noise. This figure demonstrates the measurement of the Si(111) spot. Measurement of MT spots is performed in the same way.

For an absolute evaluation of MT volume density, we can perform the rocking curves (RC) on the 4 variants and normalize their integrated intensity (measured from RC) with that of the GaP (002), supposing that the GaP epilayer contains only perfect lattice planes (00 $l$ ) and MT planes. This method is not presented in this thesis, except for the comparison of results obtained from Synchrotron and laboratory measurements. Works are in progress in our laboratory to improve and complete this method.

***(d) Correction of measurement data***

As explained earlier, the measurement on miscut substrates requires offsetting the incident angle  $\omega$  with respect to nominal (symmetric) case in order to meet the right diffraction angle of the corresponding  $hkl$  planes. This offset changes the effective penetration depth of the X-ray in the layer. We have to normalize the diffracted intensity with the expected one in the symmetric case.

**Figure 5-36** represents asymmetric scattering conditions for a thin layer of thickness  $T$ . Let's consider the integrated intensity of the diffracted beam and take into account the linear absorption coefficient:<sup>[Domp12, NiMc11]</sup>

$$I_{\text{int}} = \frac{\Phi_0}{\dot{\omega}} e^{-\mu(l_1+l_2)} A_0(dl_1) r_0^2 \frac{\lambda^3 F_T^2}{v_a^2} P \cdot L \quad (\text{Eq. 37})$$

where  $A_0(d\mathbf{l}_1)$  the elementary crystal volume  $d\mathbf{V}$  interacting with the effective flux density at the depth  $\mathbf{z}$ ,  $\Phi_0$  the incident X-ray flux,  $\dot{\omega}$  the angular rotation speed of the sample (in  $rad/s$ ),  $r_0$  the classical radius of electron and  $r_0^2$  the scattering cross-section of electron,  $\lambda$  the incoming X-ray wavelength,  $v_a$  the unit cell volume of the crystal that can be expressed in the same unit as  $\lambda$ ,  $F_T^2$  the reflection intensity factor that takes into account the structure factor and the Debye-Waller factor,  $\mu$  the linear absorption coefficient of the material,  $P$  and  $L$  respectively the polarization and the Lorentzian factor.

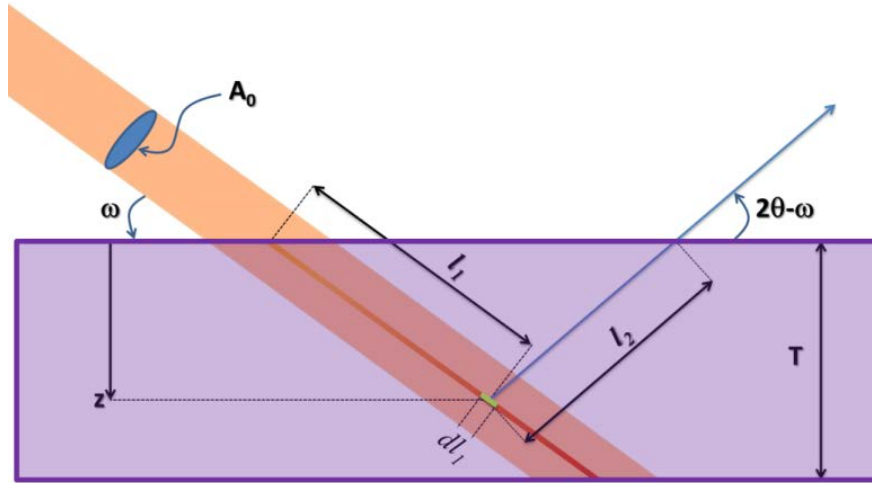


**Figure 5-36:** Sketch of asymmetric scattering conditions on a thin layer (T).

As shown in **Figure 5-36** we can see that:

$$\begin{aligned}
 l_1 &= \frac{z}{\sin \omega} \\
 l_2 &= \frac{z}{\sin(2\theta - \omega)} \\
 dl_1 &= \frac{dz}{\sin \omega}
 \end{aligned} \tag{Eq. 38}$$

Replacing (Eq. 38) into (Eq. 37) leads to:

$$I_{\text{int}} = \frac{\Phi_0}{\dot{\omega}} A_0 e^{-\mu z \left( \frac{1}{\sin \omega} + \frac{1}{\sin(2\theta - \omega)} \right)} \cdot \frac{dz}{\sin \omega} r_0^2 \frac{\lambda^3 F_T^2}{v_a^2} P \cdot L \tag{Eq. 39}$$

Integration of (Eq. 39) with the depth  $z$  varies from 0 to  $T$ , we get:

$$I_{\text{int}} = \frac{\Phi_0}{\dot{\omega}} A_0 \frac{1}{\sin \omega} r_0^2 \frac{\lambda^3 F_T^2}{v_a^2} P \cdot L \int_{z=0}^T e^{-\mu z \left( \frac{1}{\sin \omega} + \frac{1}{\sin(2\theta - \omega)} \right)} dz \tag{Eq. 40}$$

$$I_{\text{int}} = \frac{\Phi_0 A_0}{\dot{\omega}} \frac{1}{\mu \sin \omega + \sin(2\theta - \omega)} \left[ 1 - e^{-\mu T \left( \frac{1}{\sin \omega} + \frac{1}{\sin(2\theta - \omega)} \right)} \right] r_0^2 \frac{\lambda^3 F_T^2}{v_a^2} P \cdot L \tag{Eq. 41}$$

The correction factor is calculated from the penetration depth including the absorption effect ( $L$ ). This term is normalized with the one in the symmetric case (i.e.  $\omega = 2\theta - \omega$ ):

$$L = \frac{1}{\mu} \frac{\sin(2\theta - \omega)}{\sin \omega + \sin(2\theta - \omega)} \left[ 1 - e^{-\mu T \left( \frac{1}{\sin \omega} + \frac{1}{\sin(2\theta - \omega)} \right)} \right] \quad (\text{Eq. 42})$$

In this thesis we use the parameters (absorption coefficient, Debye-Waller factor, atomic scattering factor, etc.) in the reference [HeGD93]. Observation of MT in the azimuth  $\phi=0$  (MT-B and MT-D) results in offsetting  $\omega$  because of the miscut direction, their measured intensities thus have to be corrected. On the other side the MT-A and MT-C are observed in the azimuth  $\phi=90$ , in this alignment we have to offset  $\chi$  in order to put the diffraction spots in the center of the XPAD detector.[NRLC12] This offset is considered not to significantly change the penetration depth of the X-ray with respect to the symmetric case; their intensities are therefore not subjected to be corrected.

### ***(e) Evidence of MT anisotropy***

A quantitative study of the 4 MT variants on each sample shows an anisotropic behavior, which means the density of MT in the 4 variants is not the same. **Figure 5-37** shows a comparison of the 4 MT variants in the same sample (measured by Synchrotron source). These images are obtained by the sum of the 11 images from the rocking scan as described above for every variant. One can observe directly on this figure that the MT-A presents the highest volume density. These images are measured directly with the XPAD detector without correction due to difference in penetration depth and absorption effect. The data correction has to be done in order to really compare their volume density.

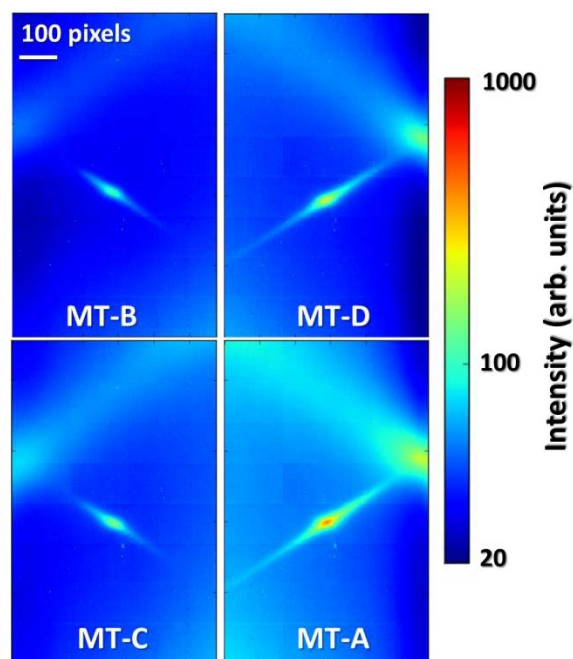


**Figure 5-37:** Superposition of the 11 images for each MT variant - Sample S1180 ( $6^\circ$  off, with Si buffer layer, Ga-prelayer) – MT-A presents the highest density. These data are not corrected by the penetration depth and absorption effect.

**Figure 5-38** reports the quantitative study of MT after correction by the penetration depth and absorption effect. The samples presented here have different prelayer (Ga, P, Sb, Al) with a silicon buffer layer on  $6^\circ$ -off Si (001) substrates.

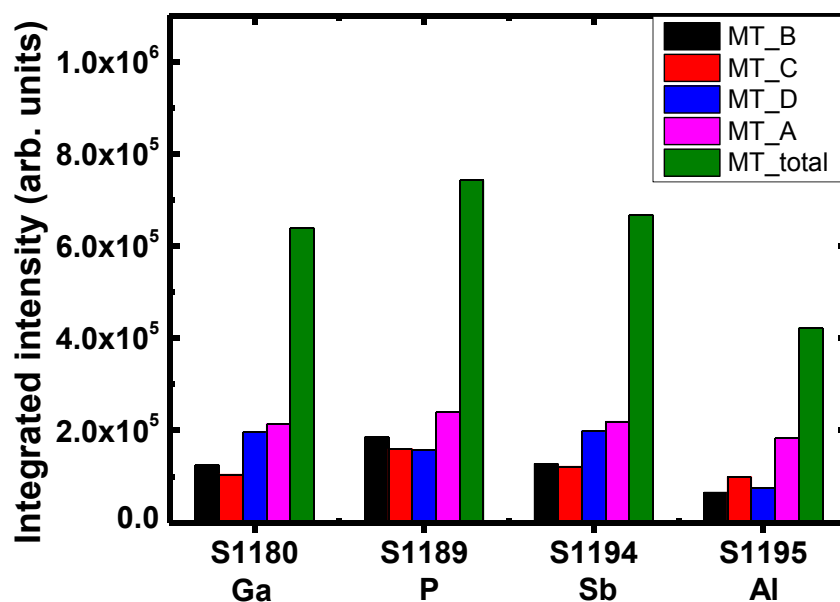


**Figure 5-38:** Anisotropy of MT on 45 nm thick GaP/Si samples grown with different prelayer on  $6^\circ$ -off Si (001) substrates (corrected data). All the samples have a Si buffer layer grown by UHV/CVD before transferring to the MBE chamber for the growth of GaP. MT\_total is the sum of the 4 variants.

The anisotropy feature is present in all of these samples where MT\_A is always the highest contribution. The same anisotropic behavior has been observed by Skibitzki *et al.*<sup>[SHYZ12]</sup> The sum of the four variants is also plotted (MT\_total) which shows that the sample with Al-prelayer (S1195) has lowest MT density whereas P-prelayer reveals highest MT density. The Al-prelayer effect is also studied in the literature.<sup>[GWNW90, LiHF11, SAPJ96]</sup> They claimed that the stronger bonding between Al-Si and Ga-Si may account for better pinning of AlGaP to Si. This results in 2D nucleation and thus reduces the stacking error and twinning effect.

An isotropic behavior is visible for the sample grown on nominal substrate (i.e.  $0.15 \pm 0.5^\circ$  miscut) as expected because of the equal number of steps oriented in the both [110] and [1-10] directions – see **Figure 5-39**. All samples presented in **Figure 5-39** are grown with Ga-prelayer. The effect of the silicon buffer layer is also remarkable. As shown in this figure, the presence of the Si buffer layer reduces the MT density by  $\sim 25\%$ . Here we attribute the increased formation of MT for the sample without Si buffer layer to the contamination and surface roughness-induced defects. MT density in the sample grown on nominal substrate is roughly the same as in the sample grown on  $6^\circ$ -off substrate (S1166 versus S1180).

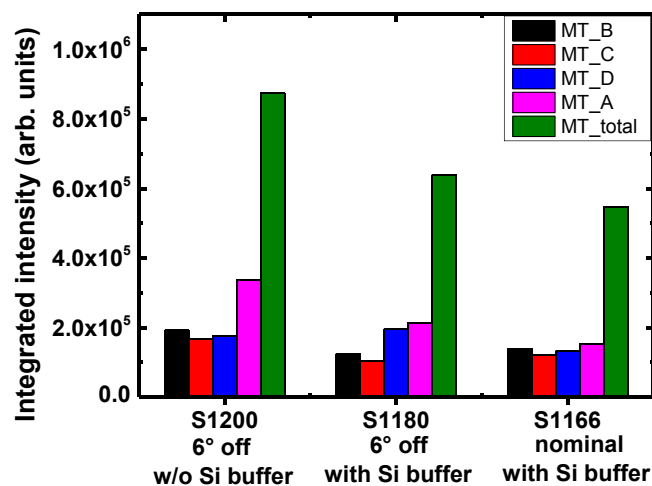


**Figure 5-39:** The presence of a Si buffer layer reduces MT density by  $\sim 25\%$  (S1200 v.s. S1180). The anisotropy effect is less visible for the sample grown on nominal substrate (S1166). All these samples are grown using Ga-prelayer.

MT quantification using laboratory source reveals the same results as obtained from Synchrotron source. For a visual comparison, **Figure 5-40** (a) presents the 4 MT variants recorded from Synchrotron source. This sample is then analyzed by laboratory XRD setup using pole figure technique as described previously (see **Figure 5-40** (b)).

MT quantification of the 4 variants is also performed and their anisotropy is compared in term of relative fraction (i.e. normalization with their total density (sum of the four variants)). **Figure 5-41** shows the comparison of MT anisotropy measured by Synchrotron and laboratory setup methods. In this figure, the measurement from the lab setup is performed using the RC method. The same results obtained by the two methods confirm the efficiency of using XRD lab-setup for MT analysis.

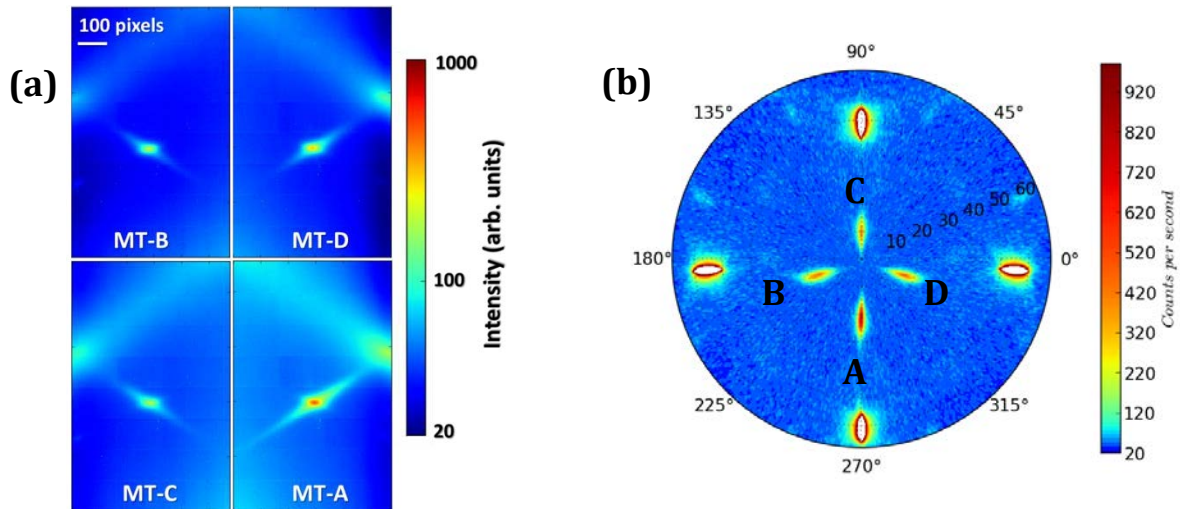


**Figure 5-40:** (a) Sum of the 11 images for every MT variant – sample S1200 (6°-off, without Si buffer, Ga-prelayer) – reveals the anisotropic behavior of the 4 variants. MT-A always presents highest density. (b) Pole figure measurement around GaP (111) on sample S1200 using laboratory source – the intensity is presented in log scale. The anisotropic behavior of the 4 MT variants is in agreement with Synchrotron measurement.

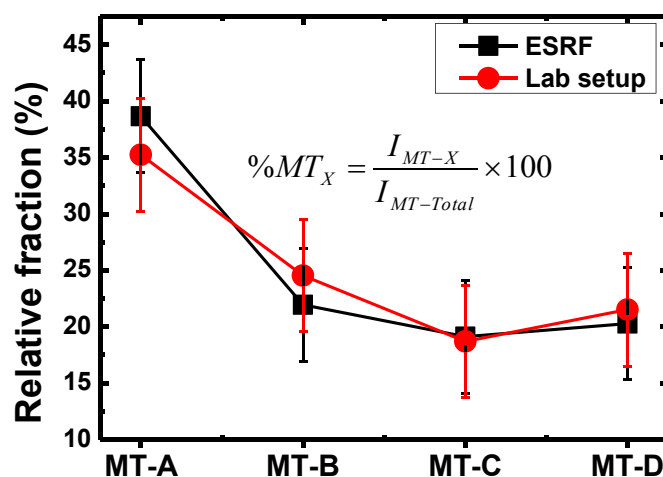


**Figure 5-41:** Relative fraction (percentage) of each variant with respect to their total density ( $\%MT_X = \frac{I_{MT-X}}{I_{MT-Total}} \times 100$ ) – sample S1200. The measurement from lab setup used the RC method. The connected lines are shown for the eyes guiding.

The anisotropic behavior of the 4 MT variants is not very clear till date. The absence of anisotropy on the nominal substrate may be attributed to the equal probability of atomic steps in the [110] and [1-10] direction on the Si surface. This suggests a relation between the MT anisotropy and the orientation of steps Si surface. Furthermore, this anisotropy may also be attributed to the anisotropy of the facets on the GaP islands, as claimed by Narayanan *et al.*<sup>[NMSB00]</sup> They suggested that the {111} facets on the islands terminated by Ga are larger than that terminated by P, because the P-terminated {111} facets have higher surface energy due to the excess of dangling bonds. Their surface area tends to shrink down to reduce their surface energy. Stacking error on Ga-terminated facets can therefore increase the MT volume. Narayanan also claimed that in the case of nominal Si substrate, there's equal probability of faceted GaP islands elongated in the two mutual directions (i.e. [110] and [1-10]). This can lead to the isotropic behavior of MT on nominal substrates.

#### 5.4 Growth optimization of GaP/Si

This study is initiated by growing GaP on freshly prepared Si (001) 6°-off substrates. The growth sequences which consist in a two-step growth are schematically presented in **Figure 5-42**. The first sequence uses MEE technique which consists in alternative exposure of Ga and P. This low temperature MEE sequence is believed to promote 2D nucleation, thus prevent the formation of islands-induced defects.<sup>[TYST98]</sup> The second sequence is performed using conventional MBE technique at high temperature in order to suppress planar defects such as MT and APD.<sup>[BiMT96, DGSS08, GBRU09, LiHF11]</sup> The growth temperature in the MBE sequence is chosen high enough to limit planar defects, but low enough to be compatible with subsequent growth of lattice-matched GaPN layer (see chapter 2). Freshly prepared Si substrate is heated up to 800°C (pyrometer) in order to desorb hydrogen. The substrate's temperature is then ramped down to 350°C and Ga-initiated MEE sequence is started. After 40 ML thin GaP layer deposited by MEE ( $\approx 10$  nm), the substrate's temperature is increased under phosphorus pressure to 500°C and 35 nm thin GaP film is grown by MBE. The growth temperature is then ramped down to room temperature under phosphorus overpressure.

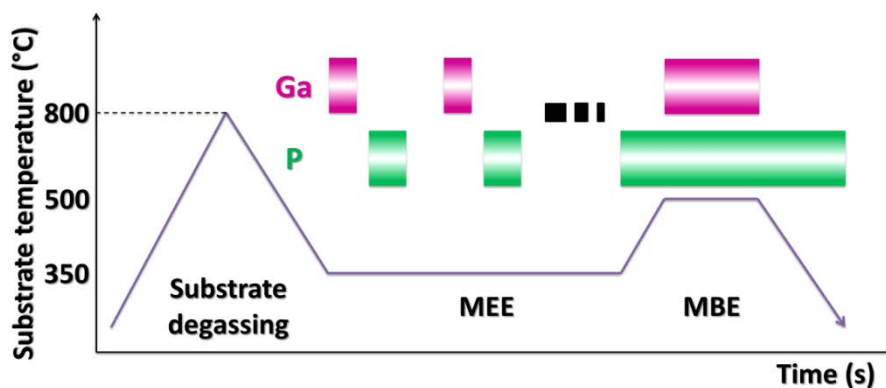


**Figure 5-42:** Two-step growth sequences of GaP on freshly prepared Si substrate.

### 5.4.1 Optimization of the MEE procedure

We have observed that optimization of the MEE step is paramount important to improve the surface and crystalline quality. As seen in **Figure 5-43**, a non-optimized MEE procedure leads to rough surface (RMS = 7.1 nm) and high MT density (fractional volume density evaluated  $\approx 12.62\%$ ).

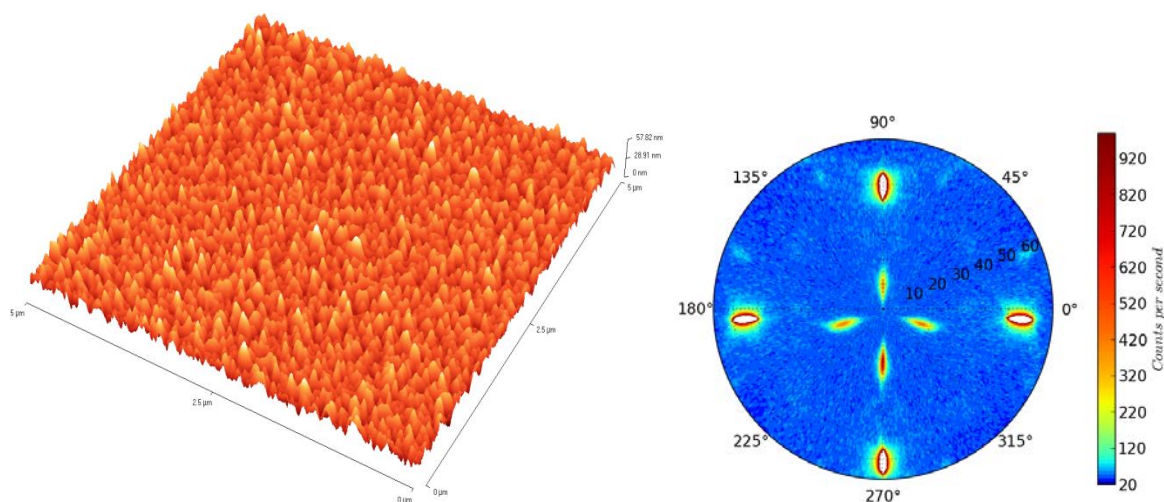


**Figure 5-43:**  $5 \times 5 \mu\text{m}^2$  AFM measurement (left) and pole figure (right) measured on non-optimized 45 nm thick GaP/Si(001)  $6^\circ$  off sample, without Si buffer, initiated by Ga. RMS roughness measured from the AFM image is 7.1nm. MT fractional volume density measured from the pole figure is 12.62 %.

A careful study of the MEE growth sequence is carried out as suggested by Grassman *et al.*<sup>[GBRU09]</sup> Ga-initiated layer is believed to provide smooth and two-dimensional nucleation and prevent surface-roughening due to reaction between phosphorus and silicon.<sup>[CSS004, NaA099]</sup> Ga-prelayer is also studied by Bi *et al.* who claimed the best results with respect to P, Al, As prelayer.<sup>[BiMT96]</sup> The total Ga dose per MEE cycle

is carefully studied because it is found to strongly affect the epilayer's smoothness and defects level.<sup>[GBRU09]</sup> Ga cell temperature is calibrated to provide a growth rate of 0.1 ML/s. After a growth interruption, the surface is exposed to phosphorus overpressure and the cycle is repeated. 20 ML thin GaP film is deposited for this study and AFM post-epitaxy analysis is performed. **Figure 5-44a,b** show AFM images of 20 ML thin GaP/Si samples with different amount of Ga per MEE cycle. Figure a) shows a very flat surface (RMS=0.226 nm). The excess of Ga dose per cycle leads to the formation of 3D islands on the surface which may correspond to Ga droplets (~16 nm high and ~300 nm large), as seen in figure b).<sup>[BTWC91, VPWK13]</sup> **Figure 5-44 (c)** shows the RMS surface roughness measured on  $5 \times 5 \mu\text{m}^2$  area with respect to Ga amount per cycle. The minimum of surface roughness is assumed to correspond to the expected 1 complete Ga atomic layer.

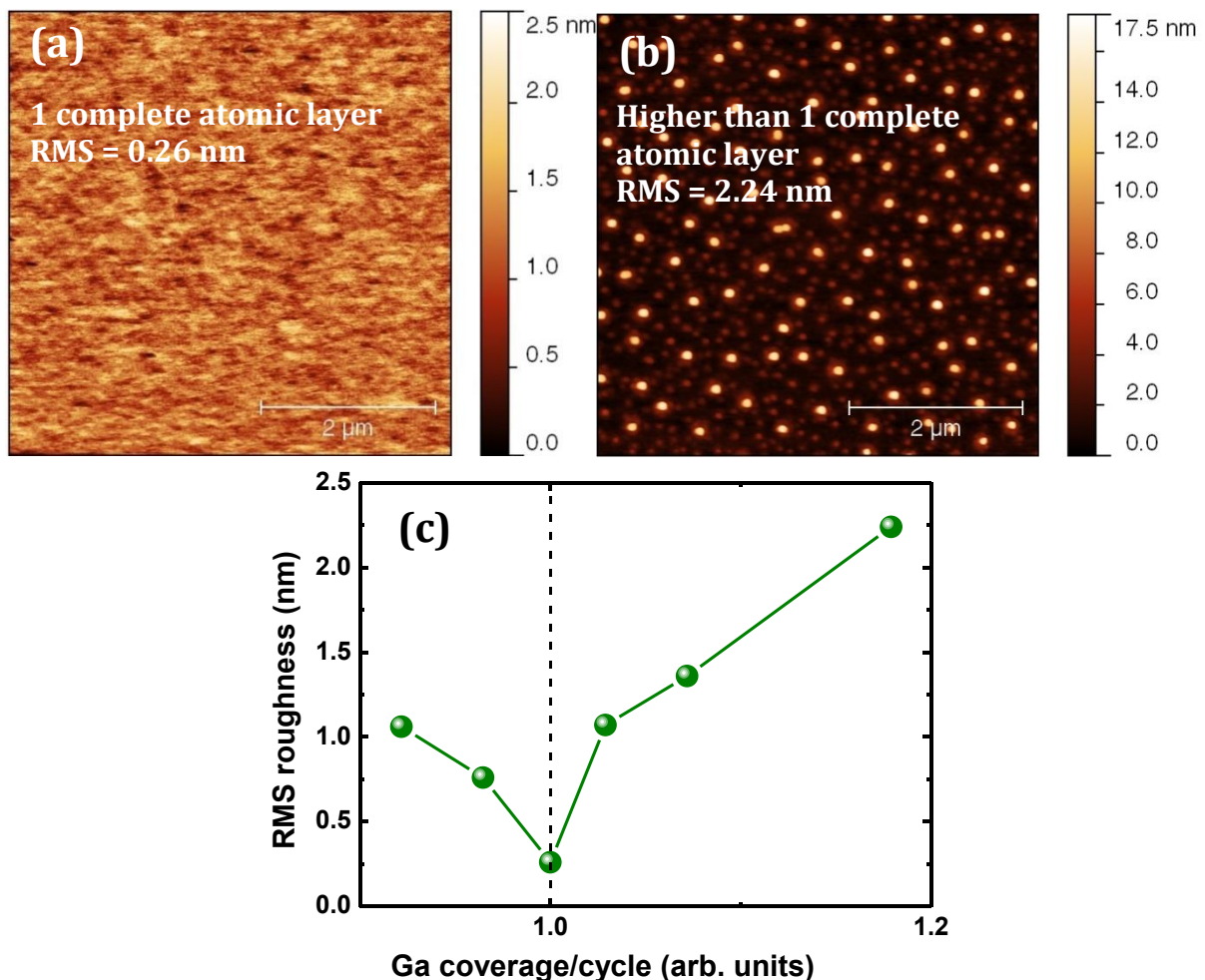


**Figure 5-44:**  $5 \times 5 \mu\text{m}^2$  AFM images of 20 ML thin GaP/Si samples grown by MEE with different Ga amount per cycle: 1 atomic layer (a) and  $>1$  atomic layer (b). AFM RMS surface roughness is plotted versus Ga coverage per cycle (c). The connected line is shown for the eyes guiding.

The optimal Ga dose is utilized to grow 40 ML of GaP by MEE and this provides a similar result (see **Figure 5-45 a**). The RMS roughness is measured to be 0.3 nm which is considered atomically flat and compatible for subsequent growth of smooth and defects-free GaP layers. Pole figure performed on this sample reveals very low MT density, as presented in **Figure 5-45b**). The fractional volume density estimated from this pole figure measurement is 1.04 %.

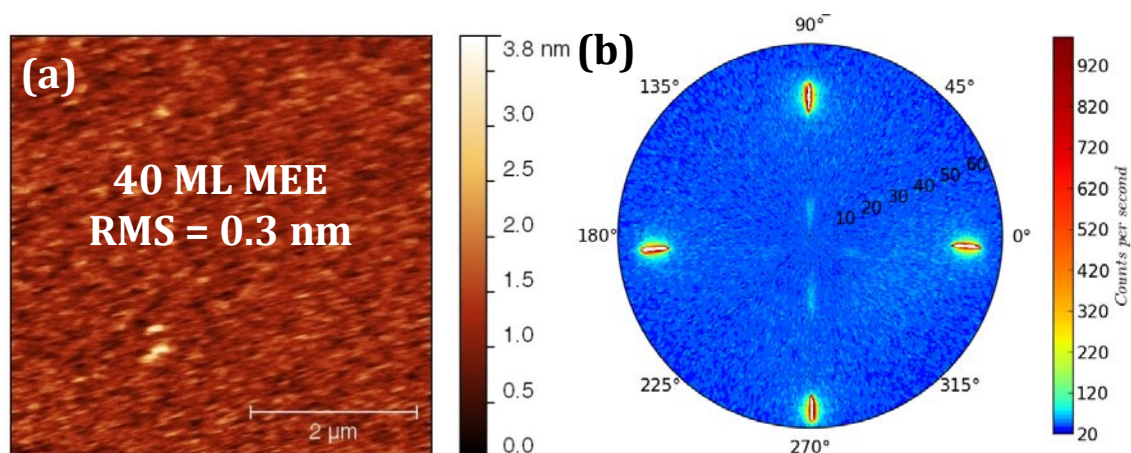


**Figure 5-45:** (a)  $5 \times 5 \mu\text{m}^2$  AFM images of MEE grown GaP/Si using optimal Ga dose per cycle (40 ML, RMS roughness = 0.3 nm); (b) Pole figure measurement on 40 ML MEE GaP/Si using the optimal MEE procedure. Microtwins fractional volume density is evaluated to 1.04 %.

## 5.4.2 Optimization of GaP MBE overgrowth

Optimal 40 ML MEE grown GaP nanolayer is followed by MBE growth of 35 nm thin GaP film. The total thickness of about 45 nm is under the critical thickness (45 – 95 nm).<sup>[TFWK10]</sup> The phosphorus flux and the growth rate are found to have an important impact on the film smoothness. Different growth conditions were tried with varying the V/III BEP ratio, growth temperature and growth rate. The results indicate that the surface roughness is strongly affected by the III-V growth conditions and nearly not by the Si surface quality. As an example, **Figure 5-46** shows AFM images of the samples grown with V/III ratio varied from 10 to 60. The RMS surface roughness is measured to be 2.59 nm, 6.38 nm and 7.86 nm, respectively for a, b and c.

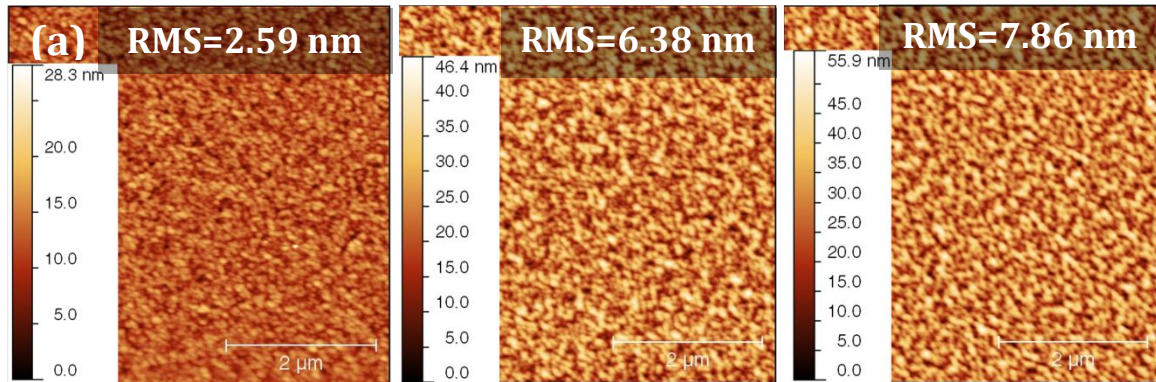


**Figure 5-46:**  $5 \times 5 \mu\text{m}^2$  AFM images measurement on GaP/Si sample with V/III ratio in the MBE sequence of 10, 30 and 60, respectively. The RMS roughnesses are 2.59 nm, 6.38 nm and 7.86 nm, respectively.

After optimization of the V/III ratio and the growth rate, we have obtained a GaP/Si reference sample. **Figure 5-47a)** shows the AFM image measured on the optimized sample. The measured RMS roughness is 0.3 nm which is considered atomically flat. Pole figure measurement has also been performed on this sample to check the defects level. As presented in **Figure 5-47b)**, the residual MT level is significantly reduced and their fractional volume density is measured to be 0.52 %. A sketch of the pseudo-substrate 45 nm thick GaP/Si is presented in **Figure 5-48** as a reference sample structure obtained from this work.

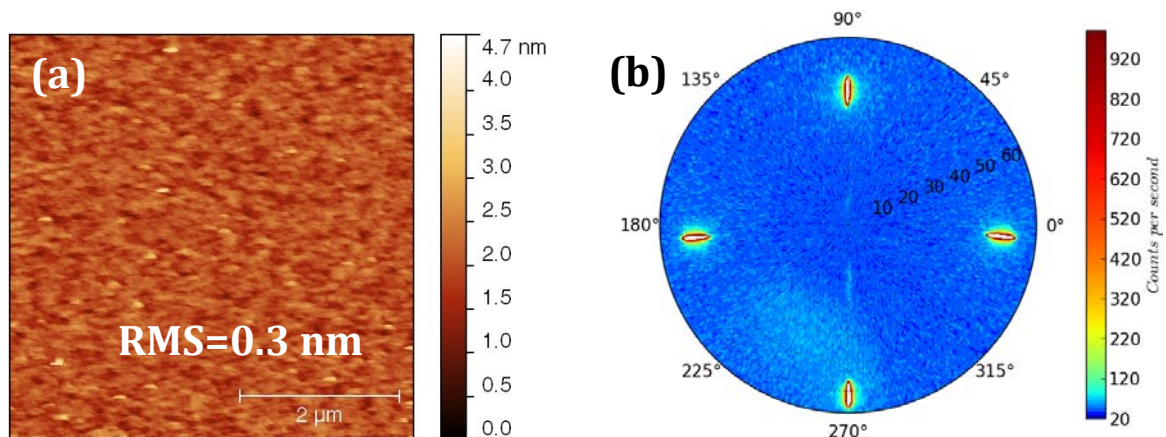


**Figure 5-47:** (a)  $5 \times 5 \mu\text{m}^2$  AFM image performed on the optimal sample shows flat surface with a RMS roughness of 0.3 nm; (b) Pole figure measurement on this sample reveals very low MT density (0.52 %);

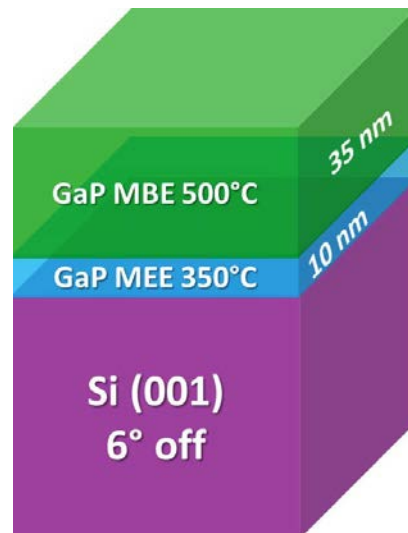


**Figure 5-48:** Sketch of the optimized pseudo-substrate GaP/Si.

## 5.5 Summary

In summary, we have developed a quantitative method using Synchrotron source and XPAD large area hybrid pixel detector to study planar defects (APD, MT) in GaP/Si thin films. MT quantification can also be analyzed using laboratory XRD setup and pole figure technique.

This study reveals an important influence of the growth temperature on the evolution of APD lateral correlation lengths and the reduction of MT. We found that high growth temperature results in significant reduction of MT density. MT anisotropic behavior is also demonstrated but its origin is still unclear. The MT-A (parallel to the step edges and inclined out of the steps) presents always the highest density with respect to the other 3 variants. The silicon buffer layer limits the MT density by ~25%. Finally we have successfully optimized the growth conditions of GaP/Si pseudo-substrate by achieving atomically flat surface and very low MT density. Works are in progress for the quantification of APD in the optimized sample. Since we are capable to obtain double atomic steps on the silicon surface, and secondly the surface of the pseudo-substrate is atomically flat, we can expect a very low APD density.

## REFERENCES

- [BBBC09] BERAR, J.-F.; BOUDET, N.; BREUGNON, P.; CAILLOT, B.; et al.: In: *Nuclear Instruments and Methods in Physics Research Section A: Accelerators, Spectrometers, Detectors and Associated Equipment* **607** (2009), No. 1, pp. 233–235
- [BiMT96] BI, W.G.; MEI, X.B.; TU, C.W.: In: *Journal of Crystal Growth* **164** (1996), No. 1–4, pp. 256–262
- [BNLO11] BEYER, Andreas; NÉMETH, Igor; LIEBICH, Sven; OHLMANN, Jens; STOLZ, Wolfgang; VOLZ, Kerstin.: In: *Journal of Applied Physics* **109** (2011), No. 8, pp. 083529–083529–6
- [BTWC91] BUUREN, T. Van; TIEDJE, T.; WEILMEIER, M. K.; COLBOW, K. M.; MACKENZIE, J. A.: In: *MRS Online Proceedings Library* **222** (1991), p. null–null
- [CLPR09] CHENG, J.; LARGEAU, L.; PATRIARCHE, G.; REGRENY, P.; HOLLINGER, G.; SAINT-GIRONS, G.: In: *Applied Physics Letters* **94** (2009), No. 23, pp. 231902–231902–3
- [CSSO04] CURSON, N. J.; SCHOFIELD, S. R.; SIMMONS, M. Y.; OBERBECK, L.; O'BRIEN, J. L.; CLARK, R. G.: In: *Physical Review B* **69** (2004), No. 19, p. 195303
- [DGSS08] DIXIT, V.K.; GANGULI, Tapas; SHARMA, T.K.; SINGH, S.D.; et al.: In: *Journal of Crystal Growth* **310** (2008), No. 15, pp. 3428–3435
- [DLRH11] DURAND, O.; LETOUBLON, A.; ROGERS, D.J.; HOSSEINI TEHERANI, F.: In: *Thin Solid Films* **519** (2011), No. 19, pp. 6369–6373
- [Domp12] DOMPOINT, Déborah: Université de Limoges, 2012
- [ErPi88] ERNST, F.; PIROUZ, P.: In: *Journal of Applied Physics* **64** (1988), No. 9, pp. 4526–4530
- [GBCF09] GUO, Weiming; BONDI, Alexandre; CORNET, Charles; FOLLIOU, Hervé; et al.: In: *physica status solidi (c)* **6** (2009), No. 10, pp. 2207–2211
- [GBCL12] GUO, W.; BONDI, A.; CORNET, C.; LÉTOUBLON, A.; et al.: In: *Applied Surface Science* **258** (2012), No. 7, pp. 2808–2815
- [GBRU09] GRASSMAN, T. J.; BRENNER, M. R.; RAJAGOPALAN, S.; UNOCIC, R.; DEHOFF, R.; MILLS, M.; FRASER, H.; RINGEL, S. A.: In: *Applied Physics Letters* **94** (2009), No. 23, pp. 232106–232106–3
- [Guo10] GUO, Weiming: INSA de Rennes, Université de Bretagne, 2010
- [GWNW90] GEORGE, T.; WEBER, E. R.; NOZAKI, S.; WU, A. T.; NOTO, N.; UMENO, M.: In: *Journal of Applied Physics* **67** (1990), No. 5, pp. 2441–2446
- [HaWa66] HALDER, N. C.; WAGNER, C. N. J.: In: *Acta Crystallographica* **20** (1966), No. 2, pp. 312–313
- [HeGD93] HENKE, B.L.; GULLIKSON, E.M.; DAVIS, J.C.: X-Ray Interactions. In: *Atomic Data and Nuclear Data Tables* **54** (1993), No. 2, pp. 181–342
- [Hull99] HULL, Robert: *Properties of Crystalline Silicon* : IET, 1999 — ISBN 9780852969335
- [HYKO95] HIRUMA, K.; YAZAWA, M.; KATSUYAMA, T.; OGAWA, K.; HARAGUCHI, K.; KOGUCHI, M.; KAKIBAYASHI, H.: In: *Journal of Applied Physics* **77** (1995), No. 2, p. 447
- [JNHL12] JUSSILA, H.; NAGARAJAN, S.; HUHTIO, T.; LIPANEN, H.; TUOMI, T. O.; SOPANEN, M.: In: *Journal of Applied Physics* **111** (2012), No. 4, pp. 043518–043518–6
- [KPMP05] KIRSTE, L.; PAVLOV, K. M.; MUDIE, S. T.; PUNEGOV, V. I.; HERRES, N.: In: *Journal of Applied Crystallography* **38** (2005), No. 1, pp. 183–192
- [Kroe87] KROEMER, Herbert.: In: *Journal of Crystal Growth* **81** (1987), No. 1–4, pp. 193–204
- [LGCB11] LÉTOUBLON, A.; GUO, W.; CORNET, C.; BOULLE, A.; et al.: In: *Journal of Crystal Growth* **323** (2011), No. 1, pp. 409–412
- [LiHF11] LIN, Angie C.; HARRIS, James S.; FEJER, M. M.: In: *Journal of Vacuum Science & Technology B* **29** (2011), p. 03C120
- [LiHS03] LIN, C.H.; HWU, R.J.; SADWICK, L.P.: In: *Journal of Crystal Growth* **247** (2003), No. 1–2, pp. 77–83

- [NaAO99] NAKADA, Yoshinobu; AKSENOV, Igor; OKUMURA, Hajime.: In: *Journal of Vacuum Science & Technology B: Microelectronics and Nanometer Structures* **17** (1999), No. 1, pp. 1–6
- [NiMc11] ALS-NIELSEN, Jens; McMORROW, Des: *Elements of Modern X-ray Physics*. 2nd edition. ed. : John Wiley & Sons, 2011 — ISBN 9781119970156
- [NKSV08a] NÉMETH, I.; KUNERT, B.; STOLZ, W.; VOLZ, K.: In: *Journal of Crystal Growth* **310** (2008), No. 23, pp. 4763–4767
- [NKSV08b] NÉMETH, I.; KUNERT, B.; STOLZ, W.; VOLZ, K.: Heteroepitaxy of GaP on Si. In: *Journal of Crystal Growth* **310** (2008), No. 7-9, pp. 1595–1601
- [NMBW02a] NARAYANAN, V.; MAHAJAN, S.; BACHMANN, K.J.; WOODS, V.; DIETZ, N.: In: *Acta Materialia* **50** (2002), No. 6, pp. 1275–1287
- [NMBW02b] NARAYANAN, V.; MAHAJAN, S.; BACHMANN, K. J.; WOODS, V.; DIETZ, N.: In: *Philosophical Magazine A* **82** (2002), No. 4, pp. 685–698
- [NMSB00] NARAYANAN, V.; MAHAJAN, S.; SUKIDI, N.; BACHMANN, K. J.; WOODS, V.; DIETZ, N.: In: *Philosophical Magazine A* **80** (2000), No. 3, pp. 555–572
- [NRGL12a] NGUYEN THANH, T.; ROBERT, C.; GUO, W.; LÉTOUBLON, A.; et al.: In: *Journal of Applied Physics* **112** (2012), No. 5, pp. 053521–053521–8
- [NRGL12b] NGUYEN THANH, T.; ROBERT, C.; GIUDICELLI, E.; LÉTOUBLON, A.; et al.: In: *Journal of Crystal Growth* **378** (2013) pp. 25-28
- [NRLC12] NGUYEN THANH, T.; ROBERT, C.; LÉTOUBLON, A.; CORNET, C.; et al.: In: *Thin Solid Films* **541**(2013) pp. 36-40
- [NSBM99] NARAYANAN, V.; SUKIDI, N.; BACHMANN, K.J.; MAHAJAN, S.: In: *Thin Solid Films* **357** (1999), No. 1, pp. 53–56
- [NZFM87] NEUMANN, D. A.; ZABEL, H.; FISCHER, R.; MORKOÇ, H.: In: *Journal of Applied Physics* **61** (1987), No. 3, p. 1023
- [QKNP13] QUINCI, T.; KUYALIL, J.; NGUYEN THANH, T.; PING WANG, Y.; et al.: In: *Journal of Crystal Growth* **380** (2013) pp. 157-162
- [RuBa09] RUBEL, Oleg; BARANOVSKII, Sergei D.: In: *International Journal of Molecular Sciences* **10** (2009), No. 12, pp. 5104–5114. — PMID: 20054465PMCID: PMC2801988
- [SAPJ96] SANTANA, C.J.; ABERNATHY, C.R.; PEARTON, S.J.; JONES, K.S.: In: *Journal of Crystal Growth* **164** (1996), No. 1–4, pp. 248–255
- [SHYZ12] SKIBITZKI, O.; HATAMI, F.; YAMAMOTO, Y.; ZAUMSEIL, P.; et al.: In: *Journal of Applied Physics* **111** (2012), No. 7, pp. 073515–073515–9
- [TFWK10] TAKAGI, Yasufumi; FURUKAWA, Yuzo; WAKAHARA, Akihiro; KAN, Hirofumi.: In: *Journal of Applied Physics* **107** (2010), No. 6, pp. 063506–063506–8
- [TYST98] TAKAGI, Y; YONEZU, H; SAMONJI, K; TSUJI, T; OHSHIMA, N.: In: *Journal of Crystal Growth* **187** (1998), No. 1, pp. 42–50
- [VBW011] VOLZ, Kerstin; BEYER, Andreas; WITTE, Wiebke; OHLMANN, Jens; NÉMETH, Igor; KUNERT, Bernardette; STOLZ, Wolfgang.: In: *Journal of Crystal Growth* **315** (2011), No. 1, pp. 37–47
- [VPWK13] VARDAR, G.; PALEG, S. W.; WARREN, M. V.; KANG, M.; JEON, S.; GOLDMAN, R. S.: In: *Applied Physics Letters* **102** (2013), No. 4, pp. 042106–042106–4
- [WBG12] WONG, C. S.; BENNETT, N. S.; GALIANA, B.; TEJEDOR, P.; BENEDICTO, M.; MOLINA-ALDAREGUIA, J. M.; McNALLY, P. J.: In: *Semiconductor Science and Technology* **27** (2012), No. 11, p. 115012
- [WHHE96] WANG, Lei; HSU, Leon; HALLER, E. E.; ERICKSON, Jon W.; FISCHER, A.; EBERL, K.; CARDONA, M.: In: *Physical Review Letters* **76** (1996), No. 13, pp. 2342–2345
- [WWHH97] WANG, Lei; WOLK, J. A.; HSU, L.; HALLER, E. E.; et al.: In: *Applied Physics Letters* **70** (1997), No. 14, pp. 1831–1833

- [YiMN09] YING, Andrew J; MURRAY, Conal E; NOYAN, I. C.: In: *Journal of Applied Crystallography* **42** (2009), No. 3, pp. 401–410
- [ZaSc08] ZAUMSEIL, P.; SCHROEDER, T.: In: *Journal of Applied Physics* **104** (2008), No. 2, pp. 023532–023532–7

---

# GENERAL CONCLUSIONS AND FUTURE WORKS

---

## Summary and conclusions

This thesis focuses on the optimization of heterogeneous growth of III-V nanostructures on misoriented Si (001) substrate toward [110]. The main purpose concerns the integration of effective light sources on Si substrate for high-speed optical interconnects inter-and intra-chip in the development of optoelectronic integrated circuits (OEIC).

In the first part, we have studied the nitrogen incorporation in GaP, since it is well-known that 2.2 % incorporation of N can make GaP(N) exactly lattice matched with Si. Nitrogen plasma spectroscopy has been first performed to optimize the nitrogen dissociation, and the atomic nitrogen production. The influence of growth conditions has been then clarified. Especially, the N content evolution with phosphorus BEP for different growth temperatures clearly demonstrates prominent dependence of the former on the latter. We thus demonstrate that there is a competition between N and P at the growth front, bringing the fact that N sticking coefficient is much lower than the unity during GaPN growth. Effects of this competition on the growth control accuracy can be limited by choosing a sufficiently low growth temperature (480°C) and a high phosphorus BEP ( $> 8 \times 10^{-6}$  Torr). The experimental accuracy is furthermore improved as growth rate and plasma cell valve opening can be efficiently used to control quantitatively the N incorporation on a wide range of N composition. On the other hand, surface roughness has been clarified to play a decisive role in the N incorporation, independently on the other growth parameters and strain effects. We have shown that substitutional nitrogen incorporation near the substrate's step edges is around 6.7 times more favorable than substitutional N incorporation on a 2D-plane terrace adsorption site in the growth conditions used. It is therefore important to control the surface roughness when growing diluted nitrides compounds. This study enables the growth of lattice matched GaPN and GaAsPN on Si substrate.

Secondly, we have attempted to find out an efficient light source on pseudo-substrate GaP/Si, we have then studied the growth of (In,Ga)As quantum dots on GaP (001) substrate. High density and good homogeneity of (In,Ga)As QDs ( $10^{11} \text{ cm}^{-2}$ ) on GaP substrate are obtained. Electronic structure and bandlineups in the (In,Ga)As/GaP material system have been determined from advanced atomistic calculations. The room temperature photoluminescence and homogeneous size distribution of these QD reveal good structural quality and electronic properties leading to an efficient optical emission. Complete temperature dependent photoluminescence analysis shows promising confinement properties. In this regard, (In,Ga)As/GaP QD seem to address some of the requirements (high density, type-I bandlineup, efficient carrier confinement, good structural quality) for the development of laser applications in the field of optoelectronic integration on silicon. The morphological analyses of single (In,Ga)As/GaP QD using STM reveal the appearance of ripened QD. The contribution to the QD formation energy is found to switch from surface to volume with the progressive ripening of the dot. This has consequences on the morphology properties: small dots exhibit high  $\{1\ 3\ 6\}$  index facets whereas low index  $\{1\ 1\ 1\}$  facets are observed for larger dots. A  $C_2$  unusual symmetry is found on regular (small and medium size) QD while ripened QD presents a  $\sigma(1-10)$  symmetric plane. The origin of this phenomenon is unclear till date and it requires further study. In short, the growth of these high density and good uniformity QD enables the possibility to integrate efficient light source on Si substrate.

The third part of this thesis has been focused on the homoepitaxial growth of Si on Si (001) substrates using UHV/CVD chamber while seeking a flat and single domain surface, represented by double atomic steps, which is necessary for subsequent growth of defects-free GaP nanolayers. This study started with the optimization of ex-situ chemical cleaning process and validation by post-growth AFM analysis. This step is considered to be the first keypoint to obtain high quality buffer layer of Si. An optimized cleaning process is obtained consisted in UV/O<sub>3</sub> oxidation and dilute HF treatment which allows obtaining atomically flat Si buffer layers. The homoepitaxial growth of Si is performed on Si (001) substrates with different miscut angles ( $0.15 \pm 0.5^\circ$ ,  $1^\circ$ ,  $2^\circ$ ,  $4^\circ$  and  $6^\circ$ ) toward the  $[110]$  direction. We have observed the achieving of flat surface and double atomic steps on one of the packs of nominal Si (001) wafers, but this is not reproducible. This suggests that a selection of nominal substrates with residual miscut is possible in order to achieve single domain and flat surface. The double atomic high steps

feature is characterized by  $2 \times n$  (with  $n \approx 7$ ) surface reconstructions, as observed by the specular beam splitting on RHEED patterns. On the contrary, these features (smooth surface and double atomic steps) are reproducible for growing on  $6^\circ$ -off Si (001) substrates. Hydrogen passivation of Si epilayers is also obtained while conserving flat surface. This study allows considering the growth of defects-free GaP/Si (001) nanolayers.

Finally, we have attempted to control planar defects (anti-phase domains, microtwins) generated in the GaP/Si (001) epilayers. The main aim of this study is to optimize the GaP/Si interface while seeking a flat surface and a minimum defects level. We have introduced a methodology to quantify APD and MT by X-ray diffraction using Synchrotron and laboratory setup. The use of high brilliance Synchrotron source and large area hybrid pixel detector XPAD is a crucial point in this study which allows fast and efficient analysis of planar defects. This has been completed by TEM analysis. The quantitative study reveals a clear influence of the growth temperature on the behavior of planar defects. For APD, the lateral coherent length is increased with increasing the growth temperature. The observation by both XRD and TEM reveals the anisotropy of APB linking to the direction of Si step edges. For MT, we observed a progressive reduction of MT with increasing of the growth temperature and a complete vanish of MT (detected by XRD) at high temperature ( $580^\circ\text{C}$ ). At this temperature, the surface roughness is too high for subsequent optical device development. The use of the growth cluster with a silicon buffer layer also plays an important role in the reduction of MT with a reduction factor of  $\sim 25\%$ . The observation of MT using XRD RSM reveals anisotropic behavior for the 4 variants where MT-A always presents the highest density (MT-A variant is parallel to the step edges and inclines out of the steps). The anisotropy of MT is believed to be linked to the misorientation direction of Si substrate. We have also developed a quantification method using XRD pole figure technique for laboratory setup. This technique consists in normalizing the integrated intensity of MT peaks with the Si (111) peak or incident beam flux and provides a relative indicator of MT density for the 4 variants. A more precise analysis consists in rocking curve scans of GaP (111) and the 4 MT variants. This method provides a rapid feedback for the optimization of growth conditions. Finally we have demonstrated very flat surface with  $\text{RMS} = 0.3 \text{ nm}$  and low MT volumic fraction ( $\sim 0.52 \%$ ) of 45 nm thin GaP layers grown on  $6^\circ$ -off Si

(001) substrate. This thickness is under the critical thickness of GaP/Si. This pseudo-substrate is suitable for subsequent growth of efficient light sources.

In conclusion, the results obtained during this work allows considering the realization of laser sources based on III-V semiconductor compounds on silicon substrate. Nevertheless, some future works are required to achieve the final goal of monolithic integration of optical interconnects on silicon substrate and realization of optoelectronic integrated circuits.

### **Suggestions for future works**

1. In this work, APD and MT are quantified using a relative indicator to evaluate their density. It is necessary to find a method to provide absolute indicator of the density, for example number of APD/MT in an area/volume unit. Rocking curves are expected to provide the absolute density. Comparison of XRD analysis with TEM plane-view observation could validate the method. The pole figure technique should be completed by recording the diffraction spot of GaP (222) instead of GaP (111) because Si (222) is a forbidden spot, thus it does not contribute to the integrated intensity of GaP (222).

2. For the Synchrotron measurements, XPAD pixel coordinates should be converted to HKL coordinates and find a precise method to quantify the MT density as well as their correlation lengths. To this end, 3D construction of MT reflections in the reciprocal space should be performed.

3. For the homoepitaxial growth of Si, it will be interesting to study the in-situ post-growth annealing effect on the formation of pits on the surface and the subsequent formation of MT in GaP/Si heterostructure as well as the UHV transfer conditions between the both growth chambers.

4. The growth of GaPN lattice-matched with Si should be optimized on the GaP/Si pseudo substrate. Then the growth of high density (In,Ga)As QD should be performed on GaPN/GaP/Si.

5. Study of the nitrogen incorporation in (In,Ga)As(N) quantum dots to reach longer wavelength emission should be performed in order to meet the telecom windows for future optical interconnects.

---



---

## **APPENDICES: DESCRIPTION OF GROWTH TECHNIQUES AND CHARACTERIZATION METHODS**

---



---

### **A. MOLECULAR BEAM EPITAXY (MBE)**

Molecular Beam Epitaxy<sup>2</sup> is a growth technique in which atom beams of constituent elements are incident upon a heated crystalline substrate in an Ultra High Vacuum (UHV) environment (as low as  $10^{-10}$  Torr). Within the ultra-high vacuum, the atoms in the chamber have a long molecular flow regime. They are thus able to travel straight without collision until they reach and stick to substrate. The length of mean free path is determined by the concentration of the atoms  $n$  and its atomic diameter  $d$ :

$$L = \frac{1}{\sqrt{2} \pi n d^2} \quad (\text{Eq. 43})$$

At the thermodynamic equilibrium, the concentration  $n$  is determined by the pressure  $P$  and temperature  $T$ :

$$n = \frac{P}{k_B T} \quad (\text{Eq. 44})$$

where  $k_B$  is the Boltzmann constant. Under the UHV condition, the mean free path is several orders higher than the distance between element source and substrate (10-20 cm).

The impinging atoms form a crystalline layer strongly bonded to the substrate and form an epitaxial film. The molecular beams can be temporally modulated either by altering the evaporating/introducing condition, or by mechanically interrupting the beam using rapid action shutter. The growth rate is around one single monolayer per second, thus a very precise control on the composition, thickness, interface quality and doping level is possible by adjusting the atomic or molecular flux and the shutter opening time.

---

<sup>2</sup> The word "Epitaxy" comes from a combination of Greek words: "επι" and "ταξι" which mean "on" and "arrangement", respectively.

The most important feature for MBE growth is that it is far from thermo-equilibrium due to UHV environment, and is mainly governed by the kinetics of surface process. The MBE growth can be described in an atomic level with four fundamental steps, as shown in **FIG. A.1**. (i) the adsorption of incident atoms or molecules on the surface. (ii) the surface migration or dissociation of the species. (iii) the incorporation of constituent atoms to the crystal lattice of substrate or epi-layers, at a site where sufficiently strong bonding occurs, in the most case at the edge of a spreading atomic layer. (iv) thermo-desorption of the species not incorporated into the crystal lattice.

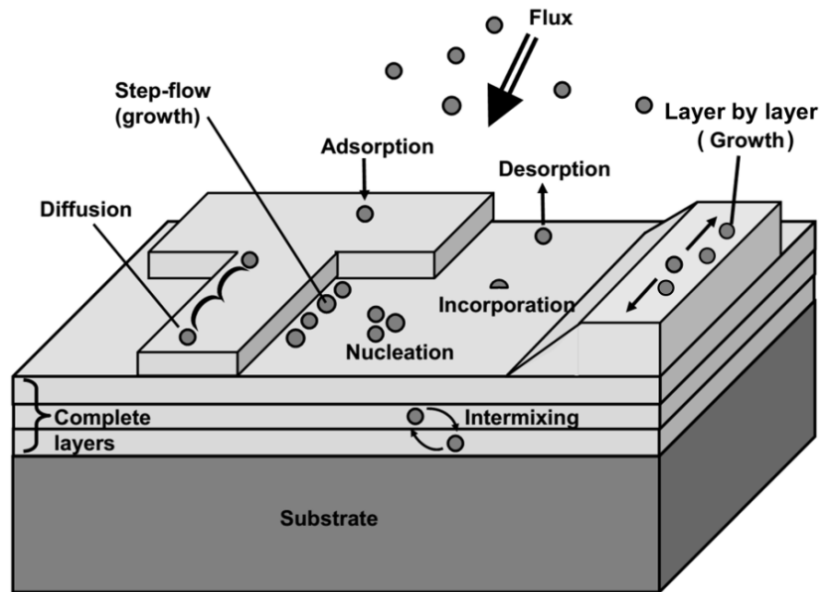


**FIG. A.1:** Illustration of different physical processes that can arise during Molecular Beam Epitaxy.

The heterogeneous crystalline growth of strained epilayers performed through MBE creates a solid-solid interface. At the thermodynamical equilibrium there exists three different growth modes in the energy point of view (see **FIG. A.2**):

- ✓ The Frank-Van der Merve mode: the sum of the energy for the interface ( $\gamma_{interface}$ ) and layer's surface ( $\gamma_{layer}$ ) is weaker than the substrate surface energy ( $\gamma_{sub}$ ):

$$\gamma_{layer} + \gamma_{interface} < \gamma_{sub} \quad (\text{Eq. 45})$$

This mode corresponds to a complete wetting of the successive deposited layers. The growth mode is thus achieved layer by layer.

- ✓ When the growth continues, there exists a strain accumulation in this wetting layer because of lattice mismatch between the layer and the substrate. When the layer's thickness exceeds a critical value, the wetting layer becomes unstable and tends to elastically relax in order to reduce the accumulated energy. This process can form 3D islands and is called Stranski-Krastanov growth mode, in that case.
- ✓ In the case where there is strong interaction between adatoms in the deposited material, the total energy of the interface and layer's surface is stronger than that of the substrate's surface, the layer cannot wet the substrate surface but it forms 3D islands:

$$\gamma_{layer} + \gamma_{interface} > \gamma_{sub} \quad (\text{Eq. 46})$$

These islands expand and coalesce when deposition continues. This growth mode without a wetting layer is called Volmer-Weber mode.

Basically these different growth modes depend on the difference between the surface energies of the two materials. For example, metal atoms deposited on a ceramic would very likely grow following the Volmer-Weber growth mode. In this case, the sum of the surface energies for layer's surface and interface is higher than that of the substrate's surface. Another example concerning the growth of self-assembled Stranski-Krastanov quantum dots such as InAs/GaAs or InGaAs/GaP, the growth is maintained layer by layer (2D) during the first few monolayers. After a critical thickness, 3D islands (or quantum dots) appear. This is because the sum of surface energies of the layer and the interface is smaller than that of the substrate for initial grown layers; this energy becomes larger than that of the substrate when the epi-thickness exceeds a critical value since the lattice elastic relaxation appears. However if the surface energies are of the same order, it is quite difficult to predict the growth mode, the difference between two modes being sometimes very small and the equilibrium conditions are rarely achieved.

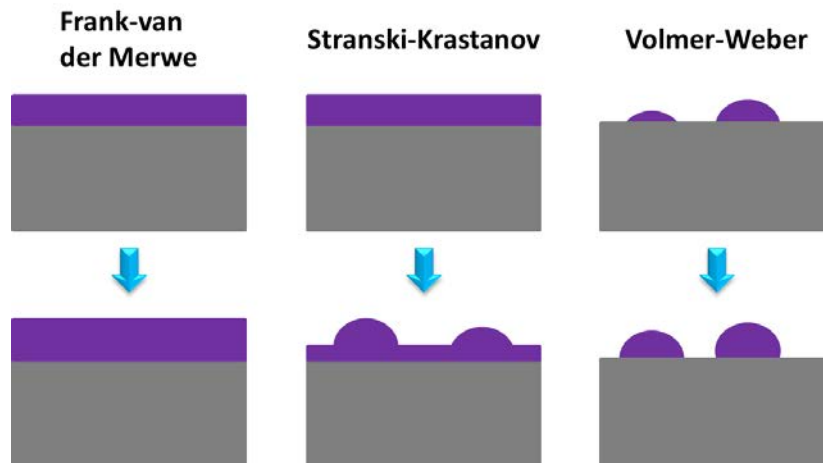


**FIG. A.2:** Schematic representation of the three typical growth modes.

### **A-1. Growth cluster UHV/CVD - MBE**

A growth cluster UHV/CVD – MBE has been installed in laboratory FOTON-OHM since 2010. It includes a Riber UHV/CVD chamber dedicated to silicon growth and a Riber compact 21 solid sources MBE chamber devoted to III-V semiconductors growth. The two chambers are connected by a UHV tunnel which is maintained at  $10^{-9}$  Torr by an ionic pump. A real picture of this cluster is shown in **FIG. A.3**. It is schematically presented in **FIG. A.4**. Both chambers are equipped with a RHEED system operating at 12 keV (MBE) or 30 keV (UHV/CVD) to monitor the growth in-situ. A nitrogen RF plasma cell (ADDON) is installed on the MBE chamber to grow dilute nitride alloys. Details about the RHEED and the RF plasma cell will be described in the following paragraphs.

**The UHV/CVD chamber** is composed of a load-lock SAS chamber where samples are introduced. This chamber is maintained at  $10^{-8}$  -  $10^{-9}$  Torr thanks to a turbo molecular pump. The load-lock pressure is measured by a Bayart-Alpert gauge.

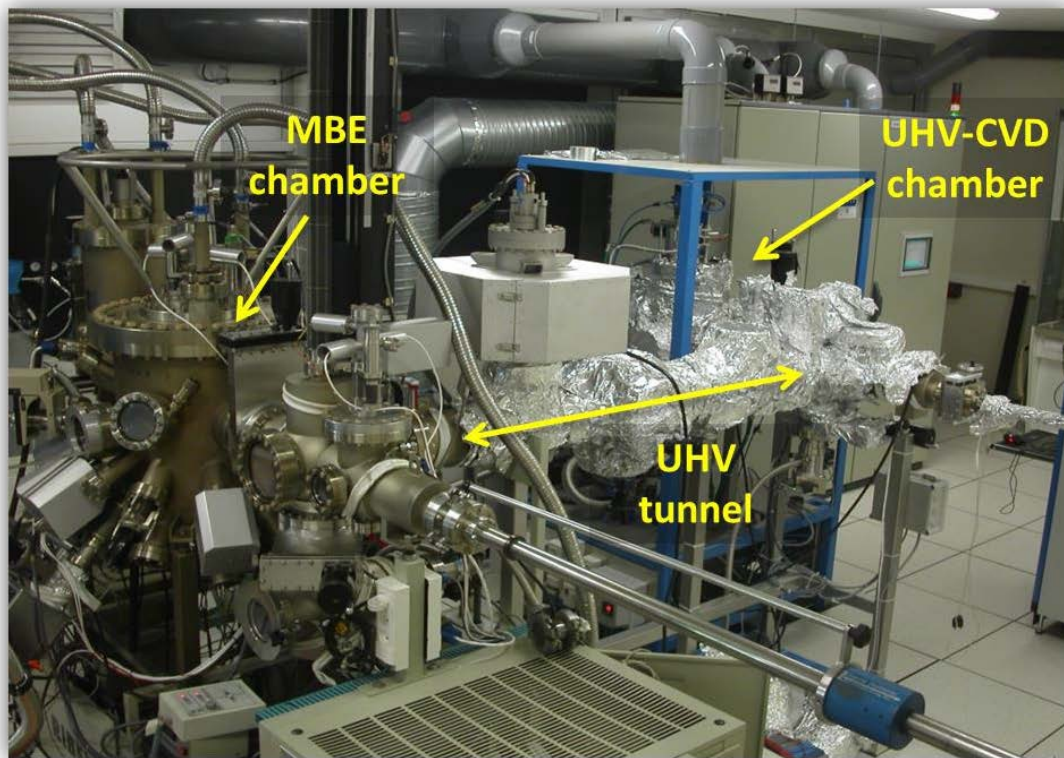


FIG. A.3: UHVCVD – MBE growth cluster at FOTON-OHM lab, installed since 2010.

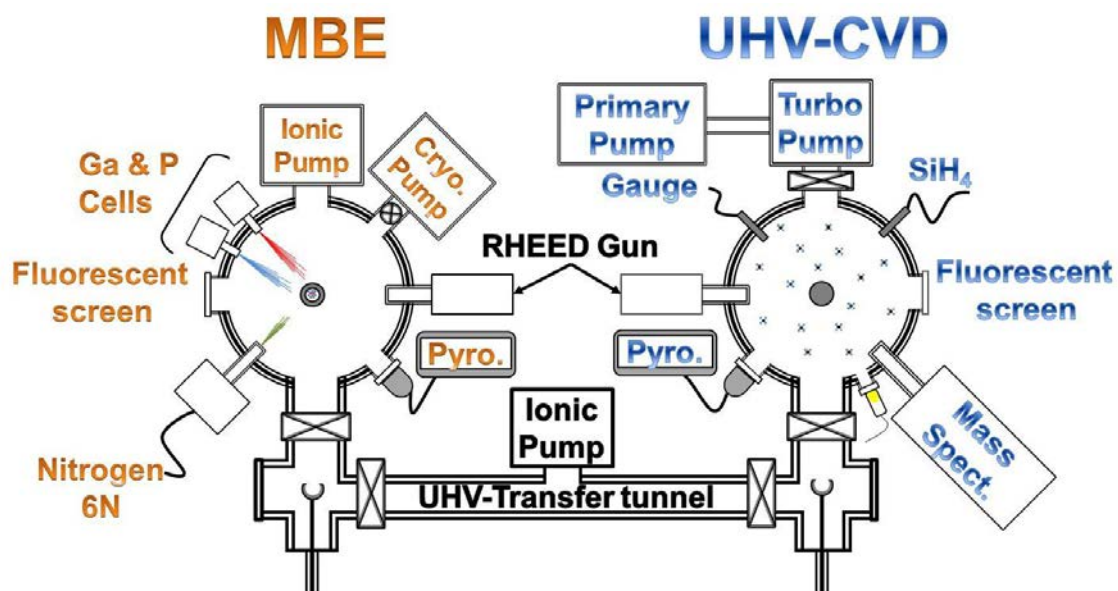


FIG. A.4: Schematic representation of the UHVCVD – MBE growth cluster.

The background pressure of the growth chamber is kept at  $10^{-10}$  Torr by a turbo molecular pump. The pressure is probed by a filament-based Extractor gauge which works in the range of  $10^{-10}$  –  $10^{-3}$  Torr. During the growth (high pressure), this Extractor

gauge has to be turned off to protect the filament. The growth pressure is thus monitored by a capacitive Baratron gauge which works in the range of  $10^{-5}$  –  $10^{-1}$  Torr. Silicon wafer with 2 inch diameter are cleaned ex-situ and then loaded to the reactor in a molybdenum holder. The substrate holder is heated in the back side by a pyrolytic boron nitride (PBN) coated graphite resistance heater. The feeding power for this heater is controlled by a Eurotherm 900 power supply. Substrate's temperature can be measured by a Eurotherm thermal couple and an infrared pyrometer which works in the range of  $575^{\circ}\text{C}$  –  $1000^{\circ}\text{C}$ . A mass spectrometer is plugged in the reactor to monitor the different species present during the substrate degassing. Silane ( $\text{SiH}_4$ ) and hydrogen ( $\text{H}_2$ ) are injected through a mass flow/Baratron flux/pressure controller where their flux/pressure can be regularized from 0 to 10 Torr before sending to the reactor.

**The solid sources MBE chamber** is devoted to III-V compounds growth. The group III elements (Ga, In, Al) are provided through conventional Knudsen effusion cells containing pure metal solid sources. The group V elements (P, As, Sb) are supplied via a thermal effusion cell where solid sources of these elements are heated, connected to a valved-cracker cell. Upon heating, phosphorus and arsenic are released in the form of tetramer ( $\text{P}_4$ ,  $\text{As}_4$ ). They are then cracked by the cracker to form  $\text{P}_2$  and  $\text{As}_2$  molecules which have higher sticking coefficient.<sup>[Guo10]</sup> The valve at the exit of the cells allows a good control of the beam flux. The growth pressure is usually in the range of  $10^{-7}$  –  $10^{-5}$  Torr. The growth rate of the III-V compounds is controlled by the group III flux.

### **A-2. The gas source MBE chamber**

In this chamber, the group III elements like Ga, In, Al are provided using solid source of pure metal which are contained in a thermal effusion cell, whereas the group V elements like As, P are provided using gas source ( $\text{AsH}_3$  and  $\text{PH}_3$ ). The gas molecules are cracked by a cracker cell to provide phosphorus and arsenic. The gas sources are controlled via a mass flow controller.

### **A-3. ADDON RF plasma cell – atomic nitrogen generation**

An ADDON RF plasma cell is installed to the solid sources MBE reactor to grow dilute nitride alloys (such as GaPN, InGaAsN, GaAsPN, etc.). **FIG. A.5** shows the position and the ensemble of the cell. High purity nitrogen gas (6N) is injected to the cell through

a 2 sccm mass flow controller which allows a precise control of the gas flux at 0.1 sccm. A plasma is generated by a copper antenna which gives radio frequency electromagnetic radiation ( $f = 13.7$  MHz). Different species could be generated inside the cell: electron, metastable ions  $N_2^+$ , atomic nitrogen (see **FIG. A.6**).<sup>[Heni05]</sup> Charged species should be eliminated because their impact on the growth surface and their incorporation into grown material will generate non-radiative defects.<sup>[Heni05, WYLN02]</sup> To reduce the impact of such high energy charged species, a mobile valve is installed at the exit of the plasma cavity. The opening distance of the valve can be adjusted to produce more or less amount of atomic nitrogen sent to the growth chamber (see **FIG. A.7**).

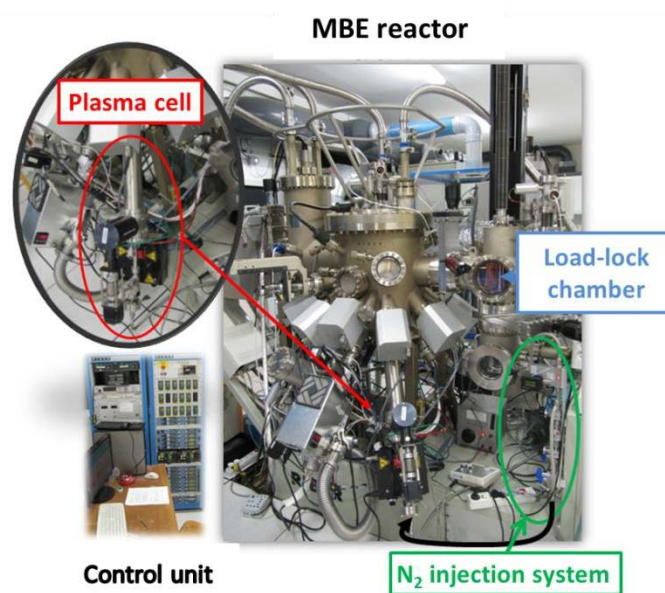


**FIG. A.5:** Presentation of the RF plasma cell installed in the solid sources MBE chamber.

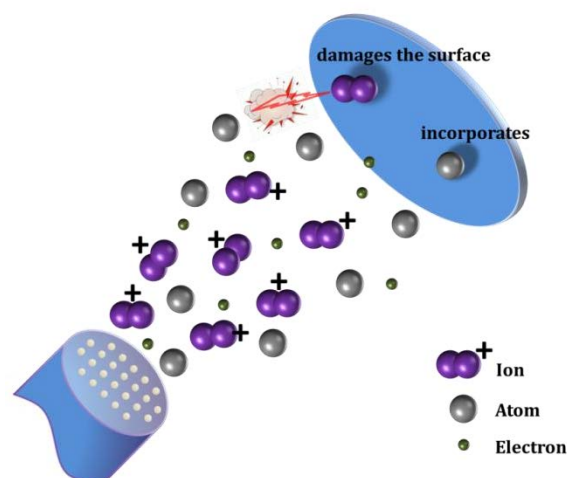


**FIG. A.6:** Different species generated in the plasma cell (electron, ions and atomic nitrogen).

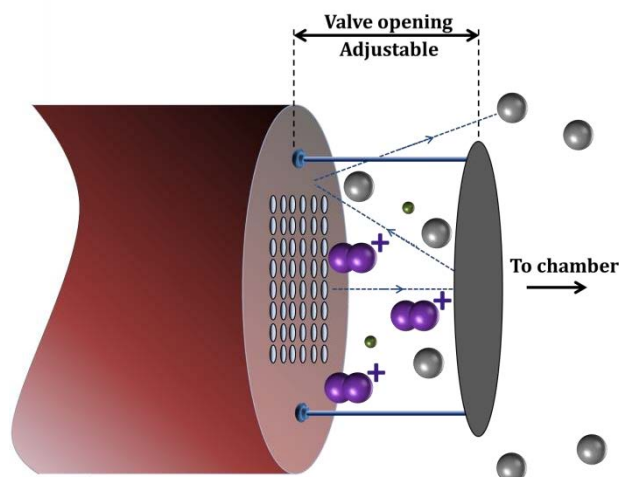


**FIG. A.7:** Plasma cell coupled with a mobile valve to reduce the impact of charged particles. The opening distance can be adjusted to produce less or more number of nitrogen sent to the growth chamber. The particles are reflected twice before going to the reactor.

The optical emission spectrum of the nitrogen plasma is monitored using a USB Ocean Optics 2000 spectrometer through a fiber optic which is installed at the observatory hub of the cell. The plasma cell parameters involved in the control of nitrogen incorporation are: RF power, nitrogen gas feeding flux and the valve opening (of course the incorporation depends also on other growth conditions which is detailed in chapter 2). By varying these parameters, two working modes can be observed:

- ✓ Low brilliance mode under a medium working power (350 W) and high nitrogen gas flux (> 1.5 sccm). The low brilliance mode produces a low amount of atomic N.
- ✓ High brilliance mode under a high working power (> 350 W) and low flux of feeding nitrogen gas (< 0.7 sccm). This mode is preferred for nitrogen incorporation because the production of atomic N is very efficient.

Both operating modes can be easily distinguished by eyes. A rigorous analysis of the optical emission spectra of the nitrogen plasma allows us to optimize the working parameters. This study is presented in chapter 2.

#### **A-4. Reflection High-Energy Electron Diffraction (RHEED)**

RHEED is an in-situ method to probe the surface structure during growth. It is mainly composed of an electron gun and a fluorescent screen. The electron beam is

produced in the RHEED gun and accelerated by a high tension (10 – 30 kV). It reaches the substrate at grazing incidence ( $0.3 - 0.5^\circ$ ) and diffracts on the sample surface. The diffraction pattern is imaged on a symmetrically placed fluorescent screen. The schema of a typical RHEED system is shown in **FIG. A.8**. Thanks to the grazing incidence and the strong interaction of the electron beam and the material, the penetration depth is limited to a few Å. We can therefore consider the electron beam is scattered in the first atomic layer which can be assimilated with a 2D lattice. Hence the diffraction pattern is determined by the structure of this two dimensional thin layer.<sup>[1cCo04]</sup> In reciprocal space, this layer is represented as series of rods passing through reciprocal lattice nodes and elongated in the direction perpendicular to the real 2D surface (**FIG. A.9**). The intersection of the consecutive series of the rods with the Ewald's sphere results in consecutive Laue zones. The diffraction happens if the Laue condition is full filled. That means the diffracted vector ( $\mathbf{k}' - \mathbf{k}$ ) is a reciprocal lattice vector. Concretely this condition is filled when the reciprocal lattice rods intersect the Ewald's sphere which has a radius of  $2\pi/\lambda$  with  $\lambda$  can be calculated based on the following equation:<sup>[1cCo04]</sup>

$$\lambda = \sqrt{\frac{150.4}{E(eV)}} \text{ (in \AA)} \quad (\text{Eq. 47})$$

For a typical electron energy of 30 keV, the electron wavelength is in the order of 0.07 Å. The corresponding Ewald sphere is thus very large and nearly flat in the spanned region of the reciprocal space.

The intersection of the rods with the Ewald sphere generates elongated streaks perpendicular to direction of the incident beam and the surface.

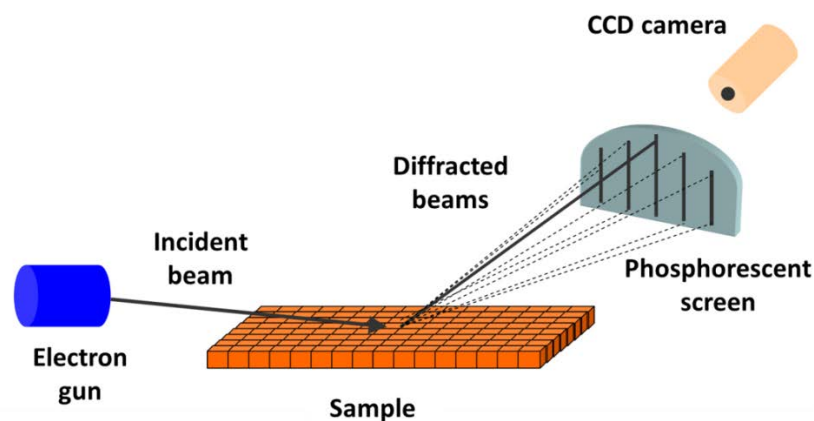


**FIG. A.8:** Schematic representation of a typical RHEED system.

The extended streaky pattern observed is a direct consequence of some reasons: firstly because the Ewald's sphere has a finite thickness (as the electron beams are never exactly monochromatic), secondly the lattice vibrations and crystal imperfections cause the reciprocal lattice rods to be of finite thickness; and thirdly because the diameter of the Ewald's sphere is significantly larger than the spacing of the rods.<sup>[Farr12]</sup> An example of a RHEED pattern is shown in **FIG. A.10**.

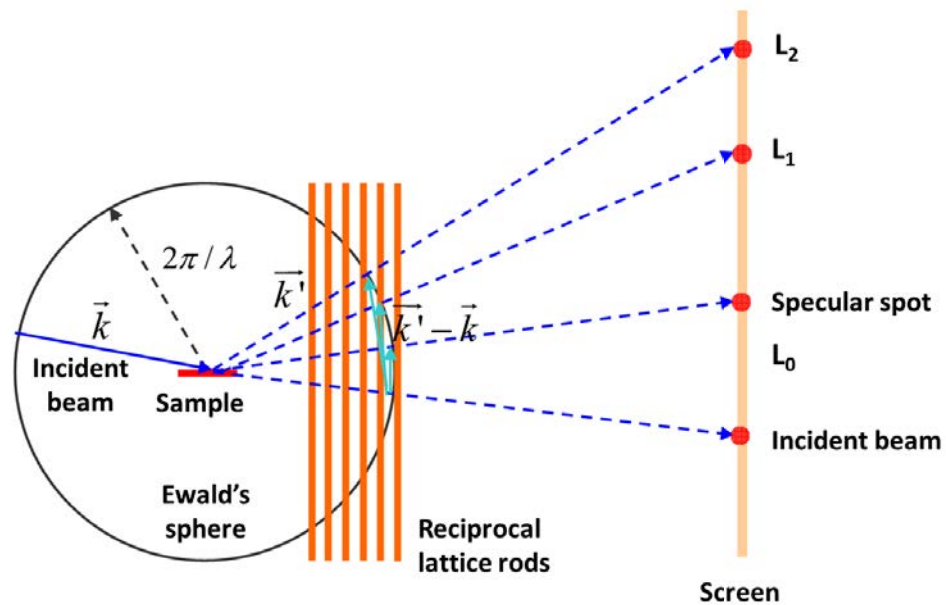


**FIG. A.9:** Schematic representation of the RHEED pattern formation. The  $L_0$  indicates zero<sup>th</sup> order Laue zone,  $L_1$ ,  $L_2$  indicate the first and second Laue zone, respectively.

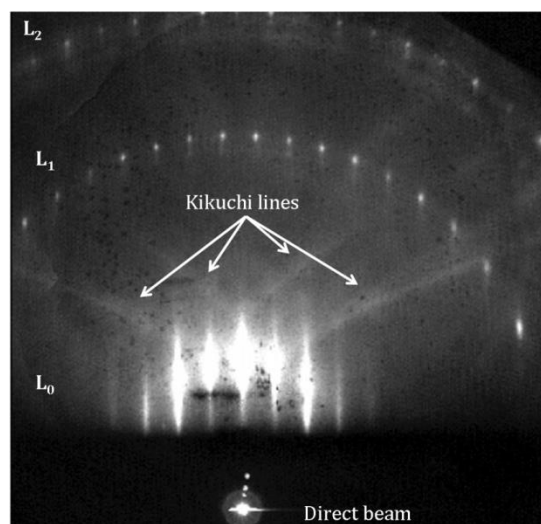


**FIG. A.10:** RHEED pattern measurement from on GaN (0001) shows a  $2 \times 2$  reconstructed surface.<sup>[IcCo04]</sup>

The Kikuchi lines appeared on RHEED patterns are formed from inelastically scattered electrons. The intensity of these Kikuchi patterns depends strongly on the surface morphology, since scattering from small terraces and steps broadens them. Sharp Kikuchi lines are obtained from crystals with perfect surfaces and perfect bulk lattices. Information given by RHEED pattern covers a large application domain: detection of growth mode, surface reconstruction or measurement of growth rate.

**a) Growth mode detection**

During the Franck – Van Der Merve growth mode (2D – layer by layer), the RHEED patterns keep streaky, but their shape may be changed. Thin streaks indicate a 2D character of the crystalline surface (**FIG. A.11** (left)). A Volmer – Weber growth mode is characterized by 3D islands on the surface during the growth. These islands cause volume diffraction and Bragg spots will be formed on the RHEED patterns. This results in “spotty” pattern as one can see in the **FIG. A.11** (middle). For the Stranski – Krastanov (SK) mode, a first 2D wetting layer is formed on the surface and results in a streaky pattern. 3D islands will be formed when the layer thickness exceeds a critical value and they create spotty patterns. The transition from streaky to spotty patterns is characteristic of SK growth mode (**FIG. A.11**(right)).

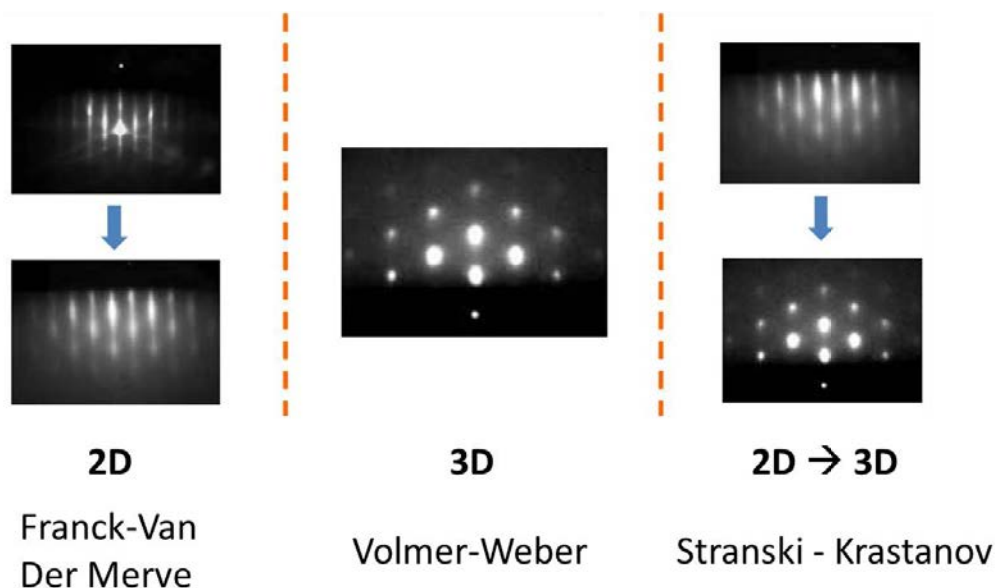


**FIG. A.11:** Example of growth mode detection by RHEED patterns.<sup>[Chen10]</sup>

**b) Surface reconstruction**

The presence of dangling bonds of surface atoms results in high surface energy. The atoms therefore tend to reorganize themselves in order to reduce the energy. The surface arrangement is thus different from the bulk crystal structure. This process is called surface reconstruction. A reconstruction  $2\times 1$  on Si (001) surface for example, means that atoms are paired to form dimers. In this case the periodicity along one azimuth (along the [110] direction) is twice longer than the normal periodicity of the bulk crystal, while in the perpendicular azimuth (along the [1-10] direction) their periodicity is the same as in the bulk. The surface reconstruction is characterized by a RHEED pattern composed of strong intensity (integer-order streaks) and weak intensity diffraction streaks (fractional-order streaks) which are placed between two integer-order streaks. The spacing between streaks are proportional to  $2\pi/a$  where  $a$  is the lattice parameter of the reconstructed surface. As shown in **FIG. A.12** (left), one-order streaks appear indicating a  $1\times$  reconstructed surface. Half order streaks appear between bright streaks in **FIG. A.12** (right) implying a  $2\times$  reconstruction of the Si (001) surface. Observation of the RHEED patterns in the two perpendicular azimuths completes the information of reconstruction type. In the example given by **FIG. A.12**, we have  $2\times 1$  reconstruction on the Si (001) surface.

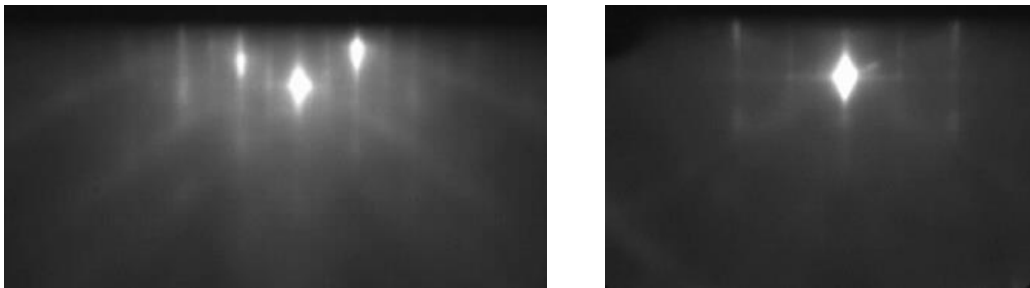


**FIG. A.12:** Si (001)  $2\times 1$  surface reconstruction. Half order streaks appear only in the [110] azimuth.

**c) Growth rate measurement**

The growth rate can be measured by monitoring the intensity of the specular spot. When the surface is flat, the specular spot presents a highest intensity. This intensity becomes weaker when the surface is rough, or in the other words when the surface is not completely covered. Lowest intensity is observed when the surface is half-covered. The periodicity of oscillation of the specular signal is believed to be equal to

one complete monolayer deposited. The RHEED oscillation as a function of the coverage ratio is schematically represented in **FIG. A.13**. Note that this method works for the layer by layer growth mode but does not work for the step-flow growth mode.

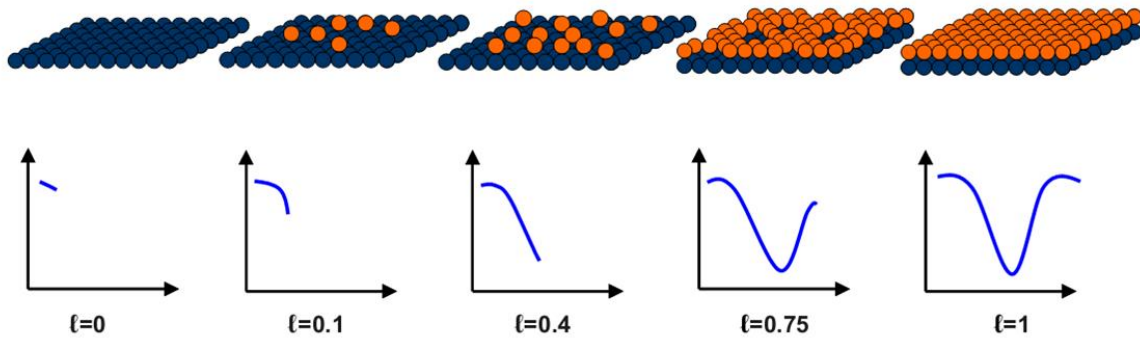


**FIG. A.13:** RHEED specular spot intensity oscillation as a function of the coverage ratio  $\theta$ .<sup>[Chen10]</sup> The period gives the coverage rate of 1 monolayer.

## B. ATOMIC FORCE MICROSCOPY (AFM)

AFM is a local probing method which allows obtaining information about the topography of surface. It is an important tool to extract surface morphology information in 3D quantitatively and qualitatively. Normally the III-V semiconductor is very stable at ambient environment. For example, the oxidation layer for InAs/GaAs system is less than 1 nm thick after exposition to air for one week.<sup>[Wilm81]</sup> Hence no special treatment of sample is needed before measurement, which makes it very easy. In this thesis, the AFM used was a 2007 Veeco diInnova experimental setup, allowing  $100 \times 100 \mu\text{m}^2$  images with a Z scale maximum amplitude of  $\sim 6 \mu\text{m}$  (**FIG. B.1**).

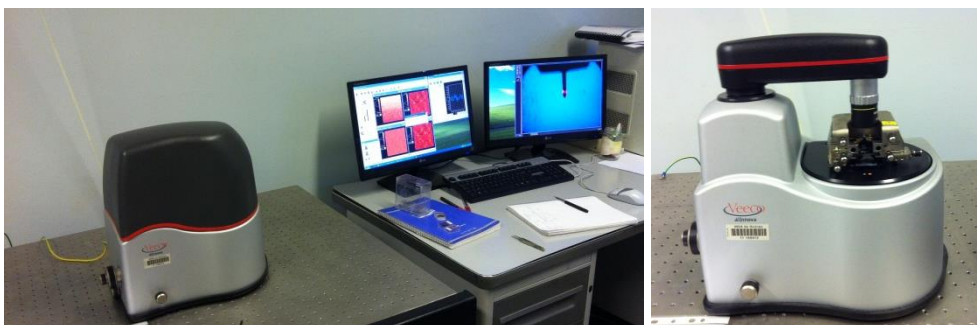


**FIG. B.1:** 2007 Veeco diInnova AFM setup in laboratory FOTON-OHM, INSA Rennes.

**Working principle of the AFM:** A tip (typically made of  $\text{Si}_3\text{N}_4$  or Si) is fixed on a deformable cantilever and probes the studied surface through the interaction between

the tip and surface. This interaction can be of various types: Van Der Waals force, capillarity, electrostatic or magnetic, depending on the sample. The deviation of the cantilever  $Z$  is proportional to the interaction force  $F$ :

$$F = kZ \quad (\text{Eq. 48})$$

This deviation is measured by a detection system: a laser source is focalized on the top of the cantilever and reflected to four quadrant photodiode detector which records the spatial variation of laser intensity due to the cantilever's deviation in  $X$ ,  $Y$  and  $Z$  direction, and cantilever's torque. Meanwhile, the substrate is moved to keep a constant interaction between the tip and substrate surface. The movement is realized by a cylinder-shaped piezoelectric tube, whose shrinkage and expansion will lead to a movement in three dimensions. Through a loop system, the  $Z$ -movement of the piezoelectric tube is indirectly controlled by the signal received by the photodiode detector.

AFM measurement can be performed in two basic working modes: tapping and contact modes. The main difference lies in the interaction between tip and sample. As shown in **FIG. B.2**, the interaction changes from attractive to repulsive when distance between tip and sample decreases. The contact mode utilizes the repulsive force while the tapping mode alternatively uses both of them. At the beginning (**FIG. B.2** - right), the probe tip is far away from the sample surface (A). However, if the tip experiences a long range attractive or repulsive force, it will deflect downwards or upwards before making contact with the surface. As the cantilever tip approaches the surface, the cantilever enters the range of surface forces and may jump into contact if it experiences a sufficient attractive force from the sample (B). Once the tip touches the surface (C), the fixed end of the cantilever still moves closer to the surface producing an increase in the cantilever deflection until retraction starts. The process is reversed when the cantilever reaches a desired force value (D). As the cantilever is withdrawn, adhesion or bonds formed during contact with the surface may cause the cantilever to adhere to the sample some distance past the initial contact point on the approach curve. At this point (E), the adhesion is broken, the cantilever is set free from the surface and the cycle may start again.

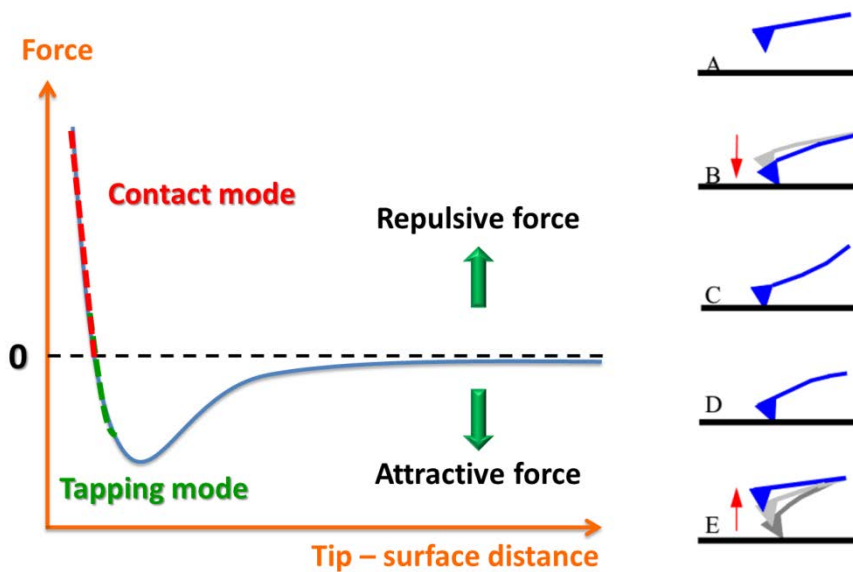


**FIG. B.2:** Force profile when the distance between the tip and the surface changes.

In **contact mode**, after the tip contacts the surface, the deviation of the cantilever from a reference position is measured when the tip sweeps along the surface. To determine the position of the tip, the laser was reflected by backside of the cantilever and detected by the photodiode. The reference is chosen when the reflected spot is at the center of the photodiode. If the cantilever moves, the position of the spot shifts correspondingly. This shift is directly related to the vertical position of the cantilever. The sample support is made of a piezoelectric ceramic, which is controlled by an electric feed-back loop. When the tip moves along the surface, the spot's relative position with respect to the reference is recorded and sent to feedback loop. At the same time, the ceramic changes the sample position according to the signal from feed-back loop so that the spot can go back to the reference position. The signal from the loop is used to plot the surface topography.

The **tapping mode** is a compensation method when contact mode doesn't give satisfying result: When surface is fragile, the strong tip-surface interaction will lead to plastic deformation. Or when surface is too soft, the friction effect makes the AFM image unclear. In this mode, the cantilever vibrates in high frequency. Thus the signal recorded by photodiode alternates. The amplitude of the vibration is sensitive to the force between tip and sample surface, which changes with the distance between them. The advantage of tapping mode is that it will not destroy fragile surface and the tip is less possible to be contaminated by the sample, because the interaction between tip and surface is six orders smaller than in contact mode.

## C. STRUCTURAL CHARACTERIZATION BY X-RAY SCATTERING

X-ray scattering techniques are very useful for thin films analysis. Readers may refer to many handbooks for a complete understanding of XRD principle and techniques.<sup>[Fews03, Warr90]</sup> In this document, only utilized techniques are described.

### C-1. High resolution X-ray diffraction (HRXRD) – lab setup

HRXRD are performed using a double crystal Bruker D8 diffractometer. A conventional setup of this system is schematically shown in **FIG. C.1**. The X-ray tube uses a copper anode to produce X-ray radiations. The feeding power is 40 kV and 40 mA. A 4-bounces Ge (022) asymmetric monochromator (Bartels) is used to reduce the divergence of the X-ray beam down to 29 arc-seconds and also to select the  $K_{\alpha 1}$  rays with a wavelength of 1.54056 Å. The goniometer is a 4-circle which allows basic translation in the Descartes space (X, Y, Z) and 4 rotation axis: omega, 2-theta (detector), phi and chi (see **FIG. C.2**).  $\omega$  is the incident beam angle with respect to the sample's surface and  $2\theta$  is the angle between the incident beam direction and the detection position. For a rocking curve measurement, an anti-diffusion slit of 8 mm large is installed at the entrance of the detector, followed by Soller slits 2.5°.

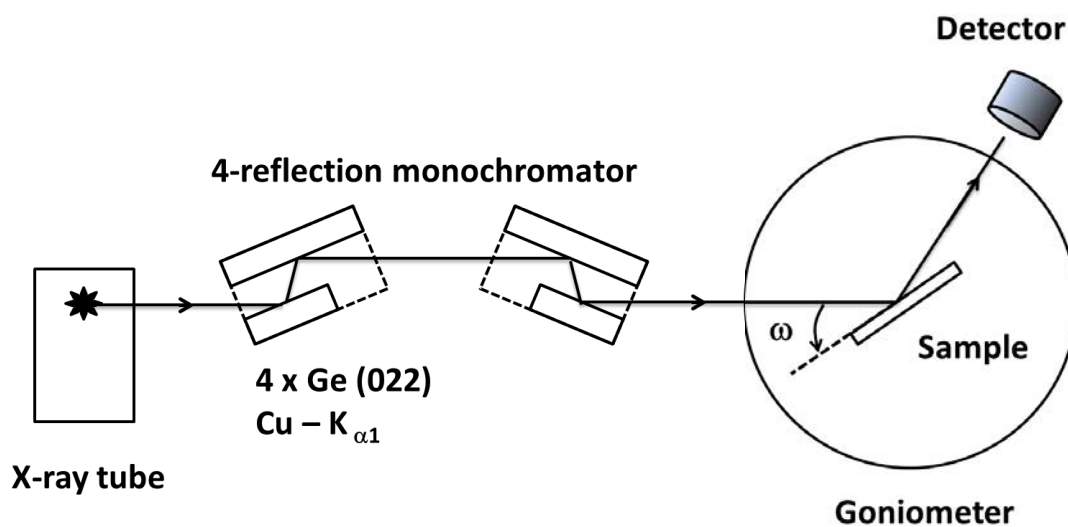


**FIG. C.1:** Schematic representation of a double crystal HRXRD setup.

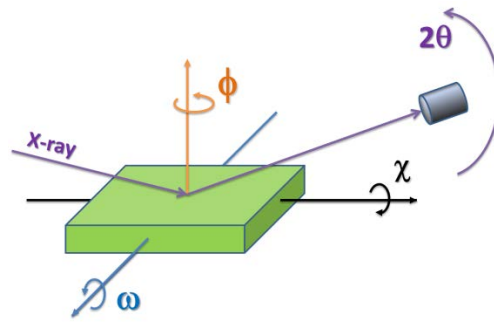


**FIG. C.2:** Sketch of the 4 rotation axis of the Bruker D8 goniometer.

**a) Representation of epitaxial layers in reciprocal space**

In reciprocal space, each lattice (substrate, epilayers) has its own reciprocal lattice. In a kinematical consideration, epitaxial layers on a substrate form a superposition of two or more reciprocal lattices. **FIG. C.3** represents the reciprocal lattices of a pseudomorphic layer (left) and relaxed layer (right) on a (001) substrate. The reciprocal lattice points (RLP) of the pseudomorphic systems are vertically aligned, while in the fully relaxed systems, the RLP are aligned on the lines which connect the RLP of the substrate to the origin (000).

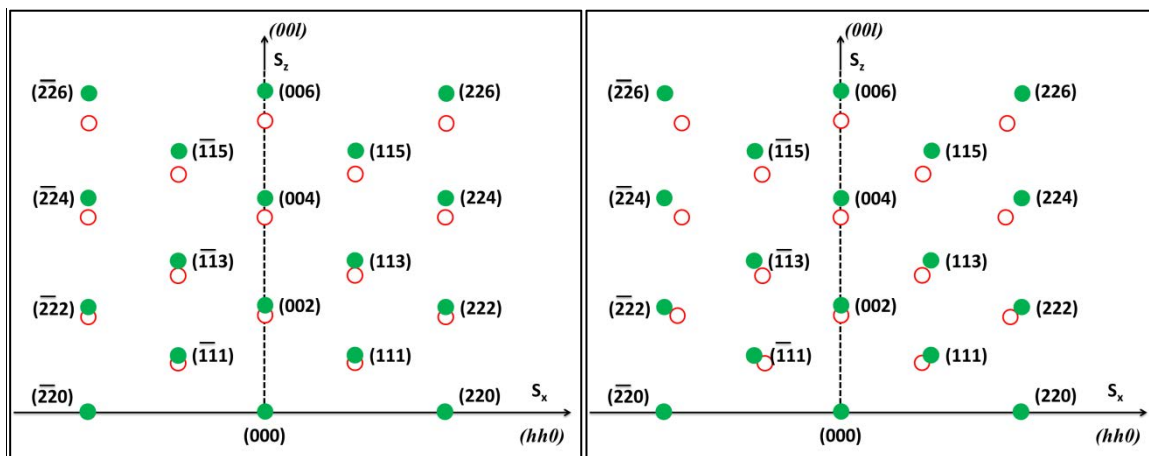


**FIG. C.3:** Reciprocal lattice of substrate ● and epilayer ○ for a pseudomorphic layer (left) and relaxed layer (right) on a (001) oriented substrate.

However, the reciprocal lattice points (RLPs) are really point-shaped only for ideal infinitely extended crystal lattices. Some sample properties cause a “structure” of the RLPs in the hkl space:

- ✓ Finite thickness, lateral granularity → The extension of all RLPs is similar and inversely proportional to the crystallite size (size of the coherent domains of diffraction).

- ✓ Mosaicity → The extension of all RLPs increases with the distance from the origin.
- ✓ Strain (tensile, compressive) → The extension of all RLPs increases parallel or perpendicular to the surface.

**b) 1D scan modes:  $\omega$ - $2\theta$  and transverse-scan**

Evaluation of lattice parameter, strain status and structural defects of epitaxial layers can be performed using symmetric and asymmetric scans. The symmetric scan consists in scanning through  $(00l)$  RLPs of a  $[001]$  oriented layer and the asymmetric one consists in scanning  $(hhl)$  RLPs. In diffraction conditions, the studied RLP intersects the Ewald's sphere so that the Bragg's condition is satisfied:

$$2d_{hkl} \sin(\theta) = n \lambda \quad (\text{Eq. 49})$$

with  $d_{hkl}$  the interplane distance,  $\theta$  the Bragg angle,  $\lambda$  the X-ray wavelength and  $n$  the diffraction order. This condition is full filled when the scattering vector ( $\mathbf{Q}$ ) is a reciprocal lattice vector. This vector is perpendicular to the lattice planes in study  $(hkl)$  (see **FIG. C.4**).

$$\mathbf{Q} = \mathbf{k}_f - \mathbf{k}_i \quad (\text{Eq. 50})$$

with  $\mathbf{k}_i$  the incident wave vector and  $\mathbf{k}_f$  the reflected wave vector.

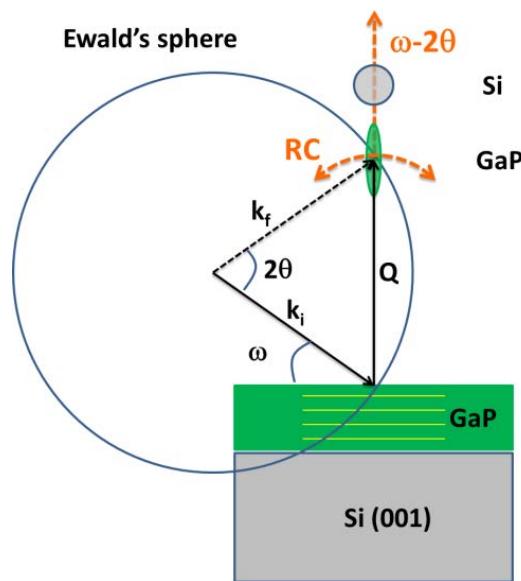


**FIG. C.4:** Sketch of the transverse-scan or rocking curve (RC) and  $\omega$ - $2\theta$  scan modes for GaP pseudomorphically grown on Si (001).

### $\omega$ -2 $\theta$ scan

In this scan mode, when the sample is rotated by an angle of  $\Delta\omega$ , the detector is rotated along with the sample by an angle of  $\Delta 2\theta = 2\Delta\omega$ . This movement keeps the scattering vector always perpendicular to the lattice planes in study (see **FIG. C.4**). If the epilayer is fully strained on the substrate, its strain state along the direction perpendicular to the surface (out-of-plane) is measured by:

$$\varepsilon^\perp = \frac{d_L^\perp - d_S}{d_S} = \frac{\Delta d^\perp}{d} = -\Delta\theta \cdot \cot(\theta_B) \quad (\text{Eq. 51})$$

where  $\Delta\theta$  is the angular distance between the substrate and the epilayer peaks,  $\theta_B$  is the Bragg angle. **FIG. C.5** shows an example of a  $\omega$ -2 $\theta$  scan through the (004) RLP of GaP from a 100 nm thin GaPN layer fully strained on GaP (001) substrate. The observed thickness fringes (or Pendellösung oscillations) on this scan indicate that the correlation length of the diffraction planes is perfectly uniform from one interface to the other. From these fringe positions and integral breadth of the epilayer diffraction peak, we can measure the thickness of the epilayer by two methods. The first one is to use the Scherrer equation:

$$t = \frac{\lambda}{\Delta(2\theta) \cos(\theta_B)} \quad (\text{Eq. 52})$$

where  $\Delta(2\theta)$  is the integral breadth of the epilayer diffraction peak,  $\theta_B$  the Bragg angle.

The other method is to use the thickness fringes, also called Pendellösung fringes, through a plot of the  $\omega$ -2 $\theta$  curves in the reciprocal coordinates, and then plot the fringes order as a function of their positions, the slope of this plot (line) gives us the thickness of the epilayer. Practically we use the **S** vector coordinates which is a reduced form of the scattering vector **Q** (see **FIG. C.6**):

$$S = \frac{Q}{2\pi} = \frac{2 \sin(\theta_B)}{\lambda} \quad (\text{Eq. 53})$$

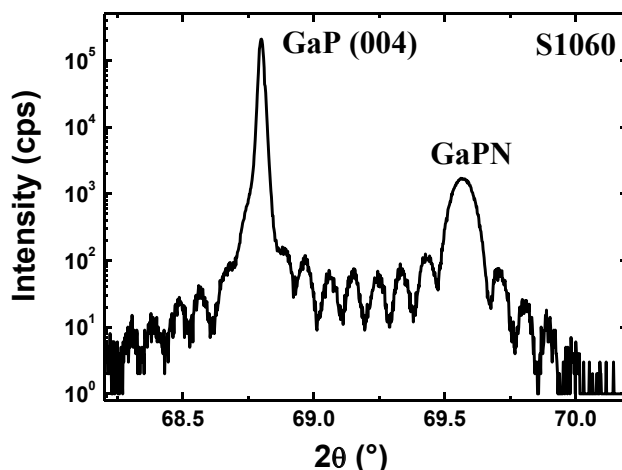


**FIG. C.5:**  $\omega$ - $2\theta$  scan over GaP (004) RLP from a 100 nm thin GaPN epitaxial grown on GaP (001). Thickness fringes are well defined which indicates very good interface quality of the epilayer.

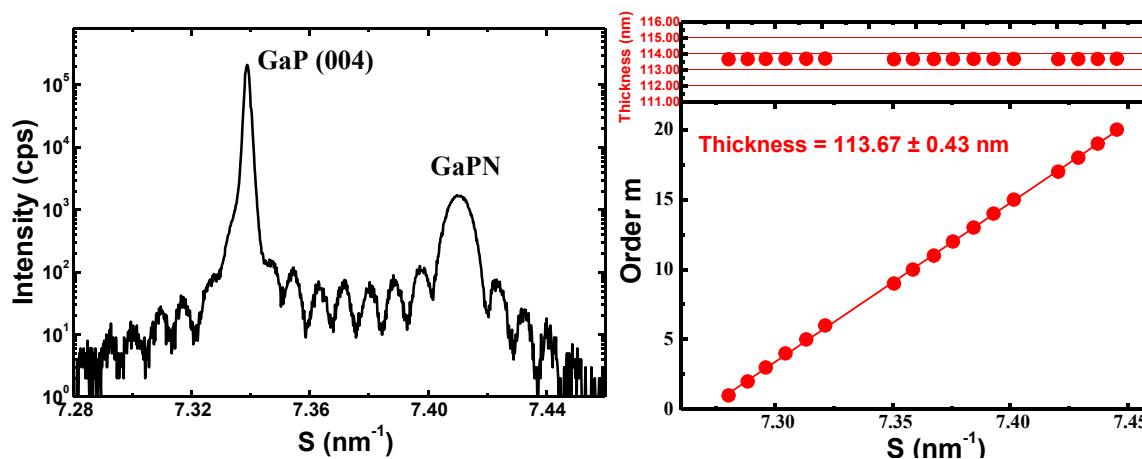


**FIG. C.6:** Thickness determination of GaPN epilayer fully strained on GaP(001) substrate.

### Transverse-scan

The transverse-scan consists in rocking (rotating) the sample while fixing the detector at the corresponding Bragg position, with a small aperture of the detector (0.375 mm). That means changing the  $\omega$  axis while fixing the  $2\theta$  axis. This scan mode is sometimes called “ $\omega$ -scan” (a “rocking curve” can be defined as a transverse-scan obtained with an open detector) (see **FIG. C.4**). A transverse-scan is useful for structural evaluation of a thin epitaxial layer. In the case of a perfect crystal, the transverse-scan profile is very sharp but has a small broadening due to instrument resolution limit. An imperfect crystal will result in a broadening of the transverse-scan profile. The main reasons for this broadening are: i) limited correlation length in the lateral direction, ii) diffuse scattering caused by defects, iii) mosaicity in the epilayer. The transverse-scan

profile therefore composes of a resolution-limited thin component and a broadened component which can be separated by a Pseudo-Voigt function fitting. Explanation for these components are found in the Ref.<sup>[DLRH11]</sup> A comparison between the area under the thin component and the broaden component gives us a quality factor of the sample.

**c) 2D scan mode: Reciprocal space mapping (RSM)**

RSM consists in mapping the intensity distribution around a specific zone in reciprocal space in which containing the RLPs that we want to study. A RSM can be performed by scanning  $\omega$  and  $2\theta$  in a 1:2 step ratio and offsetting  $\omega$  by  $\delta\omega$  before the following scan (see **FIG. C.7**). This gives a radical sector of the reciprocal space, and then can be converted into reciprocal space map in  $(S_x, S_z)$  coordinates using following equations:

$$\begin{aligned} S_x &= S \sin\left(\omega - \frac{2\theta_B}{2}\right) = S \sin(\psi) \\ S_z &= S \cos\left(\omega - \frac{2\theta_B}{2}\right) = S \cos(\psi) \end{aligned} \quad (\text{Eq. 54})$$

where  $S$  the scattering vector given by (Eq. 53),  $\psi$  the tilt angle between the lattice planes and the normal of sample surface taking into account the substrate miscut (see **FIG. C.7** – right). The reader can also refer to the paper of A. Boulle *et al.* for more description.<sup>[BCGG03]</sup>

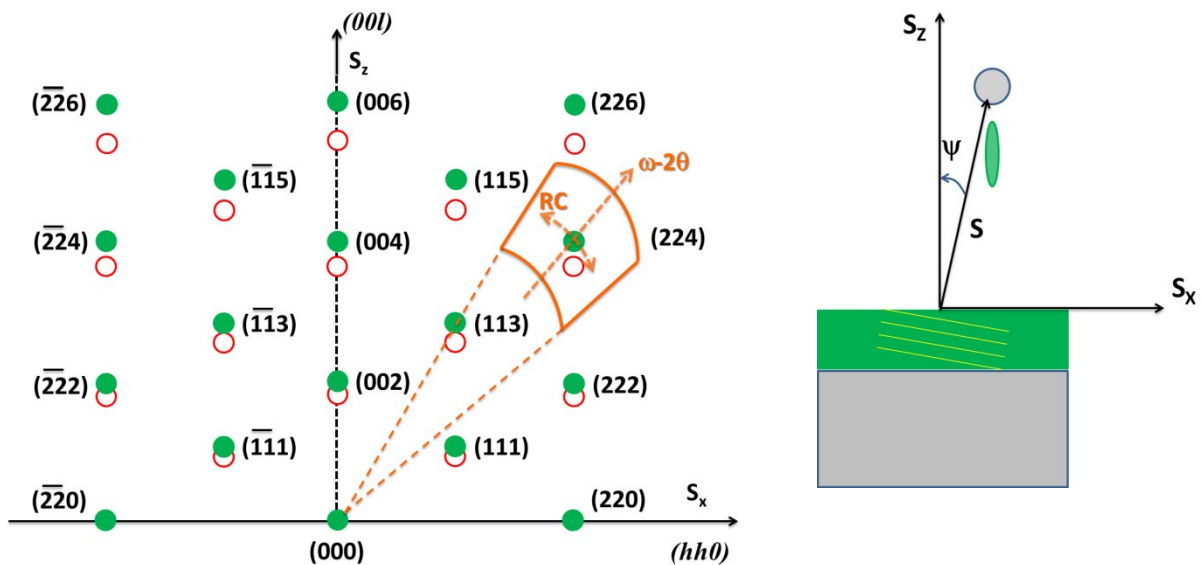


**FIG. C.7:** Schematic representation of a RSM around  $(224)$  RLP (left) and projection principle of the RSM in  $(S_x, S_z)$  coordinates map (right).

RSM's applications include the study of lattice strain-relaxation, measurement of size, shape and orientation of nanocrystalline domain in epilayers or size and shape of voids in porous epilayers.<sup>[BoTa98]</sup> **FIG. C.8** shows an example of a RSM around (224) RLP of GaP from a sample of GaPN epitaxially grown on GaP (001) substrate. Information extracted from this map give us lattice parameters of the epilayer in both the in-plane and out-of-plane direction, from which we can calculate the nitrogen content using the Vegard's law. This study is mentioned in chapter 2. In this thesis, RSM are recorded using a 1D position-sensitive detector with 2.7° opening.

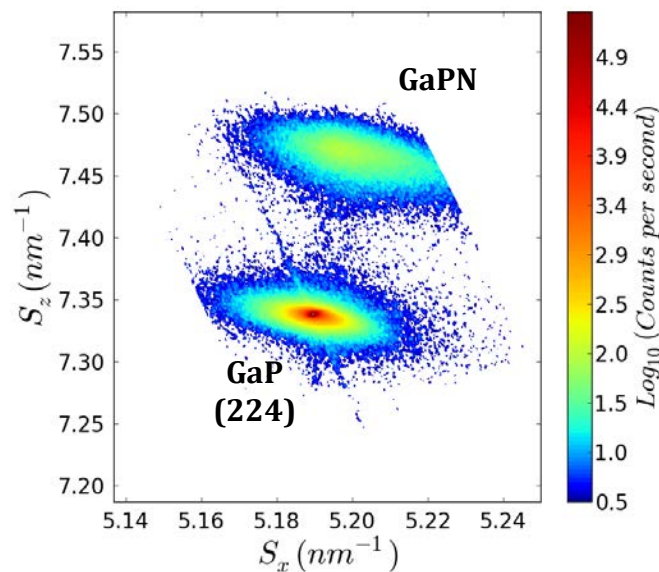


**FIG. C.8:** (224) RSM of GaPN epilayer grown on GaP (001) substrate.

#### ***d) Pole figure***

In material science, a texture corresponds to a specific distribution of crystallographic orientations in a sample. If the crystallographic orientations are not random, but have some preferred direction, then the sample displays a weak, strong or moderate texture. The degree of texture is dependent on the percentage of crystals that have the preferred orientation. Texture is seen in almost all engineered materials, and it can have a great influence on material properties. Texture is often represented using a “pole figure”, in which a specified crystallographic axis (or pole) from each of a representative number of crystallites is plotted in a stereographic projection, along with directions relevant to the material's processing history.

To understand how to construct a stereographic projection (2D), we can imagine a crystal placed in the center of a reference sphere. We call “poles” the intersections of the crystal facets normal with the sphere. These intersections form a spherical

projection (3D) of the crystal (see **FIG. C.9**– left). The advantage of this projection is that it preserves the angle between lattice plane families. The angle between two planes is defined as the angle between their normal, so is the angle between two poles (**FIG. C.9**–right). Such a spherical projection is easy to describe the angular relation between the lattice planes, but it's more difficult to manipulate on a 3D tool than on a 2D graph. It's thus preferred to project the 3D poles onto a plane (stereographic projection) while preserving their angular relation.

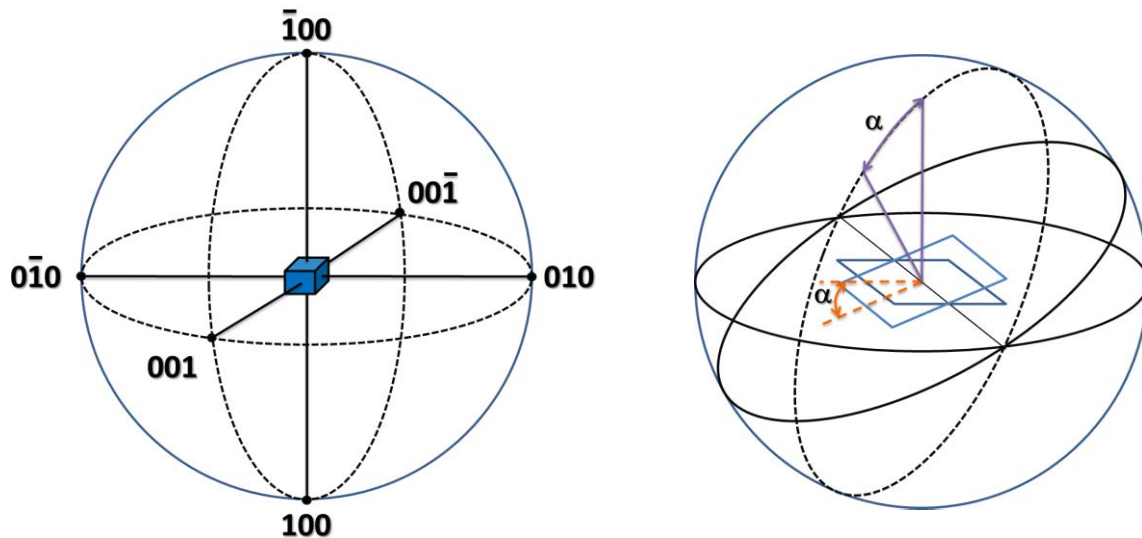


**FIG. C.9:** Spherical projection of  $\{100\}$  poles in a cubic crystal (left); preservation of angles between lattice planes (right)

The stereographic projection takes the equatorial plane of the sphere as the projection plane. The intersections between this plane with the lines connected all spherical poles to the southern pole form a 2D projection that we call the pole figure (**FIG. C.10**).

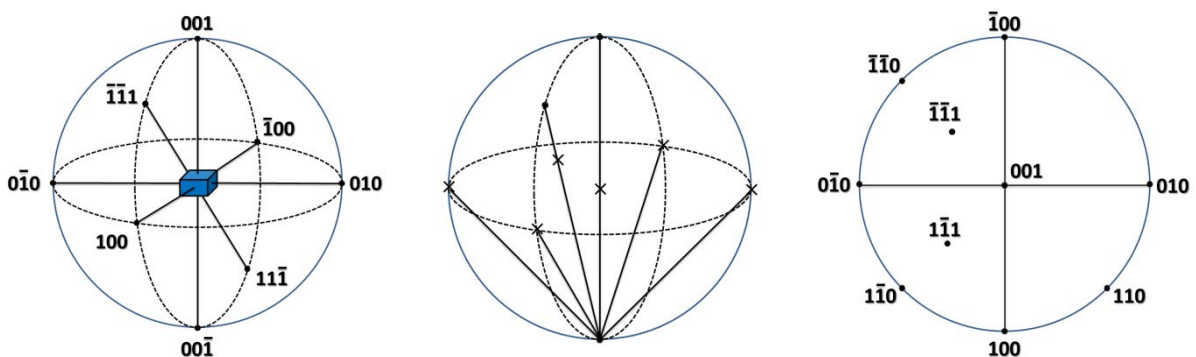


**FIG. C.10:** Example of the stereographic projection from a cubic crystal. A pole figure is obtained from the intersection of lines connected all spherical poles to the southern pole with the equatorial plane.

Practically, a pole figure is obtained by recording a coupled scan of Phi and Chi axis, while fixing  $\omega$  and  $2\theta$  (the detector) axis at a specific Bragg position (see **FIG. C.2** for description of rotation axis). **FIG. C.11** shows an example of a pole figure recorded from a GaP/Si(001) sample ( $6^\circ$  miscut towards [110]) around the Si (111) Bragg peak. The 4 large diffraction peaks correspond to the stereographic projection of 4 orientations of Si {111}; the smaller peaks correspond to the diffraction from microtwins. The shift of the 2 horizontal MT peaks and the Si(111) Bragg peaks with respect to horizontal direction ( $180^\circ$  line) is due to the effect of the vicinal surface. The use of pole figure to analyze microtwins is discussed in chapter 5.

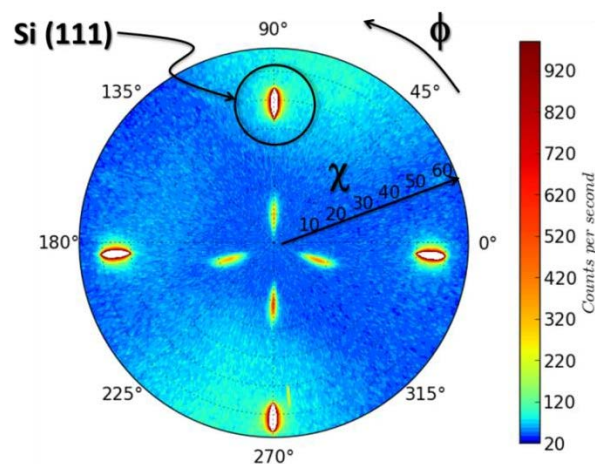


**FIG. C.11:** (111) pole figure of GaP thin film grown on Si (001) substrate with  $6^\circ$  - off miscut. The big diffraction spots correspond to the Bragg peaks of Si (111), smaller peaks correspond to the diffraction from microtwins.

## C-2. Synchrotron X-ray diffraction

Synchrotron XRD experiments in this thesis were performed on the beamline BM2 (D2AM – Diffraction et Diffusion Anomale Multilongueurs d’ondes) at the European Synchrotron Radiation Facility (ESRF) in Grenoble, France. The working energy can be adjusted over a wide range (5 – 25 keV) thanks to a two crystal monochromator with sagittal focusing made of Si (111), which is located between two cylindrically bent mirrors in a compact arrangement, with double focusing (3:1) – see **FIG. C.12**. More information can be found on the D2AM website.

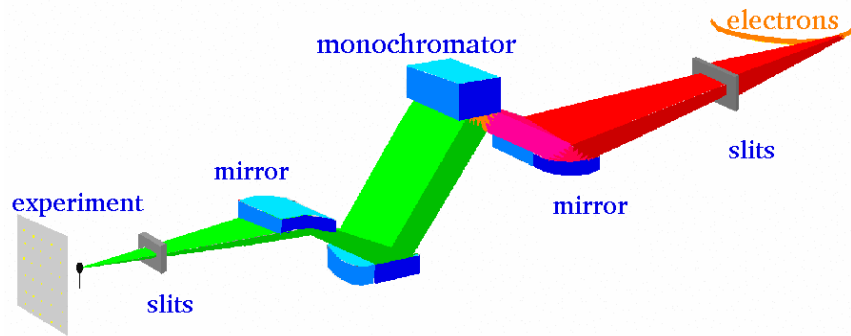


**FIG. C.12:** Sketch of the optic system on the beamline D2AM. A monochromator which can adjust the X-ray energy in a range of 5-25 keV is located between two cylindrically bent mirrors and allows a double focusing. Source: D2AM website.

**a) The Kappa goniometer**

The D2AM beamline is equipped with a Kappa goniometer that replaces the ancient 7-circle goniometer. This goniometer allows users to record intensities over a wide dynamical range for data in and out of the polarization plane. **FIG. C.13** shows a whole view of the Kappa goniometer.

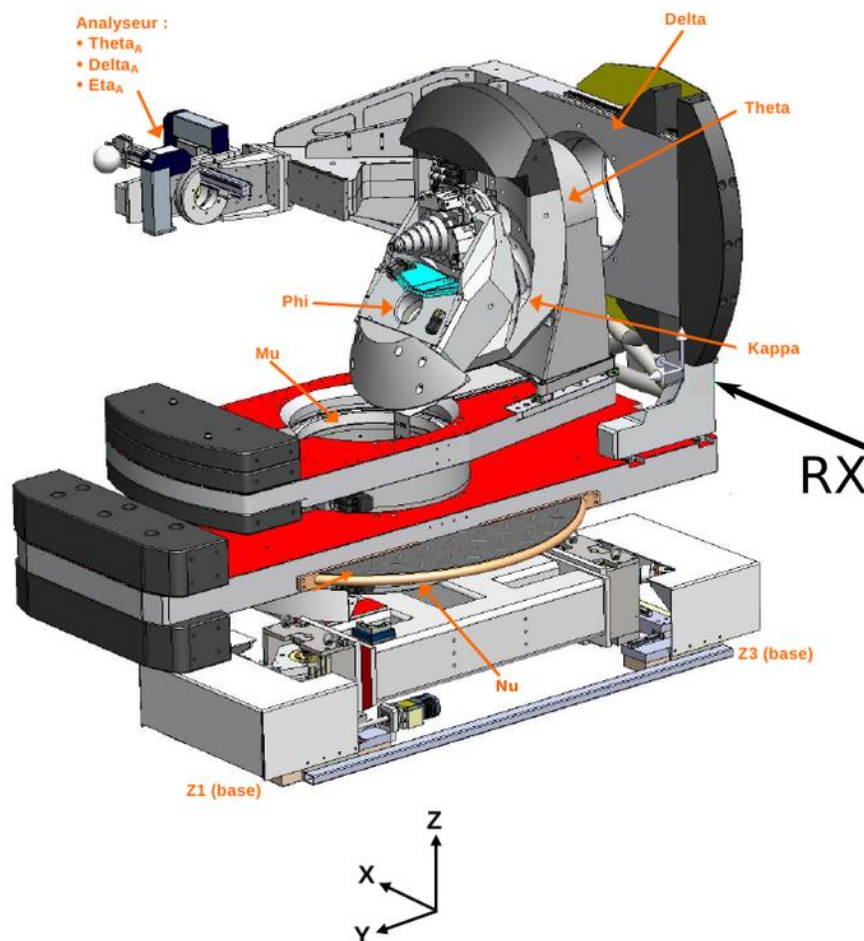


**FIG. C.13:** Sketch of the Kappa goniometer. Source: D2AM website.

The sample can be oriented through 4 circles of the instrument which can be defined both as physical axis or virtual Eulerian ones (see **FIG. C.14**– left):

- MU: sample rotation around a vertical axis (z).
- ETA - virtual Eulerian angle: sample rotation around a horizontal axis perpendicular to the incident beam (y).
- CHI - virtual Eulerian angle: sample rotation around x, it is carried by THETA. In **FIG. C.14**– left: Chi=0.
- PHI - virtual Eulerian angle: sample rotation around the sample normal. It is carried by CHI and THETA, so that the sample lies horizontal at Chi=90 (its normal is z) and vertical at Chi=0 (its normal is then y). Note that at CHI=0, ETA and PHI axis are parallel and horizontal.
- KETA: physical rotation associated with ETA
- KAPP: physical rotation around the Kappa axis.
- KPHI: physical rotation associated with PHI

The detection line uses 2 circles (**FIG. C.14**– right):

- NU: horizontal motion of the detector arm to allow measurement out of the polarization plane, its full use needs a special configuration of the experiment control program.
- DEL: vertical motion of the detector arm. It is carried by NU.

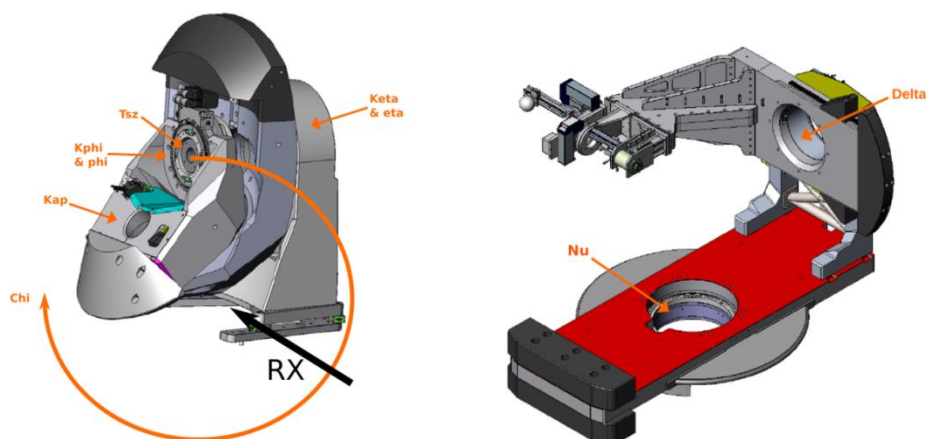


**FIG. C.14:** Sketches of the sample orientation system (left) and the detection line (right) of the Kappa goniometer. Source: D2AM website.

**b) XPAD hybrid pixel detector**

The detector used during experiments was a prototype XPAD third generation which is built from 8 Si electronic modules. Each module consists of 7 XPAD3 chips of 80x120 pixels. One pixel is 130  $\mu\text{m}$  large and can count up to above  $2 \times 10^5$  photons/s, thus allows a counting rate above  $2 \times 10^7$  photons/ $\text{mm}^2/\text{s}$  (**FIG. C.15**).



**FIG. C.15:** Side view (left), front view (middle) and one module (right) of the XPAD3 detector. Each module consists of 7 XPAD3 chips of 80x120 pixels. Source: D2AM website.

Such a 2D hybrid detector allows quick and large scale mapping in the reciprocal space. One RSM with a high resolution enough can be imaged in 30 seconds whereas it takes from 2 to 4 hours in a laboratory setup, when possible. Recorded data are stored in text files which can be then processed using the FIT2D software built by the ESRF staff.

**c) Data processing**

Data recorded by XPAD detector are stored in separated text files. It can be converted to image format using the Fit2D software available on the beamline or can be processed numerically by most of scientific programming language (such as Python). In this thesis, images are treated using a combination of the Fit2D software and Python processing. Raw data are transformed to a 2D map of 577x912 pixels. This map (image) corresponds to a detector capture of the interested zone in the reciprocal space around the corresponding reciprocal lattice points (or Bragg reflection spots) and is represented in the coordinates of the XPAD detector. Thus all of Synchrotron images presented in this thesis are presented in XPAD coordinates (in pixels). Works are in progress to convert the XPAD coordinates to HKL coordinates and this will be presented in the thesis of Y. Ping Wang.

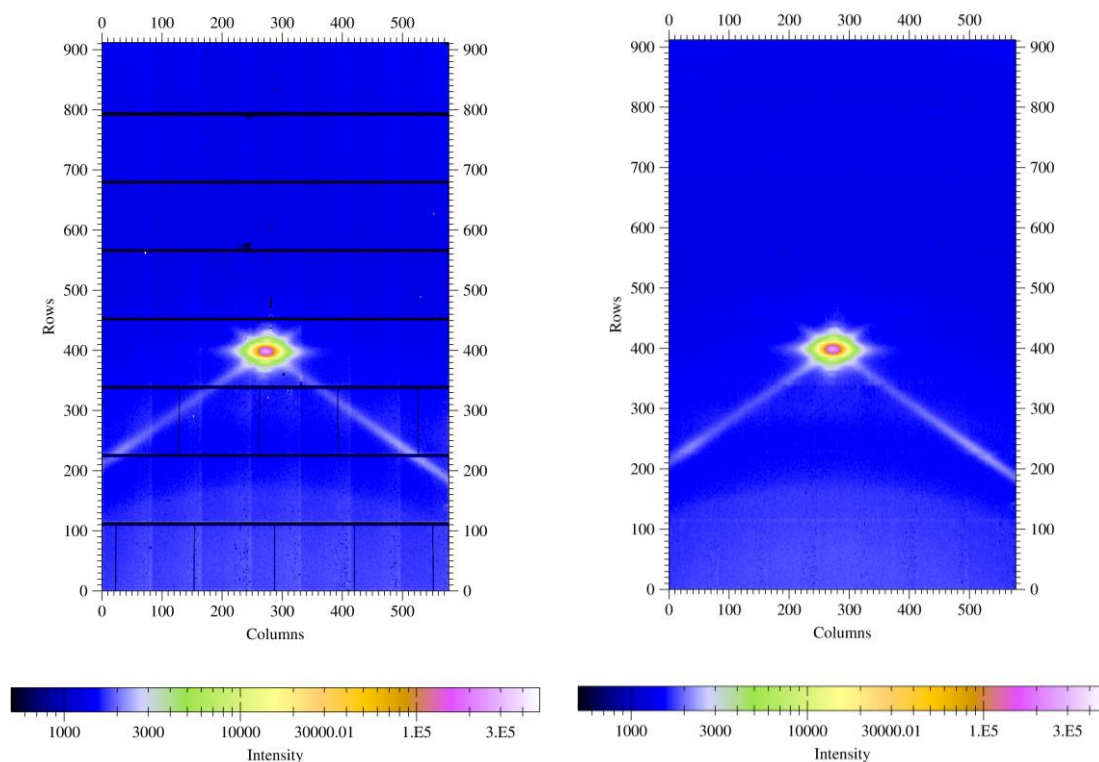


**FIG. C.16:** Synchrotron images treatment: suppression of blind lines corresponding to borders of each XPAD modules where data cannot be recorded. Left: raw image, right: treated image, intensity is in log scale.

**FIG. C.16** (on the left hand side) presents a raw image of the GaP (002) reflection for a GaP/Si sample grown at 350°C by MEE. The azimuth position was set at  $\phi = 90^\circ$ . This image presents black lines corresponding to the borders of each XPAD modules where data cannot be recorded. After suppression of these blind lines by a smoothing procedure, correct images as presented on the right hand side are obtained and this facilitates further analysis (thanks to E. Giudicelli for his contribution to the images smoothing in the framework of his Master thesis). The smoothing consists in replacing the black points (intensity zero) by average intensity of the 2 points in its vicinity (upper and lower). The halo in the lower part of the images is originated from polycrystalline diffraction of the sample holder (in copper).

Another attention should be paid to the machine current ( $I_{\text{machine}}$ ) which decays in time before each refill. As the incident X-ray beam intensity is proportional to machine current, data must be normalized to the incident beam at highest current ( $\sim 200$  mA in these experiments):

$$I_{norm} = \frac{I_{measured}(counts / s)}{monitor_{measured}(counts / s)} \cdot monitor_{ref}(counts / s) \quad (\text{Eq. 55})$$

where  $monitor_{measured}$  (*vct1\_3* column in the dataspec file) is proportional to the incident intensity at the moment of measurement,  $monitor_{ref}$  is proportional to the incident intensity at the moment where the machine current is the highest (~200 mA). All of this information is registered in the dataspec file after each scan. After normalization, all images are considered as recorded in the same conditions of incident beam.

## REFERENCES

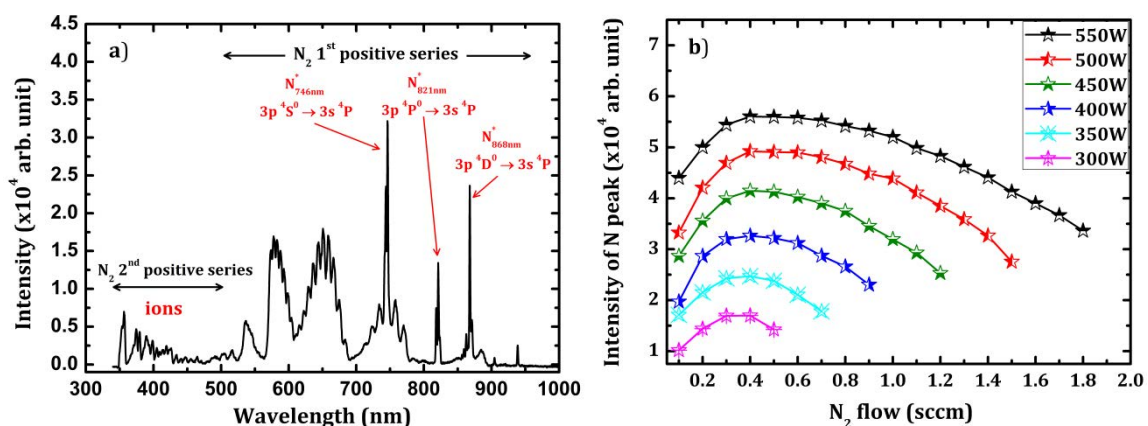
- [BCGG03] BOULLE, A.; CANALE, L.; GUINEBRETIERE, R.; GIRAULT-DI BIN, C.; DAUGER, A.: In: *Thin Solid Films* **429** (2003), No. 1–2, pp. 55–62
- [BoTa98] BOWEN, D. K.; TANNER, Brian K.: *High Resolution X-Ray Diffractometry And Topography*: CRC Press, 1998 — ISBN 9780203979198
- [Chen10] CHENG, Jun. Lyon, Ecole Centrale de Lyon, 2010
- [DLRH11] DURAND, O.; LETOUBLON, A.; ROGERS, D.J. et al.: In: *Thin Solid Films* **519** (2011), No. 19, pp. 6369–6373
- [Farr12] FARROW, Robin F. C.: *Molecular Beam Epitaxy: Applications to Key Materials*: William Andrew, 2012 — ISBN 9780080946115
- [Fews03] FEWSTER, Paul F.: *X-ray scattering from semiconductors*. 2nd Edition. London: Imperial College Press, 2003 — ISBN 1-86094-360-8
- [Guo10] GUO, Weiming: *Heterogeneous MBE growth of GaP on Silicon and nanostructure for integrated photonics*. INSA de Rennes, Université de Bretagne, 2010
- [Henl05] HENINI, Mohamed: *Dilute Nitride Semiconductors*. 1<sup>st</sup> Edition: Elsevier, 2005 — ISBN 9780080445021
- [IcCo04] ICHIMIYA, Ayahiko; COHEN, Philip I.: *Reflection High-Energy Electron Diffraction*. UK: Cambridge University Press, 2004 — ISBN 0521184029
- [Warr90] WARREN, Bertram Eugene: *X-ray diffraction*: Courier Dover Publications, 1990 — ISBN 9780486663173
- [Wilm81] WILMSEN, C. W.: In: *Journal of Vacuum Science and Technology* **19** (1981), No. 3, pp. 279–289
- [WYLN02] WANG, S. Z.; YOON, S. F.; LOKE, W. K. et al.: In: *Journal of Vacuum Science & Technology B: Microelectronics and Nanometer Structures* **20** (2002), No. 4, pp. 1364–1367



## RESUME DE THESE

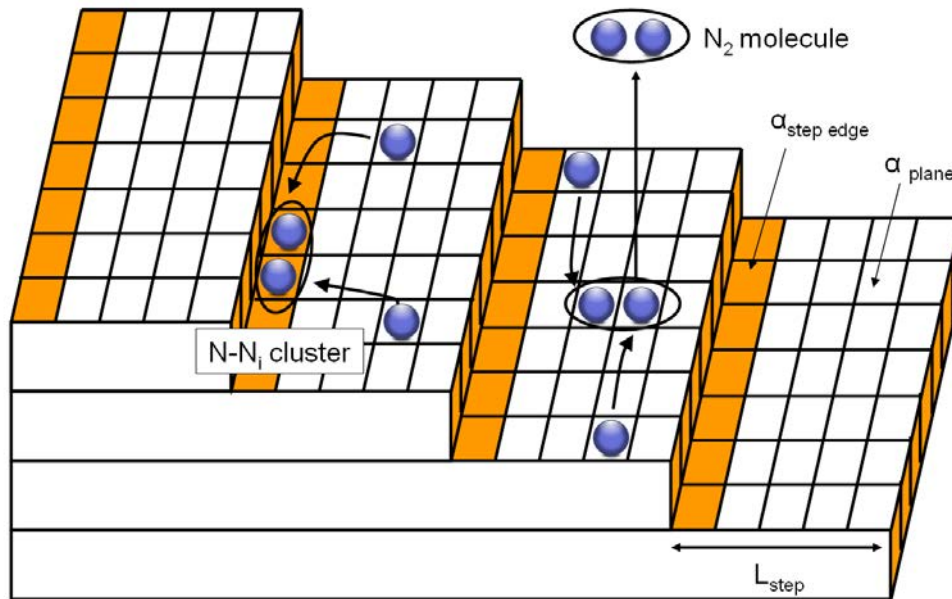
Cette thèse porte sur l'optimisation de la croissance hétérogène de nanostructures III-V sur substrat de Si(001) dans l'approche pseudomorphique. Le but principal concerne la réalisation de sources optiques efficaces sur substrat de Si pour les interconnexions optiques à très haut débit inter- et intra- puces, dans le cadre du développement de circuits optoélectroniques intégrés (OEIC – optoelectronic integrated circuit).<sup>[LiBo10]</sup>

Dans un premier temps, nous avons étudié l'incorporation d'azote dans le GaP, car il est bien connu que l'incorporation de 2.2 % de N permet de rendre GaP(N) exactement accordé en maille avec le silicium. Le plasma d'azote est d'abord analysé par spectroscopie optique pour optimiser la dissociation du diazote et la production d'azote atomique (F-1).<sup>[KNQA13]</sup>



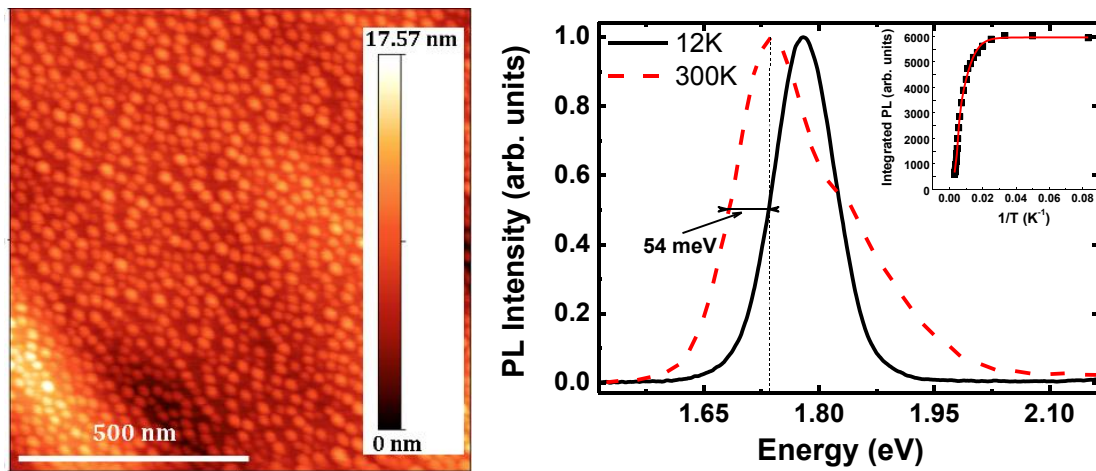
**F-1:** Optimisation des paramètres de plasma d'azote. (a) Spectre optique du plasma d'azote à une puissance de 400W et un flux entrant de N<sub>2</sub> de 0.5 sccm ; (b) Evolution de l'intensité intégrée du pic d'azote atomique (746 nm) en fonction du flux de N<sub>2</sub> et de la puissance plasma.

L'influence des conditions de croissance est ensuite clarifiée. En particulier, l'évolution de la teneur en N avec le flux de phosphore pour différentes températures de croissance démontre clairement la dépendance importante de la première sur la dernière. Nous démontrons ainsi qu'il existe une compétition à l'incorporation entre N et P, sous-entendant que le coefficient de collage de N est différent de l'unité pendant la croissance de GaPN. L'influence de cette compétition sur le contrôle de l'incorporation d'azote peut être limitée en choisissant une température de croissance assez faible (480 °C) et un flux de phosphore (BEP) élevé ( $> 8 \times 10^{-6}$  Torr). La précision sur le contrôle de l'incorporation d'azote est en outre encore améliorée en faisant varier l'ouverture de la vanne de la cellule plasma ce qui permet d'atteindre une large gamme de composition en azote. Parmi les paramètres influençant l'incorporation de l'azote, La rugosité de surface a été clairement identifiée comme jouant un rôle décisif, indépendamment des autres paramètres de croissance et des effets de contrainte/déformation. Nous avons montré que l'incorporation d'azote substitutionnel à proximité des bords des marches à la surface de l'échantillon est d'environ 6,7 fois plus favorable que l'incorporation sur un site d'adsorption plan (2D) dans les conditions de croissance utilisées.<sup>[CNQA12]</sup> Il est donc important de contrôler la rugosité de la surface lors de la croissance des composés de nitrures dilués. Cette étude permet finalement de maîtriser les conditions de croissance des composés GaPN et GaAsPN en accord de maille avec le silicium.



**F- 2:** L'incorporation d'azote aux bords des marches est 6.7 fois plus favorable que l'incorporation sur les sites d'adsorption plane 2D.

Ensuite, nous avons étudié la croissance des boîtes quantiques (In,Ga)As sur substrat de GaP (001) tout en visant une source de lumière efficace sur pseudo-substrat GaP/Si. Nous avons obtenu une densité élevée et une bonne homogénéité des boîtes (In,Ga)As/GaP ( $10^{11} \text{ cm}^{-2}$ ). La structure électronique et le raccord de bandes dans le système (In,Ga)As/GaP ont été étudiés à partir de calculs atomistiques. La photoluminescence à température ambiante et la distribution homogène en taille de ces boîtes révèlent une bonne qualité structurale et des propriétés électroniques conduisant à une émission optique efficace. Une analyse complète de photoluminescence dépendant de la température montre des propriétés de confinement quantique prometteuses **(F-3)**.<sup>[NRCP11]</sup> En ce sens, les boîtes quantiques (In,Ga)As/GaP semblent répondre à certaines exigences (haute densité, raccord de bande de type I, confinement des porteurs efficaces, bonne qualité structurale) nécessaires au développement des applications laser pour l'intégration optoélectronique sur silicium.



**F-3:** (A gauche) image AFM des boîtes quantiques (In,Ga)As/GaP présentant une forte densité ( $1.37 \times 10^{11} \text{ cm}^{-2}$ ); (A droite) spectres de photoluminescence à basse température (12K) et à température ambiante des boîtes quantiques (In,Ga)As/GaP.

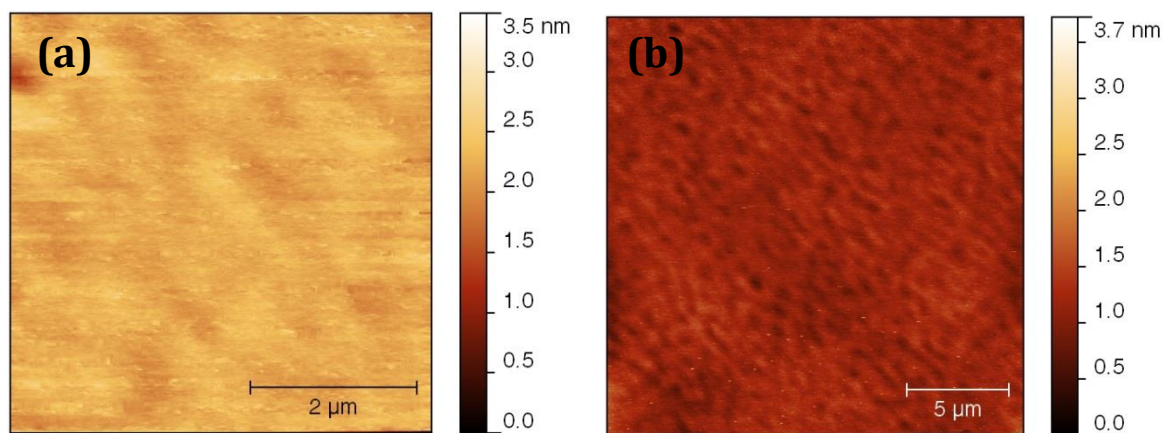
Les analyses morphologiques des boîtes uniques à partir d'images STM révèlent l'apparition de boîtes ayant mûri (**F-4**).<sup>[RCTN12]</sup> Lors du mûrissement, l'analyse des facettes met en évidence le fait que le terme dominant dans l'énergie de formation des boîtes passe d'un terme d'énergie de surface à un terme d'énergie de volume. Les petites boîtes présentent des facettes à indice élevé {1 3 6}, tandis que des facettes de faible indice {1 1 1} sont observées pour les grosses boîtes. Les boîtes standard (de taille petite et moyenne) présentent une symétrie  $C_2$  inhabituelle tandis que les boîtes ayant mûri présentent un plan de symétrie  $\sigma$  (1-10). En bref, la croissance de ces boîtes quantiques de haute densité et de bonne uniformité permet d'envisager l'intégration des sources de lumière efficaces sur substrat de silicium.



**F-4:** Image STM ( $75 \times 75 \text{ nm}^2$ ) des boîtes quantiques (In,Ga)As/GaP.

La troisième partie de ce travail porte sur la croissance homoépitaxiale de Si par UHV/CVD nécessaire pour enterrer des contaminants résiduels à la surface, et obtenir une surface propice à l'hétéroépitaxie de GaP de qualité structurale optimale, incluant la formation de doubles marches atomiques afin de limiter l'apparition de défauts structuraux. Cette étude a débuté par l'optimisation de la préparation chimique de surface et validation par analyse AFM après croissance. Cette étape est considérée comme le premier point clé pour obtenir la couche tampon de haute qualité de Si. Un procédé de nettoyage optimisé obtenu consiste en oxydation par ozonolyse (UV/O<sub>3</sub>) et traitement par HF dilué qui permet d'obtenir des couches tampon de Si parfaitement planes. La croissance homoépitaxiale de Si est effectuée sur des substrats de Si (001) avec des angles de désorientations différents ( $0,15 \pm 0,5^\circ$ ,  $1^\circ$ ,  $2^\circ$ ,  $4^\circ$  et  $6^\circ$ ) vers la direction [110].<sup>[QKNP13]</sup> Une bonne qualité de surface de silicium, avec des bimarches atomiques, a été obtenue sur certains lots de substrats, mais une variation est constatée d'un lot à l'autre. Ceci suggère qu'une sélection de substrats nominaux avec une désorientation résiduelle est possible afin de parvenir à la formation des doubles marches atomiques et une surface plate. Le travail s'est ensuite concentré sur les

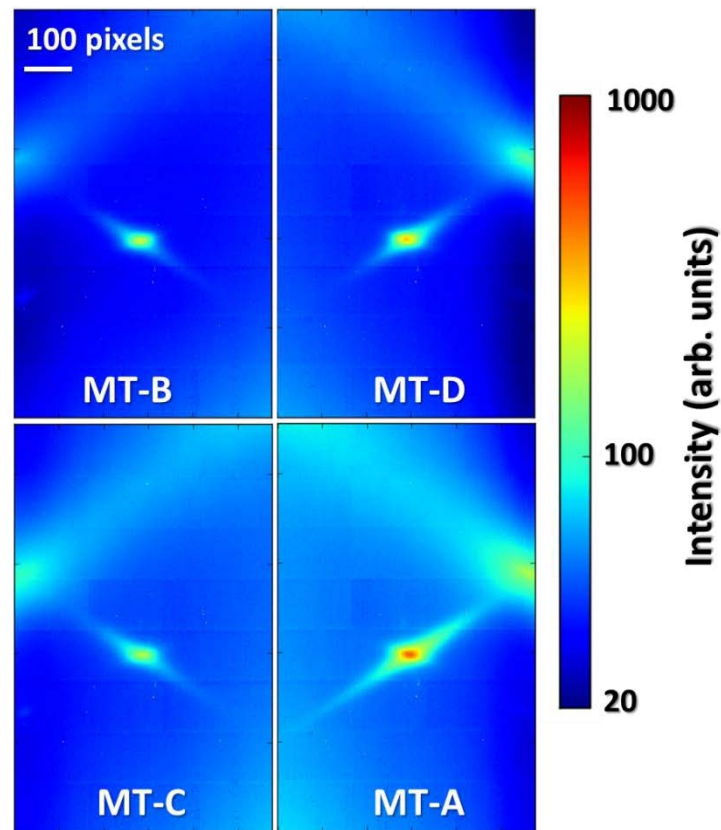
substrats désorientés de  $6^\circ$ , avec lesquels l'apparition des doubles marches atomiques est caractérisée par la reconstruction de surface de type  $2 \times n$ ,  $n=7$ , observé par la séparation du faisceau spéculaire sur diagrammes de diffraction RHEED. Au contraire, ces caractéristiques (surface lisse et doubles marches atomiques) sont reproductibles pour tous les substrats de silicium (001) avec une désorientation de  $6^\circ$ . Nous avons également étudié la passivation de surface de silicium par de l'hydrogène tout en conservant une surface lisse, ce qui permet de protéger la surface des contaminants quand elle est soumise à l'air. Finalement, nous arrivons à obtenir une croissance homoépitaxiale du silicium avec les critères visés : une surface lisse et présentant des doubles marches atomiques (F-5). Cette étude permet d'envisager la croissance d'une hétérostructure GaP/Si en limitant les défauts de type parois d'antiphase.



**F-5:** Images AFM d'un échantillon de Si déposé sur substrat de Si (001) désorienté de  $6^\circ$  vers la direction [110], (a)  $5 \times 5 \mu\text{m}^2$ , RMS = 0.13 nm, (b)  $20 \times 20 \mu\text{m}^2$ , RMS = 0.15 nm.

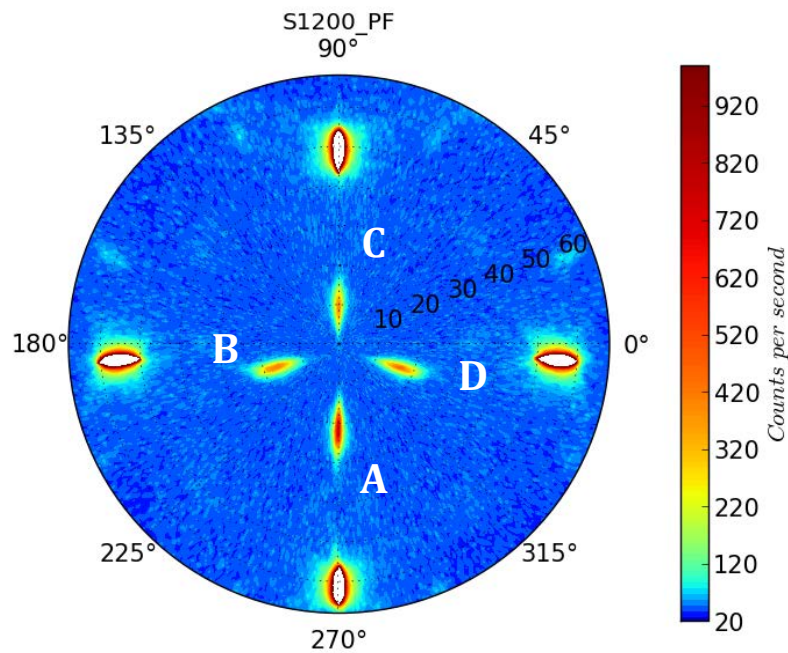
Finalement, nous avons cherché à optimiser l'interface de GaP/Si en minimisant les défauts structuraux planaires (domaines d'anti-phase (APD), micromacles (MT)), tout en visant une surface plane. Nous avons mis en place une méthodologie pour

quantifier les APD et MT par diffraction des rayons X utilisant le rayonnement Synchrotron et des expériences de laboratoire. L'utilisation du rayonnement Synchrotron de haute brillance et d'un grand détecteur 2D XPAD est un point crucial dans cette étude qui permet une analyse rapide et efficace des défauts planaires.<sup>[BBBC09, NRGL12, NRLC12]</sup> L'étude quantitative révèle une influence très nette de la température de croissance sur le comportement des défauts planaires. Pour les APD, la longueur de cohérence latérale est augmentée avec l'augmentation de la température de croissance. L'observation à la fois par DRX et MET révèle l'anisotropie des APB reliant leur origine aux bords des marches de Si. Pour les MT, nous avons observé une réduction progressive des MT avec l'augmentation de la température de croissance et une disparition complète des MT (détectée par XRD) à haute température (580°C). La croissance de GaP sur substrat de Si, en couche mince d'épaisseur inférieure à l'épaisseur critique et obtenue spécifiquement avec un cluster de croissance composé d'un bâti Si UHV/CVD connecté sous ultra-vide avec un bâti III-V MBE, montre une réduction importante des défauts structuraux.<sup>[QKNP13]</sup> L'observation de MT en utilisant des cartographies dans l'espace réciproque révèle un comportement anisotrope des 4 variants. MT-A présente toujours la plus forte densité. Le variant MT-A est parallèle aux bords des marches du silicium vicinal et incliné vers l'extérieur des marches (**F-6**).



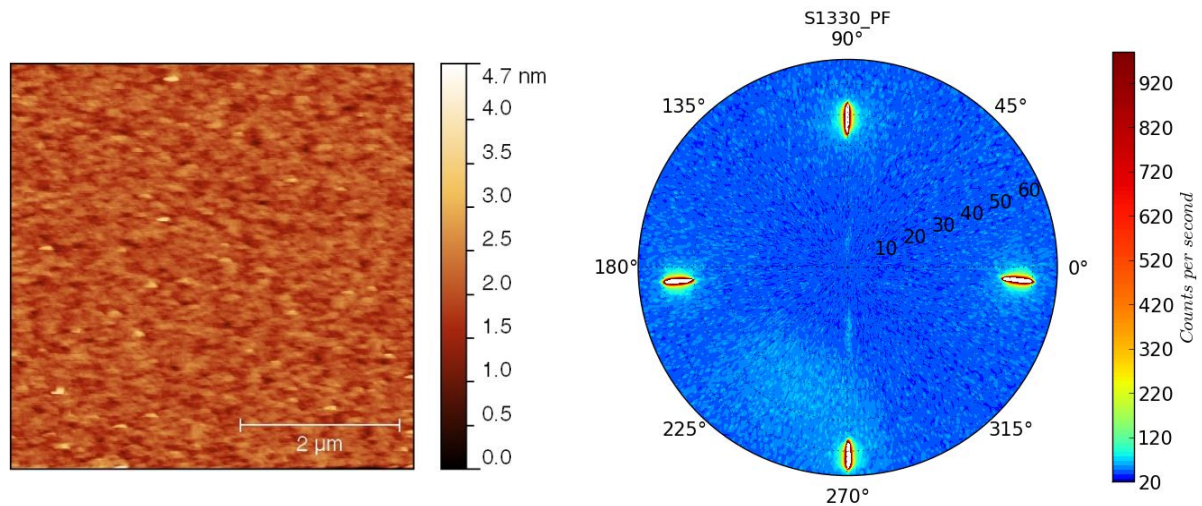
**F-6:** L'anisotropie des micro macles (MT) – les MT-A présentent toujours la plus forte intensité. Images mesurées par DRX au Synchrotron ESRF.

Nous avons également mis au point une méthode de quantification utilisant la technique de figure de pôle pour les expériences de laboratoire. Cette technique consiste à normaliser l'intensité intégrée des pics de MT avec le pic de Si (111) ou avec le flux du faisceau incident et fournit un indicateur relatif de densité de MT pour les quatre variants (**F-7**). Une analyse plus précise consiste à analyser par des scans transverses sur la raie GaP (111) et les 4 variants de MT. Ce procédé fournit un retour d'information rapide pour l'optimisation des conditions de croissance.



**F-7:** Une figure de pôle (DRX) obtenue au laboratoire, autour du pic Si (111), qui présente les réflexions des différents MT (A, B, C, D dans la figure).

Enfin, ces techniques nous ont permis d'optimiser rapidement les croissances de GaP sur silicium, avec des techniques dites de croissances alternées (MEE). Nous avons ainsi obtenus une surface très plate (rugosité rms de 0.3 nm) et une faible densité de défauts dans les couches de GaP d'épaisseur 45 nm déposées sur substrat de Si (001) avec un miscut de 6° (**F-8**). Cette épaisseur est en dessous l'épaisseur critique de GaP/Si.<sup>[TFWK10]</sup> Ce pseudo-substrat est approprié pour la croissance ultérieure des sources luminescences efficaces.



**F-8:** (à gauche) Image AFM  $5 \times 5 \mu\text{m}^2$  obtenue sur un échantillon GaP/Si optimisé présente une surface lisse,  $\text{RMS} = 0.3 \text{ nm}$ ; (à droite) Figure de pôle mesurée sur le même échantillon montrant une très faible densité de MT (0.52 %).

En conclusion, les résultats de recherche présentés dans ce travail de thèse permettent d'envisager la réalisation de sources laser à base de composés semi-conducteurs III-V sur substrat de silicium, avec l'obtention d'un pseudo-substrat GaP/Si, le développement d'alliages Ga(As)PN en accord de maille, et l'obtention d'émetteurs optiques sur silicium.

---

**REFERENCES**

- [BBBC09] BERAR, J.-F.; BOUDET, N.; BREUGNON, P.; CAILLOT, B.; et al.: In: *Nuclear Instruments and Methods in Physics Research Section A: Accelerators, Spectrometers, Detectors and Associated Equipment* **607** (2009), No. 1, pp. 233–235
- [CNQA12] CORNET, C.; NGUYEN THANH, T.; QUINCI, T.; ALMOSNI, S.; et al.: In: *Applied Physics Letters* **101** (2012), No. 25, pp. 251906–251906–4
- [KNQA13] KUYALIL, J.; NGUYEN THANH, T.; QUINCI, T.; ALMOSNI, S.; et al.: In: *Journal of Crystal Growth* **377** (2013), pp. 17–21
- [LiBo10] LIANG, Di; BOWERS, John E.: In: *Nat Photon* **4** (2010), No. 8, pp. 511–517
- [NRCP11] NGUYEN THANH, T.; ROBERT, C.; CORNET, C.; PERRIN, M.; et al.: In: *Applied Physics Letters* **99** (2011), No. 14, pp. 143123–143123–3
- [NRGL12] NGUYEN THANH, T.; ROBERT, C.; GIUDICELLI, E.; LÉTOUBLON, A.; et al.: In: *Journal of Crystal Growth* **378** (2013) pp. 25-28
- [NRLC12] NGUYEN THANH, T.; ROBERT, C.; LÉTOUBLON, A.; CORNET, C.; et al.: In: *Thin Solid Films* **541** (2013) pp. 36-40
- [QKNP13] QUINCI, T.; KUYALIL, J.; NGUYEN THANH, T.; PING WANG, Y.; et al.: In: *Journal of Crystal Growth* **380** (2013), pp. 157–162
- [RCTN12] ROBERT, C.; CORNET, C.; TURBAN, P.; NGUYEN THANH, T.; et al.: In: *Physical Review B* **86** (2012), No. 20, p. 205316
- [TFWK10] TAKAGI, Yasufumi; FURUKAWA, Yuzo; WAKAHARA, Akihiro; KAN, Hirofumi.: In: *Journal of Applied Physics* **107** (2010), No. 6, pp. 063506–063506–8



---

---

## LIST OF PUBLICATIONS ISSUED FROM THIS THESIS

---

---

### REGULAR ARTICLES

- [1] **T. Nguyen Thanh**, C. Robert, C. Cornet, M. Perrin, *et al.* "Room temperature photoluminescence of high density (In,Ga)As/GaP quantum dot" *Applied Physics Letters*, vol. **99**, p. 143123, 2011.
- [2] **T. Nguyen Thanh**, C. Robert, W. Guo, A. Létoublon, *et al.* "Structural and optical analyses of GaP/Si and (GaAsPN/GaPN)/GaP/Si nanolayers for integrated photonics on silicon" *Journal of Applied Physics*, vol. **112**, p. 053521, 2012.
- [3] **T. Nguyen Thanh**, C. Robert, E. Giudicelli, A. Létoublon, *et al.* "Quantitative study of microtwins in GaP/Si thin film and GaAsPN quantum wells grown on silicon substrates" *Journal of Crystal Growth*, vol. **378**, p. 25-28, 2013.
- [4] **T. Nguyen Thanh**, C. Robert, A. Létoublon, C. Cornet, *et al.* "Synchrotron X-ray diffraction analysis for quantitative defect evaluation in GaP/Si nanolayers" *Thin Solid Films*, vol. **541**, p. 36-40, 2013.
- [5] C. Cornet, **T. Nguyen Thanh**, T. Quinci, S. Almosni, *et al.* "Preferential incorporation of substitutional nitrogen near the atomic step edges in diluted nitride alloys" *Applied Physics Letters*, vol. **101**, p. 251906, 2012.
- [6] J. Kuyyalil, **T. Nguyen Thanh**, T. Quinci, S. Almosni, *et al.* "Nitrogen-phosphorus competition in the molecular beam epitaxy of GaPN" *Journal of Crystal Growth*, vol. **377**, p. 17-21, 2013.

- [7] S. Almosni, C. Robert, **T. Nguyen Thanh**, C. Cornet, *et al.* "Evaluation of InGaPN and GaAsPN materials lattice-matched to Si for multi-junction solar cells" *Journal of Applied Physics*, vol. **113**, p.123509, 2013.
- [8] C. Robert, A. Bondi, **T. Nguyen Thanh**, J. Even, *et al.* "Room temperature operation of GaAsP(N)/GaP(N) quantum well based light-emitting diodes: Effect of the incorporation of nitrogen" *Applied Physics Letters*, vol. **98**, p. 251110, 2011.
- [9] T. Quinci, J. Kuyyalil, **T. Nguyen Thanh**, Y. Ping Wang, *et al.* "Defects limitation in epitaxial GaP on bstepped Si surface using UHVCVD-MBE growth cluster" *Journal of Crystal Growth*, vol. **380**, p. 157-162, 2013.
- [10] C. Robert, C. Cornet, P. Turban, **T. Nguyen Thanh**, *et al.* "Electronic, optical and structural properties of (In,Ga)As/GaP quantum dots" *Physical Review B*, vol. **86**, p. 205316, 2012.

### **CONFERENCE PAPERS**

- [1] **T. Nguyen Thanh**, C. Robert, C. Cornet, W. Guo, *et al.* "Coherent integration of photonics on silicon through the growth of nanostructures on GaP/Si" *Proc. SPIE 8268, Quantum Sensing and Nanophotonic Devices IX*, 82681H (January 20, 2012), DOI: 10.1117/12.910279
- [2] C. Robert, **T. Nguyen Thanh**, C. Cornet, P. Turban, *et al.* "Theoretical and experimental studies of (In,Ga)As/GaP quantum dots" *Nanoscale Research Letters*, vol. **7**, p. 643, 2012.
- [3] C. Robert, **T. Nguyen Thanh**, M. Perrin, C. Cornet, *et al.* "Structural and optical properties of AlGaP confinement layers and InGaAs quantum dots light emitters onto GaP substrate : towards photonics on silicon applications" *Thin Solid Films*, vol. **541**, p. 87, 2013.

- [4] W. Guo, **T. Nguyen Thanh**, G. Elias, A. Letoublon, *et al.* "Structural characterisation of GaP/Si nanolayers" in **Compound Semiconductor Week (CSW/IPRM), 2011 and 23rd International Conference on Indium Phosphide and Related Materials**, 2011, pp. 1–4.
- [5] C. Cornet, C. Robert, **T. Nguyen Thanh**, W. Guo, *et al.* "Carrier injection in GaAsPN/GaPN quantum wells on Silicon" in **Compound Semiconductor Week (CSW/IPRM), 2011 and 23rd International Conference on Indium Phosphide and Related Materials**, 2011, pp. 1–4.
- [6] O. Durand, C. Robert, **T. Nguyen Thanh**, S. Almosni, *et al.* "Structural and optical properties of (In,Ga)As/GaP quantum dots and (GaAsPN/GaPN) diluted-nitride nanolayers coherently grown onto GaP and Si substrates for photonics and photovoltaics applications" **Proc. SPIE 8631, Quantum Sensing and Nanophotonic Devices X**, 863126 (February 4, 2013); DOI: 10.1117/12.2012670

## AVIS DU JURY SUR LA REPRODUCTION DE LA THESE SOUTENUE

**Titre de la thèse:**

Photonique sur silicium à base de nanostructures III-V épitaxiées sur silicium

**Nom Prénom de l'auteur : NGUYEN THANH TRA**

**Membres du jury :**

- Madame FONTAINE Chantal
- Monsieur BOUCHIER Daniel
- Monsieur SAINT-GIRONS Guillaume
- Monsieur BOULLE Alexandre
- Monsieur BERTRU Nicolas
- Monsieur DURAND Olivier
- Monsieur CORNET Charles

Président du jury : *Nicolas BERTRU*

Date de la soutenance : 17 Septembre 2013

Reproduction de la these soutenue

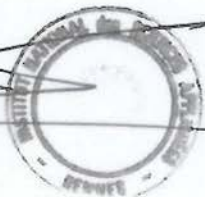
- Thèse pouvant être reproduite en l'état  
 Thèse pouvant être reproduite après corrections suggérées

Fait à Rennes, le 17 Septembre 2013

Signature du président de jury

Le Directeur,

M'hamed DRISSI



Cette thèse porte sur l'optimisation de la croissance hétérogène de nanostructures III-V sur substrat de Si(001) désorienté selon [110]. Le but principal concerne la réalisation de sources optiques efficaces sur substrat de Si pour les interconnexions optiques à très haut débit inter et intra puces, dans le cadre du développement de circuits optoélectroniques intégrés (OEIC – optoelectronic integrated circuit).

Dans un premier temps, cette étude porte sur l'optimisation de l'incorporation d'azote dans GaPN sur substrat de GaP (001), de façon à obtenir l'accord de paramètre de maille avec le Si. Cette étude est intéressante pour la croissance des composés III-V à azote dilué, tels que GaAsPN, qui sont très attractifs pour des applications lasers à grande longueur d'onde et des applications photovoltaïques à haut rendement, sur substrats de Si. Nous avons ensuite étudié la croissance d'une couche active à base de boîtes quantiques (In,Ga)As sur substrat de GaP(001). Ces boîtes présentent une haute densité et une bonne uniformité en taille. La photoluminescence à température ambiante est également obtenue sur ces boîtes quantiques, ce qui est très encourageant pour la réalisation de sources optoélectroniques intégrées sur substrat de silicium. Dans la troisième partie, nous avons étudié la croissance homoépitaxiale de Si par UHV/CVD nécessaire pour enterrer des contaminants résiduels à la surface, et obtenir une surface propice à l'hétéroépitaxie de GaP de qualité structurale optimale. L'étude de croissance inclue la formation de doubles marches atomiques, favorisée par la désorientation du substrat, permettant de limiter l'apparition de défauts structuraux. Finalement, l'interface GaP/Si est optimisée, tout en obtenant une surface de GaP plane et une densité de défauts minimale. Une méthodologie pour quantifier les défauts structuraux (domaines d'antiphase, micro-macles) par diffraction des rayons X au Synchrotron et en laboratoire est présentée. Cette étude révèle une anisotropie d'orientation des micro-macles, liée à la direction de désorientation du substrat de Si, et une forte réduction de la densité de macles à haute température de croissance. La croissance de GaP sur substrat de Si, en couche mince d'épaisseur inférieure à l'épaisseur critique est obtenue spécifiquement avec un cluster de croissance composé d'un bâti Si UHV/CVD connecté sous ultra-vide avec un bâti III-V MBE. Les résultats montrent une réduction importante des défauts structuraux ce qui permet d'obtenir un pseudo-substrat GaP/Si présentant une surface plane, appropriée pour la croissance ultérieure de sources optiques efficaces.

Les résultats obtenus permettent d'envisager la réalisation de sources lasers à base de composés III-V sur substrat de silicium.

**Mots clés :** Photonique sur silicium, GaP/Si, boîtes quantiques InGaAs/GaP, semi-conducteurs III-V, MBE, CVD, XRD, RSM, figures de pôle, Rayonnement synchrotron, AFM, Micro-macles, Domaines d'antiphase, composés à azote dilué.

This thesis focuses on the heterogeneous growth optimization of III-V nanostructures on Si (001) substrate displaying a miscut toward [110]. The main purpose concerns the integration of efficient light sources on Si substrate for high-speed optical interconnects inter-and intra-chip, as a cornerstone for the development of optoelectronic integrated circuits (OEIC).

First, this study focuses on the optimisation of nitrogen incorporation in GaPN on GaP(001) substrate, while reaching the lattice-matching condition with Si. This study is also interesting for the growth of any GaPN-based dilute nitride compounds, such as GaAsPN, which are very attractive for long wavelength laser applications and high-efficiency photovoltaic applications on Si substrates. In a second step, we studied the growth of an active layer based on (In,Ga)As quantum dots (QD) on GaP (001) substrate. These QD display a high density and good uniformity in size. Room temperature photoluminescence is also obtained on these QD, which is very promising for the fabrication of integrated optoelectronic sources on a silicon substrate. In the third part, this study focuses on the homoepitaxial growth of Si by UHV/CVD necessary to bury residual contaminants initially present on the Si surface, and to obtain a Si surface suitable for the subsequent heteroepitaxial growth of optimal structural quality GaP layer. This includes the formation of double atomic steps, by step bunching and favors by the substrate miscut, in order to limit the structural defects. Finally, the GaP/Si interface is optimized, while obtaining a flat GaP surface and a minimum defects density. A methodology to quantify the structural defects (anti-phase domains, micro-twins) by X-ray diffraction using Synchrotron and laboratory sources is presented. This study reveals an anisotropic behavior of the micro-twins, linked to the miscut direction of the Si substrate, and a dramatic reduction of the micro-twins density at high growth temperature. The growth of thin GaP layers on Si substrates, with thickness less than the critical one and obtained with a purposely dedicated growth cluster composed of a Si UHV/CVD chamber connected under UHV with a III-V MBE chamber, shows a significant reduction of the structural defects and provides a GaP/Si pseudo-substrate with a flat surface suitable for subsequent growth of efficient light sources.

The results obtained in this thesis allow considering the realization of laser sources based on III-V compounds on silicon substrate in a near future.

**Keywords:** photonics on silicon, GaP/Si, InGaAs/GaP quantum dots, III-V semiconductors, CVD, MBE, XRD, RSM, pole figures, Synchrotron radiation, , AFM, Microtwins, Antiphase domains, dilute nitride compounds.